UNIVERSITY OF Southampton

University of Southampton Research Repository
ePrints Soton

Copyright © and Moral Rights for this thesis are retained by the author and/or other copyright owners. A copy can be downloaded for personal non-commercial research or study, without prior permission or charge. This thesis cannot be reproduced or quoted extensively from without first obtaining permission in writing from the copyright holder/s. The content must not be changed in any way or sold commercially in any format or medium without the formal permission of the copyright holders.

When referring to this work, full bibliographic details including the author, title, awarding institution and date of the thesis must be given e.g.

AUTHOR (year of submission) "Full thesis title", University of Southampton, name of the University School or Department, PhD Thesis, pagination

http://eprints.soton.ac.uk

UNIVERSITY OF SOUTHAMPTON

FACULTY OF ENGINEERING, SCIENCE AND MATHEMATICS

School of Physics and Astronomy

AGN Outflows and the Cluster Cooling Flow Conundrum

Ilja Jonathan Klees

Thesis for the degree of Doctor of Philosophy

June 2011

UNIVERSITY OF SOUTHAMPTON

ABSTRACT

FACULTY OF ENGINEERING, SCIENCE AND MATHEMATICS
SCHOOL OF PHYSICS AND ASTRONOMY

Doctor of Philosophy

AGN Outflows and the Cluster Cooling Flow Conundrum

Ilja Jonathan Klees

Temperature distributions within cores of galaxy clusters indicate gas in the core should cool down rapidly and contract. The cooling flow problem involves the hypothesis that the rapidly cooling gas should eventually condensate into unobserved molecular clouds. Active galactic nuclei (AGNs) are thought to be able to counter catastrophic cooling.

This thesis provides an overview of the theory and design philosophy of hydrodynamical simulations and a hydrodynamical code called FLASH, which was created by Fryxell et al. (2000). This code is expanded with gravity and AGN outflow units to support the simulation of a pair of outflows in the intracluster medium whilst using classical fluid dynamics.

The three simulation chapters involve a single parameter being varied and its impact on jet morphology and the heating process studied. The jet opening angle was found not to impact the heating process, while a study on wave heating demonstrated the presence of sound waves. The third project involved varying the jet heating power as a trade-off of thrust, while keeping the energy output constant. That proved to greatly influence the morphology of the backflow and the bubble inflation process.

The simulations show that despite the superficial simplicity of the model, the results provide valuable insight into the physics behind an AGN outflow and the available heating mechanisms. Future challenges include the extension of the model, which would require more reliable data and hypotheses on cluster cores.

Contents

Declaration Of Authorship

I, Ilja Jonathan Klees, declare that this thesis entitled *AGN Outflows and the Cluster Cooling Flow Conundrum* and the work presented in it are my own and has been generated by me as the result of my own original research. I confirm that:

- This work was done wholly while in candidature for a research degree at this University;
- Where any part of this thesis has previously been submitted for a degree or any other qualification at this University or any other institution, this has been clearly stated;
- Where I have consulted the published work of others, this is always clearly attributed;
- Where I have quoted from the work of others, the source is always given. With the exception of such quotations, this thesis is entirely my own work;
- I have acknowledged all main sources of help;
- None of this work has been published before submission.

Signed: _____

Date: _____

Acknowledgements

Special thanks I would like to give to Marcus Brüggen. The lively discussions we had about my simulations reminded me to persevere and enjoy the experience of computational astronomy. After studying in an observers' bulwark like Southampton it was a great experience to discuss my project with someone who is knowledgeable in and enthusiastic about the field of research. In the end the combination makes all the difference.

Then I'd like to thank Tony Bird, who after my original supervisor left accepted the task of seeing me through the rest of my research. Despite the fact that hydrodynamical simulations on AGNs is far from within his field of expertise he was interested, tried to learn by asking me questions which could be very helpful for me to get my own thoughts together. Together with my advisor Tom Maccarone he also advised me when I had difficulty seeing the light at the end of the tunnel, and when this thesis was written they supplied me with valuable comment. Georgi Pavlovski, who de facto was my supervisor during the first 1.5 years, I'd also like to thank for his efforts and Christian Kaiser for giving me the opportunity to do the research in the first place.

Friends and family have proved invaluable during my stay in England, and a general thanks to them. Andy and Hardo, we had fun in Southampton and I hope we keep in touch! Papa en mama, dit is even goed jullie werk als het mijne. Mijn zusje Nienke, met wie ik zoveel goede tijden in Finland en ook in Ierland gehad heb (Bunratty!), en mijn broer Joeri, waarmee ik wetenschap en computer techniek zo vaak met veel plezier bespreek. Tot slot mijn vrienden, in het bijzonder Lennart.

Chapter 1

Introduction

In the 20th century it emerged that many galaxies are encountered in associations. The Milky Way is a larger member of the Local Group, a group of some thirty members. Associations with more than about 50 member galaxies are called *clusters of galaxies*. While visual observation indicates that space between member galaxies in clusters is empty, X-ray observations revealed that galaxy clusters are endowed with an atmosphere of hot, tenuous gas, known as the *intracluster medium*.

The amount of thermal radiation is inferred to be significant in the cores of some clusters. Significant radiative cooling results in the gas cooling down and contracting, which amounts to an inflow of hot gas from the cluster periphery known as a *cooling flow*. Though these flows are indeed observed, a conundrum arises when the fate of the cold gas is considered, as the hypothetical presence of cool gas in these cluster cores was refuted by recent *XMM-Newton* observations. The consensus is that a heating mechanism is influencing the cooling process in the cluster core.

Active galactic nuclei (AGNs) are systems of accreting supermassive black holes found most cooling clusters, and are inferred to be able to generate sufficient heat output by emitting a pair of supersonic, relativistic, highly collimated outflows. Modelling the heat generation and transfer process to test the viability of the hypothesis is an arduous task, because of the exotic physics involved – including general relativity and electrodynamics. Instead, the issue is negotiated by addressing only part of the process. In this chapter the cooling flow problem and heating mechanisms are outlined, followed by an overview of research presented in this thesis.

1.1 Optical observations of galaxy clusters

In places were the sky does not bathe in city light, a casual glance at the celestial sphere reveals a band of pale white light known as the Milky Way. Though widely observed across the world, it was not until the 17th century that Galileo realised the vast expanse of pale light constitutes a collection of radiant stars. In explaining the structure, Immanuel Kant and Thomas Wright proposed a century later that the Sun is also part of the Milky Way, and that constituent stars of the Milky Way form a flat, disc-like structure. Kant proposed that diffuse objects observed on the night sky might be distant structures similar to the Milky Way, but residing beyond the its rim as "island universes" – modern science favours the term *galaxies*.[1]

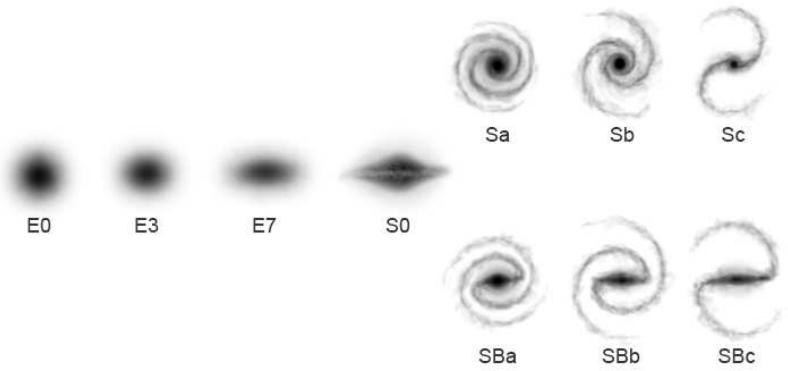

Figure 1.1: Hubble sequence for galaxy classification. The scheme include *elliptical galaxies* (E), *spiral galaxies* (S), and *barred spirals* (SB). The cross-breed type S0 is a *lenticular galaxy*, and galaxies without any apparent structure are termed *irregular* (Irr) galaxies. (Credit: NASA/ESA Hubble)

The nature of these nebulae would be debated until in Edwin Hubble (1923) ascertained the extragalactic nature of the Andromeda galaxy upon finding a Cepheid variable star.[2] Hubble proposed a classification scheme for galaxies, based on their apparent visual morphology as projected on the sky (figure 1.1).

[1] The word "galaxy" comes from Ancient Greek and means *milky*, referring to the Milky Way.
[2] Cepheids have a reliable relation between their pulsation period and luminosity.

Elliptical galaxies are featureless ellipsoidal structures. The surface brightness of an elliptical galaxy as a function of the projected distance to the centre r is found to approximate a *de Vaucouleurs profile*

$$\lg\left(\frac{S}{S_\mathrm{e}}\right) = -3.3307\left[\left(\frac{r}{r_\mathrm{e}}\right)^{1/4} - 1\right], \tag{1.1}$$

where S_e is the surface brightness at an *effective radius* r_e. They comprise both the smallest and largest of galaxies, with diameters ranging from 1 kpc to 200 kpc and masses of $10^8\,\mathrm{M}_\odot$ to $10^{13}\,\mathrm{M}_\odot$ on average. Elliptical galaxies have an older star population, with little interstellar gas and star formation activity. Globular concentrations of stars orbit the galactic core in (compared to a spiral galaxy with similar luminosity) large numbers. The Hubble scheme elliptical galaxies defines subtypes by ellipticity only. More recent observations has showed ellipticals are a varied lot, comprising the smallest and largest of galaxies. Within the scope of this thesis it is useful to mention the *cD galaxy*, a very bright giant elliptical galaxy with an extended envelope and a large number of associated globular clusters.

The core of a *spiral galaxy* has a similar surface brightness profile and stellar population as an elliptical galaxy. This bulge is embedded in a disc comprised of stars, gas, and dust, and a pair of spiral structures with ongoing star formation. The system is enveloped by a halo with field stars and globular clusters.

Nearly all galaxies in the Universe are encountered in *groups* or *clusters of galaxies*. Galaxy clusters were extensively catalogued by notably Abell (1958) and Zwicky, Herzog and Wild (1961). A number of classification sequences were formulated based on galaxy richness (the number of member galaxies), apparent order of galaxies within the cluster, or the brightness contrast of the brightest galaxy to that of other member galaxies – but these systems show a high degree of correlation. *Regular clusters* are rich and spherically condensed, and its brightest galaxy (an ordinary giant elliptical galaxy, often a cD galaxy) is markedly brighter than the other members. *Irregular clusters* are less rich, lack an overall galaxy concentration profile with sub-clustering of galaxies throughout the system. Typical observables of the galactic population include the projected distribution of galaxies, and the line-of-sight velocity component from Doppler-shifted emission lines. Using Hubble's law and the mean velocity, the distance to the galaxy cluster can also be determined.

1.2 Dark matter

It has been often assumed regular clusters are relaxed (i.e. in a steady state). This seems to be confirmed by inferred cluster diameters $l \sim 1\,\mathrm{Mpc}$ and standard deviation of the galaxy velocity distribution $v_\mathrm{s} \sim 10^3\,\mathrm{km\,s^{-1}}$, which suggests a free galaxy embedded in a regular formation would require a *crossing time*

$$t_\mathrm{cr} \equiv \frac{l}{v_\mathrm{s}} \sim 1\,\mathrm{Ga} \tag{1.2}$$

to cross the system from one side to the other. Assuming the cluster age approximates the Hubble time $t_\mathrm{H} > t_\mathrm{cr}$, an initially regular galaxy configuration would have been disrupted by unconstrained motion of the galaxies.

Equating the cluster to the aggregate of gravitationally interacting galaxies, the moment of inertia is $I = \sum_i M_i r_i^2$, with energy $E = E_\mathrm{k} + E_\mathrm{g}$ comprising kinetic energy $E_\mathrm{k} = \sum_i \frac{1}{2} M_i v_i^2$ and gravitational potential energy $E_\mathrm{g} = -\frac{1}{2}\sum_i \sum_{j\neq i} \frac{GM_iM_j}{r_{ij}}$. Differentiating twice with respect to time and applying the Newtonian equation of motion with the only force being the gravitational force between the galaxies,

$$\frac{1}{2}\frac{d^2 I}{dt^2} = 2E_\mathrm{k} + E_\mathrm{g} \tag{1.3}$$

Assuming steady state yields $E_\mathrm{g} = -2E_\mathrm{k}$ and thus $E = -E_\mathrm{k}$, which is the *virial theorem*. The theorem can be expressed in observable quantities by defining the cluster mass $M = \sum_i M_i$, $\langle v^2 \rangle \equiv E_\mathrm{k}/M$ and the gravitational radius $r_\mathrm{g} \equiv M^2/E_\mathrm{g}$, yielding

$$M = \frac{r_\mathrm{g}\langle v^2 \rangle}{G}. \tag{1.4}$$

Deprojecting the line-of-sight velocity by assuming isotropy $\langle v^2 \rangle \approx 3v_\mathrm{s}^2$, and r_g can be equated to a typical scale length in a galaxy distribution function. This yields typical cluster masses of $M \sim 10^{15}\,\mathrm{M_\odot}$, which combined with luminosities of $L \sim 10^{13}\,\mathrm{L_\odot}$ yields mass-to-light ratios of $M/L \sim 100\,\mathrm{M_\odot/L_\odot}$ (cf. Smith (1936), Neyman, Page and Scott (1961)). The high mass-to-light ratio can be explained if a typical stellar population is appended by *dark matter*, which is defined as unobserved mass. Dark matter might include sub-stellar objects (brown dwarfs, planets, comets, and asteroids), compact objects (cool white dwarfs, neutron stars, black holes), or weakly interacting particles (such as neutrinos).

1.3 The intracluster medium

In the post-World War II years. Herbert Friedman had been involved in a project concerning the search for airborne radioactive material by launching captured German V2 rocket equipped with Geiger counters as sounding rockets. Upon obtaining grants to employ these rockets for astrophysical research, Friedman, Lichtman and Byram (1951) was able to measure X-ray and ultraviolet radiation emanating from the solar corona from an altitude of up to 150 km.

Giacconi et al. (1962) promoted the field and detected the first extrasolar source subsequently named Scorpius X-1,[3] which was followed by Byram, Chubb and Friedman (1966) detecting extragalactic X-ray sources associated with radio galaxies Virgo A and Cygnus A in April 1965. Launched in December 1970, the first X-ray satellite *Uhuru* confirmed the presence of extended sources of X-rays in clusters of galaxies (Kellogg et al., 1973).

Telescope	Lifetime	Energy range	Remarks
Uhuru	1970 - 1973	2 keV to 20 keV	First comprehensive all sky survey
Einstein	1978 - 1981	0.2 keV to 20 keV	First imaging X-ray telescope in space
ROSAT	1990 - 1999	0.1 keV to 2.5 keV	All sky-survey in the soft X-ray band
ASCA	1993 - 2001	0.4 keV to 10 keV	
BeppoSAX	1996 - 2002	0.1 keV to 300 keV	Broad-band energy
Chandra	1999 -	0.1 keV to 10 keV	Superb spatial resolution $< 1''$
XMM Newton	1999 -	0.15 keV to 15 keV	Very large collecting area

Table 1.1: A list of X-ray observatories mentioned in this thesis

X-ray astronomy comprises very short wavelengths with photons having an energy ranging from 0.1 keV to 100 keV. At these high photon energies the photons tend to be absorbed rather than reflected by a telescope, requiring near-parallel grazing incidence. Discounting rocket-borne mirrors, the first observatory equipped with a grazing telescope rather than detectors similar to Geiger counters was *Einstein Observatory* (1978). An overview of X-ray observatories mentioned in this thesis is provided in table 1.1.

[3]Scorpius X-1 is a low-mass X-ray binary, comprising a neutron star and a sub-solar mass star.

1.3.1 Coronal plasma

Uhuru (1971) identified clusters of galaxies as extended X-ray sources. Considering the source morphology (see figure 1.2) and spectrum, the interpretation was put forward that the emission originates from a hot, tenuous gas, i.e. the *intracluster medium* (ICM). Evidence in support of this interpretation was soon found in a highly ionised iron line feature in the spectrum of clusters near 6.7 keV (Mitchell et al. (1976), Serlemitsos et al. (1977)), which is difficult to attribute to any process but thermal emission.

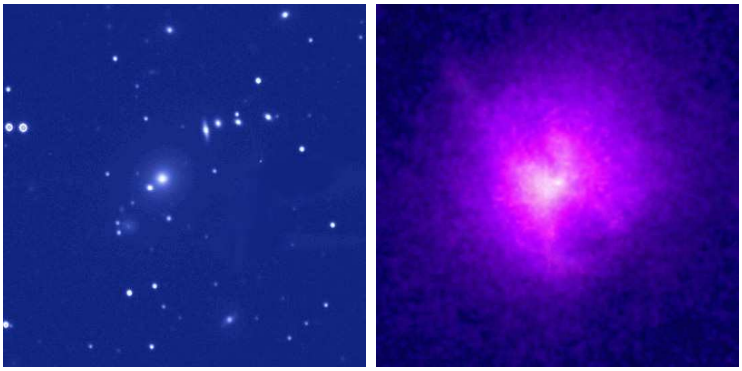

(a) Optical. (b) X-ray.

Figure 1.2: Optical and X-ray images (not to scale) of Hydra A provides evidence of the intracluster medium. (Credit: La Palma/B. McNamara; NASA/CXC/SAO)

The ICM is modelled as a *plasma*, an ionised gas in which ions and electrons interact through self-generated electromagnetic fields. X-ray emission is usually the result of an electron-photon process, involving electrons bound in an atom, or free due to earlier ionisation. A process is *thermal* if the generating electron population obeys a Maxwell-Boltzmann energy distribution characterised by a single temperature.

A basic model applicable to the ICM is the *coronal plasma*, originally designed for the solar corona (see Mewe (1999) and references therein). The model applies to optically thin plasmas – few photons are to be scattered or absorbed on a path. Ions are excited by collisions, but due to long collision times radiatively de-excite. Radiation losses are balanced by mechanical heating. Ions and electrons obey a Maxwell-Boltzmann energy distribution function characterised by a common temperature, ionisation equilibrium is assumed.

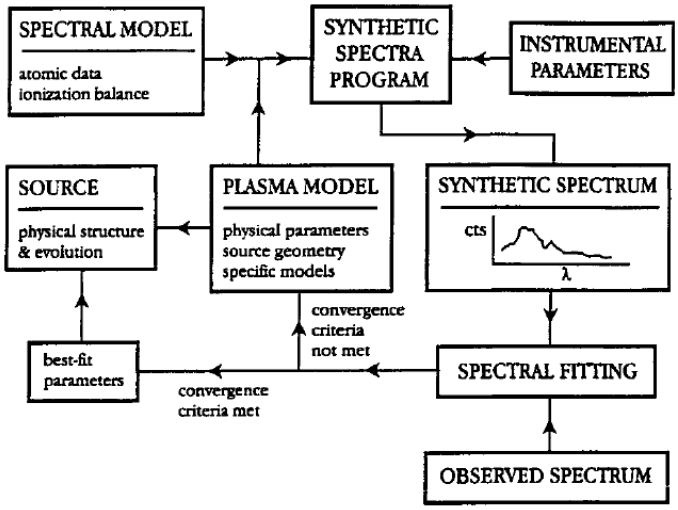

Figure 1.3: Processing diagram detailing the steps taken to analyse the spectrum of a plasma (Credit: Mewe (1999)).

An observed spectrum is analysed by applying a *radiation code* (e.g. Mekal/SPEX, see figure 1.3). A synthetic plasma is set up by initialising the model parameters. These are in this case the electron density $n_{\rm e}$, the common temperature T, and the abundances. A plasma in ionisation equilibrium is produced, and a synthetic spectrum constructed using telescope specifications. The synthetic spectrum is compared to the observed spectrum, and the model parameters are adjusted until differences are no longer considered significant. The best-fit parameters are then presumed to describe the observed emitting plasma.

Emission processes can be divided into thermal and non-thermal processes, where in case of thermal processes the generating electron population obeys a Maxwell-Boltzmann distribution characterised by a temperature. In a coronal plasma one of two processes are dominant, depending on the temperature. For $T \gtrsim 10^8\,\mathrm{K}$, the emitted radiation is *thermal bremsstrahlung*, which involves a free electron slowing down and emitting a photon while interacting with a nearby ion through Coulomb forces. *Discrete line emission* determines the spectrum for $T \lesssim 5 \times 10^7\,\mathrm{K}$; this involves an excited ion returning to a lower excited state or the ground state, emitting a photon in the process carrying the precise difference in energy. As ions have a set of intrinsically-determined energy levels, each ion species is represented by a unique set of recognisable emission lines in the spectrum.

Other emission mechanisms include *radiative recombination*, in which a free electron is captured by an ion. *Dielectronic recombination* is similar but while recombining part of the energy surplus is used to excite a different bound electron to a higher energy level. Bound electrons in an excited but metastable state cannot return to the ground state without violating selection rules, and return by emitting two photons simultaneously. As only the sum of the photon energies is determined by the ion species and the two photons can have any energy otherwise, a group of metastable ions will produce a continuum rather than a set of discrete lines in the spectrum.

1.3.2 Observable properties

Space between between cluster galaxies is inferred to be filled with a corona of hot ($T \sim 10^7\,\mathrm{K}$ to $10^8\,\mathrm{K}$), tenuous ($n_\mathrm{e} \sim 10^2\,\mathrm{m}^{-3}$ to $10^4\,\mathrm{m}^{-3}$) plasma. The ICM is contained within a radius of 1 Mpc to 2 Mpc, its mass surpassing that of all member galaxies combined.

The ICM is thought to have formed and heated as result of collapse of concentrations of gas in the primeval medium when the cluster of galaxies first formed (Gunn and Gott, 1972). Observations are consistent with primordial abundances, where the distribution of baryonic particles is 90% hydrogen, 10% helium, with traces of heavier elements. Relatively high iron abundances (about 1/3 solar, Mushotzky et al. (1978), Mushotzky (1984), Edge and Stewart (1991)) suggest that a fraction of the ICM has been processed by stars in cluster galaxies.

The required enrichment rules out normal stellar processes as a source; Renzini et al. (1993) suggests supernova activity in elliptical cluster galaxies. ASCA-acquired data on O, Ne, Mg, Si, S, Ar, Ca, and Ni abundances by Mushotzky et al. (1996) on four clusters indicates that metal enrichment of the intracluster medium is best explained by contributions from core collapse supernovae, though Finoguenov and Ponman (1999) note supernova Ia activity becomes more predominant toward the cluster core. De Grandi et al. (2004) and Böhringer et al. (2004) associate the central abundance peak of associated elements (Fe, Ni, Si-group elements) with stellar processes occurring in centrally-located giant elliptical galaxies.

1.3.3 Intracluster magnetic field

A plane-polarised electromagnetic travelling through a magnetised ICM is affected by the line-of-sight component of the magnetic field by the magneto-optic Faraday effect. Discovered empirically in 1845 by Micheal Faraday, the underlying theory involves a quantum-mechanical treatment of dispersion. The Faraday effect has a similar effect on dispersion as the Zeeman effect has on degeneracy, and makes the plasma birefringent with respect to left and right-polarised waves. Decomposing the plane-polarised wave into a superposition of one clockwise and one counter-clockwise circular-polarised waves, the plane of polarisation is consequentially rotated by

$$\Delta\theta = R_{\mathrm{m}}\lambda^2, \tag{1.5}$$

where λ is the wavelength of the radiation and

$$R_{\mathrm{m}} = \frac{e^3}{8\pi^2\epsilon_0 m_{\mathrm{e}}^2 c^3}\int_0^d n_{\mathrm{e}} B_{\parallel} dl \approx 2.62\times10^{-13}\,\mathrm{T}^{-1}\int_0^d n_{\mathrm{e}} B_{\parallel} dl \tag{1.6}$$

is the *rotation measure* (Spitzer, 1978). The ray is presumed to follow a path parametrised by l which ranges from 0 at the source to d at the observer. If the plane of polarisation is known to be the same at two wavelengths, measuring the polarisation at the two wavelengths determines both the original plane of polarisation and the rotation measure R_{m}.

Radio galaxies in the ICM are found to be reliable sources of synchrotron radiation, with degrees of plane-polarisation in excess of 70%. Studies of large statistical samples of clusters yield intracluster magnetic field strengths of $\sim 0.1\,\mathrm{nT}$ (e.g. Kim, Tribble and Kronberg (1991), Clarke, Kronberg and Böhringer (2001)).

1.3.4 The ICM in fluid approximation

A *fluid* is defined a substance which continuously deforms when shearing forces act upon it, and is used to model liquids, gases, and plasmas.

Equation of state

Assume particles constituting the plasma are non-interacting and spineless. Deriving the canonical partition function and potential (the Helmholtz free energy), the ideal gas law (an equation of state for pressure) is found

$$p = 2n_{\mathrm{e}}k_{\mathrm{B}}T. \tag{1.7}$$

Quasi-neutrality

Given the kinetic theory interpretation of pressure the kinetic energy of an electron equals $\frac{3}{2}k_{\mathrm{B}}T$, yielding the root-mean-square electron speed

$$v_{\mathrm{rms,e}} = \sqrt{\frac{3k_{\mathrm{B}}T}{m_{\mathrm{e}}}}. \tag{1.8}$$

Describing an electron population as a continuous distribution subject to mass and momentum conservation, a displaced electron population is derived to oscillate due to the Coulomb restoring force at the *plasma frequency* (Spitzer, 1962)

$$\omega_{\mathrm{p}} = \sqrt{\frac{n_{\mathrm{e}}e^2}{\epsilon_0 m_{\mathrm{e}}}}. \tag{1.9}$$

The *Debye length* defines the length scale at which local charge concentrations are significant, and is estimated

$$\lambda_{\mathrm{D}} = \frac{v_{\mathrm{rms,e}}}{\sqrt{3}\omega_{\mathrm{p}}}. \tag{1.10}$$

where the electron speed component is taken in any one direction. On length scales much larger than $\lambda_{\mathrm{D}} \sim 10^4\,\mathrm{m}$, the ICM can be considered quasi-neutral.

Mean free path in an unmagnetised plasma

The frequency at which electrons and ions collide in an unmagnetised hydrogen plasma is derived by Spitzer (1962) as

$$\nu_{\rm ei} = \frac{n_{\rm e} e^4}{4\pi\epsilon_0^2 m_{\rm e}^2 v_{\rm rms,e}^3} \ln\Lambda, \tag{1.11}$$

where the Coulomb logarithm $\ln\Lambda = \ln(\frac{2\lambda_{\rm D}}{\hbar/m_{\rm e} v_{\rm rms,e}})$. From this the *mean free path*

$$\lambda_{\rm mfp} = \frac{v_{\rm rms,e}}{\nu_{\rm ei}}, \tag{1.12}$$

yielding values of $\lambda_{\rm mfp} \sim$ kpc. If other physical processes operate on scales in excess of this, particles constituting the ICM will collide sufficiently frequently for the ICM to react as a continuum.

Mean free path in a magnetised plasma

In a magnetised hydrogen plasma, electrons will execute cyclotron motion about magnetic field lines at the *Larmor frequency*

$$\omega_{\rm L} = \frac{eB}{m_{\rm e}}. \tag{1.13}$$

This yields a gyroradius $r_{\rm g} \approx v_{\rm rms,e}/\omega_{\rm L} \sim 10^6$ m, and impairs the mobility of electrons in directions perpendicular to the field lines, as the cyclotron radius is much smaller than the Coulomb mean free path. The effective mean free path therefore depends on the configuration of the magnetic field. As there is evidence the field lines in the ICM may be tangled (e.g. Clarke (2004), Enßlin, Vogt and Pfrommer (2005)), and theory suggests electrons moving along field lines may be scattered by self-generated plasma waves, it is generally assumed the effective mean free path is a few times the gyroradius.

Magnetic pressure

The dynamics of a magnetised plasma is affected by magnetic pressure and tension, the first of which tends to be the most influential. The ratio of the thermal pressure p and magnetic pressure $B^2/2\mu_0$ is a measure for the impact of the magnetic field on the dynamics of the plasma, and is known as the *plasma* β

$$\beta = \frac{p}{B^2/2\mu_0}. \tag{1.14}$$

Substituting pressure and magnetic field estimates for the ICM yields $\beta \sim 10^3$, suggesting the effect of magnetic forces on the dynamics of the magnetised ICM is negligible.

Viscous forces and thermal conduction

In such a fluid inter-particle interaction will lead to internal forces, which leads to momentum transport which is described by the stress tensor, where one index defines the momentum component and the other the orientation of the surface across which the momentum is transferred. For subsonic flow the stress tensor is modified by

$$\overleftrightarrow{\sigma}' \approx \eta \left(\vec{\nabla}\vec{v} + (\vec{\nabla}\vec{v})^{\mathsf{T}} \overleftrightarrow{I}_3 \right), \tag{1.15}$$

where η is the *dynamical viscosity*. This viscosity will change the fluid velocity by $\nu\Delta\vec{v}$ (Landau and Lifshitz, 1987), where the *kinematic viscosity* $\nu \equiv \eta/\rho$. As the fluid acceleration due to convection is $-(\vec{v}\cdot\nabla)\vec{v}$, it is possible for characteristic length scale L and velocity scale U to define the *Reynolds number*

$$Re \equiv \frac{U^2 L^{-1}}{\nu U L^{-2}} = \frac{UL}{\nu}, \tag{1.16}$$

where large values for Re implies the fluid is practically inviscid.

In a fluid a temperature gradient will lead to a heat flux $-\kappa\vec{\nabla}T$, where κ is the *thermal conductivity* (Landau and Lifshitz, 1987). In an inviscid fluid, the time-derivative of temperature is modified by $\alpha\Delta T$, where $\alpha \equiv \kappa/\rho c_p$ is the *thermal diffusivity* with c_p the specific heat capacity at constant pressure. Heat convection contributes a term $-\vec{v}\cdot\vec{\nabla}T$, which leads the *Péclet number*

$$Pe \equiv \frac{UL}{\alpha}. \tag{1.17}$$

Spitzer (1962) finds for dynamical viscosity and thermal conductivity in a fully-ionised unmagnetised hydrogen plasma in thermal equilibrium

$$\eta = 2.93\,\mathrm{kg\,m^{-1}\,s^{-1}} \left(\frac{k_\mathrm{B}T_\mathrm{e}}{1\,\mathrm{keV}}\right)^{5/2} \left(\frac{\ln\Lambda}{34.5}\right)^{-1}, \tag{1.18}$$

$$\kappa = 2.45\times10^{6}\,\mathrm{W\,m^{-1}\,K^{-1}} \left(\frac{k_\mathrm{B}T_\mathrm{e}}{1\,\mathrm{keV}}\right)^{5/2} \left(\frac{\ln\Lambda}{34.5}\right)^{-1}. \tag{1.19}$$

If therefore the plasma is polytropic and uniform in composition, then the specific heat $c_\mathrm{p} = (\gamma/\gamma-1)(R/M)$ is constant and the Prandtl number

$$Pr = \frac{Pe}{Re} = \frac{\nu}{\chi} = \frac{\eta c_\mathrm{p}}{\kappa} = (1.20\times10^{-6}\,\mathrm{J\,kg^{-1}\,K^{-1}})\,c_\mathrm{p}. \tag{1.20}$$

In ideal gas models of the ICM the Péclet number is a fixed few per cent of the Reynolds number. An unmagnetised hydrogen plasma that is viscous is therefore thermally conducting as well.

In a tangled magnetic field dynamic thermal conductivity Narayan and Medvedev (2001) find thermal conductivity to be suppressed by a factor 10^{-2} to 0.2. Roediger and Brüggen (2007) infer based on upper limit estimates for the kinematic viscosity in the Coma cluster by Schuecker et al. (2004) that the suppression factor ranges from 10^{-2} to unity. It is convenient to maintain the relation between Pe and Re by setting the suppression factors of viscosity and thermal conductivity to the same number (e.g. Brüggen, Ruszkowski and Hallman (2005), Fabian et al. (2005)).

Estimates of these suppression factors are notoriously difficult to make as they are sensitive the orientation of the intracluster magnetic field. As yet, there is no consensus on the role of viscous forces and thermal conductivity in the ICM. Unless stipulated otherwise, any fluid mentioned in this thesis is *ideal*, i.e. inviscid and thermally non-conducting.

1.3.5 Hydrostatic model

The condensed distribution of galaxies suggests the cluster has reached hydrostatic equilibrium. Different parts of a fluid communicate by the emission of sound waves. Applying statistical mechanics, equations of state for pressure (the ideal gas law) and entropy (the Sackur-Tetrode equation) are obtained in terms of ρ and T,

$$p = \frac{R}{\mu}\rho T, \tag{1.21}$$

$$s = \frac{1}{\gamma - 1}\frac{R}{\mu}\ln\left(\frac{R}{\mu}\frac{T}{\rho^{\gamma-1}};\right), \tag{1.22}$$

where the specific entropy s is arbitrarily set to zero at $T = 0$. Combining these equations yields the *speed of sound* c_s

$$c_\mathrm{s} \equiv \left(\frac{\partial p}{\partial \rho}\right)_s = \sqrt{\frac{\gamma R T}{\mu}}, \tag{1.23}$$

where γ is the ratio of specific heats ($\gamma = 5/3$ for a monatomic gas) and μ is the molar mass of the plasma. Dividing a typical cluster diameter $l \sim 1\,\mathrm{Mpc}$ by the speed of sound yields sound crossing times

$$t_\mathrm{cr,s} \equiv \frac{l}{c_\mathrm{s}} \lesssim 1\,\mathrm{Ga}. \tag{1.24}$$

As this is much smaller than the Hubble time t_H (the assumed age of the galaxy cluster), the ICM is thought to be in hydrostatic equilibrium. Fluid dynamics simulations confirm a hydrostatic atmosphere of hot gas is likely to form as the result of spherical collapse of primordial gas surrounding a cluster of galaxies (e.g. Gull and Northover (1975)).
Assume the ICM is spherically symmetric, then hydrostatic equilibrium implies

$$\frac{dp}{dr} = -\frac{GM_r\rho}{r^2}, \tag{1.25}$$

where M_r denotes the mass contained in a sphere with radius r centred on the centre of mass. The ideal gas law implies

$$\frac{dp}{dr} = \frac{R}{\mu}\left(\frac{d\rho}{dr}T + \rho\frac{dT}{dr}\right). \tag{1.26}$$

Combining equations 1.26 with equation 1.25 implies

$$M_r = -\frac{RTr}{G\mu}\left(\frac{r}{\rho}\frac{d\rho}{dr} + \frac{r}{T}\frac{dT}{dr}\right). \tag{1.27}$$

Luminous mass in clusters of galaxies is thought to account for ∼15% of the cluster mass (e.g. Ostriker, Bode and Babul (2005), Vikhlinin et al. (2006)).

1.3.6 Cooling-core clusters

As a hot, coronal plasma, the ICM radiatively cools mostly by emitting thermal bremsstrahlung. Rybicki and Lightman (1979) derive that for such a plasma the emissivity is

$$j_{\mathrm{brem}} = \frac{8}{3}\left(\frac{2\pi}{3}\right)^{1/2} g_{\mathrm{ff}} \left(\frac{e^4}{(4\pi\epsilon_0)^2 m_{\mathrm{e}} c^2}\right)^{3/2} \exp\left(-\frac{E_{\mathrm{ph}}}{k_{\mathrm{B}}T}\right) \frac{\sum_i n_{\mathrm{e}} n_i Z_i^2}{(k_{\mathrm{B}}T)^{1/2}}. \tag{1.28}$$

where $\gamma = \frac{5}{3}$ is the adiabatic index for a non-relativistic monatomic gas, g_{ff} is the Gaunt factor (Sutherland, 1998), and $\mu = 0.5968 \times 10^{-3}\,\mathrm{kg\,mol^{-1}}$ is the molar mass of the ICM (assuming primordial abundances for a composite single particle). Integrating j_{brem} over frequency and time yields the radiated heat $đq$.

For a monatomic ideal gas, the specific enthalpy is found to be

$$h = \frac{\gamma}{\gamma - 1}\frac{R}{\mu}T; \tag{1.29}$$

the gauge constant is chosen such that $h = 0$ implies $T = 0$.

The *cooling time* is defined as the time it takes to cool the ICM isobarically from its current temperature to 0 K, which implies $dh = đq$ and (Sarazin, 1988)[4]

$$t_{\mathrm{cool}} \equiv \left(\frac{1}{h}\frac{dh}{dt}\right)^{-1} = 9.9\,\mathrm{Ga} \times \left(\frac{n_{\mathrm{e}}}{10^3\,\mathrm{m^{-3}}}\right)^{-1} \left(\frac{T}{10^8\,\mathrm{K}}\right)^{1/2}. \tag{1.30}$$

The cooling time tends to be large in comparison to the cluster age (which is assumed to approximate the Hubble time t_{H}), and for this reason cooling is in general is not a terribly significant process.

In over seventy per cent of the clusters, however, the cooling time drops below the Hubble time within 100 kpc distance of the cluster centre (e.g. Edge, Stewart and Fabian (1992), Peres et al. (1998), Vikhlinin et al. (2006)). If these clusters were created in this state, the cores of these clusters are cooler than the cluster periphery at the current time. For this reason, these clusters are known as *cooling-core clusters*. Considering a sample of 27 cD-type galaxies in the cores of rich cooling-core clusters, Burns (1990) finds 71% to be radio-loud active galactic nuclei, a finding which has more recently been confirmed by Mittal et al. (2009).

[4]Sarazin (1988) uses proton density instead of electron density; given primordial abundances $n_{\mathrm{p}} \approx 0.86 n_{\mathrm{e}}$.

1.4 Active galactic nuclei

The first published encounter of *active galactic nuclei* (AGNs) by Fath (1909) involved the observing of six unusual emission lines superposed on the regular stellar continuum in the spectrum of the nucleus of spiral nebula NGC 1068. more of these objects were observed, all having very luminous stellar nuclei emitting an unusually high fraction of the total light of the system. Seyfert (1943) selected the six brightest of these *Seyfert galaxies* from the sample with preferably the brightest nucleus, and cross-compared this class of objects, and found broad emission lines, which if interpreted as Doppler broadening yield gas velocities of $\sim 10^3\,\mathrm{km\,s^{-1}}$, with the highest value at $8.5 \times 10^3\,\mathrm{km\,s^{-1}}$. Additionally, some lines were associated with ionised atoms in high degrees of excitation.

A decade before Carl Seyfert made his publication, Jansky (1933) accidentally stumbled upon radio astronomy after constructing a 30 m radio antenna to study sources of interference of short wave radio transmission and recording signals of extraterrestrial origin. Reber (1944) built a radio telescope and published radio contour maps of the sky, showing the disc of the Milky Way. Groups of enthusiastic engineers (Hey, Parsons and Phillips (1946), Bolton (1948)) catalogued radio sources, which were subsequently matched with optical counterparts.

Baade and Minkowski (1954) associated radio source Cygnus A with a condensed cD-type elliptical *radio galaxy* embedded in a rich cluster. The source was found to be elongated (Hanbury Brown, Jennison and Gupta, 1952), later resolved into a double-lobed structure (Jennison and Das Gupta, 1953) with lengths $\sim$100 kpc connected to the nucleus, with a radio power equivalent to the optical power.

The 3C survey (1959) led to discovery of incredibly distant *quasi-stellar objects* (QSOs) (Minkowski, 1960), with unfamiliar spectral lines later discovered to be Doppler-shifted (Schmidt, 1963). Sandage (1965) discovered a much larger population of similar but radio-quiet quasars by using colour-colour diagrams, suggesting QSOs may be distant relations to Seyferts and radio galaxies. Ambartsumian (1971) first spoke of the activity of the nucleus; obvious similarities between the classes led to the name AGNs.

1.4.1 Continuum emission

The continuum spectra of these sources were initially found to fit simple power law distributions, with a monochromatic energy flux $F_\nu \propto \nu^{-\alpha}$. As initial estimates in the optical band yielded $\alpha \approx 1$, the spectrum was referred to as *flat* – though more recent data implicates the index varies between 0.5 and 2, with the index being constant on part of the spectrum (figure 1.4).

The bimodality caused by the ratio of optical to radio flux seems to be intrinsic to the AGN. *Radio loudness* can be quantified by considering the ratio of the radio flux at 5 GHz and the optical B-band flux, where the radio-loud and radio-quiet population are separated by a ratio of 10 (Schmidt, 1970).

The continuum spectrum of AGNs can extend across 20 orders of magnitude of frequency. Early observations provided evidence of the spectral emission being variable with periods as small as days (Matthews and Sandage (1963), Fitch, Pacholczyk and Weymann (1967)), and can be highly polarised for radio-loud sources (e.g. Baade (1956)).

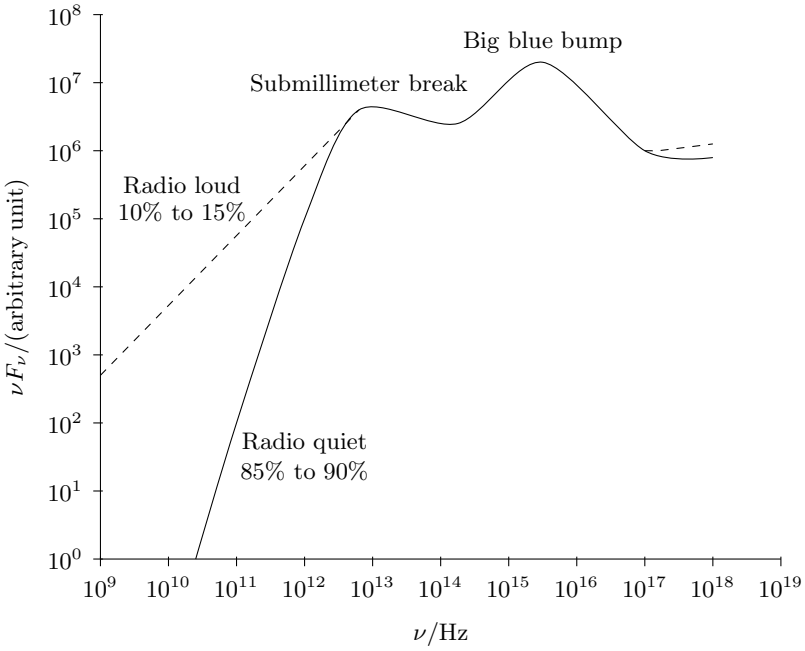

Figure 1.4: A sketch of the continuum spectrum of typical active galactic nuclei. (Credit: Carroll and Ostlie (1996))

1.4.2 Line emission

Most AGN also display strong emission lines in UV-optical-NIR spectra superposed on the continuum discussed previously. Subtracting the continuum and fitting a spectral line to a Gaussian profile, full width at half maximum (FWHM) is the most reliable measurable observable associated with a line. Typical values for the FWHM of lines in AGNs are $200\,\mathrm{km\,s^{-1}}$ to $500\,\mathrm{km\,s^{-1}}$, exceeding $1000\,\mathrm{km\,s^{-1}}$ in a few cases. Useful forbidden lines include the notably strong O[III] line, but also coronal lines associated with highly-ionised atoms such as Ca[V], Fe[VII], or Fe[X].

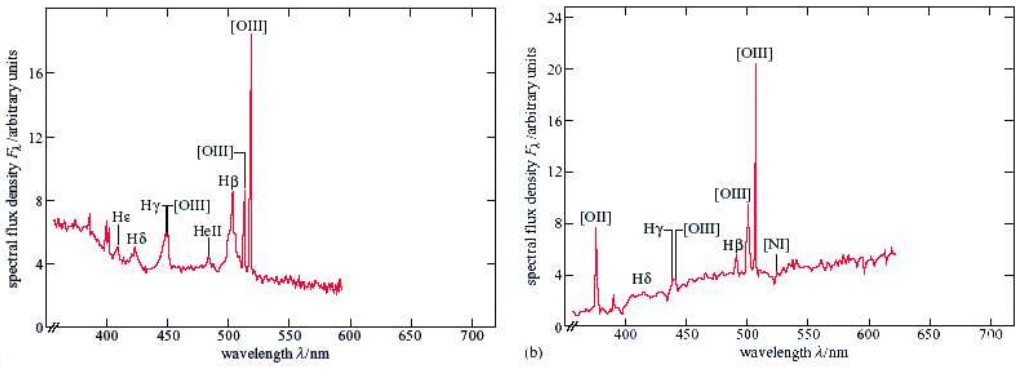

(a) Markarian 290, a type 1 Seyfert. (b) Markarian 270, a type 2 Seyfert.

Figure 1.5: e

mission lines. (Credit: Netzer (1990))]Seyfert galaxies can be classified based on relative width of for example the Balmer Hβ and O[III] emission lines. (Credit: Netzer (1990))

Khachikian and Weedman (1974) found Seyfert galaxies can be classified based on the ratio of the FWHM of a forbidden lines and a Balmer line.

- **Type I:** the Balmer lines are broader than the forbidden lines, and
- **Type II:** the Balmer lines are as wide as forbidden lines.

Figures 1.5(a) and 1.5(b) show spectra of typical type I and II Seyferts, where the FWHM of Balmer line Hβ and forbidden line O[III] are used as indicator. The width ratio is a continuous rather than a discrete scale, which resulted in intermediate types Osterbrock and Koski (1976), which are occasionally identified as e.g. type 1.5 or 1.9. The spectral typing is not confined to radio-quiet AGNs, but extends to their radio-loud counterparts as well (e.g. Osterbrock (1977)).

1.4.3 Unified model

In principle, AGNs are radiant cores of nuclei, with a brightness rivalling or outright outshining the host galaxy. The nucleus itself has not been resolvable, which puts a constraint to the size of the source. As the optical brightness varies sometimes in a matter of days, the required causal connection of the extended source puts a firm constraint on the size, making it similar to our solar system ($\sim 100\,\mathrm{AU}$. Given typical luminosities of $10^{37}\,\mathrm{W}$ to $10^{39}\,\mathrm{W}$, stellar nucleosynthesis does not seem to be a obvious candidate as an energy source due its low efficiency (less than 1% of the mass of processed matter is released as heat). $1\,\mathrm{M}_\odot$ would need to be burnt every 10 a to 1 ka. Salpeter (1964), Zel'Dovich (1964) and Lynden-Bell (1969) instead suggested an accreting black hole; a Kerr (spinning) black hole can transform mass to heat at a theoretical 42% efficiency.

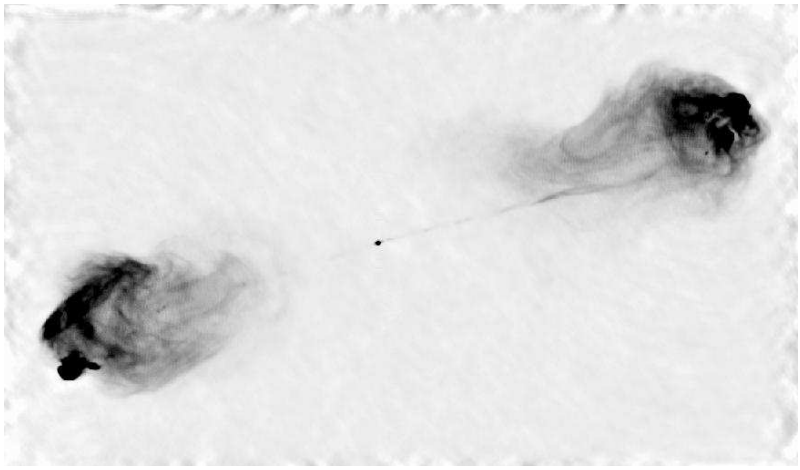

Figure 1.6: Cygnus A observed with the VLA at a wavelength of 6 cm. (Credit: Perley, Dreher and Cowan (1984))

Further evidence comes from observations of jets in extended radio sources. Figure 1.6 of radio galaxy Cygnus A, produced with the Very Large Array of telescopes (VLA) using interferometry techniques to boost the resolution, yield suggest the presence of *jets*. A jet is defined as a continuous efflux of fluid from a collimator projected into a surrounding medium, though it is difficult to observe motion within the assumed jet as no emission line can be attributed to the protrusion.

Considering the synchrotron signature of the continuum emission (the power-law spectrum and polarisation), relativistic jet velocities are inferred which might for some observers result in apparent superluminal motion. Indirect evidence of superluminal motion of the jet material (Cohen et al., 1971) supports the presence of a supermassive black hole as relativistic jets are difficult to create in an environment without a steep potential well.

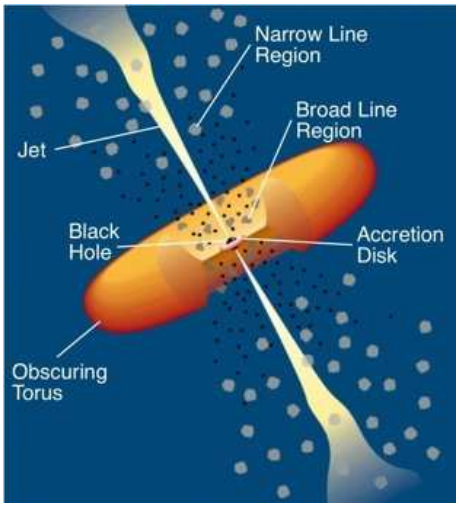

Figure 1.7: The unified AGN model. (Credit: Urry and Padovani (1995))

The bimodal unified model (Urry and Padovani, 1995) is best characterised as a heuristic interpretation, comprising a central supermassive black hole feeding on an accretion disc, optionally generating a pair of bipolar jets. The broad-line region is situated in proximity to the black hole; the swift accretional motion in the strong gravitational field near the black hole explains the width of the broad lines observed in type 1 AGNs. The system is viewed edge-on for type 2 AGNs; the dusty torus that surrounds the system obscures the core and broad-line region, and thus only the narrow-line region of slower-moving gas, which envelopes the AGN as a halo, is observed.

Unusual types explained by the model include blazars, in which the line of sight to the (radio-loud) AGN coincides with one of its jets. Quasi-stellar objects are grouped with their corresponding nearby equivalents, though narrow-line quasi-stellar objects have been found rare relative to their more proximate cousins.

1.5 The cooling flow problem

The quantity and composition of the ICM, in addition to a number of simulations (e.g. Gull and Northover (1975)) indicate the ICM formed when primordial gas underwent spherical collapse into a stratified, hydrostatic atmosphere of hot gas, presumably during the formation of the cluster of galaxies. This atmosphere loses energy due to emission of thermal bremsstrahlung, with an emissivity that is highest about the centre of the cluster.

As time progresses a region about the centre where the age of the cluster exceeds the cooling time cools significantly (figures 1.8(a), 1.8(b)). The cool core can no longer support the hotter envelope, and collapses spherically (figure 1.8(c)), i.e. a *cooling flow*. Accreted cold matter either piles up in the core or condenses into clouds and contribute to star formation (figure 1.8).

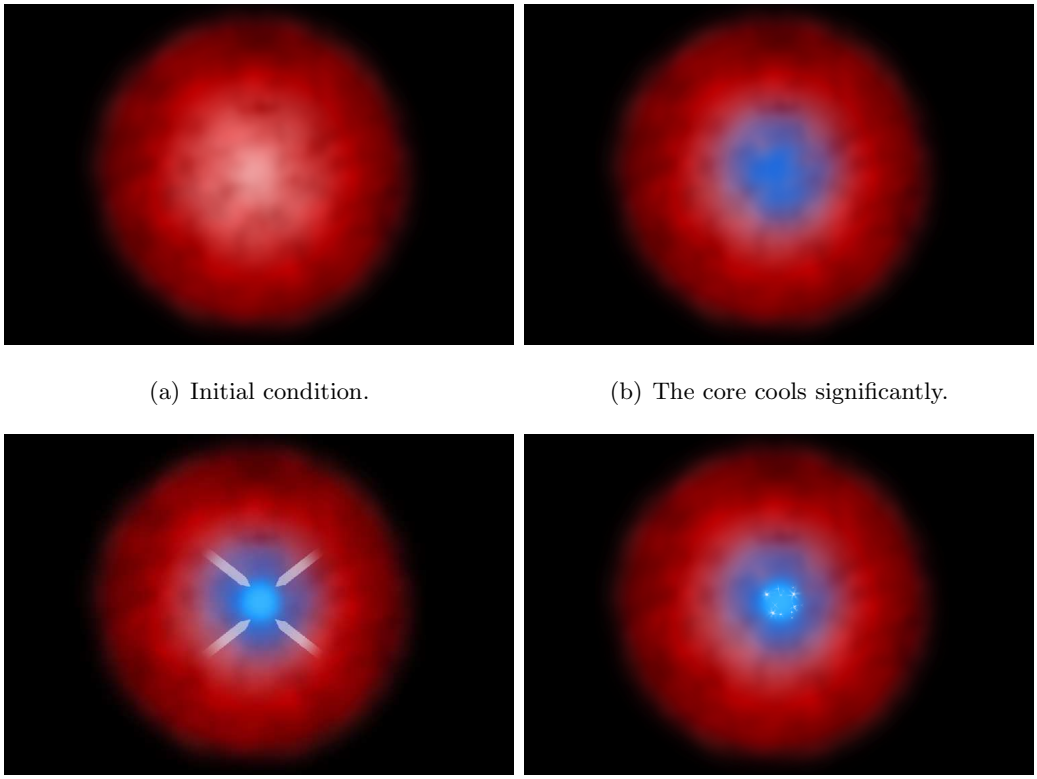

(a) Initial condition. (b) The core cools significantly.

(c) The core collapses. (d) Cold gas condenses and forms stars.

Figure 1.8: The classical cooling flow model. In the periphery the gas is presumed to be replenished by member galaxies ejecting gas processed by stars into the ICM. (Credit: NASA/NASA/CXC/M.Weiss)

1.5.1 The cooling flow model

Shortly after the *Uhuru* surveys, it became apparent that the cooling time in some cluster cores approaches the Hubble time. Considering these cooling times, Silk (1976) suggested that catastrophic cooling might during early epochs of galaxy cluster formation may have led to galaxy formation in the cluster core,

Cowie and Binney (1977) proposed stellar gas ejected by member galaxies would replenish the ICM in the periphery as that region is vacated as a consequence of the cooling flow. Cowie and Binney (1977) remarked the stellar gas constitutes a coolant in the hot ICM, and the continuous ejection process will establish a steady cooling flow given sufficient time. The model proposed involved a steady subsonic isotropic mass flow toward the cluster centre, while maintaining hydrostatic equilibrium and compensating radiative losses by heat advection. The ICM is modelled as an unmagnetised ideal fluid and obeys the ideal gas equations of state.

In spherical coordinates in which the origin coincides with the cluster centre conservation of mass, momentum, and energy[5] indicate

$$4\pi r^2 \rho v = \dot{M}, \tag{1.31}$$

$$\frac{dp}{dr} = -\rho g, \tag{1.32}$$

$$\frac{dL}{dT} = \frac{\gamma}{\gamma - 1}\frac{R}{\mu}\dot{M}. \tag{1.33}$$

In these equations pressure p and gravitational acceleration g are functions of r. The change of gas mass contained in a sphere with radius r centered on the origin is denoted $\dot{M}$. In classical models radiative cooling is attributed entirely to thermal bremsstrahlung, but alternatively Sutherland and Dopita (1993) has tabulated cooling luminosities for thin plasmas with temperatures ranging from 10^4 K to $10^{8.5}$ K, considering a range of emission processes.

Fabian and Nulsen (1977) applied the model to NGC 1275 in the Perseus cluster and discuss various flow configurations, and obtain mass deposition rates of $\dot{M} = 100\,\mathrm{M}_\odot$. Developments of co-moving thermal instabilities in the cooling flow were also discussed, and more explicitly detailed by Mathews and Bregman (1978).

[5] The heat flux is $\dot{M}h$, with $h = \frac{\gamma}{\gamma-1}\frac{R}{\mu}T$ for an ideal gas.

1.5.2 Multiphase cooling flow model

If the observed X-ray luminosity is identified with the bolometric luminosity, mass deposition rates up to $100\,\mathrm{M}_\odot\,\mathrm{a}^{-1}$ are inferred (Jones and Forman, 1984). Spatially resolved images obtained using *Einstein observatory* of the Perseus cluster (Fabian, Nulsen and Canizares, 1984), Virgo cluster (Stewart et al., 1984*a*), and 36 other clusters (Stewart et al., 1984*b*) indicates $\dot{M} \propto r$ rather than constant. Considering this the inhomogeneous, or multiphase cooling flow model (Nulsen (1986), Thomas, Fabian and Nulsen (1987)) instead models a flow comprised of gas with a range of densities and temperatures co-exists without exchanging heat at any location. Deposited mass cooled below X-ray temperatures will then be found distributed across the cooling core.

1.5.3 The fate of the cold gas

As cooling material cools below X-ray temperatures it essentially disappears through a mass-sink, as observations in the X-ray band no longer account for it. Cowie and Binney (1977) suggest that the cold gas will recombine and processed in star formation, or alternatively pile up as cool clouds of gas. Given mass is deposited at rates of 10s to 100s $\mathrm{M}_\odot\,\mathrm{s}^{-1}$, there is at least $10^{11}\,\mathrm{M}_\odot$ of mass to be accounted for.

Fabian, Nulsen and Canizares (1982) considered star formation by deposited mass, and found an initial mass function based on a population of stars with a mass distibution similar to the solar environment results in a cluster core too bright in comparison to observations in the visual band, and suggests a different initial mass function favouring low-mass stars. Johnstone, Fabian and Nulsen (1987) find that a model assuming less than 10% of the gas is turned into stars is in accordance with the observed Hβ line-flux; the rest constitutes gas and low-mass stellar objects without any optical signature. McNamara and O'Connell (1992) cross-compared optical observations in different bands and concluded only a few per cent of the deposited mass could be converted into stars without violating colour and optical luminosity observations.

Optical spectra of cooling core clusters cores in particular are surrounded by extensive and luminous nebulae, with emission lines indicating it concerns a low-ionisation plasma. The Hα lines were thought to be caused by cool gas from the cooling flow, but that would result in a luminosity orders of magnitude fainter than observed (Cowie et al., 1983). In the UV using O VI emission lines were found inconsistent with X-ray observations (Oegerle et al., 2001). Observation of absorption or emission features associated with neutral hydrogen restricted the amount of present hydrogen such that the deposited mass cannot substantially end up as optically thin neutral hydrogen (e.g. Dwarakanath, van Gorkom and Owen (1994), O'Dea, Gallimore and Baum (1995), O'Dea, Payne and Kocevski (1998)). O'Dea et al. (1994) and Braine et al. (1995) similarly found a lack in CO-emission and absorption and concluded that gas cannot be present in quantities suggested by the cooling flow model.

Malagoli, Rosner and Bodo (1987) demonstrated density perturbations (the Field (1965) mechanism) do not lead to accelerated cooling in a stratified ICM, but oscillatory motion. As this mechanism was thought to enable mass drop-out, the nature of this mechanism became uncertain.

1.5.4 Soft X-ray cooling flow problem

The superior spectral resolution of *XMM Newton* allowed for applying the energy conservation equation (equation 1.33) to a temperature interval in the form

$$L_{\rm line} = \frac{\gamma}{\gamma - 1}\frac{R}{\mu}\dot{M}\int_T \xi_T \, dT, \tag{1.34}$$

where ξ_T denotes the fraction of luminosity emitted in the considered line. A synthetic spectrum can be constructed using an inferred value of $\dot{M}$, which should then be equal to dL/dT across the spectrum.

Comparing the synthetic to the observed spectrum (figure 1.9) provides evidence of a lack of line-emission in emission lines associated with gas at temperatures lower than about a third of the average cluster temperature (e.g. Peterson et al. (2001), Tamura et al. (2001), Kaastra et al. (2001), Sakelliou et al. (2002), Peterson et al. (2003), Bauer et al. (2005), and Sanders et al. (2008)).

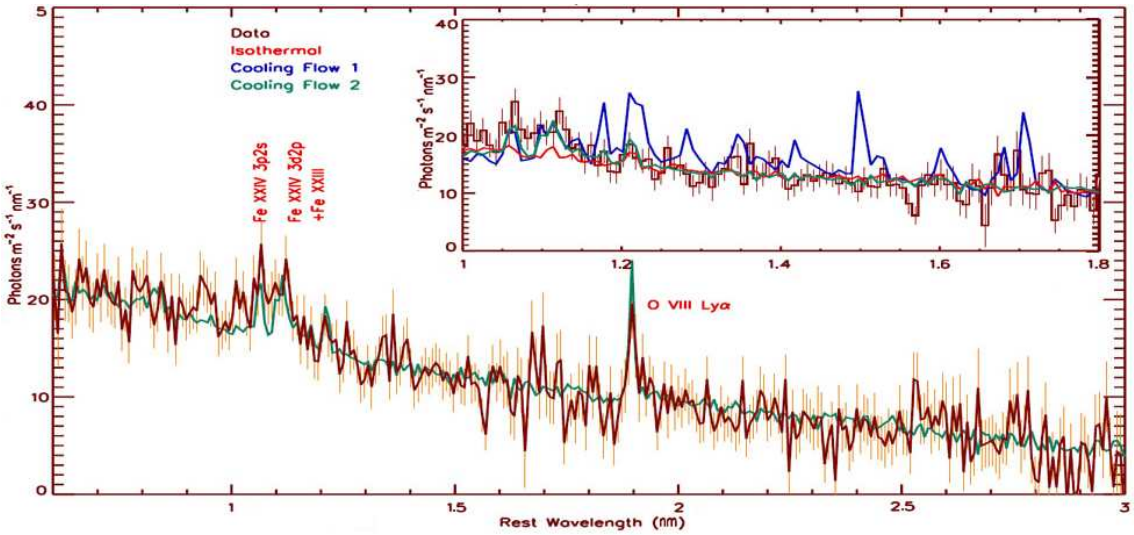

Figure 1.9: Peterson et al. (2001) compared *XMM Newton* acquired data on Abell 1835 with model data and found some soft X-ray spectral lines associated with cool gas are missing (compare cooling flow 1 to data), while removing all cooling gas at temperatures lower than 3.1×10^7 K (cooling flow 2) matches quite well.

Soft X-ray emitting gas may of course be present, with its radiation being removed from the spectrum by photoelectric absorption. Such processes are, however, not observed in nearby Virgo and Perseus clusters (Böhringer et al. (2002), Churazov et al. (2003)), and neither have any supporting evidence of such absorption been found as a consequence of RGS data analysis.

Alternatively the lack of soft X-ray emission lines can be explained if cool gas is not observed as it cools non-radiatively, e.g. via turbulent mixing (Fabian et al., 2002) or thermal conduction (Soker, Blanton and Sarazin, 2004) with cold gas.

Neither of these hypotheses are complete, as they do not offer an explanation of the apparent lack of a mass sink. Implementing a heat source to counter cooling might conceivably stop cooling altogether and offer a solution for both cooling flow problems at once.

1.6 A toolbox of heating mechanisms

Failing to find a consistent explanation for this behaviour with mechanisms already part of the cooling flow model, heating by external mechanisms is considered. Assuming the cooling core still cools radiatively, and observing the temperature profile of the intracluster medium essentially remains frozen in time, there are three main requirements of a heat source for it to be a viable solution to the cooling flow problem:

- sufficient energy needs to be injected to compensate the combined cooling of the gas in the cooling core,
- all the heat needs to be distributed, so that cooling is quenched homogeneously throughout the cooling core, and
- a thermostat mechanism needs to be in place, regulating the heating by the radiative cooling activity in the intracluster medium.

1.6.1 Thermal conduction between periphery and core

One obvious source of heat is the vast reservoir of heat that is the cluster periphery. Heat transport from the periphery to the core has been studied extensively (e.g. Narayan and Medvedev (2001), Fabian, Voigt and Morris (2002), Voigt et al. (2002), Voigt and Fabian (2004), Balbus and Reynolds (2008)). The indication of a strong correlation between the configuration of magnetic field lines and thermal conductivity, any research into the role of thermal conductivity is hindered by the unknown configuration of the magnetic field permeating the intracluster medium. Furthermore, the thermal conductivity has a different temperature dependence than radiative cooling does, leading to net cooling at lower temperatures. And in some clusters the temperature profile becomes flat in the cluster core, making heat transport by thermal conduction inefficient.

1.6.2 Gravitational energy released during accretion

If cooling flows are thermally unstable, the sound speed will drop locally and the flow will granulate. Quantities of gas that find themselves over-dense with respect to the surrounding flow will sink, releasing gravitational potential energy as kinetic energy, which in turn will be released as thermal energy once the gas reaches its equilibrium position.

Given the virial theorem, the amount of gravitational potential energy is of the same order as the blob's kinetic energy, indicating a vast reservoir of energy can be tapped into by such a flow (Fabian, 2003). The issue with the gravitational heating mechanism is the dependence on the inhomogeneous nature of the cooling flow. While there is plenty of energy available in the gravitational field to do heating with, it is unclear whether thermal conductivity allows for sustaining an inhomogeneous flow.

1.6.3 Cold fronts as a result of merging events

Cold fronts are temperature discontinuities often observed in cluster cores (e.g. Markevitch et al. (2000), Vikhlinin, Markevitch and Murray (2001*a*), Markevitch et al. (2002)). These discontinuity fronts are now thought to be the result of cluster merging events, which disturbs the mechanical equilibrium of the intracluster medium (Ascasibar and Markevitch, 2006).

Cold fronts seem to be a sufficiently frequent phenomenon (Ghizzardi, Rossetti and Molendi, 2010), but it is difficult to see how the intracluster medium could arrange the formation of cold fronts if minor mergers are required.

It should be noted the mere presence of cold fronts suggests thermal conduction is indeed insignificant. The width of these fronts is observed to be smaller than the Coulomb mean free path (Vikhlinin, Markevitch and Murray, 2001*a*). If the effective mean free path would even approach that number, cold fronts would be very unstable structures and not persist as observed (Vikhlinin, Markevitch and Murray, 2001*b*).

1.6.4 Dynamical friction of moving galaxies

Galaxies do not need to undergo merger events to transfer heat to the intracluster medium. As a galaxy progresses along its path, it faces an intracluster gas headwind that generates dynamical friction. A study on the effect based on seven central galaxies in the Perseus cluster by Miller (1986) indicated that dynamical friction could generate sufficient heat (cf. El-Zant, Kim and Kamionkowski (2004)).

Kim, El-Zant and Kamionkowski (2005), however, performed a series of simulations in one dimension and found that dynamical friction alone is unlikely to produce observed temperature profiles, though the mechanism may still have a role of some significance in conjunction with other heating mechanisms (e.g. thermal conduction, Ruszkowski and Oh (2010)).

1.6.5 Heating by supernovae

Supernovae have been considered as a source of heating of the intracluster medium for decades, given the high metallicity of the gas already suggests interference of supernovae — core collapse supernovae spread evenly across the intracluster medium and type Ia dominating in the cluster core (Finoguenov and Ponman, 1999).

As measured by heavy element abundances the energy output of all supernovae combined about matches the radiative losses of the intracluster medium (Finoguenov, David and Ponman (2000), Pipino et al. (2002)), but assuming the stellar population is generated by a regular initial mass function the available supernovae have to release their energy at maximum efficiency (Kravtsov and Yepes, 2000). Simulations considering supernova heating of the intracluster medium have been met with very limited success (e.g. Domainko et al. (2004)).

1.6.6 Heating by AGNs

In the centre of clusters of galaxies the *brightest cluster galaxy* (BCG) resides, largest, brightest, and most massive galaxy of the cluster under consideration (von der Linden et al., 2007). It is thought the BCG is closely tied to the formation history of the cluster, as the BCG grows through a succession of minor mergers (De Lucia and Blaizot, 2007) and accretion of infalling gas in cooling flows (Best et al., 2007). Their physical properties seem to be correlated with quantities relating to the cluster as a whole, such as galaxy richness and X-ray luminosity (e.g. Edge (1991), Lin and Mohr (2004)). In cooling core cluster cores the BCG is often a radio-loud AGN (Burns (1990), Mittal et al. (2009)), with associated jet activity (figure 1.6.6).

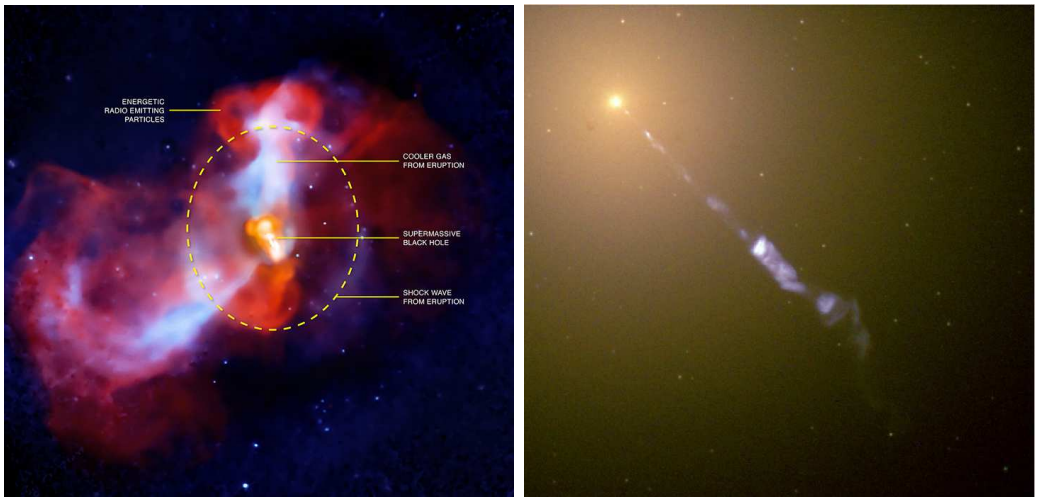

(a) Virgo cluster core. (b) Jet in the Virgo cluster core.

Figure 1.10: Composite X-ray/radio image of the core of the Virgo cluster, with associated optical image of the jet. (Credit: X-ray (NASA/CXC/KIPAC/N. Werner, E. Million et al); Radio (NRAO/AUI/NSF/F. Owen); Hubble Heritage Team (STScI /AURA), NASA)

Observed cavities in X-ray emission associated with NGC 1275, dominant galaxy in the Perseus cluster radio emission (Böhringer et al., 1993) were identified as under-dense *bubbles* of jet gas rising buoyantly through the ICM (Churazov et al., 2000). These cavities were found to be a common phenomenon for AGNs (Bîrzan et al. (2004), Dong, Rasmussen and Mulchaey (2010)).

Weight and velocity contrast along the bubble perimeter results in development of instabilities[6], which will cause the bubble to lose structural integrity, break up, and mix with the ambient medium. Also relevant may be the work done by the bubble as it expands while rising through the ICM (effervescent heating, e.g. Begelman (2001)). Observations of ripples in the Perseus (Fabian et al. (2003*a*), Fabian et al. (2003*b*)) and Virgo (Forman et al., 2005) also suggest the possibility of heating by emitted sound or shock waves (see figure 1.11).

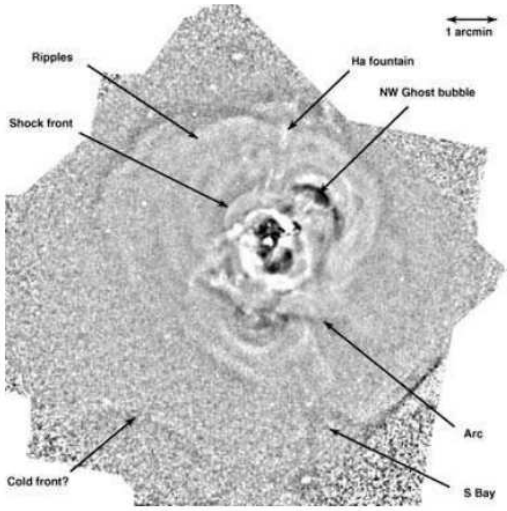

Figure 1.11: Observed ripples in the Perseus cluster in the 0.3 to 7 keV band, showing bubbles, ripples, weak shocks, and a cold front. (Credit: Fabian et al. (2006))

AGN jets are also seen to be enveloped by a bow shock, which may directly transfer heat to the ICM (Soker et al., 2001). While initially dismissed in favour of bubble-related heating mechanisms, observed strong shocks enveloping the outflow of Centaurus A (Kraft et al., 2003) and NGC 3801 (Croston, Kraft and Hardcastle, 2007) suggest this may have been in err. Across a shock discontinuity, pressure and entropy are discontinuous, and kinetic energy of gas flowing across is released as heat.

Heating power can be estimates by determining the enthalpy content of the X-ray cavity, and this is found to be sufficient to balance radiative cooling (Bîrzan et al., 2004). Shock heating relates to the heat content of the shocked gas. Evidence of interaction between black hole and ICM was found when Allen et al. (2006) established a correlation between the mass accretion rate and jet power.

[6]This concerns Kelvin-Helmholtz and Rayleigh-Taylor instabilities respectively.

1.7 Project summary

The heating mechanisms were presented as a toolbox, and indeed some have been applied in combination – such as thermal conduction and AGNs. In recent years the idea that AGNs play a pivot role in countering catastrophic cooling has gained popularity. As the length scale of AGN jets changes by a factor 10^9 from nucleus to jet tip, involving strong relativistic and electromagnetic effects during acceleration and collimation, analytical treatment is arduous and numerical simulations notoriously complicated. A complete inclusion of all physics with a resolution on nucleus scales, while still encompassing the jet, yields an impossible task for any computer.

Confining the discussion to heating by AGNs, it is noted that heating mechanisms considered are observed at larger length scales. If by some means bubbles and shocks could be reproduced while bypassing implementing an AGN, the computational strain due to excessive resolution is alleviated. This strategy allows for simulating various processes relating to AGN heating in cool cluster cores. In this thesis jets will be injected through a face-to-face nozzle positioned in the centre of the computational domain, thus taking care of jet collimation and acceleration. Relativistic effects are presumed unimportant, while the plasma parameter is likewise taken much larger than unity, rendering inclusion of magnetic fields unnecessary.

It can be argued how well these assumptions relate to true AGN jets. The Coulomb mean free path of constituent electrons exceeds 20 kpc, and while the gyroradius limits this figure somewhat it remains to be seen whether a fluid approximation is justified. Relativistic and magnetic effects are known to play a role of significance on smaller resolved scales near the nozzle. That said, if the jet produces observed features as bubbles and shocks, their heating effect on the ICM can be studied without any loss of generality.

The thesis now continues with a general introduction on fluid dynamics. The used CFD-code FLASH and its algorithms, with associated algorithms involved with a numerical fluid, is outlined in chapter 3. A model of the Virgo cluster core is discussed in chapter 4, followed by a chapter on astrophysical jets in chapter 5.

Then there is three chapters on projects on the AGN-heating mechanism. In the first project (chapter 6) the effect of a changing opening angle of a conical outflow is measured in the model cluster core. In the second heating by sound and gravity waves is investigated (chapter 7), while chapter 8 weighs the importance jet thrust against heating power when it comes to heating the ICM.

The main purpose of the project is to gain more insight in how these simple parameters affect the heating process of the AGN, and in the mean time gain valuable insight on the mechanisms governing the evolution of the intracluster medium.

Chapter 2

Fluid dynamics

A fluid is defined as a substance which continuously deforms when shearing forces act upon it. This chapter is designed to explain the set of physical laws describing the motion of a fluid under the action of a force field from a classical mechanical perspective, a theory known as fluid dynamics.

2.1 Fundamental equations

Consider an isolated quantity of fluid, characterised by three measurable properties

- mass,
- momentum,
- energy.

The conservation laws as formulated in classical mechanics are empirical laws that state the amount of mass, momentum, and energy of an isolated quantity of fluid does not change over time, and have the status of axiom within classical fluid dynamics.

2.1.1 Conservation of mass

Conservation of mass implies the change in mass in a fluid element with volume V must be equal to the mass transfer across the surface of the element ∂V, or

$$\frac{\partial M}{\partial t} + \oint_{\partial V} \rho \vec{v} \cdot d\vec{A} = 0. \tag{2.1}$$

The mass flow divided by area $\rho\vec{v}$ through the boundary of the fluid element is known as the *mass flux density*, a quantity that must be continuous in order to prevent ambiguity of mass transfer and violation of mass conservation. Using $M = \int_V \rho \, dV$ and applying the divergence theorem (Arfken and Weber, 1995) yields

$$\frac{\partial \rho}{\partial t} + \vec{\nabla} \cdot (\rho \vec{v}) = 0, \tag{2.2}$$

under the condition that $\rho\vec{v}$ is differentiable as well as continuous.

2.1.2 Conservation of momentum

Momentum change in the fluid element is the result of advection $\rho\vec{v} \otimes \vec{v}$, pressure across the element surface on the surrounding environment and dissipative forces represented by the stress tensor $\overleftrightarrow{\sigma}$, and external forces acting on the fluid $\vec{f}_{\text{ext}}$ (Landau and Lifshitz, 1987)

$$\frac{\partial}{\partial t} \int_V \rho \vec{v} \, dV + \oint_{\partial V} (\rho \vec{v}\vec{v} - \overleftrightarrow{\sigma}) \, d\vec{A} = \int_V \rho \vec{f}_{\text{ext}} \, dV. \tag{2.3}$$

The stress tensor reflects momentum transfer through pressure and viscous forces and is given by

$$\overleftrightarrow{\sigma} = -p\overleftrightarrow{I}_3 + \overleftrightarrow{\sigma}'. \tag{2.4}$$

The viscous stress tensor $\overleftrightarrow{\sigma}'$ reflects pressure by frictional shear forces as a result of a present velocity gradient in the fluid, and is found to be (Landau and Lifshitz, 1987)

$$\overleftrightarrow{\sigma}' = \eta \left(\vec{\nabla}\vec{v} + (\vec{\nabla}\vec{v})^{\mathsf{T}} - \frac{2}{3}(\vec{\nabla} \cdot \vec{v})\overleftrightarrow{I}_3 \right) + \zeta(\vec{\nabla} \cdot \vec{v})\overleftrightarrow{I}_3. \tag{2.5}$$

where η is the *dynamic viscosity*, and ζ the *second viscosity* coefficient.

If the *momentum flux density* of an fluid $\rho\vec{v}\vec{v} - \overleftrightarrow{\sigma}$ is differentiable as well as continuous, applying the divergence theorem yields

$$\frac{\partial \rho \vec{v}}{\partial t} + \vec{\nabla} \cdot (\rho \vec{v}\vec{v} - \overleftrightarrow{\sigma}) = \rho \vec{f}_{\text{ext}}. \tag{2.6}$$

Cast in non-conservative form, one obtains the *Navier-Stokes equation*

$$\frac{\partial \vec{v}}{\partial t} + (\vec{v} \cdot \nabla)\vec{v} = -\frac{1}{\rho}\vec{\nabla} p + \frac{\eta}{\rho}\Delta \vec{v} + (\frac{\zeta}{\rho} + \frac{1}{3}\frac{\eta}{\rho})\vec{\nabla}\vec{\nabla} \cdot \vec{v} + \vec{f}_{\text{ext}}, \tag{2.7}$$

where $\nu \equiv \eta/\rho$ is defined as the *kinematic viscosity*. For *inviscid fluids* both viscosity coefficients are zero. The Navier-Stokes equation for the special case of an inviscid fluid is also known as *Euler's equation*

$$\frac{\partial \vec{v}}{\partial t} + (\vec{v} \cdot \nabla)\vec{v} = -\frac{1}{\rho}\vec{\nabla} p + \vec{f}_{\text{ext}}. \tag{2.8}$$

2.1.3 Conservation of energy

Applying conservation law of energy to the same fluid element yields (Landau and Lifshitz, 1987)

$$\frac{\partial E}{\partial t} + \oint_{\partial V} \left[(\rho e + p)\vec{v} - \vec{v} \cdot \overleftrightarrow{\sigma}' - \kappa\vec{\nabla} T\right] \cdot d\vec{A} = \int_V \rho \vec{f}_{\text{ext}} \cdot \vec{v}\, dV + \dot{Q}. \tag{2.9}$$

The energy transfer is determined by energy transferred to the fluid element as work or heat, combined with work done by the pressure forces within the fluid and external work by external forces $\vec{f}_{\text{ext}}$ plus any work done by dissipating (viscous) forces and heat transport by thermal conduction (represented by the heat flux $-\kappa\vec{\nabla} T$), and the heat transferred to the fluid represented by $\dot{Q}$.

Combining the advective and stress terms under ideal fluid conditions yields the *energy flux density* $(\rho e + p)\vec{v} - \vec{v} \cdot \overleftrightarrow{\sigma}' - \kappa\vec{\nabla} T$, which again must be a continuous quantity to permit energy conservation.

If the energy flux density is differentiable as well as continuous, applying the divergence theorem yields

$$\frac{\partial \rho e}{\partial t} + \vec{\nabla} \cdot \left[(\rho e + p)\vec{v} - \vec{v} \cdot \overleftrightarrow{\sigma}' - \kappa\vec{\nabla} T\right] = \rho \vec{v} \cdot \vec{f}_{\text{ext}} + \dot{q}, \tag{2.10}$$

where $\dot{Q} \equiv \int_V \dot{q}\, dV$, $\dot{q}$ representing the amount of heat transferred to the fluid divided by volume and time.

An *ideal fluid* is by definition inviscid and thermally non-conductive (i.e. $\kappa = 0$) fluid.

2.2 Equations of state for an ideal gas

Consider a fluid of which density, temperature and molar mass are measured quantities. A fluid element comprising 1 kg of fluid then occupies a volume $1/\rho$, consists of N_A/μ particles. The fluid element can exchange heat with the environment, but volume and number of particles are fixed, which suggests modelling the fluid element as a canonical ensemble (Landau and Lifshitz, 1980).

If the fluid is comprised of a collective of randomly moving non-relativistic non-interacting spineless particles, it is referred to as an *ideal gas*). The partition function $\mathcal{Z}$ then yields the associated characteristic state function

$$a = -k_\mathrm{B} T \ln \mathcal{Z}, \tag{2.11}$$

which is the specific Helmholtz free energy.

Given the specific Helmholtz free energy, pressure and specific entropy can be determined via the thermodynamic relation

$$da = \frac{p}{\rho^2}\, d\rho - s\, dT. \tag{2.12}$$

The total differential for the Helmholtz free energy yields a pair of *equations of state*

$$p = \rho^2 \left(\frac{\partial a}{\partial \rho}\right)_T = \frac{R}{\mu}\rho T, \tag{2.13}$$

$$s = -\left(\frac{\partial a}{\partial T}\right)_\rho = \frac{1}{\gamma - 1}\frac{R}{\mu} \ln\left(\frac{R}{\mu}\frac{T}{\rho^{\gamma-1}}\right); \tag{2.14}$$

s is arbitrarily set to zero at $T = 0$. The adiabatic index $\gamma = (k + 2)/k$, where k is the number of degrees of freedom of the particles — in this case $k = 3$ and therefore $\gamma = 5/3$. Equations 2.13 and 2.14 are known as the *ideal gas law* and the *Sackur-Tetrode equation* respectively.

The specific internal energy can be derived from the definition of specific Helmholtz free energy[1]

$$a \equiv e_\mathrm{int} - Ts \Rightarrow e_\mathrm{int} = \frac{1}{\gamma - 1}\frac{R}{\mu}T, \tag{2.15}$$

where $e_\mathrm{int} = e - \frac{1}{2}v^2$. Similarly the specific enthalpy is found to be

$$h \equiv e_\mathrm{int} - \frac{p}{\rho} = \frac{\gamma}{\gamma - 1}\frac{R}{\mu}T. \tag{2.16}$$

[1]Integration constants have been defined such that all potentials are zero when $T = 0$.

2.3 Isentropicity in ideal fluids

In an ideal fluid by definition no kinetic energy is lost because of dissipating forces. If the fluid is isolated, all processes are adiabatic and (assuming reversibility) isentropic, given $ds = đq/T = 0$. This yields a conservation law for entropy

$$\frac{\partial s}{\partial t} + \vec{v} \cdot \vec{\nabla} s = 0. \tag{2.17}$$

In an ideal gas the Sackur-Tetrode equation (equation 2.14) yields for an isentropic process $T\rho^{1-\gamma} = \text{constant}$ and $p\rho^{-\gamma} = \text{constant}$.

2.4 Steady flow – Bernoulli's equation

Steady flow is defined as a flow in which the velocity is independent of time. Using the vector relation

$$\frac{1}{2}\vec{\nabla} v^2 = \vec{v} \times (\vec{\nabla} \times \vec{v}) + (\vec{v} \cdot \nabla)\vec{v}$$

Euler's equation then yields for a steady flow

$$\frac{1}{2}\vec{\nabla} v^2 - \vec{v} \times (\vec{\nabla} \times \vec{v}) = -\frac{1}{\rho}\vec{\nabla} p + \vec{f}_{\text{ext}}. \tag{2.18}$$

For isentropical flow the enthalpy differential $dh = dp/\rho$, which implies $\vec{\nabla}(p)/\rho = \vec{\nabla} h$. If the only external force is a gravitational field

$$\vec{g} = -\vec{\nabla} \cdot \Phi. \tag{2.19}$$

In this equation Φ denotes the gravitational potential. In this case equation 2.18 can be written as

$$\frac{1}{2}\vec{\nabla} v^2 - \vec{v} \times (\vec{\nabla} \times \vec{v}) = -\vec{\nabla}(h + \Phi). \tag{2.20}$$

Parametrising the flow along the direction of flow results for steady flow in paths along which the fluid flow, known as *streamlines*. Given that along a streamline $\vec{v} \perp \vec{\nabla} \times \vec{v}$, thus parametrising using a parameter l implies

$$\frac{\partial}{\partial l}\left(\frac{1}{2}v^2 + h + \Phi\right) = 0. \tag{2.21}$$

Integrating over l yields *Bernoulli's equation*

$$\frac{1}{2}v^2 + h + \Phi = \text{constant}. \tag{2.22}$$

2.5 Incompressible flow

Incompressible flow is an approximation valid for a great number of fluids and gases in Nature. The type of flow is based on the assumption that $\rho =$ constant. Mass conservation then implies

$$\vec{\nabla} \cdot v = 0. \tag{2.23}$$

A fluid can be considered incompressible if $\Delta\rho/\rho \ll 1$.

For a fluid to be modelled as incompressible, $\Delta\rho/\rho$ should be much smaller than 1 at all times. In steady flow without an external force Bernoulli's equation yields along a streamline (cf. equation 2.22)

$$\frac{1}{2}v^2 + h = \text{constant}. \tag{2.24}$$

Under assumed isentropic conditions the equation of state relating pressure to density can be written

$$\Delta p = \left(\frac{\partial p}{\partial \rho}\right)_s \Delta\rho. \tag{2.25}$$

Defining the *speed of sound* $c_\mathrm{s}^2 \equiv (\partial p/\partial\rho)_s$ and using Bernoulli's equation with $h = e_\mathrm{int} + p/\rho$ which leads to $\Delta p \sim \rho v^2$ then yields

$$\frac{\Delta\rho}{\rho} \sim \mathcal{M} \ll 1. \tag{2.26}$$

where $\mathcal{M} \equiv v/c_\mathrm{s}$ is the *Mach number*. If the Mach number of a steady flow is small, the fluid can therefore be modelled as incompressible.

2.6 Vorticity and irrotational flow

If the vorticity of a flow $\vec{\nabla} \times \vec{v}$ is zero, the flow is referred to as *potential* or *irrotational* flow. In this case it is possible to define a velocity potential ϕ such that

$$\vec{v} = \vec{\nabla}\phi. \tag{2.27}$$

2.7 Signals in fluids: characteristics

Combining the conservation equations and an equation of state, the state of a fluid can be uniquely identified by a set of three observables: the velocity field $\vec{v}$ and two thermodynamic variables. Consider a state in mechanical equilibrium to which ideal gas equations of state apply, being evolved into x-direction. Imposing conservation of mass, momentum, and entropy yields

$$\frac{\partial \rho}{\partial t} + v\frac{\partial \rho}{\partial x} = -\rho\frac{\partial v}{\partial x}, \tag{2.28}$$

$$\frac{\partial v}{\partial t} + v\frac{\partial v}{\partial x} = -\frac{1}{\rho}\frac{\partial p}{\partial x}, \tag{2.29}$$

$$\frac{\partial s}{\partial t} + v\frac{\partial s}{\partial x} = 0. \tag{2.30}$$

This set of hydrodynamic equations is supplemented by a generic equation of state $p = p(\rho, s)$, and an associated exact differential

$$dp = \left(\frac{\partial p}{\partial \rho}\right)_s d\rho + \left(\frac{\partial p}{\partial s}\right)_\rho ds. \tag{2.31}$$

This system of equations can be simplified by a simple change of variables

$$\rho, v \rightarrow v \pm \frac{2}{\gamma - 1} c_\mathrm{s}, \tag{2.32}$$

where $c_\mathrm{s} \equiv \sqrt{(dp/d\rho)_s}$. Inserting these variables yields

$$\left[\frac{\partial}{\partial t} + [v \pm c_\mathrm{s}]\frac{\partial}{\partial x}\right]\left(v \pm \frac{2c_\mathrm{s}}{\gamma - 1}\right) = 0, \tag{2.33}$$

$$\left[\frac{\partial}{\partial t} + v\frac{\partial}{\partial x}\right] s = 0. \tag{2.34}$$

The three variables $J_0 = s$ and $J_\pm = v \pm 2c_\mathrm{s}/\gamma - 1$ are known as *Riemann invariants*. The equations themselves are the simplest linear wave equations, with solutions

$$J_\pm = J_\pm[x - (v \pm c_\mathrm{s})t] \qquad\qquad J_0 = J_0(x - vt) \tag{2.35}$$

(Arfken and Weber, 1995). The conservation equations for a one-dimensional fluid therefore yield states that are essentially a superposition of three signals, known as *characteristics*. Characteristic C_0, associated with Riemann invariant J_0, and characteristics $C_\pm$, associated with Riemann invariants $J_\pm$.

2.8 Wave solutions in uniform flow

Waves in fluid are studied by applying a linear perturbation to a state, such that a generic quantity $u \to u + \delta u$, and imposing that conservation laws hold both for the perturbed and unperturbed state. For a uniform fluid conservation of mass and entropy imply

$$\frac{\partial(\delta\rho)}{\partial t} + \vec{v}\cdot\vec{\nabla}(\delta\rho) + \rho\vec{\nabla}\cdot(\delta\vec{v}) = 0, \tag{2.36}$$

$$\frac{\partial(\delta s)}{\partial t} + \vec{v}\cdot\vec{\nabla}(\delta s) = 0. \tag{2.37}$$

As $\delta\rho = \delta p/c_\mathrm{s}^2 + (\partial\rho/\partial s)_p\delta s$ these equations can be combined to yield

$$\frac{\partial(\delta p)}{\partial t} + \vec{v}\cdot\vec{\nabla}(\delta p) + \rho c_\mathrm{s}^2\vec{\nabla}\cdot(\delta\vec{v}) = 0. \tag{2.38}$$

In addition Euler's equation imposes

$$\frac{\partial(\delta\vec{v})}{\partial t} + (\vec{v}\cdot\nabla)\delta\vec{v} + \frac{\vec{\nabla}(\delta p)}{\rho} = 0. \tag{2.39}$$

A *wave* is oscillatory motion resulting in alternate compression and rarefaction. Trying a plane wave solution of the form $\exp(i\vec{k}\cdot\vec{r} - i\omega t)$ yields

$$(\vec{v}\cdot\vec{k} - \omega)\delta s = 0, \tag{2.40}$$

$$(\vec{v}\cdot\vec{k} - \omega)\delta p + \rho c_\mathrm{s}^2\vec{k}\cdot\delta\vec{v} = 0, \tag{2.41}$$

$$(\vec{v}\cdot\vec{k} - \omega)\delta\vec{v} + \vec{k}\frac{\delta p}{\rho} = 0. \tag{2.42}$$

Based on equation 2.40 two sets of solutions can be distinguished.

For *entropy-vortex waves* $\delta s \neq 0$, implying the dispersion relation

$$\omega = \vec{v}\cdot\vec{k}, \tag{2.43}$$

and $\vec{\nabla}\cdot\delta\vec{v} = \vec{k}\cdot\delta\vec{v} = 0$ (i.e. the wave is incompressible), and $\delta p = 0$, whereas the vorticity $\vec{\nabla}\times(\delta\vec{v}) = i\vec{k}\times\delta\vec{v} \neq 0$ and $\delta\rho = (\partial\rho/\partial s)_p\delta s$.

In the case of *sound waves* $\delta s = 0$, which yields the dispersion relation

$$(\omega - \vec{v}\cdot\vec{k})^2 = c_\mathrm{s}^2k^2, \tag{2.44}$$

and $\delta p = c_\mathrm{s}^2\delta\rho$, $\rho c_\mathrm{s}^2\vec{\nabla}\cdot(\delta\vec{v}) = (\vec{v}\cdot\vec{k} - \omega)\delta p$ and $\vec{\nabla}\times(\delta\vec{v}) = 0$ (i.e. the wave is irrotational).

2.9 Shock discontinuities and expansion waves

Sound waves perturb the pressure profile by δp, while the sound speed

$$c_{\mathrm{s}} = \sqrt{\left(\frac{dp}{d\rho}\right)_s} \tag{2.45}$$

is for an ideal gas a function of pressure. The sub-wavelength variation of the sound speed will cause deformation and ultimately steepening of a sound wave (figure 2.9).

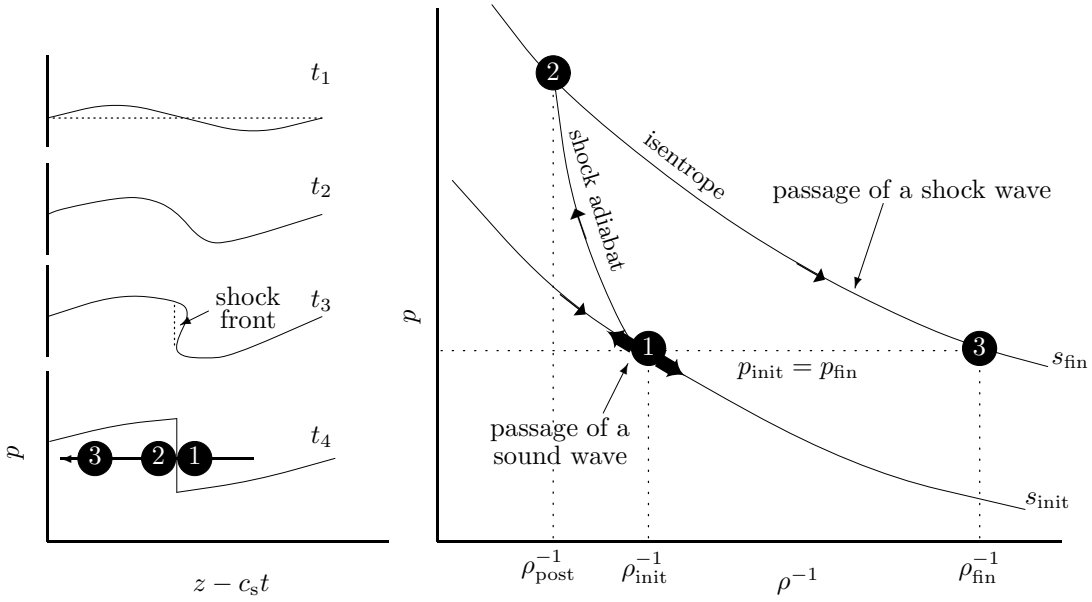

Figure 2.1: The fluctuating pressure in a sound wave on wavelength scale gives in time rise to steepening. When the profile results in pressure being multivalued, the wave breaks and a shock discontinuity forms. While the fluid stays on an isentrope when a sound wave passes, the shock discontinuity forces the fluid on a Hugoniot. (Credit: figure adapted from Los Alamos Science, number 12, 1985.)

Eventually the sound wave will break as the pressure profile becomes multivalued (which is unphysical), forming a *shock discontinuity* instead. Upon traversing the discontinuity the fluid moves across the $p\rho^{-1}$-diagram in an irreversible process across a line known as a *shock adiabat*.

2.9.1 The shock adiabat

The conservation equations dictating the dynamics of a fluid impose continuity on mass flux density $\rho\vec{v}$, the momentum flux density $\rho\vec{v}\vec{v} + p\overleftrightarrow{I}_3$, and the energy flux density $\rho\vec{v}(e + p/\rho)$. This is independent on the continuity of the state variables or the reversibility of processes taking place.

Consider a fluid divided by a shock discontinuity embedded in the xy-plane. Continuity of mass, momentum, and energy flux density implies

$$\rho_{\mathrm{u}} v_{\mathrm{u},z} = \rho_{\mathrm{d}} v_{\mathrm{d},z}, \tag{2.46}$$

$$p_{\mathrm{u}}\vec{e}_z + \rho_{\mathrm{u}}\vec{v}_{\mathrm{u}} v_{\mathrm{u},x} = p_{\mathrm{d}}\vec{e}_z + \rho_{\mathrm{d}}\vec{v}_{\mathrm{d}} v_{\mathrm{d},x}, \tag{2.47}$$

$$\rho_{\mathrm{u}} v_{\mathrm{u},z}\left(e_{\mathrm{u}} + \frac{p_{\mathrm{u}}}{\rho_{\mathrm{u}}}\right) = \rho_{\mathrm{d}} v_{\mathrm{d},z}\left(e_{\mathrm{d}} + \frac{p_{\mathrm{d}}}{\rho_{\mathrm{d}}}\right), \tag{2.48}$$

where the two regions adjacent to the discontinuity are marked u and d respectively. Given the nature of shock discontinuities $p_{\mathrm{u}} \neq p_{\mathrm{d}}$, implying

$$\rho_{\mathrm{u}} v_{\mathrm{u},z} = \rho_{\mathrm{d}} v_{\mathrm{d},z} \neq 0 \wedge v_{\mathrm{u},z} \neq v_{\mathrm{d},z}. \tag{2.49}$$

The fluid is defined to flow from u (upstream) to d (downstream).

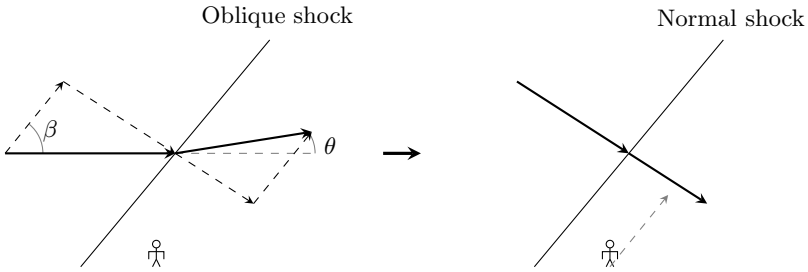

Figure 2.2: Conservation laws implicate velocity components parallel to the shock discontinuity are continuous across said discontinuity. As a consequence, an oblique shock is a normal shock in a reference frame co-moving with velocity component tangential to the surface of discontinuity.

Combing mass and momentum flux density continuity then yields $v_{\mathrm{u},x} = v_{\mathrm{d},x}$ and $v_{\mathrm{u},y} = v_{\mathrm{d},y}$. Any oblique shock can thus be transformed to a normal shock ($\vec{v} \parallel \vec{e}_x$) by transforming to the appropriate frame of reference (see figure 2.2).

For a normal shock conservation laws imply

$$\rho_{\mathrm{u}} v_{\mathrm{u}} = \rho_{\mathrm{d}} v_{\mathrm{d}}, \tag{2.50}$$

$$p_{\mathrm{u}} + \rho_{\mathrm{u}} v_{\mathrm{u}}^2 = p_{\mathrm{d}} + \rho_{\mathrm{d}} v_{\mathrm{d}}^2. \tag{2.51}$$

$$e_{\mathrm{u}} + \frac{p_{\mathrm{u}}}{\rho_{\mathrm{u}}} = e_{\mathrm{d}} + \frac{p_{\mathrm{d}}}{\rho_{\mathrm{d}}}. \tag{2.52}$$

The first two relations yield

$$p_{\mathrm{u}} - p_{\mathrm{d}} = -\rho_{\mathrm{d}}^2 v_{\mathrm{d}}^2 \left(\rho_{\mathrm{u}}^{-1} - \rho_{\mathrm{d}}^{-1}\right). \tag{2.53}$$

Given $e = e_{\mathrm{int}} + \frac{1}{2}v^2$, continuity of energy flux density (equation 2.48) and the shock adiabat relation (equation 2.53) the change in specific internal energy is found to be

$$e_{\mathrm{int,u}} - e_{\mathrm{int,d}} + \frac{1}{2}(\rho_{\mathrm{u}}^{-1} - \rho_{\mathrm{d}}^{-1})(p_{\mathrm{u}} + p_{\mathrm{d}}) = 0. \tag{2.54}$$

This relation is the mathematical description of the shock adiabat and indicates shocks are dissipative, as kinetic energy is transferred to internal energy.

Modelling the fluid as an ideal gas the jump conditions can be expressed as a function of one variable. Landau and Lifshitz (1987) derive the *Rankine-Hugoniot jump conditions* across a shock discontinuity

$$\frac{\rho_{\mathrm{d}}}{\rho_{\mathrm{u}}} = \frac{(\gamma+1)\mathcal{M}_{\mathrm{u}}^2}{(\gamma-1)\mathcal{M}_{\mathrm{u}}^2 + 2}, \tag{2.55}$$

$$\frac{p_{\mathrm{d}}}{p_{\mathrm{u}}} = \frac{2\gamma\mathcal{M}_{\mathrm{u}}^2 - (\gamma-1)}{\gamma+1}, \tag{2.56}$$

$$\frac{T_{\mathrm{d}}}{T_{\mathrm{u}}} = \frac{\left(2\gamma\mathcal{M}_{\mathrm{u}}^2 - (\gamma-1)\right)\left((\gamma-1)\mathcal{M}_{\mathrm{u}}^2 + 2\right)}{(\gamma+1)^2\mathcal{M}_{\mathrm{u}}^2}, \tag{2.57}$$

$$\mathcal{M}_{\mathrm{d}}^2 = \frac{2 + (\gamma-1)\mathcal{M}_{\mathrm{u}}^2}{2\gamma\mathcal{M}_{\mathrm{u}}^2 - (\gamma-1)}. \tag{2.58}$$

It follows that while the pressure and temperature jump can be arbitrarily high, the density jump for a monatomic gas increases up to a limiting value of $\rho_{\mathrm{d}}/\rho_{\mathrm{u}} \to 4$. Applying the Sackur-Tetrode equation (equation 2.14) and the second law of thermodynamics yields

$$s_{\mathrm{d}} - s_{\mathrm{u}} \propto \ln\left[\frac{p_{\mathrm{d}}}{p_{\mathrm{u}}}\left(\frac{\rho_{\mathrm{d}}}{\rho_{\mathrm{u}}}\right)^{-\gamma}\right] \geq 0, \tag{2.59}$$

implying $\mathcal{M}_{\mathrm{u}} \geq 1$ and in turn (using equation 2.58) $\mathcal{M}_{\mathrm{d}} \leq 1$.

2.9.2 Oblique shocks

In case of oblique shocks consider the flow comes in onto the shock discontinuity at an angle $\beta < \pi/2$, and being deflected by a deflection angle θ (figure 2.2). Considering the velocity component normal to the surface of discontinuity, upon transition to the normal shock frame of reference treats the oblique shock as a normal shock with upstream Mach number $\mathcal{M}_\mathrm{u} \sin\beta$, and downstream Mach number $\mathcal{M}_\mathrm{d} \sin(\beta - \theta)$. Inserting this in the jump conditions yields the θ-β-$\mathcal{M}$ relation

$$\tan\theta = 2\cot\beta \frac{\mathcal{M}_\mathrm{u}^2 \sin^2\beta - 1}{\mathcal{M}_\mathrm{u}^2(\gamma + \cos(2\beta)) + 2}. \tag{2.60}$$

Figure 2.2 indicates there are two solutions of β for a combination of $\mathcal{M}$ and θ. The larger value is associated with a *strong shock*, while the smaller value is a *weak shock* solution.

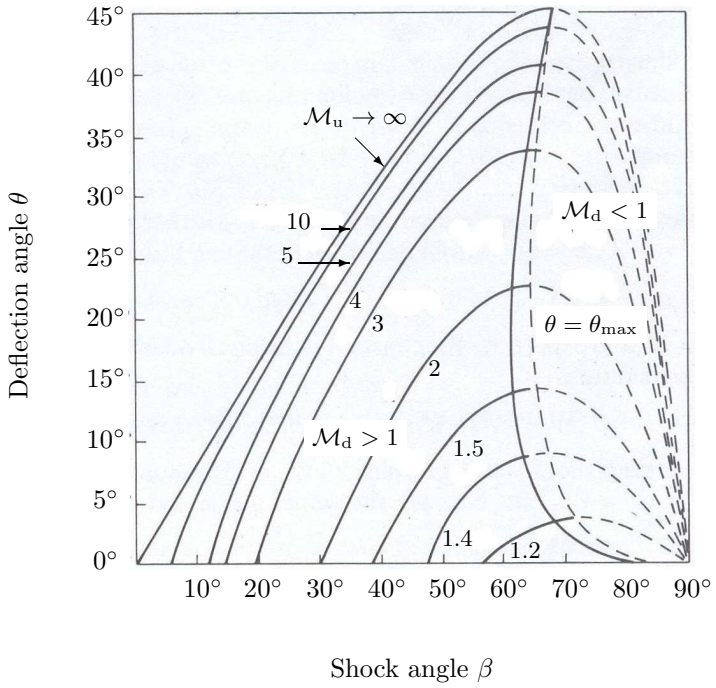

Figure 2.3: θ-β-$\mathcal{M}$ curves of oblique shocks for an ideal gas with $\gamma = 1.4$. Dashed curves represent strong shocks. (Credit: Landau and Lifshitz (1987).)

Given that $\mathcal{M}_\mathrm{u} \sin\beta \geq 1$, the shock angle β is confined to the range

$$\beta \in \left[\arcsin\left(\frac{1}{\mathcal{M}_\mathrm{u}}\right), \frac{\pi}{2}\right]. \tag{2.61}$$

where $\mu \equiv \arcsin(1/\mathcal{M}_\mathrm{u})$ is known as the *Mach angle* of the flow, and $\beta = \pi/2$ corresponds to the normal shock solution.

2.9.3 Detached shocks

Consider a wedge-shaped object being put in the path of a supersonic flow, forcing the flow to bend with at least the wedge angle (figure 2.4(a)). If the wedge angle exceeds $\theta_{\max}$ given the Mach number of the flow and the angle of incidence (as in figure 2.4(b)), the shock forms ahead of he object as a *detached shock*.

(a) Sharp (b) Blunt

Figure 2.4: Supersonic flow past a finite body gives rise to an oblique shock in the flow, which detaches if the object faces the flow under an angle exceeding $\theta_{\max}$. (Credit: based on Landau and Lifshitz (1987)).

2.9.4 Weak shocks

In very weak shocks there is but a small discontinuity in all quantities. The pressure jump condition (equation 2.56) indicates

$$\frac{p_{\mathrm{d}} - p_{\mathrm{u}}}{p_{\mathrm{u}}} = \frac{2\gamma}{\gamma + 1}(\mathcal{M}_{\mathrm{u}}^2 + 1) \tag{2.62}$$

Taylor expansion of a generic equation of state $h(p, s)$ and the thermodynamic relation $dh = Tds + (1/\rho)dp$ (Landau and Lifshitz, 1987) implicates

$$s_{\mathrm{d}} - s_{\mathrm{u}} = \frac{1}{12T_{\mathrm{u}}} \left(\frac{\partial^2 (1/\rho)}{\partial p^2} \right)_s (p_{\mathrm{d}} - p_{\mathrm{u}})^3. \tag{2.63}$$

For an ideal gas

$$\left(\frac{\partial^2 (1/\rho)}{\partial p} \right)_s = \frac{\gamma + 1}{\gamma^2} \frac{1}{\rho p^2} > 0. \tag{2.64}$$

In the limiting case of Mach waves the shock angle approaches the Mach angle ($\beta \approx \beta_{\mathrm{Ma}}$). The deflection angle is very small ($\tan\theta \approx \theta$), and thus

$$\theta \propto (\mathcal{M}_{\mathrm{u}}^2 \sin^2 \beta - 1). \tag{2.65}$$

This implies $p_{\mathrm{d}} - p_{\mathrm{u}} \propto \theta$ and $s_{\mathrm{d}} - s_{\mathrm{u}} \propto \theta^3$.

2.9.5 Prandtl-Meyer flow

Consider a steady supersonic flow along a wall, which suddenly bends in a convex manner (figure 2.5). Dividing the turn in a large number of segments n each deflecting the flow by an angle θ in the Mach wave approximation, the dependence of s on θ^3 means the flow can be modelled as isentropic if $n \to \infty$. The pressure, on the other hand, is proportional to θ and so a finite pressure change remains.

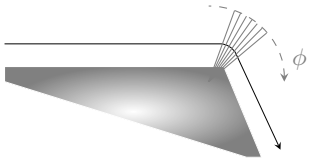

Figure 2.5: When a fluid flows about a convex corner, rarefaction waves are introduced in the flow. This expansion can be approximated by a Prandtl-Meyer expansion fan.

In the gradual transitional area, a polar coordinate system (r, ϕ) can be used to describe the fluid in (figure 2.5). None of the fluid parameters is to depend on r, and so conservation of mass and momentum impose

$$\rho v_r + \frac{\partial}{\partial \phi}(\rho v_\phi) = 0, \tag{2.66}$$

$$\frac{v_\phi}{r}\frac{\partial v_r}{\partial \phi} = 0, \tag{2.67}$$

$$\frac{v_\phi}{r}\frac{\partial v_\phi}{\partial \phi} + \frac{v_r v_\phi}{r} = -\frac{1}{r}\frac{\partial p}{\partial \phi}. \tag{2.68}$$

For isentropic flow $\partial p = c_\mathrm{s}^2 \partial \rho$, and thus the equations can be combined to yield

$$\left(v_r + \frac{\partial v_\phi}{\partial \phi}\right)\left(1 + \frac{v_\phi^2}{c_\mathrm{s}^2}\right) = 0. \tag{2.69}$$

Given $\partial p / \partial \phi \neq 0$, this yields

$$v_\phi = c_\mathrm{s}. \tag{2.70}$$

For steady flow, Bernoulli's equation (equation 2.22) implies that along a streamline

$$\frac{1}{2}v^2 + h = h_0, \tag{2.71}$$

where $v^2 = v_r^2 + v_\phi^2$ and $h = h_0$ if $v = 0$, and therefore

$$v_r = \sqrt{2(h_0 - h) - c_\mathrm{s}^2}. \tag{2.72}$$

Conservation of mass (equation 2.66) in the form $d\phi = -d(\rho v_\phi)/\rho v_r$ then yields in conjunction with the velocity components (equations 2.70 and 2.72)

$$\phi = -\int \frac{d(\rho v_\psi)}{\rho v_r} = -\int \frac{d(\rho c_\mathrm{s})}{\rho\sqrt{2(h_0 - h) - c_\mathrm{s}^2)}} \tag{2.73}$$

For an ideal gas $h = c_\mathrm{s}^2/(\gamma - 1)$, and given isentropic conditions[2] one obtains (Landau and Lifshitz, 1987)

$$\phi = -\sqrt{\frac{\gamma+1}{\gamma-1}}\int \frac{dc_\mathrm{s}}{\sqrt{c_{\mathrm{s},*}^2 - c_\mathrm{s}^2}}, \tag{2.74}$$

where $c_{\mathrm{s},*} \equiv c_{\mathrm{s},0}\sqrt{2/\gamma+1}$. Integrating yields

$$\phi = \sqrt{\frac{\gamma+1}{\gamma-1}}\arccos\left(\frac{c_\mathrm{s}}{c_{\mathrm{s},*}}\right) + \text{constant}. \tag{2.75}$$

Given that if $\phi = 0$, then $v_r = 0$,

$$v_\phi = c_\mathrm{s} = c_{\mathrm{s},*}\cos\left(\sqrt{\frac{\gamma-1}{\gamma+1}}\phi\right), \tag{2.76}$$

$$v_r = \sqrt{\frac{\gamma+1}{\gamma-1}}c_{\mathrm{s},*}\sin\left(\sqrt{\frac{\gamma-1}{\gamma+1}}\phi\right). \tag{2.77}$$

As the fan of Mach waves is oriented in the r-direction where the flow impacts the shocks under the Mach angle

$$\cot\mu = \frac{v_\phi}{v_r} = \sqrt{\frac{\gamma+1}{\gamma-1}}\tan\left(\sqrt{\frac{\gamma-1}{\gamma+1}}\phi\right), \tag{2.78}$$

where the Mach angle $\mu = \arcsin(1/\mathcal{M})$ and thus $\cot\mu = \sqrt{\mathcal{M}^2 - 1}$. Rearranging terms yields

$$\phi = \sqrt{\frac{\gamma+1}{\gamma-1}}\arctan\sqrt{\frac{\gamma-1}{\gamma+1}(\mathcal{M}^2 - 1)}. \tag{2.79}$$

The Prandtl-Meyer function is defined as the angle through which a flow, initially at Mach 1, must be expanded to reach a supersonic Mach number $\mathcal{M}$.

$$\nu \equiv \phi + \mu - \frac{1}{2}\pi \tag{2.80}$$

$$= \sqrt{\frac{\gamma+1}{\gamma-1}}\arctan\sqrt{\frac{\gamma-1}{\gamma+1}(\mathcal{M}^2 - 1)} - \arctan\sqrt{\mathcal{M}^2 - 1}. \tag{2.81}$$

[2]Using $p \propto \rho^\gamma$ and $c_\mathrm{s}^2 = \gamma p/\rho$ relations between ρ or p on one side and c_s on the other are derived.

2.10 Tangential discontinuities

When considering discontinuous solutions for a fluid state, a non-zero mass transfer across the surface of discontinuity had to be imposed in order to allow for a pressure discontinuity. Here the trivial solution is considered, which entails

$$\rho_{\mathrm{u}} v_{\mathrm{u},z} = \rho_{\mathrm{d}} v_{\mathrm{d},z} = 0. \tag{2.82}$$

Applying this to relations 2.46 to 2.48 yields $v_{\mathrm{u},z} = v_{\mathrm{d},z} = 0$ and $p_{\mathrm{u}} = p_{\mathrm{d}}$, as the density ρ can be zero in neither region u nor d. Given the fluid flows parallel to the surface of discontinuity on both sides of the divide this is known as a *tangential discontinuity*.

All tangential discontinuities have discontinuous density and temperature profiles (e.g. cold fronts, paragraph 1.6.3). The tangential velocity component jump is not constrained by the conservation laws. *Contact discontinuities* are tangential discontinuities with the velocity field continuous across the surface of discontinuity ($\vec{v}_{\mathrm{d}} = \vec{v}_{\mathrm{u}}$).

2.11 Weak discontinuities

Based on the conservations equations of mass, momentum, and energy. three categories of solutions can be distinguished. If all variables are continuously differentiable, the divergence theorem can be applied to find solutions. In the previous two sections two scenarios in which a number of variables are discontinuous. Weak discontinuities comprise the third category, for which all variables are continuous but some are not differentiable across the surface under consideration.

2.12 Stability and turbulence

Obeying the conservation laws is not sufficient for a state to occur in nature. In addition, a state also needs to be stable. The stability is measured by perturbing the state with a linear wave perturbation (cf. paragraph 2.8). If the equations of fluid dynamics indicate the amplitude of the wave increases rapidly with time, the state is identified as unstable. Eventually the laminar (layered) flow becomes turbulent.

2.12.1 Kelvin-Helmholtz instability

Consider two layers of incompressible fluid in contact, separated by a tangential discontinuity and slipping past one another (figure 2.6).

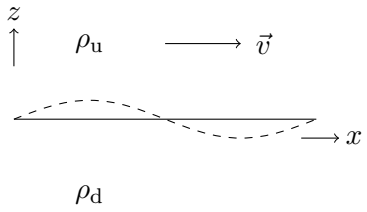

Figure 2.6: Incompressible perturbation in a stratified fluid separated by a tangential discontinuity with $\rho_u > \rho_d$ results in Kelvin-Helmholtz instability.

The surface of discontinuity is displaced, its perturbed z coordinate given by

$$z_{sd} = A \exp(ikx - i\omega t). \tag{2.83}$$

Conservation of mass and momentum imply

$$\vec{\nabla} \cdot (\delta\vec{v}) = 0, \tag{2.84}$$

$$\frac{\partial \delta\vec{v}}{\partial t} + (\delta\vec{v} \cdot \nabla)\delta\vec{v} = -\frac{\vec{\nabla}(\delta p)}{\rho}. \tag{2.85}$$

Taking the divergence of the second equation yields $\Delta(\delta p) = 0$.

Seeking a solution of the form $\delta p = \eta(z) \exp(ikx - i\omega t)$ and inserting this into Laplace's equation yields $d^2\eta/dz^2 - k^2\eta = 0$ and thus

$$\delta p_{\pm} = B_{\pm} \exp(\pm kz + ikx - i\omega t). \tag{2.86}$$

Here $-$ applies in region u, and $+$ applies in region d (otherwise the perturbation will not vanish at infinity). Inserting this in Euler's equation yields for the z-component of the velocity

$$\delta\vec{v}_{\pm,z} = \frac{k\delta p_{\pm}}{i\rho_{\pm}}(kv_{\pm} - \omega). \tag{2.87}$$

Given the small amplitude of the oscillations, any point that is on the surface remains on the surface. Therefore

$$\delta v_{\pm,z} z = z_{\mathrm{sd}} = \frac{\partial z_{\mathrm{zd}}}{\partial t} + v_{\pm}\frac{\partial z_{\mathrm{zd}}}{\partial x}. \tag{2.88}$$

Thus $\delta v_{\pm,z} = iz_{\mathrm{sd}}(kv_{\pm} - \omega)$ and

$$\delta p_{\pm} = \pm\frac{z_{\mathrm{sd}}\rho_{\pm}(kv_{\pm} - \omega)^2}{k}. \tag{2.89}$$

As pressure is continuous across a tangential discontinuity $\delta p_u = \delta p_d$, which implies $\rho_u(kv - \omega)^2 = -\rho_d\omega^2$ and thus

$$\omega = kv\frac{\rho_{\mathrm{u}} \pm i\sqrt{\rho_{\mathrm{u}}\rho_{\mathrm{d}}}}{\rho_{\mathrm{u}} + \rho_{\mathrm{d}}}. \tag{2.90}$$

The solution with $\Im(\omega) > 0$ is unstable. The signature of resulting turbulent flow is given in figure 2.7.

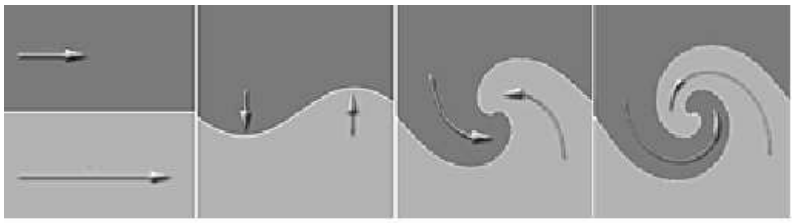

Figure 2.7: Two layers of gas gliding against each other gives rise to Kelvin-Helmholtz instability.

2.12.2 Rayleigh-Taylor instability

Consider two layers of incompressible fluid of uniform (but different) density in mechanical equilibrium, embedded in a uniform gravitational field and separated by a contact discontinuity (figure 2.8).

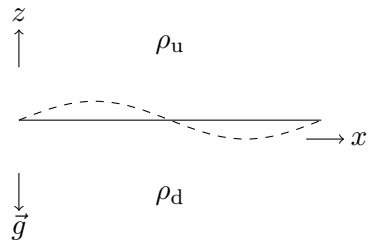

Figure 2.8: Incompressible perturbation in a stratified fluid separated by a tangential discontinuity with $\rho_{\rm u} > \rho_{\rm d}$ results in Rayleigh-Taylor instability.

If the surface of discontinuity is displaced, its perturbed z coordinate is given by $z_{\rm sd} = A\exp(ikx - i\omega t)$. For incompressible and irrotational perturbations a velocity potential ϕ can be defined

$$\delta\vec{v} = \vec{\nabla}\phi, \tag{2.91}$$

for which mass conservation and incompressibility implies $\nabla^2\phi = 0$.

If the velocity potential is of the form $\phi = \eta(z)\exp(ikx - i\omega t)$, then inserting this into Laplace's equation yields $d^2\eta/dz^2 - k^2\eta = 0$ and thus

$$\phi_\pm = B_\pm \exp(\pm kz + ikx - i\omega t). \tag{2.92}$$

These waves are known as *surface gravity waves*. The $-$ applies in region u, and $+$ applies in region d (otherwise the perturbation will not vanish at infinity as required by earlier assumptions).

A boundary condition is that given the small amplitude of the oscillations, any point that is on the surface stays on (or better: co-moves with) the surface. Therefore

$$\left(\frac{\partial\phi_\pm}{\partial z}\right)_{z=z_{\rm sd}} = \frac{\partial z_{\rm zd}}{\partial t} \tag{2.93}$$

As the perturbation are small, it is acceptable to take the derivatives at $z = 0$ instead of $z = z_{\mathrm{sd}}$. Inserting ϕ and z_{sd} then yields

$$\pm k B_{\pm} = -i\omega A. \tag{2.94}$$

Pressure is also known to be continuous across a tangential discontinuity. Euler's equation yields

$$\frac{\partial \vec{v}}{\partial t} = -\frac{1}{\rho}\vec{\nabla} p - g\vec{e}_z. \tag{2.95}$$

The term $(\vec{v} \cdot \nabla)\vec{v}$ in Euler's equation has been neglected in comparison with $\partial\vec{v}/\partial t$ for gravity waves with an amplitude much smaller than its wavelength. Inserting the velocity potential and integrating then implies

$$\frac{\partial \phi}{\partial t} = -\frac{p}{\rho} - gz, \tag{2.96}$$

Continuity of pressure is therefore equivalent to imposing the condition

$$\rho_- \left(g z_{\mathrm{sd}} + \frac{\partial \phi_-}{\partial t} \right) = \rho_+ \left(g z_{\mathrm{sd}} + \frac{\partial \phi_+}{\partial t} \right), \tag{2.97}$$

Evaluating this expression at $z = 0$ results in

$$\rho_- \left(-i\omega B_- + gA \right) = \rho_+ \left(-i\omega B_+ + gA \right). \tag{2.98}$$

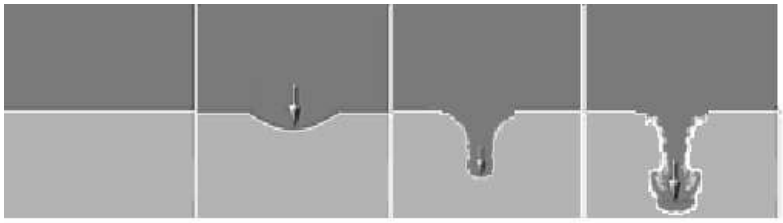

Figure 2.9: A layer of denser gas rests on top of a layer of light gas in a gravitational field pointing down. When a perturbation disturbs the pressure equilibrium, the gravity potential gradient will attract further gas and amplify the perturbation.

Combining this result with the amplitude relation given by equation 2.94 yields

$$\omega^2 = \left(\frac{\rho_{\mathrm{d}} - \rho_{\mathrm{u}}}{\rho_{\mathrm{u}} + \rho_{\mathrm{d}}} \right) gk, \tag{2.99}$$

where $(\rho_{\mathrm{d}} - \rho_{\mathrm{u}}/(\rho_{\mathrm{u}} + \rho_{\mathrm{d}})$ is known as the *Atwood number*. Unstable states with $\Im(\omega) > 0$ result in wave amplification known as *Rayleigh-Taylor instability*. As a result the heavier fluid penetrates into underlying lighter fluid (figure 2.9).

2.12.3 Richtmyer-Meshkov instability

The Richtmyer-Meshkov instability involves a setting of two layers of fluid at rest, separated by a perturbed contact discontinuity traversed by an incoming shock wave (figure 2.10).

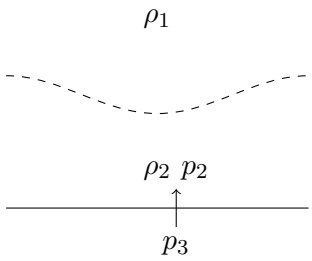

Figure 2.10: Richtmyer-Meshkov instability is the result of a shock wave traversing a perturbed contact discontinuity.

Upon impact the angle between $\vec{\nabla}\rho$ and $\vec{\nabla}p$ varies across the contact discontinuity. From Euler's equation one can deduct (Landau and Lifshitz, 1987) that the time derivative of vorticity is boosted by the baroclinic vector

$$\frac{1}{\rho^2}\left(\vec{\nabla}\rho \times \vec{\nabla}p\right).$$

The resulting vorticity profile results in an amplification of the perturbation, resembling the turbulence profile of the Rayleigh-Taylor instability. In the impulsive approach the same derivation is used as for Rayleigh-Taylor approximation, but with

$$g \to [v_{\mathrm{cd}}]\delta_{\mathrm{D}}(t),$$

where $[v_{\mathrm{cd}}]$ is the change in contact discontinuity surface velocity due to the impacting shock wave, and $\delta_{\mathrm{D}}(t)$ is the Dirac delta-function. Whether $\rho_1 > \rho_2$ or vice versa, this analysis shows the contact discontinuity is unstable under the circumstances outlined here. For a more thorough review on Richtmyer-Meshkov instability one is referred to Brouillette (2002).

2.13 Magneto-fluid dynamics

Magneto-fluid dynamics describes the motion of a conducting fluid in a magnetic field. An *ideal conducting fluid* is defined as an ideal fluid with perfect electrical conductivity ($\sigma \to \infty$), an assumption which yields upon substitution in Ohm's law

$$\vec{J} = \sigma\left(\vec{E} + \vec{v} \times \vec{B}\right) \qquad \Rightarrow \qquad \frac{\vec{J}}{\sigma} = \vec{E} + \vec{v} \times \vec{B} \to 0. \tag{2.100}$$

In an ideal conducting fluid no Lorentz force therefore acts on a charged particle moving with the flow.

Consider the plasma as a non-relativistic conductive fluid. As local charge concentrations are accounted for by motion due to electromagnetic forces, it is noted charge is essentially irrelevant beyond the Debye length. Limiting the scope to larger scales, the plasma can be considered quasi-static, and therefore Gauss's law implies $\vec{\nabla} \cdot \vec{E} = 0$. Continuing with Ampère's law

$$\vec{\nabla} \times \vec{B} = \mu_0 \vec{J} + \mu_0 \epsilon_0 \frac{\partial \vec{E}}{\partial t}, \tag{2.101}$$

a typical length scale L, time scale T, and velocity scale $U = L/T$ is defined. As $E \sim UB$ and $c^2 \equiv (\mu_0 \epsilon_0)^{-1}$

$$\frac{\mu_0 \epsilon_0 \left|\frac{\partial \vec{E}}{\partial t}\right|}{\left|\vec{\nabla} \times \vec{B}\right|} \sim \frac{1}{c^2} \frac{E/T}{B/L} = \frac{U^2}{c^2} \to 0 \tag{2.102}$$

in a non-relativistic limit. Thus the displacement current $\mu_0 \epsilon_0 \partial \vec{E}/\partial t$ is neglected within the scope of ideal magneto-fluid dynamics and Ampère's law yields for the current density

$$\vec{J} = \frac{1}{\mu_0} \vec{\nabla} \times \vec{B}. \tag{2.103}$$

Faraday's law is employed to evolve the magnetic field, as

$$\frac{\partial \vec{B}}{\partial t} = -\vec{\nabla} \times \vec{E} = \vec{\nabla} \times (\vec{\nabla} \times B), \tag{2.104}$$

while the remaining Maxwell equation $\vec{\nabla} \cdot \vec{B} = 0$ acts as an extra condition.

Mass conservation applies to a conducting fluid just as it does to a non-conducting fluid and so

$$\frac{\partial \rho}{\partial t} + \vec{\nabla} \cdot (\rho \vec{v}) = 0. \tag{2.105}$$

The electromagnetic field gives rise to a magnetic force[3]

$$\vec{J} \times \vec{B} = \frac{\vec{\nabla} \times \vec{B}}{\mu_0} \times \vec{B} = \frac{1}{\mu_0}(\vec{B} \cdot \nabla)\vec{B} - \vec{\nabla}\left(\frac{B^2}{2\mu_0}\right). \tag{2.106}$$

The term $(\vec{B} \cdot \nabla)\vec{B}$ represents magnetic tension and the second

$$p_{\rm m} \equiv \frac{B^2}{2\mu_0} \tag{2.107}$$

magnetic pressure. Given $\vec{\nabla} \cdot \vec{B} = 0$, this result can be written as

$$\vec{J} \times \vec{B} = \vec{\nabla} \cdot \left(\frac{\vec{B}\vec{B}}{\mu_0}\right) - \vec{\nabla} \cdot \left(p_{\rm m} \overleftrightarrow{I}_3\right). \tag{2.108}$$

Defining $p_{\rm t} \equiv p + p_{\rm m}$ the momentum conservation equation reads

$$\frac{\partial \rho \vec{v}}{\partial t} + \vec{\nabla} \cdot \left[\rho \vec{v}\vec{v} - \frac{1}{\mu_0}\vec{B}\vec{B} + p_{\rm t} \overleftrightarrow{I}_3\right] = \rho \vec{f}_{\rm ext}. \tag{2.109}$$

The energy density in the fluid is appended by the magnetic energy density $B^2/2\mu_0$

$$\rho e = \rho e_{\rm int} + \frac{1}{2}\rho v^2 + \frac{B^2}{2\mu_0}, \tag{2.110}$$

while the electromagnetic energy flux density is given by the Poynting vector

$$\vec{S} = \frac{1}{\mu_0}\vec{E} \times \vec{B} = \frac{1}{\mu_0}\vec{B} \times (\vec{v} \times \vec{B}) = \frac{1}{\mu_0}\left[B^2\vec{v} - \vec{B}(\vec{B} \cdot \vec{v})\right]. \tag{2.111}$$

The energy conservation equation consequentially reads

$$\frac{\partial \rho e}{\partial t} + \vec{\nabla} \cdot \left(\rho e \vec{v} + p_{\rm t}\vec{v} - \frac{1}{\mu_0}\vec{B}(\vec{B} \cdot \vec{v})\right) = \rho \vec{v} \cdot \vec{f}_{\rm ext}. \tag{2.112}$$

The set of conservation equations is now appended two of the electromagnetic relations

$$\frac{\partial \vec{B}}{\partial t} = \vec{\nabla} \times (\vec{\nabla} \times B), \tag{2.113}$$

$$\vec{\nabla} \cdot \vec{B} = 0, \tag{2.114}$$

which are employed to evolve the magnetic field. The plasma parameter, defined as the ratio of thermal and magnetic pressure, is now demonstrated to mark the difference between normal and magnetic fluid dynamics.

[3]The electric force is not significant given the quasi-neutral nature of the fluid.

Chapter 3

The FLASH CFD code

Simulations in this thesis have been done with the FLASH code version 3.1.1, which was developed by the DOE-supported ASC / Alliance Center for Astrophysical Thermonuclear Flashes at the University of Chicago (Fryxell et al., 2000). The activity diagram of the FLASH code as applicable for all simulations run in this thesis is shown in diagram 3.1.

3.1 Parameter file and unit initialization

In the initialisation phase the simulation is initiated by reading in a user-supplied parameter file, by means of which the user can customise parameters from all involved FLASH modules without having to recompile (figure 3.2).

The FLASH code is modular with the unit as building block. All variables and subroutines are associated with one of the units (table 3.1), some of which require allocating memory that consequentially needs to be deallocated when the simulation terminates. Parameter values are set by default or by the parameter file.

Table 3.1: List of FLASH units.

Driver	IO	Particles	RuntimeParameters
flashUtilities	monitors	PhysicalConstants	Simulation
Grid	Multispecies	physics	

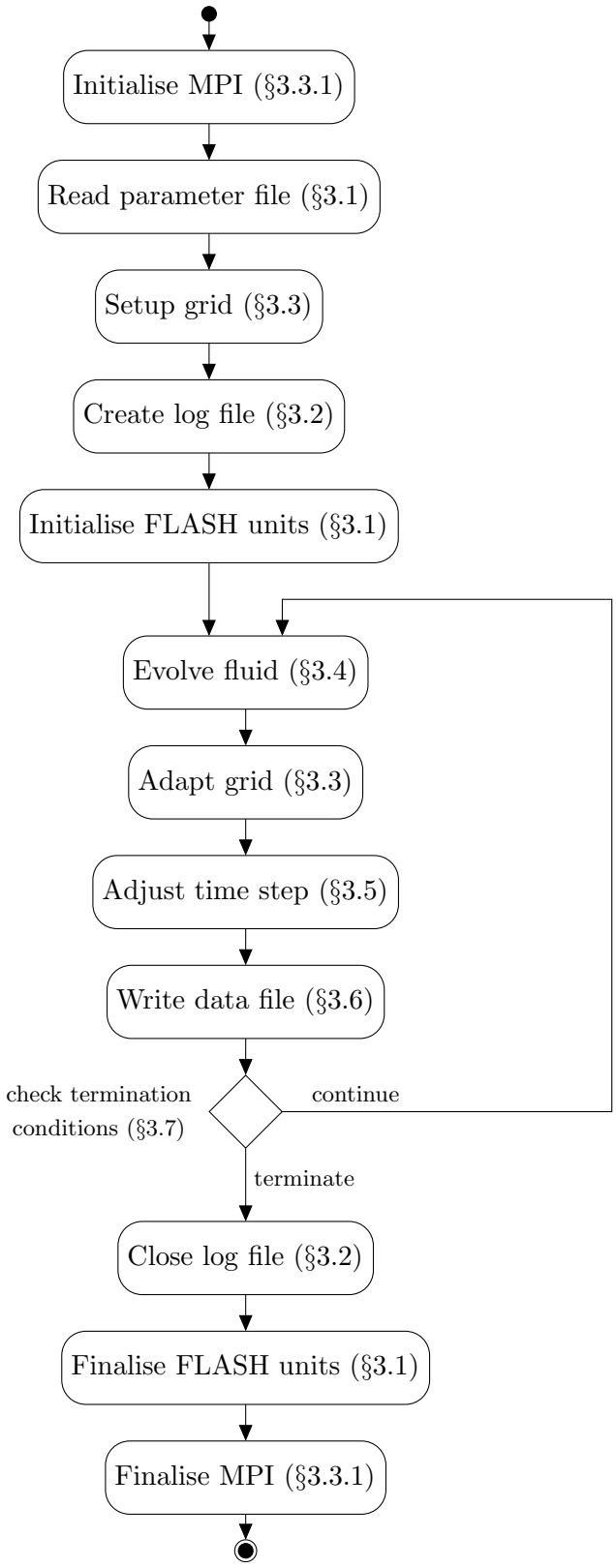

Figure 3.1: Activity diagram of the FLASH code.

```
# Adaptive mesh refinement


lrefine_min                = 3
lrefine_max                = 6
nrefs                      = 1
refine_var_1               = "dens"
refine_var_2               = "pres"
```

Figure 3.2: An extract from a FLASH parameter file.

The nature of these parameters can differ widely; most have default values. In the extract the grid is refined everywhere to at least refinement level 3, while the maximum refinement level is 6. The grid is evaluated for adaption every time step, and the refinement criterion is tested against the density and pressure profiles. The number sign `#` indicates a comment line.

3.1.1 Simulation unit

The Simulation unit is special in that it contains units that are project-specific. The user can define additional variables and subroutines, or alternatively extent or adjust existing parts of the FLASH code within the scope of the project unit.

3.2 Log file

A subunit of the monitors unit is the Logfile unit, that maintains a log file on the simulation progress. The extract listed below prints the local time, details of a single step, with the step number, the current simulation time and time step (in Ma). As grid refinement takes place during this time step associated details are also reflected.

```
[ 09-09-2010  20:11:31.646 ] step: n=111 t/Ma=6.180652E+00 dt/Ma=1.833447E-02
[ 09-09-2010  20:11:49.624 ] [GRID amr_refine_derefine]: initiating refinement
[GRID amr_refine_derefine] min blks 138  max blks 139 tot blks 1106
[GRID amr_refine_derefine] min leaf blks 121 max leaf blks 121 tot leaf blks 968
[ 09-09-2010  20:11:49.995 ] [GRID amr_refine_derefine]: refinement complete
```

3.3 Grid geometry

Fluid dynamics by definition describes a continuum, and that itself poses a problem for any computer since computers can only store discrete data sets. In the FLASH code solving this problem is delegated to the PARAMESH grid toolkit (version 4.0), a toolkit developed at the NASA Goddard Space Flight Center and Drexel University under NASA's HPCC and ESTO/CT projects and under grant NNG04GP79G from the NASA/AISR project (MacNeice et al. (2000), Olsen and MacNeice (2005), Olsen (2006)).

PARAMESH's discretization algorithm is based on the *finite volume method*, which involves splitting the domain into elements of finite volume (figure 3.3). A volume element i contains an amount of mass m_i, momentum $\int_{V_i} \rho\vec{v}\, dV$, and energy E_i, for which the conservation laws imply

$$\frac{\partial M_i}{\partial t} + \oint_{\partial V_i} \rho\vec{v} \cdot d\vec{A} = 0, \tag{3.1}$$

$$\frac{\partial}{\partial t}\int_{V_i} \rho\vec{v}\, dV + \oint_{\partial V_i} (\rho\vec{v}\vec{v} - \overleftrightarrow{\sigma})\, d\vec{A} = \int_{V_i} \rho\vec{f}_{\text{ext}}\, dV \tag{3.2}$$

$$\frac{\partial E_i}{\partial t} + \oint_{\partial V_i} (\rho e + p)\vec{v} \cdot d\vec{A} = \int_{V_i} \rho\vec{f}_{\text{ext}} \cdot \vec{v}\, dV + \dot{Q}. \tag{3.3}$$

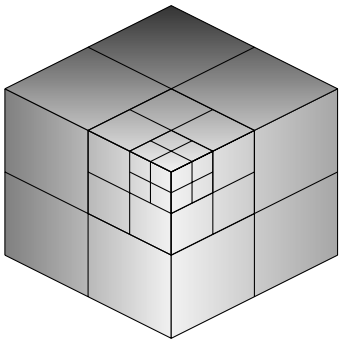

Figure 3.3: The finite volume method splits the continuous fluid up in finite volume elements. To conserve on computational resources the element size can be varied across the fluid as the fluid is evolved; this strategy is known as adaptive mesh refinement (AMR).

3.3.1 PARAMESH: A parallel, adaptive, grid tool

Grid configurations can be divided into structured and unstructured topologies. PARAMESH uses block-structured topology, with a cubic domain divided into similarly cubic *blocks* placed on a regular grid. The actual block morphology can differ from cubic because of, for instance, a non-Cartesian geometry, or different domain dimensions.

For high performance computing purposes PARAMESH is designed to operate in parallel. This is achieved by deploying the Message Passing Interface library (Gropp, Lusk and Thakur, 1999), which is initialised and finalised in the beginning and end respectively of the activity diagram (figure 3.1).

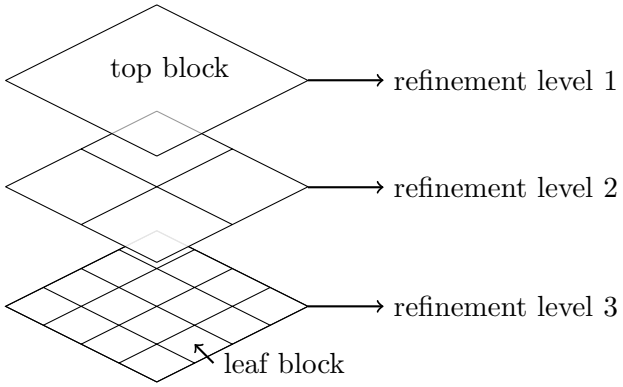

Figure 3.4: The grid structure used by PARAMESH is adaptive. A block can split into identical child blocks, which can be derefined once greater resolution is no longer required. The dashed lines indicate where the block is divided upon refinement.

The adaptive qualifier refers to the ability PARAMESH has to refine the grid locally. In many cases in which very high resolution in but a small area is required refining the entire grid results in high computational overhead and a waste of resources. As an *adaptive mesh refinement* (AMR) tool, PARAMESH regulates this waste by locally refining and derefining the grid as the fluid evolves. The refinement procedure used by PARAMESH is depicted in figure 3.4. The grid is first built with a configuration of blocks outlined by the user. When refinement conditions are met, these *top blocks* can split into 2^k, k being the dimensionality of the simulation, identical child blocks.

Refinement level

This procedure can be repeated as many times as deemed desirable. Each iteration of refinement spawns a generation of blocks half the size of the parent block. These generations are therefore referred to as *refinement levels*. Top blocks by definition belong to the first refinement level, while blocks without child blocks are *leaf blocks*. The top block configuration and the allowed range of refinement levels is defined in the user-supplied parameter file.

Derefinement

Derefinement is defined as the inverse procedure of refinement, i.e. 2^k child blocks that spawned from a common parent block are removed from the tree, thus returning leaf block status to their parent. In order to preserve the structural integrity of the grid tree blocks from mixed parentage cannot derefine collectively.

Global identification of blocks

A block is globally identified by the id of the processor that handles it, and the id it has been given on that processor (an integer number ranging from 1 to the total number of blocks the processor is handling). Relative positioning within the array is monitored by keeping track of the parent id, the child ids, and the ids of neighbours at the same refinement level. If all neighbour leaf blocks have courser resolution than the block under consideration, -1 is returned as neighbour id.

Constraint to the refinement process

PARAMESH constrains the grid such that blocks can only neighbour each other if their refinement level difference is equal to or smaller than one level. It is therefore possible to request the parent's neighbour in the same direction, which is guaranteed to yield result unless the requested direction brings one beyond the boundaries of the computational domain.

3.3.2 Subgrid structure: cells

The performance bottleneck for high performance computing is communication between processors, as processors are not equally fast and will often have to wait for one another in such situations. To limit communications to the minimum, each block is endowed with a sub-grid of *cells* (figure 3.5). Each cell again has cubic topology, and the number of cell in each dimension is prefixed by the user and the same for all blocks regardless of refinement level. The onus of data-managing moves therefore from the blocks to the cells; the role of blocks is confined to grid management. One can now achieve greater resolution with fewer blocks, and neighbouring cells are usually part of the same block. As all cells of the same block are also evolved by the same processor, this results in an overall reduction of inter-processor communication as was the objective of this construction.

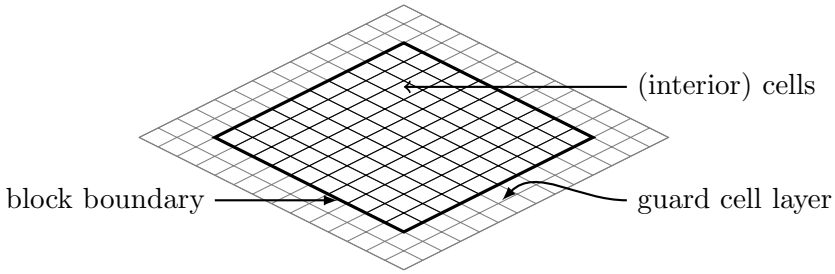

Figure 3.5: Each block is endowed with a substructure of cells. For evolution purposes the horizon of each block is widened by supplying a guard cell padding, in which data copies of adjacent cells in neighbouring blocks are stored.

Guard cells

In order to provide the processors with independence of inter-processor communication during the grid evolution stage, each block is endowed with a padding of *guard cells*. Prior to applying the conservation laws, data from zones in neighbouring blocks are copied into the guard cell storage, thus extending the horizon of each block to such an extent that it has all the information required to evolve without further need for communication. External boundaries are defined in the parameter file; in this thesis reflecting and outflow boundary conditions are implemented.

3.3.3 State variables

Each cell contains an amount of mass, momentum and energy. In volume-averaged units this yields

$$\langle\rho\rangle_i = M_i/V_i, \qquad \langle\rho\vec{v}\rangle_i = (1/V_i)\int_{V_i}\rho\vec{v}\,dV, \qquad \langle\rho e\rangle_i = E_i/V_i, \tag{3.4}$$

where the average value of a generic quantity u within a volume V is defined

$$\langle u\rangle \equiv \frac{1}{V}\int_V u\,dV. \tag{3.5}$$

In actuality, FLASH stores *primitive variables*, i.e. physical observables. The conserved quantity values are related by (Fryxell et al., 2000)

$$\langle\rho v_{x,y,z}\rangle \approx \langle\rho\rangle\,\langle v_{x,y,z}\rangle, \qquad \langle\rho e\rangle \approx \langle\rho\rangle\,\langle e\rangle. \tag{3.6}$$

Requirements on performance demand that only leaf block data is maintained during the simulation.

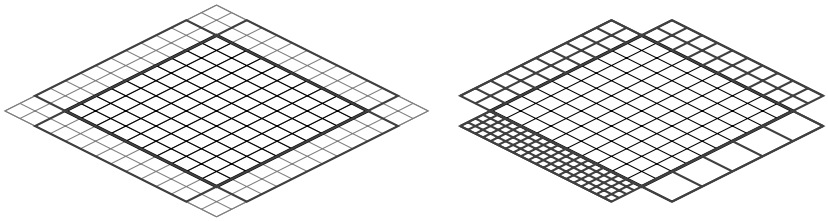

Figure 3.6: Guard cell filling involves importing data from cells belonging to adjacent blocks. A problem arises when there is a refinement jump on a block boundary, in which case guard cell data is interpolated from the finer/courser cells.

3.3.4 Data prolongation and restriction

Prior to evolving the grid the guard cell layer of each block is filled with data from adjacent blocks. In case of a difference in resolution (figure 3.6), data points are interpolated using quadratic interpolation. The midpoint rule is employed to associate coordinates with cells. The procedure is referred to as *prolongation* if the data is mapped from a course to a fine grid, and *restriction* if the data is mapped from a fine to a course grid.

3.3.5 Grid refinement criteria

The refinement criteria themselves are within PARAMESH user-defined. However, embedded in the FLASH code a default (de)refinement criterion is supplied. Two variables are selected to be used to mark for refinement or derefinement; in the simulations discussed in this thesis density and pressure are selected.

The refinement criterion is based on the second derivative in these two state variables. As each block sub-grid has all the information relevant for that block to be evolved, and the block sub-grid is regular, it is possible to restrict the discussion to determining numerical derivatives on a regular grid.

Within a block a cell can be identified by a combination of three indices (i, j, k), which mark the grid point number in x, y and z directions respectively. The x-component of the gradient over a generic state variable u is then approximated by

$$\left.\frac{\partial\langle u\rangle}{\partial x}\right|_{(i,j,k)} \approx \frac{\langle u\rangle_{(i+1,j,k)} - \langle u\rangle_{(i-1,j,k)}}{2\Delta x}, \tag{3.7}$$

In this formula Δx is the grid spacing in the x-direction. The y and z-components are calculated similarly. The second derivative of equation 3.7 with respect to y is

$$\left.\frac{\partial\langle u\rangle}{\partial y\partial x}\right|_{(i,j,k)} \approx \frac{\left.\frac{\partial\langle u\rangle}{\partial x}\right|_{(i+1,j,k)} - \left.\frac{\partial\langle u\rangle}{\partial x}\right|_{(i-1,j,k)}}{2\Delta y}, \tag{3.8}$$

Δy being the grid spacing in y-direction. Given three gradient terms and three directions, a nine-term second derivative is associated with a single cell. Lohner (1987) defined an error term by summing over all nine terms weighed by the square of the first derivatives to make each term dimensionless. For an exact formulation of the error term one is referred to Fryxell et al. (2000). The essence is that if the dimensionless error term exceeds a certain value, the cell is marked for refinement. If the value is too low, the cell is marked for derefinement. In simulations discussed in this thesis, FLASH evaluates the grid for refinement each iteration using density and pressure as indicators.

A block is refined the moment one of its cells is marked for refinement. Conversely, a block is derefined the moment all its cells meet the derefinement criterion. Additional refinement is imposed by PARAMESH if the difference in refinement level between adjacent blocks is about to differ by more than one level.

3.4 Fluid evolution: the piecewise parabolic method

FLASH offers a range of methods to evolve a fluid. Within the scope of this thesis only the *piecewise parabolic method* (PPM, Colella and Woodward (1984)) is relevant. This method essentially implements a numerical method employing the conservation laws to construct the fluid state at a later time.

3.4.1 Dimensional splitting

To evolve the fluid FLASH employs the conservation equations in differential form, a set which can be written as

$$\frac{\partial \mathbf{U}}{\partial t} + \frac{\partial \mathbf{F}}{\partial x} + \frac{\partial \mathbf{G}}{\partial y} + \frac{\partial \mathbf{H}}{\partial z} = \mathbf{S}. \tag{3.9}$$

In this equation the *state vector* is

$$\mathbf{U} = \begin{bmatrix} \rho \\ \rho v_x \\ \rho v_y \\ \rho v_z \\ \rho e \end{bmatrix}, \tag{3.10}$$

where the fluxes and source terms are determined by the conservation equations. With *dimensional splitting* equation 3.9 by setting $\mathbf{G} = \mathbf{H} = 0$. The solution is similarly evolved, but with $\mathbf{F} = \mathbf{H} = 0$, followed by a similar procedure with $\mathbf{F} = \mathbf{G} = 0$. The procedure is then repeated the other way around.

The process is thus divided into two- half-steps, the first being the *xyz-sweep* and the second the *zyx-sweep*. The error introduced by this procedure is insignificant compared to other numerical errors in a hydrodynamical simulation (LeVeque, 2002). By splitting the evolution in six steps, the three-dimensional problem is essentially exchanged for six one-dimensional problems.

3.4.2 Reconstruction step

Within the scope of the finite volume method, data points are voxels; any information on state variable distributions inside voxels is lost. The first step of the evolving stage is therefore reconstructing variable profiles within each voxel.

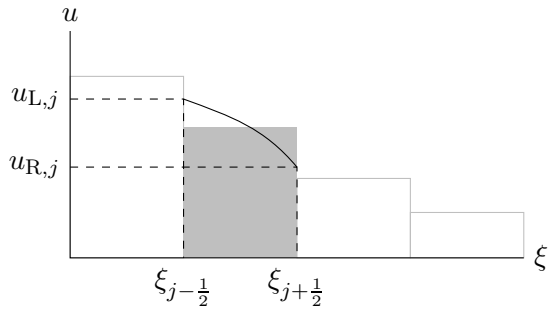

Given dimensional splitting the discussion can be confined to solving the problem in one dimension, characterised by ξ (i.e. either x, y or z). For a generic state variable u the mean value across the cell is (with $\Delta\xi \equiv \xi_{j+\frac{1}{2}} - \xi_{j-\frac{1}{2}}$)

$$\langle u \rangle_j = \frac{1}{\Delta\xi} \int_{\xi_{j-\frac{1}{2}}}^{\xi_{j+\frac{1}{2}}} u(\xi)\, d\xi. \tag{3.11}$$

The function $u(\xi)$ is modelled as piecewise parabolic

$$u(\psi) = u_{\mathrm{L},j} + \psi(\Delta u + u_{6,j}(1-\psi)) \tag{3.12}$$

$$\psi = \frac{\xi - \xi_{j-\frac{1}{2}}}{\Delta\xi} \qquad (\xi \in [\xi_{j-\frac{1}{2}}, \xi_{j-\frac{1}{2}} + \Delta\xi]) \tag{3.13}$$

where $\Delta u \equiv u_{\mathrm{R},j} - u_{\mathrm{L},j}$ and $u_{6,j} = 6(u_j - \frac{1}{2}(u_{\mathrm{L},j} + u_{\mathrm{R},j}))$.

Clearly the left and right boundary values $u_{\mathrm{L},j}$ and $u_{\mathrm{R},j}$ determine the profile. In the reconstruction step the profile is presumed to be uniformly continuous. Thus $u_{\mathrm{L},j} = u_{\mathrm{R},j-1}$. Defining the function

$$U(\xi) = \int u(\xi)\, d\xi \tag{3.14}$$

then $U(\xi_{j+\frac{1}{2}}) = \langle u \rangle_j\, \Delta\xi + U(\xi_{j-\frac{1}{2}})$. Selecting a five-point grid $(\xi_{j+k+\frac{1}{2}}, U_{j+k+\frac{1}{2}})$ with $k \in \{-2,-1,0,1,2\}$ and the integration constant determined by setting $U(\xi_{j-\frac{1}{2}}) \equiv 0$ a quartic polynomial can be fitted. Differentiation of $U(\xi_{j+\frac{1}{2}})$ then yields

$$u_{\mathrm{R},j} = \frac{7}{12}(\langle u \rangle_j + \langle u \rangle_{j+1}) - \frac{1}{12}(\langle u \rangle_{j+2} + \langle u \rangle_{j-1}) \tag{3.15}$$

(Colella and Woodward, 1984). In deriving this result one adjustment has been made to the profiles. The substitution done is replacing

$$\frac{d\langle u\rangle_j}{d\xi} = \frac{\langle u\rangle_{j+1} - \langle u\rangle_{j-1}}{2\Delta\xi} \qquad (j \in \mathbb{Z}) \tag{3.16}$$

by

$$\left(\frac{d\langle u\rangle_j}{d\xi}\right)' = \min\left(\left|\frac{d\langle u\rangle_j}{d\xi}\right|, 2|\langle u\rangle_j - \langle u\rangle_{j-1}|, 2|\langle u\rangle_j - \langle u\rangle_{j+1}|\right)\operatorname{sgn}\left(\frac{d\langle u\rangle_j}{d\xi}\right) \tag{3.17}$$

if $(\langle u\rangle_{j+1} - \langle u\rangle_j)(\langle u\rangle_j - \langle u\rangle_{j-1}) > 0$ or by 0 otherwise. This ensures that $u_{\mathrm{R},j}$ falls between $\langle u\rangle_j$ and $\langle u\rangle_{j+1}$, and sharpens discontinuities to an extent. This adjustment is such that the algorithm still yields results up to fourth order accuracy.

Tangential discontinuity steepening

The next modification is disputable, as it has no theoretical basis but is purely empirical. This means that a number of simulations indicated that steepening the profiles near a contact discontinuity yields a more realistic simulation. The essence of the problem is that tangential discontinuities tend to suffer unrealistically badly from dissipation. The surface of discontinuities in a dissipating discontinuity broadens until the sharp discontinuity becomes a gentle slope.

To check for a tangential discontinuity one first has to select a state variable that is most likely to provide evidence of their presence. Pressure is obviously not a viable option as that variable is continuous across a tangential discontinuity.

Instead, the density profile is considered. With the first derivative of the density profile $\rho_j^{(1)}$ numerically defined by equation 3.16, and supplementing it with a definition for half-integer j

$$\rho_j^{(1)} = \frac{\langle\rho\rangle_{j+\frac{1}{2}} - \langle\rho\rangle_{j-\frac{1}{2}}}{\Delta\xi} \qquad \left(j \in \{\ldots, -\frac{3}{2}, -\frac{1}{2}, \frac{1}{2}, \frac{3}{2}, \ldots\}\right) \tag{3.18}$$

The second and third derivatives are defined

$$\rho_j^{(2)} = \frac{\rho_{j+\frac{1}{2}}^{(1)} - \rho_{j-\frac{1}{2}}^{(1)}}{\Delta\xi} \qquad \rho_j^{(3)} = \frac{\rho_{j+1}^{(2)} - \rho_{j-1}^{(2)}}{2\Delta\xi}. \tag{3.19}$$

The half-integer trick means the derivatives can be resolved on a five-point instead of a seven-point grid, which is computationally fortuitous.

The typical density profile about a surface of discontinuity (both of tangential and shock varieties) is sketched in figure 3.7. With the stereotype density profile in mind three profile criteria are now formulated for discontinuity detection.

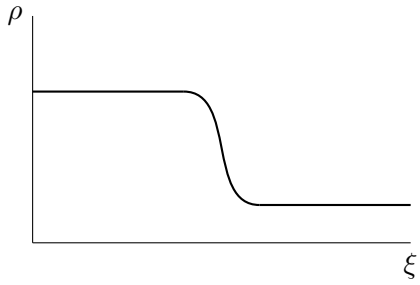

Figure 3.7: Typical density profile about a surface of discontinuity.

- $\rho^{(2)}$ has to change sign across the cell: $\rho^{(2)}_{j-1} \cdot \rho^{(2)}_{j+1} < 0$,
- $\rho^{(3)}_j$ and $\rho^{(1)}_j$ must have opposite signs, and
- the density jump has to be significant

$$|\langle\rho\rangle_{j+1} - \langle\rho\rangle_{j-1}| - 0.01 \min(\langle\rho\rangle_{j-1}, \langle\rho\rangle_{j+1}) > 0. \tag{3.20}$$

The number 0.01 has been determined empirically (i.e. by comparing a lot of simulations to actual experiments). As shock discontinuities tend to be far less dissipative, shock discontinuities are excluded by demanding (with an ideal gas in mind)

$$\frac{|\langle p\rangle_{j+1} - \langle\langle p\rangle_{j-1}|}{\min(\langle p\rangle_{j-1}, \langle p\rangle_{j+1})} \leq 0.1\gamma \frac{|\langle\rho\rangle_{j+1} - \langle\rho\rangle_{j-1}|}{\min(\langle\rho\rangle_{j-1}, \langle\rho\rangle_{j+1})}. \tag{3.21}$$

The dimensionless steepness parameter is defined[1]

$$\varsigma_j \equiv -\frac{(\Delta\xi)^2}{6} \frac{\rho^{(3)}_j}{\rho^{(1)}_j}, \tag{3.22}$$

which defines a switch parameter (Colella and Woodward, 1984)

$$\eta_j \equiv \max(0, \min(20(\varsigma_j - 0.05), 1)). \tag{3.23}$$

The following substitutions are now made:

$$u_{\mathrm{L},j} \to u_{\mathrm{L},j}(1 - \eta_j) + u^{\mathrm{d}}_{\mathrm{L},j}\eta_j \qquad u_{\mathrm{R},j} \to u_{\mathrm{R},j}(1 - \eta_j) + u^{\mathrm{d}}_{\mathrm{R},j}\eta_j, \tag{3.24}$$

where

$$u^{\mathrm{d}}_{\mathrm{L},j} = \langle u\rangle_{j-1} + \frac{1}{2}\left(\frac{d\langle u\rangle_{j-1}}{d\xi}\right)' \qquad u^{\mathrm{d}}_{\mathrm{R},j} = \langle u\rangle_{j+1} + \frac{1}{2}\left(\frac{d\langle u\rangle_{j+1}}{d\xi}\right)' \tag{3.25}$$

[1]The factor 1/6 was put in to bring the result in line with Colella and Woodward (1984), who do the same derivation for a non-uniform grid. This is more generally valid but not terribly insightful due to mathematical complexity, which is the derivation was confined to the uniform case.

Shock discontinuity flattening

Unlike tangential discontinuities, shock discontinuities tend to over-steepen because of little numerical dissipation. Overly narrow shocks are known to lead to non-physical oscillations in the solution.

Shock discontinuities are identified in the grid by the pressure jump

$$\frac{|\langle p\rangle_{j+1} - \langle p\rangle_{j-1}|}{\min(\langle p\rangle_{j-1}, \langle p\rangle_{j+1})} \geq \frac{1}{3}, \tag{3.26}$$

and fluid in a shock discontinuity to be compressed is expected to be compressed

$$\langle v\rangle_{j+1} - \langle v\rangle_{j-1} < 0. \tag{3.27}$$

These two conditions together are empirically found to correctly identify shocks in most situations (Fryxell et al., 2000).

The shock width is defined as the ratio of pressure derivatives using a 2-point or 4-point interval respectively

$$w \equiv \frac{\langle p\rangle_{j+1} - \langle p\rangle_{j-1}}{\langle p\rangle_{j+2} - \langle p\rangle_{j-2}}. \tag{3.28}$$

In smooth flows $w \approx \frac{1}{2}$. For a 1-cell wide shock, the shock pressure jump is localised, and hence $w = 1$. A two-cell wide shocks yields $w = \frac{2}{3}$, and as FLASH is experimentally found to be able to properly handle two-cell wide shocks a pre-switch parameter is (Fryxell et al., 2000)

$$\tilde{\eta}_j \equiv \max(0, \min(10(w - 0.75), 1)). \tag{3.29}$$

The switch parameter is

$$\eta_j \equiv \begin{cases} \max(\tilde{\eta}_j, \tilde{\eta}_j + 1) & \langle p\rangle_{j+1} - \langle p\rangle_{j-1} < 0 \\ \max(\tilde{\eta}_j, \tilde{\eta}_j - 1) & \text{otherwise} \end{cases} \tag{3.30}$$

Flattening of narrow shocks is achieved by implementing

$$u_{\mathrm{L},j} \to u_{\mathrm{L},j}(1 - \eta_j) + \langle u\rangle_j \eta_j \qquad u_{\mathrm{R},j} \to u_{\mathrm{R},j}(1 - \eta_j) + \langle u\rangle_j \eta_j. \tag{3.31}$$

Enforcing monotonicity

It is possible that the parabolic profile of zone j takes a outside the interval $[a_{\mathrm{L},j},_{\mathrm{R},j}]$. Local extrema of this sort are known to lead to unphysical oscillations in the solution (Fryxell et al., 2000; Colella and Woodward, 1984). For this reason a monotonicity condition is imposed on the variable profiles. These conditions can be expressed in the form of three statements

$$(u_{\mathrm{R},j} - \langle u_j \rangle)(\langle u_j \rangle - u_{\mathrm{L},j}) \leq 0 \Rightarrow u_{\mathrm{L},j} = \langle u_j \rangle = \langle u_j \rangle \wedge u_{\mathrm{R},j} = \langle u_j \rangle, \tag{3.32}$$

$$u_{6,j} > \Delta u \Rightarrow u_{\mathrm{L},j} = 3\langle u_j \rangle - 2u_{\mathrm{R},j}, \tag{3.33}$$

$$u_{6,j} < \Delta u \Rightarrow u_{\mathrm{R},j} = 3\langle u_j \rangle - 2u_{\mathrm{L},j}. \tag{3.34}$$

The second and third modifications are based on demanding that

$$\frac{du}{d\psi} = 0 \Rightarrow \psi \notin \langle 0, 1 \rangle \tag{3.35}$$

using the formula for the piecewise parabola (equation 3.13).

3.4.3 Solution step

The second phase of the piecewise parabolic method revolves about updating the state variables. This involves solving the equation (cf. paragraph 3.4.1)

$$\frac{\partial \mathbf{U}}{\partial t} + \frac{\partial \mathbf{F}}{\partial x} = \mathbf{S}. \tag{3.36}$$

(sweeping in x-direction), and similar equations with $\mathbf{G}$ and $\mathbf{H}$. Discretising the equation using finite differences given $\mathbf{F} \propto \mathbf{U}$ amounts to a Forward-Time-Centred-Space scheme – which is unconditionally unstable for numerical perturbations as per Von Neumann stability analysis (LeVeque, 2002), and the piecewise parabolas are not guaranteed to be continuous so that some of the boundary values may be ambiguous.

Instead, FLASH opts for a Riemann solver, which determines the state at the surface of discontinuity by superposing characteristics (paragraph 2.7) incoming from both sides of the divide. This scheme is stable provided the Courant-Friedrichs-Lewy (CFL) condition is met (Fryxell et al., 2000), i.e. as long as no signal in the grid is able to traverse a cell width Δx in a time step Δt.

3.5 Time step determination

After the grid has been refined, the time step for the next iteration is determined. The time step is taken as large as possible but without running the risk of destabilising the solution. The code is found to destabilise if time steps are taken larger than 0.8 times the CFL-time step.

3.6 Input/Output

FLASH outputs two types of files. *Checkpoint files* are designed to contain all the information the FLASH code needs to restart the simulation from the point of termination. *Plot files* contain complete data sets for analysis purposes.

Though other formats are available within FLASH, simulations described in this thesis made use of the Hierarchical Data Format package (HDF5, The HDF Group (2011)). This library creates a structured data file that resembles a database. The internal structure of an HDF5-file is tree-like; interface functions allow the user to navigate through the tree and access specific data sets and elements thereof.

Checkpoint and plot files are created at set simulation time intervals provided in the user-supplied parameter file. Alternatively the user can during run time force the creation of a checkpoint or plot file by creating a file with name `.dump_checkpoint` or `.dump_plotfile` respectively in the directory of the executable.

3.7 Conditions for termination

The simulation terminates when the user-defined maximum simulation time or maximum number of steps is reached, the simulation has run for an amount of time corresponding to the indicated reserved wall clock time interval, or the user forces the simulation to terminate by creating a file with name `.dump_restart` in the directory of the executable. In such case the program leaves the evolution loop and enters the finalisation stage. When the code is exited in one of these ways, a checkpoint file (paragraph 3.6) is created to restart the simulation from the point where it exited.

Chapter 4

Virgo simulation environment

The regular units and activity diagram of the FLASH code is not sufficient to run a simulation. Instead, additional units need to be added, describing the problem at hand and introducing units customising or extending the FLASH code in order to include all required physics. In the astrophysical challenge that is the cooling flow problem a model of a cooling core cluster has been defined.

The model discussed in this chapter is empirical rather than deduced. It is based on observations of the relatively nearby and extensively studied Virgo cluster.

4.1 Structure of the Virgo cluster

With almost 1300 confirmed members, a few hundred potential member galaxies (Binggeli, Sandage and Tammann (1985), Binggeli, Tammann and Sandage (1987)), and at a distance of between 14 Mpc and 22 Mpc (Binggeli, Huchra and Murdin, 2000), the Virgo cluster qualifies as the nearest rich cluster to the solar system. The Virgo cluster is an irregular rich cluster with an apparent diameter on the celestial sphere of about 10° (about 3 Mpc), with a number of subsystems, which are encircled in the figure. If the number and total luminosity of galaxies in a cell of size half degree squared is plotted (figure 4.2), the M87 cluster emerges as the dominant subsystem, with the highest number count and luminosity. By either galaxy number density (Binggeli, 1999) or X-ray luminosity (Böhringer et al., 1994) the cluster centre is, though slightly displaced toward M86, close to giant elliptical galaxy M87.

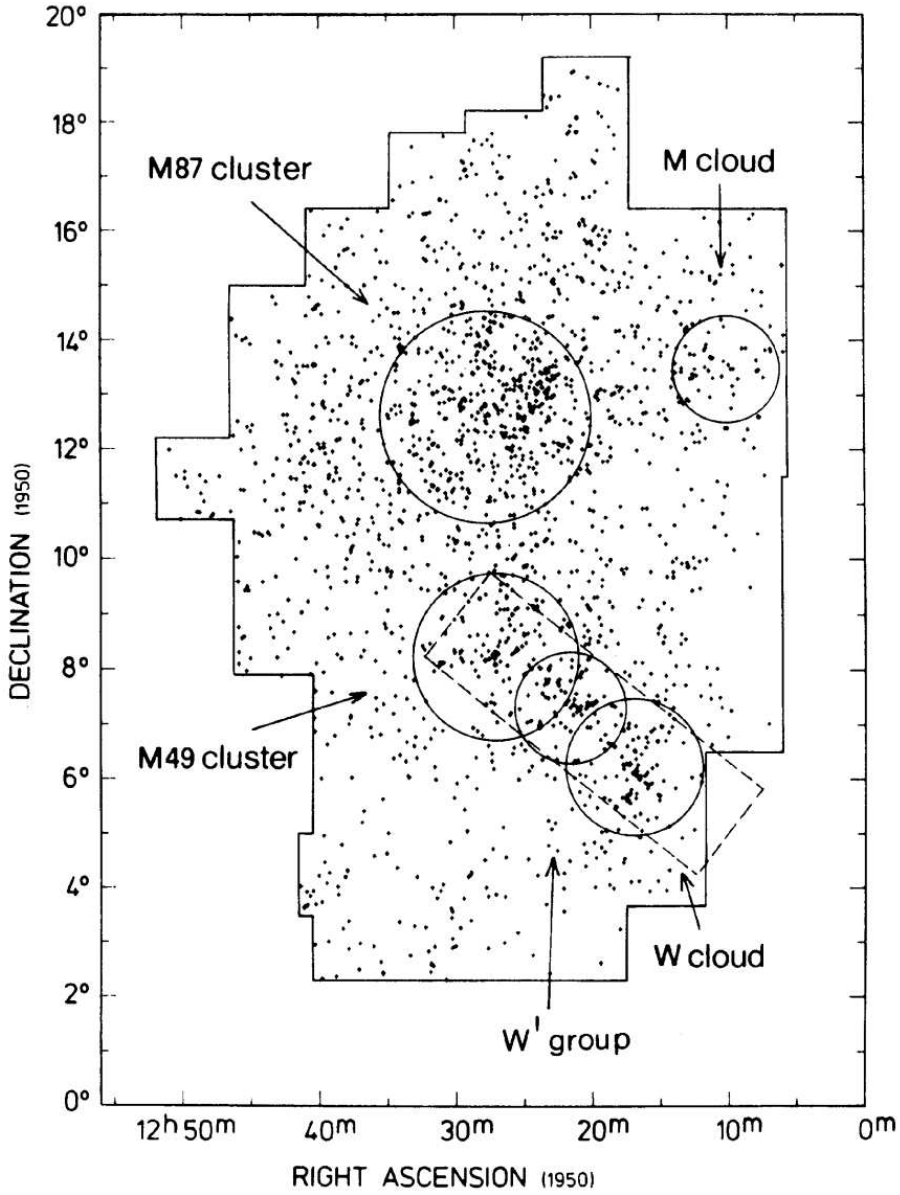

Figure 4.1: An overview Virgo cluster member galaxies as seen on the celestial sphere. The symbol size increases with increasing luminosity, and the most prominent member galaxies are marked. (Credit: Binggeli, Tammann and Sandage (1987).)

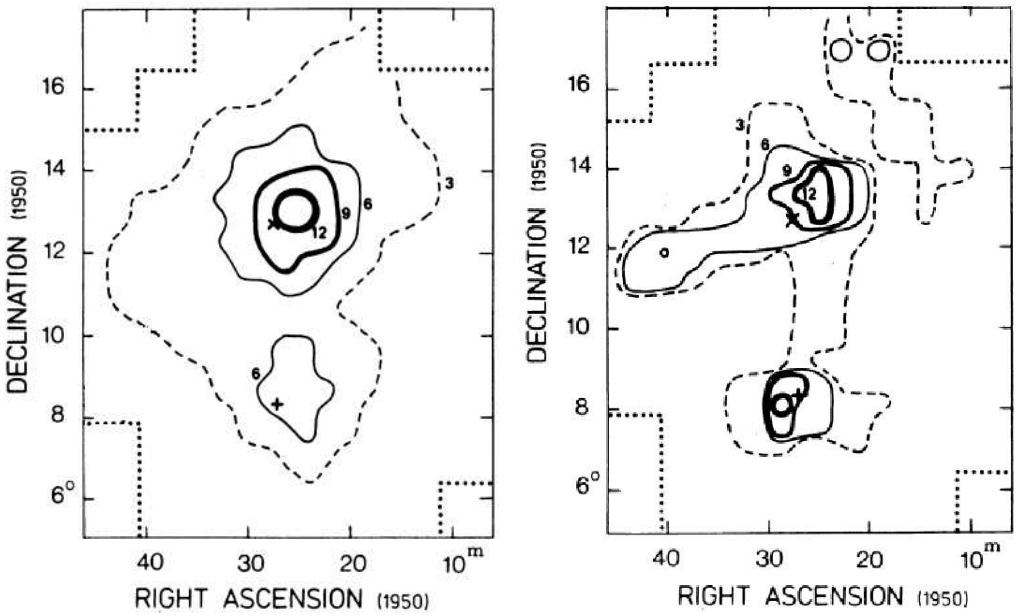

Figure 4.2: Isophleths reflecting number counts in cells of size $0.5° \times 0.5°$ (left), and similar luminosity-weighed isophleths (right, in units of $10^{10}\,L_{\odot}$). The position of giant elliptical galaxy M87 is marked with $\times$; ellipticals M49 and M59 are marked with $+$ and $\circ$ respectively. (Credit: Binggeli, Tammann and Sandage (1987).)

4.2 Density and temperature distribution about M87

Ghizzardi et al. (2004) analysed the gas profiles about giant elliptical galaxy M87 based on observational data from telescopes *Chandra* (for the innermost 10 kpc), *XMM-Newton* (up to 80 kpc), and *BeppoSAX* observatories (out to 120 kpc). Data from the *Chandra* and *XMM Newton* fitted both to a single-temperature model and two-temperature model, while *BeppoSAX* data is only fitted to a single-temperature model.[1]

BeppoSAX and *XMM-Newton* profiles were deprojected, yielding radial-dependent electron density (figure 4.3) and temperature (figure 4.4) profiles. *Chandra* provided too few data points and was deemed unsuitable for deprojection, and is for that reason left unrepresented in these figures. Error bars were produced by Monte Carlo simulations varying projected profiles about their mean, assuming a normal distribution of data points.

[1]See paragraph 1.5.2 for a discussion on multiphase fluid models.

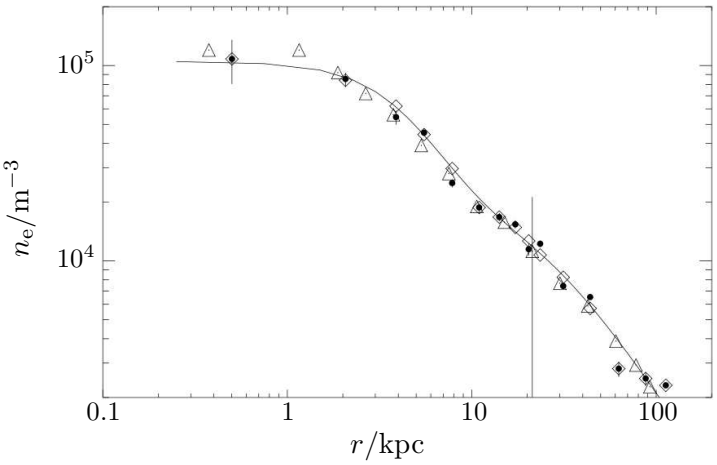

Figure 4.3: Electron density profile about giant elliptical galaxy M87 in the centre of the Virgo cluster. Deprojected data points are marked with ·, which after smoothing yields ⋄. For comparison, Matsushita et al. (2002) retrieved △ using a different algorithm. Error bars are the result of 1000 Monte-Carlo simulations varying projected parameters within their mean value assuming Gaussian distributions. (Credit: Ghizzardi et al. (2004))

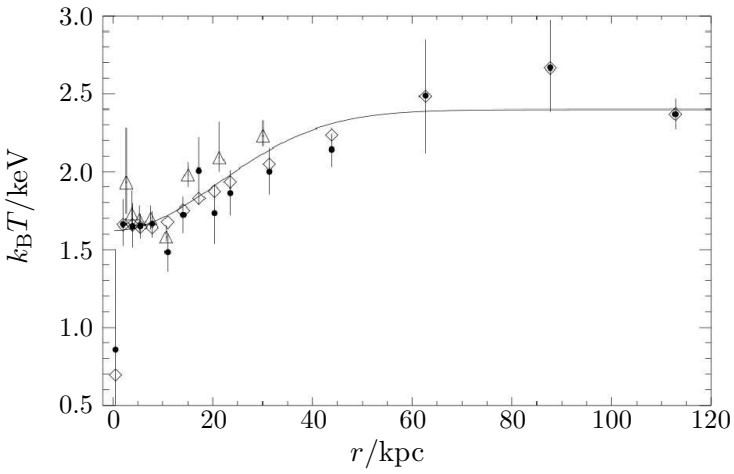

Figure 4.4: Temperature profile about giant elliptical galaxy M87 in the centre of the Virgo cluster. For explanation on symbols and error bars, see the caption of figure 4.3. (Credit: Ghizzardi et al. (2004))

Ghizzardi et al. (2004) concluded the deprojected electron density data set is fit well by a double-β profile[2]

$$n_e = \frac{n_1}{[1+(r/r_1)^2]^{\alpha_1}} + \frac{n_2}{[1+(r/r_2)^2]^{\alpha_2}}, \tag{4.1}$$

and the deprojected temperature data set by

$$k_{\mathrm{B}}T = k_{\mathrm{B}}T_0 - k_{\mathrm{B}}T_1 \exp\left(-\frac{r^2}{2\sigma_T^2}\right). \tag{4.2}$$

As the degrees of freedom in this model are many, statistical errors are large. For this reason two parameters have been fixed, defining r_2 equal to σ_T (acceptable considering error margins), and the slope at large radii α_2 to the value slope at large radii as obtained by Böhringer et al. (1994) from RASS measurements. The complete set as obtained by Ghizzardi et al. (2004) is listed in table 4.1.

Table 4.1: Electron density and temperature profile parameters (Ghizzardi et al., 2004).

$n_1 = 8.9 \times 10^4\,\mathrm{m}^{-3} \pm 1.1 \times 10^4\,\mathrm{m}^{-3}$	$k_{\mathrm{B}}T_0 = 2.399\,\mathrm{keV} \pm 0.090\,\mathrm{keV}$
$n_2 = 1.9 \times 10^4\,\mathrm{m}^{-3} \pm 2 \times 10^4\,\mathrm{m}^{-3}$	$k_{\mathrm{B}}T_1 = 0.776\,\mathrm{keV} \pm 0.097\,\mathrm{keV}$
$r_1 = 0.834' \pm 0.175'$	$\sigma_T = 3.887' \pm 0.731'$
$r_2 = 3.887'$	
$\alpha_1 = 1.518 \pm 0.317$	
$\alpha_2 = 0.705$	

Arbitrarily placing M87 at a distance of 20.6 Mpc, apparent distances on the celestial sphere can be converted to kiloparsecs using

$$1' \hat{=} 5.99\,\mathrm{kpc}. \tag{4.3}$$

Relating apparent distances on the sky in table 4.1 to kiloparsecs yields

$$r_1 = 4.99\,\mathrm{kpc} \pm 1.05\,\mathrm{kpc}, \tag{4.4}$$

$$r_2 = 23.3\,\mathrm{kpc}, \tag{4.5}$$

$$\sigma_T = 23.3\,\mathrm{kpc} \pm 4.38\,\mathrm{kpc}. \tag{4.6}$$

[2]Each of the terms of the double-β-profile is a β-profile.

4.3 Gravitational mass

Assuming the gas about M87 has uniformly primordial abundances[3], the molar mass is $\mu = 0.5968 \times 10^{-3}\,\mathrm{kg\,mol^{-1}}$ and

$$\rho = \left(\frac{0.75}{m_\mathrm{p} + m_\mathrm{e}} + \frac{0.5}{m_\alpha + 2m_\mathrm{e}} \right)^{-1} n_\mathrm{e} \approx (1.911 \times 10^{-27}\,\mathrm{kg})\, n_\mathrm{e}. \tag{4.7}$$

If the observed gas about M87 obeys the ideal gas law and is in hydrostatic equilibrium, the gravitational mass contained in a sphere of radius r centred on M87 is[4]

$$M_r = -\frac{RTr}{G\mu} \left(\frac{r}{n_\mathrm{e}} \frac{dn_\mathrm{e}}{dr} + \frac{r}{T} \frac{dT}{dr} \right), \tag{4.8}$$

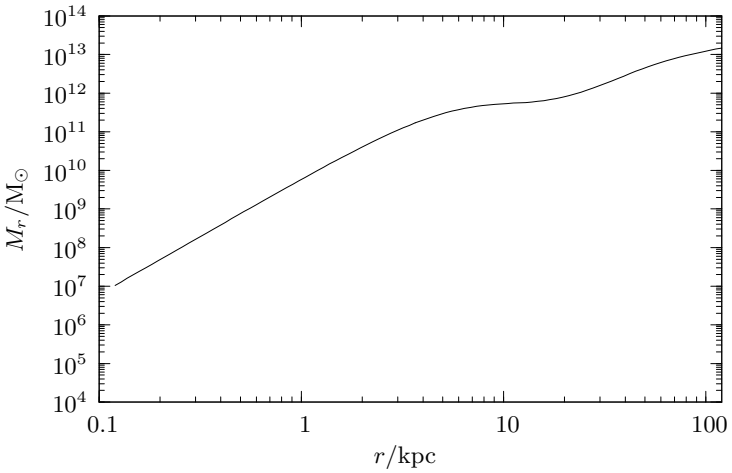

Figure 4.5: Distribution of gravitational mass about M87 (cf. Ghizzardi et al. (2004)).

Figure 4.5 presents the gravitational mass as a function of the radial distance to the centre r. The gravitational acceleration of the gas at distance r from M87's centre is found to be

$$\vec{g} = -\frac{GM_r}{r^2}\vec{e}_r = \frac{RT}{\mu r} \left(\frac{r}{n_\mathrm{e}} \frac{dn_\mathrm{e}}{dr} + \frac{r}{T} \frac{dT}{dr} \right) \vec{e}_r. \tag{4.9}$$

Self-gravity is considered negligible as the dark matter halo represents around 85% of the gravitational mass (e.g. Ostriker, Bode and Babul (2005), (Vikhlinin et al., 2006)).

[3]Here defined 75% hydrogen, 25% helium by mass; both species are assumed to be fully ionised.

[4]See paragraph 1.3.5 for the derivation of this relation.

4.4 Cooling core cluster

The time scale specifying the amount of time is required to radiate away all available heat is known as the cooling time.[5] Figure 4.6 presents the cooling time profile for the gas in proximity of M87, with the graph providing evidence of cooling times of the order Ga or smaller in the cluster core. This can be considered sufficient evidence to identify the Virgo cluster as a cooling core cluster.

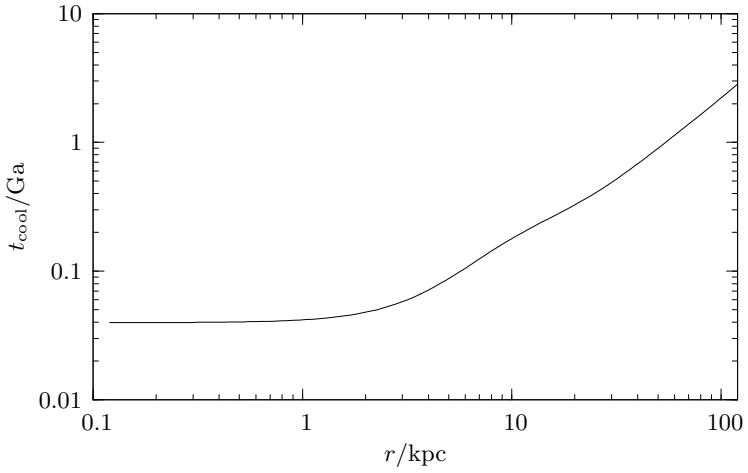

Figure 4.6: The cooling time in proximity of M87.

4.5 FLASH model of the Virgo cluster core

An initial state defined by discussed profiles for electron density (equation 4.1) and temperature (equation 4.2) is implemented within the Simulation unit, using cell centre coordinates. Whenever a function parameter has an error bar, the model opts for the best-fit value. Other thermodynamic variables are using ideal gas equations of state. Hydrostatic equilibrium implies the velocity field is uniformly zero.

The gravitational field is implemented as a variant in the Gravity unit, which is part of the physics unit. It hosts subroutines specifying the gravitational acceleration (given by equation 4.9 using the initial conditions) as a function of position. The gravitational acceleration in a cell is determined using the cell centre coordinates.

[5]See also paragraph 1.3.6 for a derivation of the cooling time.

4.6 FLASH module test

Given the theoretical background underlying the setup, a fluid initialised under described conditions is expected to

- set up density and temperature profiles as given by a double-β profile for electron density (equation 4.1) and the exponential profile for temperature (equation 4.2), using best-fit parameters with scaling $1' \hat{=} 5.99\,\mathrm{kpc}$, and
- maintain approximate mechanical equilibrium for the duration of a typical simulation period of 90 Ma.

Five variables define the system, i.e. density, temperature, and the three components of velocity. For density and temperature the measure to which the intended profiles are matched is quantified for cell i as

$$\eta_\rho \equiv \left| \frac{\rho_i}{\rho_{\mathrm{theory}}} - 1 \right|, \tag{4.10}$$

$$\eta_T \equiv \left| \frac{T_i}{T_{\mathrm{theory}}} - 1 \right|. \tag{4.11}$$

The velocity components are scaled with respect to the speed of sound

$$\mu_{x,y,z} \equiv \left| \frac{v_{x,y,z}}{c_{\mathrm{s}}} \right|, \tag{4.12}$$

as the physics of the fluid changes as the fluid becomes compressible.

Risk of irregularities originate from two sources: the difficulty to map a spherical symmetrical distribution on a Cartesian grid, and unwanted effects emanating from the edge of the computational domain. These risks are charted by measuring the deviation parameters as a functions of

1. the distance r to the centre of the computational domain, which coincides with the centre of the Virgo cluster, and
2. the shortest distance to the edge of the computational domain d.

The compound quality of a collection of cells is determined by the cell with the highest deviation.

4.6.1 Data acquisition

The simulation takes place in a 400 kpc × 200 kpc × 200 kpc cuboidal computational domain.

The Cartesian grid comprises 2 cubic top blocks of identical shape lined up in x-direction. The refinement level in the grid varies between 3 and 6, which implies a resolution of 390 pc. The grid is kept maximally refined within a distance of 1 kpc of the centre of the computational domain. External boundary conditions are set to outflow, meaning all variables have zero gradient across the boundary. Therefore gas can enter or leave simulation scope if the velocity field configuration creates appropriate conditions along the boundary.

The Virgo cluster is modelled using empirical density and temperature profiles as outlined by equations 4.1 and 4.2, using best-fit parameter values. As mentioned in previous paragraph, the centre of the cluster coincides with the centre of the computational domain (corresponding to coordinates (200 kpc, 100 kpc, 100 kpc)).

The physical time covered by the simulation is 90 Ma, with time steps ranging from a minimum of 5 ka to a maximum of 100 ka.

4.6.2 Test specification

The module test is built up out of a series of separate tests.

1. Initial conditions test – initial setup is compared with formulae.
2. Evolution test – maximum deviation in grid is plotted as a function of time.
3. Stability test: given the dynamic time scale t_{dyn} of a volume V defined

$$t_{\mathrm{dyn}}|_{\mathrm{V}} \equiv (t_{90} - t_0)\frac{\int_V \rho_0}{\int_V \rho_{90} - \int_V \rho_0}, \tag{4.13}$$

   profile as a function of distance to the centre of the computational domain, in order to localise developed irregularities.

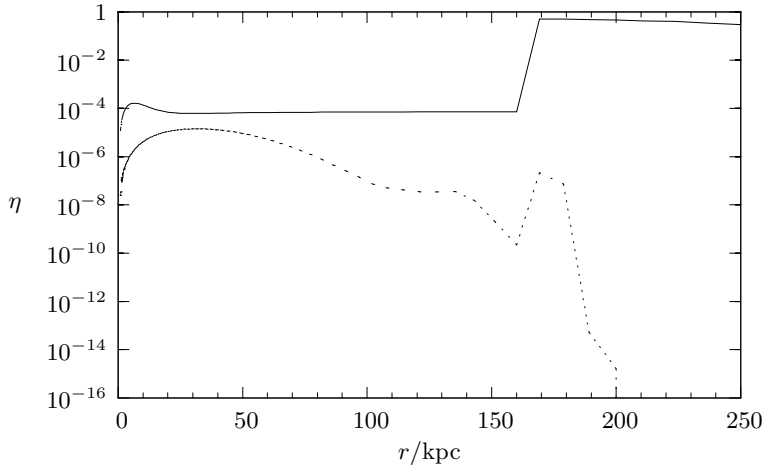

Figure 4.7: Initial conditions test – density (solid line) and temperature (dashed line) profile deviation from intended profiles as a function of distance to the domain centre.

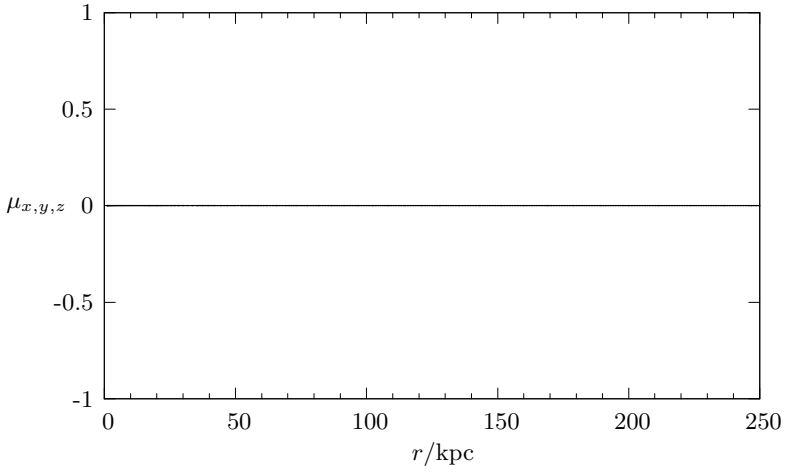

Figure 4.8: Initial conditions test – velocity profile scaled by local speed of sound as a function of distance to the domain centre; all three components are uniformly zero.

4.6.3 Findings

The initial conditions test (figures 4.7 and 4.8) indicates the density profile deviation is four orders of magnitude higher further out than 160 kpc than in closer proximity to the domain centre. The temperature deviation is much smaller than unity throughout the domain, while the velocity components are uniform zero.

Denoting bigger perturbations of hydrostatic equilibrium lead to more motion, it is assumed that the maximum deviation of velocity components in the grid is a good indicator for the process of perturbation development in the grid. Figure 4.9 indicates this process is a gradual one, with the biggest deviation developing for the velocity component corresponding to the direction in which the computational domain is elongated.

Figures 4.10 and 4.11 indicate hydrostatic equilibrium is maintained poorly at large distances from the domain centre and closer to the domain edge. The first is attributable to the initial conditions, which were implemented rather poorly to start with. From the domain centre, the equilibrium is maintained very good up to 22 kpc out in the yz-plane, and up to 122 kpc out in x-direction.

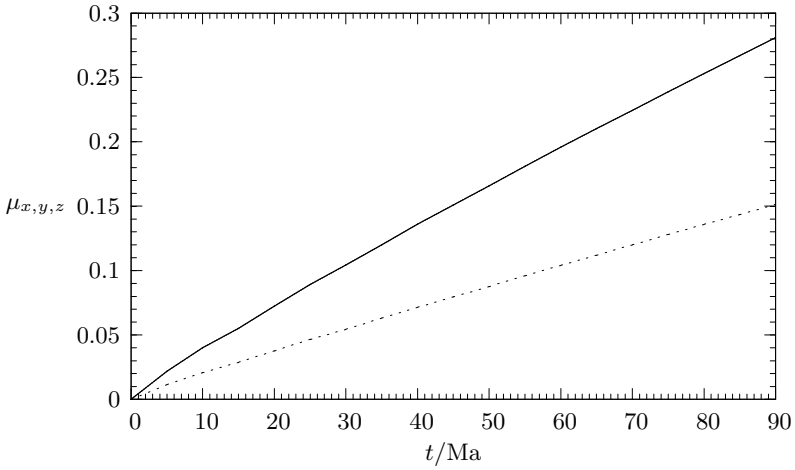

Figure 4.9: Evolution test – velocity profile (the dashed line represents the x component; the y and z components coincide on the solid line) scaled by local speed of sound as a function of time.

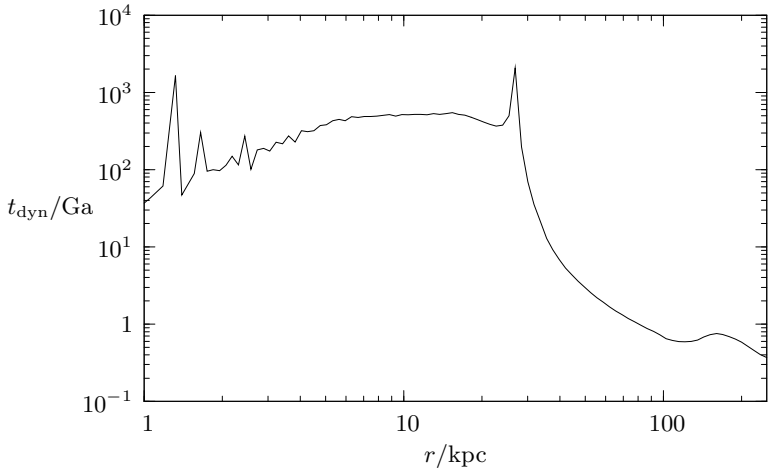

Figure 4.10: Dynamic time scale – profile as a function of distance to the domain centre.

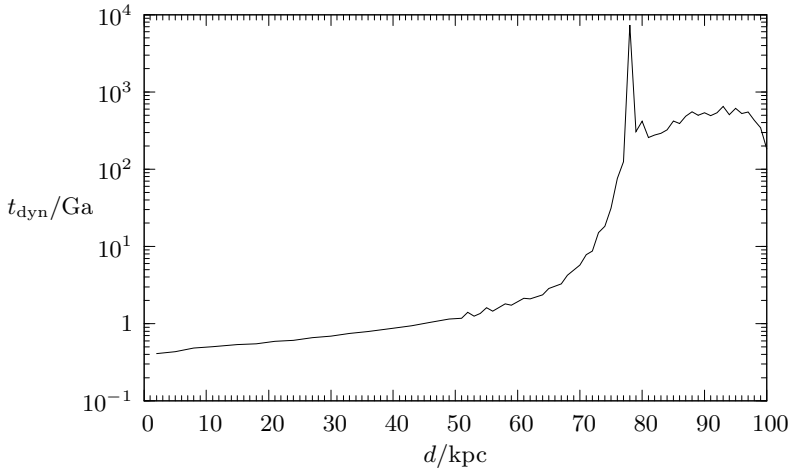

Figure 4.11: Dynamic time scale – profile as a function of distance to the domain edge.

Chapter 5

AGN jet simulations

A jet is defined as a continuous efflux of fluid from a collimator projected into a surrounding medium. The first astrophysical jet was found when Baade and Minkowski (1954) qualitatively identified the optical protrusion associated with elliptical galaxy M87 in the Virgo cluster as a fluid jet breaking into droplets.[1]

The majority of observed stellar jets originate from young stellar objects (YSOs), involving a protostellar system beaming a sub-parsec scale jet into the surrounding molecular cloud (Reipurth and Bally, 2001). High-mass X-ray binaries with an accreting black hole as source (Mirabel and Rodríguez, 1999) are also known to generate jets, and are called *microquasars* in deference to the structural similarity to systems found in galactic nuclei. Other binary systems with an accreting neutron star (X-ray binary) or white dwarf are observed to give rise to jet formation as well.

Extragalactic objects comprise active galactic nuclei (AGNs), which are thought to involve accreting supermassive black holes in galactic centres.[2] These relativistic jets are huge in comparison with YSO jets, reaching lengths of up to $\sim 100\,\mathrm{kpc}$. Their sources are similarly exotic, supermassive black holes with masses of $10^6\,\mathrm{M}_\odot$ to $10^9\,\mathrm{M}_\odot$ and luminosities of $10^{43}\,\mathrm{L}_\odot$ to $10^{48}\,\mathrm{L}_\odot$ (figure 5.1).

In this chapter the physics of astrophysical jets is reviewed, along with physical considerations pertaining to modelling such a jet within the scope of computational fluid dynamics.

[1] The jet of M87 is depicted in figure 1.6.6.

[2] See paragraph 1.4 for a description of active galactic nuclei.

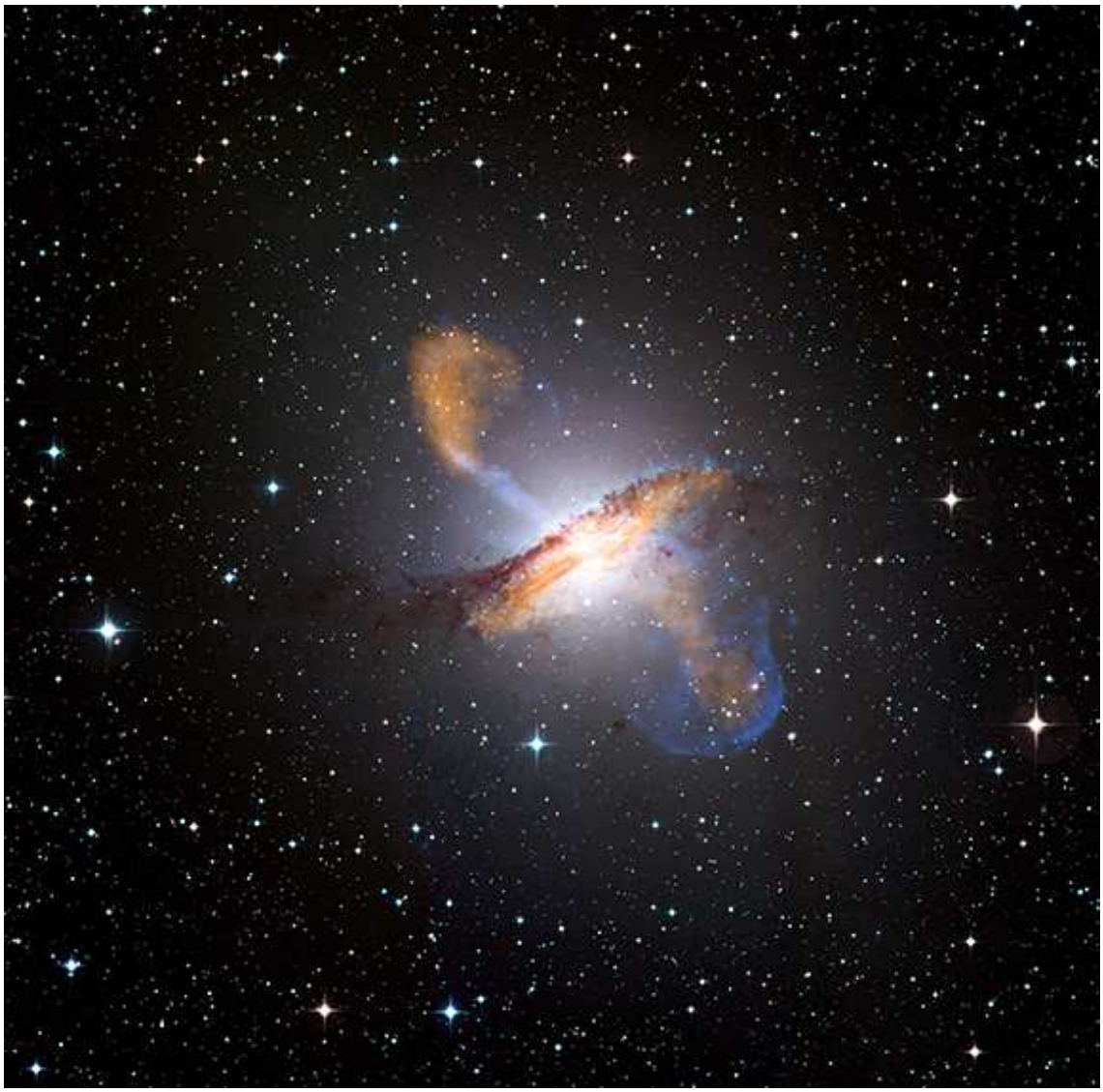

Figure 5.1: NGC 5128 is associated with a strong radio source Centaurus A. With its pronounced dusty disc but otherwise distinct elliptical morphology NGC 5128 is thought to be a lenticular galaxy. The image depicts optical observations combined with features in the submillimeter band (orange) and X-ray band (blue). Interesting objects include a pair of narrow features connecting the galaxy's apparent centre to submillimeter lobes on both sides of the dusty disc. (Credit: X-ray: NASA/CXC/CfA/R.Kraft et al.; Submillimeter: MPIfR/ESO/APEX/A.Weiss et al.; Optical: ESO/WFI.)

5.1 Astrophysical jets

An image of NGC 5128 (Centaurus A), the nearest ($d \leq 3.4\,\mathrm{Mpc}$) AGN to the Milky Way, is depicted in figure 5.1. This is an extragalactic jet, but all characteristics discussed here are typical for any kind of astrophysical jet. The image is comprised of data in three different bands superimposed: optical, submillimeter, and X-ray bands. Clearly the object is extended mostly in the submillimetre band; in fact, traditionally these sources have been studied mostly on even longer radio wavelengths.

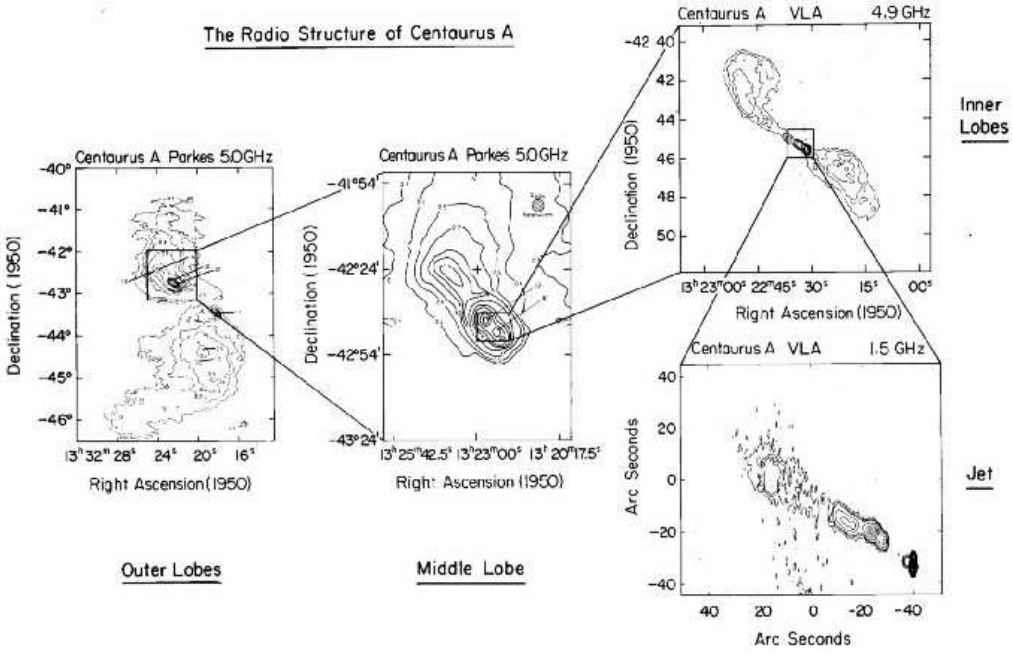

Figure 5.2: Radio structure of the outflow of NGC 5128 (Credit: Burns, Feigelson and Schreier (1983)).

Figure 5.2 depicts the structure of NGC 5128 in the radio band. The extended radio-emitting regions are called *emission lobes*, which are connected to the apparent galaxy centre by a narrow features conventionally called *jets*. Usually a pair of jets and lobes of similar size and power are found on each side of the parent object. *Sidedness* can be quantified by considering the brightness contrast between the two jets; Bridle and Perley (1984) define an astrophysical jet one-sided if the brightness ratio of brightest to faintest jet exceeds four to one.

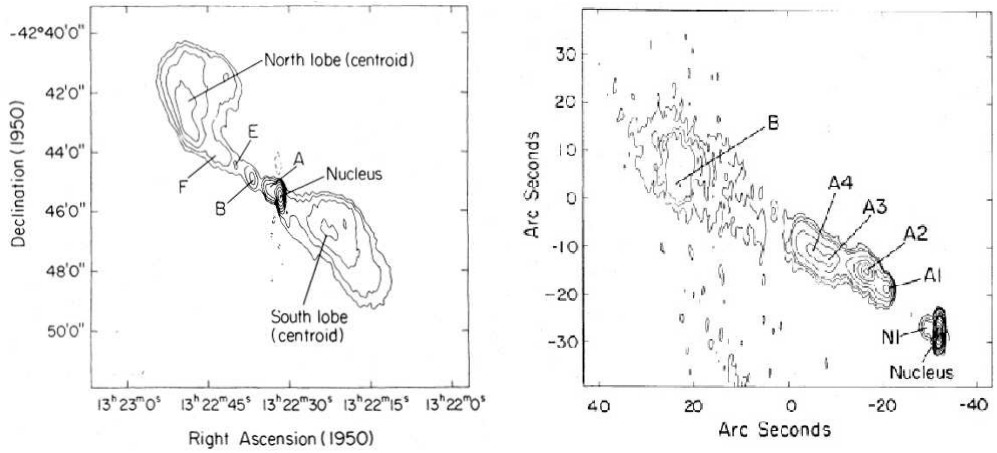

(a) (b)

Figure 5.3: Emission knots as observed in the NGC 5128 jet in the radio band (Credit: Burns, Feigelson and Schreier (1983)).

The jet is not a smooth emitter in the radio band; instead, a granulated emission pattern emerges with noticeable *emission knots*, marked by A to F on figure 5.3(a). The close-up of knot A reveals it actually consists of several knots, which are numbered separately on figure 5.3(b).

The last directly observable characteristic all astrophysical jets share is a significant associated electromagnetic field, as reflected by polarisation measurements which give evidence of a significant electromagnetic field in NGC 5128 (figure 5.4). Polarisation degrees from 10 to 30 per cent are common in astrophysical jets.

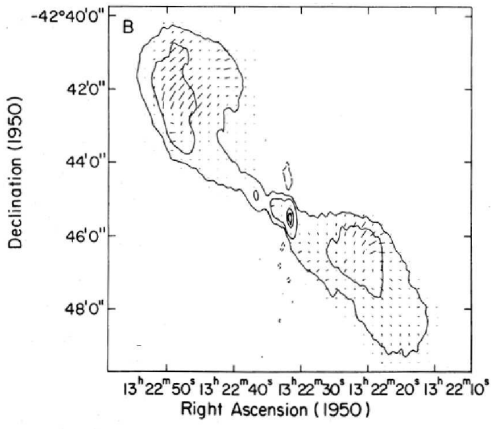

Figure 5.4: Polarisation measurements superposed on radio band contours about the NGC 5128 jet. (Credit: Burns, Feigelson and Schreier (1983))

The physical systems producing astrophysical jets give evidence of similarities, which is already mentioned to comprise a compact object (protostar, white dwarf, neutron star, or black hole – solitary or binary).[3] Additionally, the presence of a disc of diffuse interstellar material surrounding protostars has been inferred by an excess of infrared radiation compared to similar main-sequence stars (see Beckwith and Sargent (1993) and references therein). The presence of accretion discs is inferred in all types of X-ray binary systems (e.g. Mirabel and Rodríguez (1999), van Paradijs and McClintock (1995)), and incorporated into the unified model explaining observed spectra of all AGNs (e.g. Antonucci (1993), Urry and Padovani (1995)).

Figure 5.5: The systems of origin of astrophysical jets are inferred to comprise a compact object and a surrounding accretion disc (Credit: L. Calçada, ESO).

Jets have been part of astrophysics since Curtis (1918) qualified the observed protrusion of M87 as such on grounds of morphological similarities. True jets, however, require that material in observed narrow features is flowing. Such information can be obtained by measuring Doppler shift of line emission associated with the jet. Galactic jets such as YSOs provide emission lines at plenty, primarily in optical and infrared bands. In contrast, the radiation spectrum of extragalactic AGN jets constitutes synchrotron or inverse Compton radiation without any emission line, and as such no direct evidence for flow in extragalactic jets exists.

[3]See paragraph 1.4 for an outline of the system conjectured to be present in galactic nuclei.

5.2 Fanaroff-Riley dichotomy

An abrupt transition is found in the radio band morphology of extragalactic jets around a spectral radiant intensity of $I_{178\,\mathrm{MHz}} = 2 \times 10^{25}\,\mathrm{W\,Hz\,sr^{-1}}$, which is formalised by the Fanaroff-Riley classification scheme (Fanaroff and Riley, 1974). If the lobes are the brightest component, the AGN is *lobe-dominated*; if most of the radio emission is emitted close to the core, the AGN is *core-dominated*.

An FR I source (figure 5.6(a)) is edge-darkened[4] and core-dominated. The outflow bears the signature of turbulent flow, with the lobe taking the shape of a plume. FR II sources (figure 5.6(b)) are edge-brightened in the radio band, with a bright *hot spot* of radio emission at the jet tips; the outflow appears to be fairly laminar.

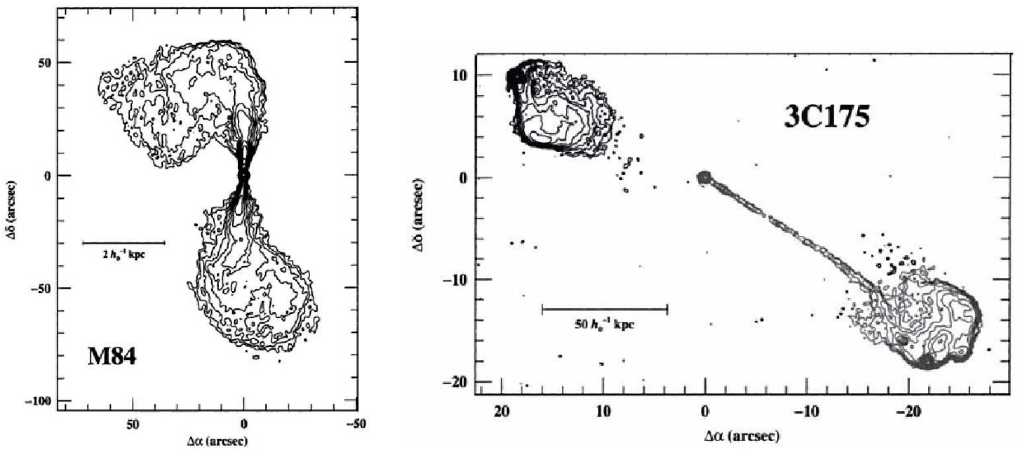

(a) FR I. (b) FR II.

Figure 5.6: Jet morphology is categorised in a Fanaroff-Riley (FR) classification system comprising two classes. Typical examples of FR I (left) and FR II (right) are shown in the figures. (Credit: Bridle and Perley (1984), Bridle et al. (1994).)

Host galaxies of radio-loud AGNs are predominantly elliptical galaxies (e.g. Martel et al. (1999)). FR I sources tend to be associated with cD galaxies in rich environments, while FR II sources are found in giant elliptical galaxies and are rare in rich regions at low redshift (e.g. Zirbel (1996), Zirbel (1997)).

[4] I.e. the edge brightness is much smaller than unity.

5.3 Jet composition

In absence of spectral lines, the composition of AGN jets remains disputed. As an electron population is observed via emitted synchrotron radiation, possible positive charge carriers are considered protons or positrons. Considering a population of emitting particles n_γ, γ being the Lorentz factor with a lower limit $\gamma_{\min}$. Considering a steep decrease of the function n_γ and required energy output, $\gamma_{\min}$ has to be appreciatively less than 100 for an electron-positron jet, while the cut-off is about 100 for an electron-proton jet (e.g. Celotti and Fabian (1993), Wardle et al. (1998), Dunn, Fabian and Celotti (2006)). Evidence gathered by comparing a sample of AGN jets has led to different interpretations, and so the matter remains inconclusive.

5.4 Jet kinematics

In absence of emission lines, the speed of flow is difficult to determine. Upper limits are obtained using the brightness contrast often observed between the two components of extragalactic jets by assuming Doppler beaming (Blandford and Königl (1979), Scheuer and Readhead (1979)), which suggests the approaching jet appears brighter due to the bulk motion of emitting material at relativistic speeds (Rees, 1966). Doppler beaming is also thought to explain observed single-jet systems, in which case the other is considered too faint to be observed. The apparent position of knots at different epochs have also been used to infer relativistic motion (e.g. M87, Biretta, Sparks and Macchetto (1999)).

Pursuing the alternative explanation that there is no counterjet in an observed single-jet system, Clarke and Burns (1991) modelled alternating ejection and found jet launching conditions were severely influenced by activity by previous jets, yielding an unsymmetrical system and a hot spot in the disconnected lobe that was too faint to be reconciled with observations.

5.5 Theoretical progress

Theoretical progress on astrophysical jets commenced when extended radio sources were associated with their optical counterparts in the 1950s. The sources were inferred to produce non-thermal synchrotron emission with powers of up to $10^{14}\,L_{\odot}$ (Burbidge, 1956). The plasmon (single outburst) model was discredited when Burbidge (1959) estimated the total energy content of a sample of radio sources using equipartition, as light plasmons were found to have insufficient range while heavy plasmons required an immense amount of kinetic energy.

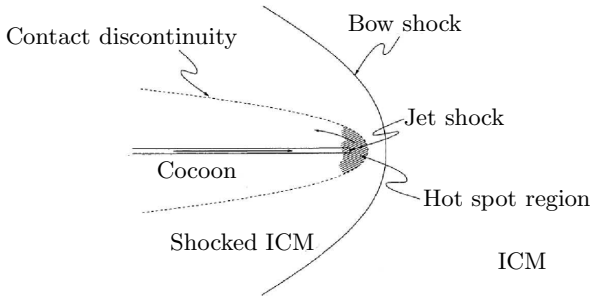

Figure 5.7: The general structure of a relativistic astrophysical jet. Jet material is abruptly halted at the jet shock and flows back into the cocoon, a vast reservoir of waste gas enveloping the double jets. The jet is preceded by the bow shock, a detached shock formed as the jet constitutes a bluntish object inserted in the ICM at supersonic speed. The cocoon with waste jet gas is separated from the shocked intracluster gas by a contact discontinuity. (Credit: Kaiser and Alexander (1997))

As an alternative continuous supply by supersonic jets was suggested (e.g. Rees (1971)). This idea was developed into a jet model by Scheuer (1974) and Blandford and Rees (1974). Jets were observed in following years (see Miley (1980) for a review).

The life cycle of jet material can be divided into three phases: acceleration, propagation, and termination. Blandford and Rees (1974) suggested that light gas from the source might find its way through thin patches in the surrounding medium shaped as a de Laval nozzle,[5] a model known as the *twin exhaust model*.

[5] A de Laval nozzle is a nozzle that narrows and widens again, see Landau and Lifshitz (1987)).

As the collimated outflow remains presumably confined by the enveloping ambient medium, the most interesting features are produced in the termination phase (figure 5.7). The blunt jet head clashes with the ICM, which leads to the formation of a detached shock known as a *bow shock*. Jet material traversing the jet head clashes with shocked intracluster gas and a powerful *jet shock* forms at the jet tip.

Jet gas traversing the shock is bent by the denser medium beyond and turns back into the *cocoon*, a reservoir of waste gas enveloping the jet system. This *backflow* is separated from shocked intracluster gas by a contact discontinuity. The jet shock acts as the 'working surface'; jet material traversing it releases a lot of heat, resulting in the *hot spot* region observed in FR II jets.

5.5.1 Jet acceleration

Given the extent of the source had been limited to sub-parsec scales, it was known the source had to be an accreting black hole. Considering this, Lovelace (1976) and Blandford (1976) suggested the disc endowed with a magnetic field may act as a dynamo. Charged particles in the disc carry with them a magnetic field, and due to accretion this field is amplified near the black hole. Resulting potential difference across the disc and the Lorentz force result in ultrarelativistic jets. Blandford and Payne (1982) developled a similar model based on frozen field lines in a magneto-fluid dynamics. As gas accretes inward, magnetic field lines are dragged along, which eventually results in a slingshot effect.

Both of the discussed mechanisms extract rotational energy from the accretion disc. Blandford and Znajek (1977) derive it is also possible to extract energy from the spinning black hole, which is essentially based on magnetic field lines not being swallowed by the black hole as the accreted gas is, but lingering on the event horizon of the spinning black hole. event horizon spin along, which generates a Lorentz force.

Disc- and black hole-based models are viable models, as it has proven arduous to design a simulation which replicates the black hole and disc system with perceived reasonable accuracy. Accurately duplicating the jet acceleration mechanism is not relevant for any of the simulations discussed in this thesis.

5.5.2 Jet propagation

AGN jets emerge as free jets but are subsequently brought into pressure equilibrium with the surroundings by a reconfinement shock, and are thought to stay in pressure equilibrium with their surrounding (Miley, 1980). Thermal pressure confinement is likely, as the cocoon is observed to be overpressured with respect to the ICM (Begelman and Cioffi, 1989) and simulations considering magnetic pressure do not comply with observations (e.g. Clarke, Norman and Burns (1986), Lind et al. (1989)).

The simplest jet that matches the illustrated scenario is the equilibrium jet, i.e. a laminar steady jet in pressure equilibrium with the surrounding medium. It is determined by mass conservation and Bernoulli's law

$$\rho v A \propto p^{1/\gamma} v A = \text{constant}, \tag{5.1}$$

$$\frac{1}{2}v^2 + h + \Phi = \text{constant}. \tag{5.2}$$

denoting the surface area of the cross-section by A using $p \propto \rho^\gamma$ for an isentropic process. For very large Mach numbers (hypersonic jets) $p^{\frac{\gamma-1}{\gamma}}\mathcal{M}^2 \approx$ constant, and therefore $\mathcal{M} \propto p^{\frac{1-\gamma}{2\gamma}}$, yielding $A \propto p^{-1/\gamma}$. The pressure profile therefore determines the opening half-angle of such a jet rather than the aperture geometry at the collimator.

Early two-dimensional simulations by Norman et al. (1982) indicate occurring internal shocks do not de-confine the jet. Jets are stable unless the jet is transonic and the density contrast is minimal. Bodo et al. (1994) found perturbations first grow linearly, then produce shocks, and finally result in entrainment and diffusion of the jet, where heavy jets develop a broader layer of entrained material. The first three-dimensional simulations indicated mixing is more effective especially in lighter jets than suggested by two-dimensional jets, in which cylindrical or slab symmetry is assumed (Bodo et al., 1998). Observed emission knots are thought to be the consequence of variations in the jet velocity field causing shocks (Rees, 1978).

Kaiser and Alexander (1997), Kaiser and Alexander (1999) and Alexander (2000) described FR II source evolution by expressing jet, cocoon, and bow shock parameters in terms of a characteristic length scale, ambient density, jet discharge and power. This resulted in a geometrically self-similar model.

5.5.3 Jet termination

As detailed in the original jet model, laminar jets terminate with a jet shock and a hot spot. The turbulent FR I jets, such as the jet of NGC 5128 (figure 5.1), dwindle into a *plume*. The structure of FR I jets indicates these jets must decelerate gradually, as no jet shock would form in transonic flow. Entrainment of gas from the surrounding medium is a plausible mechanism accounting for the inferred deceleration (Bicknell (1984), Bicknell (1986*a*), Bicknell (1995)).

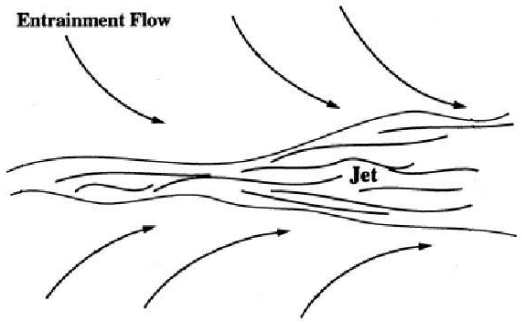

Figure 5.8: FR I jets are turbulent and entrain gas from the surrounding medium. (Credit: Bicknell (1994))

Laminar jets instead remain supersonic and relativistic until they terminate abruptly with a jet shock. Considering pressure equilibrium in the rest frame of the hotspot

$$\frac{v_{\rm j}}{v_{\rm h}} = 1 + \left(\frac{\rho_{\rm a}}{\rho_{\rm j}}\right)^{1/2}, \tag{5.3}$$

suggesting the flow in an underdense jet overtakes the hotspot at greater speed than a denser jet, and converts more of its kinetic energy to thermal energy. Diffuse secondary hot spots observed near jet tips (Lonsdale and Barthel, 1986) can be the consequence of a change of jet direction (Cox, Gull and Scheuer, 1991).

Shocked jet gas is diverted back toward the system core as a backflow. Modelling the backflow as steady, Bernoulli's equation and the Rankine-Hugoniot conditions relate the jet Mach number to the backflow Mach number. Waste matter piles up in an expanding cocoon enveloping the jets. The cocoon surface is Kelvin-Helmholtz unstable, and if the density distribution of the ICM is sufficiently steep that cocoon expansion accelerates, it is Rayleigh-Taylor unstable as well.

The cocoon expands into the ICM until its expansion speed drops below the free-fall velocity. The cocoon then splits down the middle and rises as a pair of buoyant *bubbles*. First introduced by Gull and Northover (1973) based on radio observations, these components were consequently observed as cavities in X-ray emission (e.g. Böhringer et al. (1993), McNamara et al. (2000)), occasionally surrounded by rings of presumably displaced gas (e.g. Abell 2052, Blanton et al. (2001)).

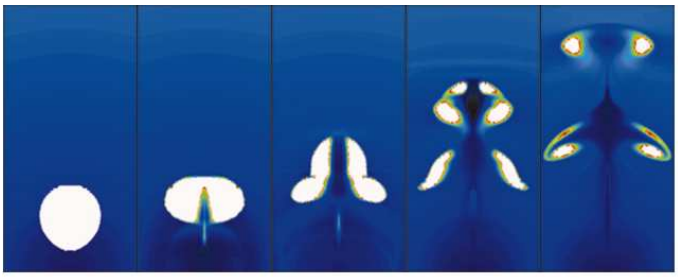

Figure 5.9: Temperature profile in a bubble simulation at five time steps, where white indicates hot gas and blue cold gas. (Credit: Churazov et al. (2001))

An analytical model by Churazov et al. (2000) portrayed these bubbles as initially spherical and expanding supersonically per the ram pressure condition, while as expansion slows down to subsonic speed the injected energy directly adds to the enthalpy of the bubble. The bubble velocity is assumed equal to the terminal velocity $\sqrt{2g/SC}$ assuming equilibrium between buoyancy and drag force. Here S is the surface and $C = 0.75$ the assumed drag coefficient (Churazov et al., 2001). Simulations indicate the bubble, that is in pressure equilibrium with its surroundings, transforms into a rotating torus on Rayleigh-Taylor time-scales, which continues to rise until the density of the torus matches that of the ambient medium (figure 5.9). Instabilities developing along the bubble surface eventually shred the bubble.

Radio-quiet *ghost bubbles* are sometimes observed in outlying regions (e.g. Fabian et al. (2003*a*)), with larger relics beyond (e.g. Fujita et al. (2002)). These observations are explained by intermittent activity of the AGN. The duration of an episode is of the order of the radiative cooling time of the synchrotron-emitting bubble gas. Evidence of episodic activity can similarly be acquired by assuming observed ripples are sound waves emitted at successive outbursts, yielding ripple ages of similar order of magnitude as bubble ages (Fabian et al., 2003*a*).

5.6 Evidence of heating in cooling cores

A bubble with volume V expanding adiabatically and in pressure equilibrium has done work on the ICM equal to its enthalpy $H_\mathrm{b} = \frac{\gamma}{\gamma-1} pV$. The bubble age t_age is estimated in three ways (Bîrzan et al., 2004), the first two obtained by dividing the apparent distance to the source by local speed of sound or terminal speed, the third by setting it equal to the time it takes local gas to fill the cavity by a free-fall $t_\mathrm{age} \sim 2\sqrt{r/g}$. The mechanical power of the bubble is then $P_\mathrm{b} = H_\mathrm{b}/t_\mathrm{age}$.

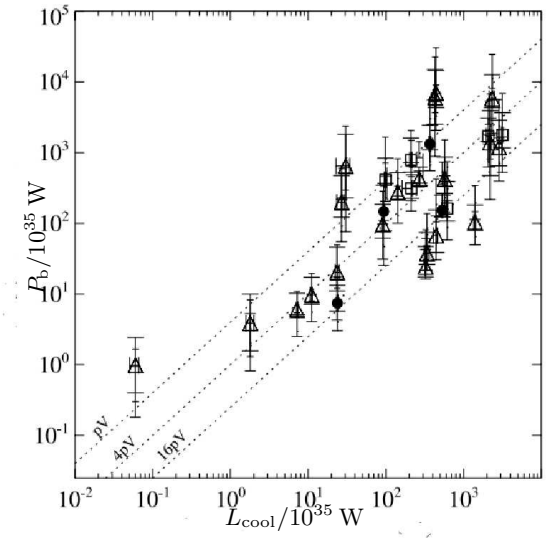

Figure 5.10: Bubble power versus the X-ray luminosity deficit; the symbols indicate the definability of the bubble perimeter. (Credit: Rafferty et al. (2006))

Spectroscopic estimates using the MKCFLOW module, which is based on a cooling flow model by Mushotzky and Szymkowiak (1988), yields a luminosity attributable to the cooling flow. Subtracting this from the observed X-ray luminosity yields the cooling luminosity L_cool. Comparing bubble power and cooling luminosity, figure 5.10 shows bubble heating is significant (Bîrzan et al. (2004), Rafferty et al. (2006)).

Shock waves are observed in some systems, as has been predicted by theory. The Mach numbers can be obtained by applying Rankine-Hugoniot conditions on density or temperature profiles; the shock heating power is equal to the heat content of the ICM between shock and bow shock. Croston, Kraft and Hardcastle (2007) infer that shock heating in NGC 3801 rivals heat transfer by bubbles.

5.7 Simulations of heating in cooling cores

In terms of observed features, AGNs can heat the surrounding gas by inflating bubbles, emitting sound or shock waves observed as ripples, or by unobserved means. Limited capability of computational facilities mean highly-resolved simulated AGN jets cannot cover extended evolutionary times. Possible strategies include commencing the simulation at courser resolution with an evolved structure, such as a collimated jet or an inflated bubble, or exchanging physical accuracy for higher resolution by reducing the dimensionality.

5.7.1 Heating by inflated bubbles

Early simulations involve placing a fully developed bubble (Churazov et al. (2001), Brüggen and Kaiser (2001)) or an gas source (e.g. Brüggen and Kaiser (2002), Brüggen et al. (2002), Brüggen (2003)) in a demarcated region in a stratified medium. Simulations are usually performed in grid-codes similar to FLASH.[6] These simulations indicate rising bubbles uplift cool gas and disrupt the cooling flow. Brüggen et al. (2002) found bubbles to be easily overlooked.

Development of Rayleigh-Taylor and Kelvin-Helmholtz instability on the bubble surface is inevitable, but observations in the Perseus cluster suggest intact bubbles can venture far out of the cluster core prior to shredding (Fabian et al., 2006). Simulations by Reynolds et al. (2005) report premature shredding inconsistent with observations unless the gas is modelled as viscous. Analytical considerations by De Young (2003) indicate the terminal velocity of the bubble is too slow for Kelvin-Helmholtz instability to develop, and Kaiser et al. (2005) analytically derived the observations by Reynolds et al. (2005). Robinson et al. (2004) denoted a magnetic field draped about the bubble made it more resistant to developing instabilities, which was analytically confirmed by Lyutikov (2006). Alternative stabilising mechanisms include decelerating bubble growth (Pizzolato and Soker, 2006). Scannapieco and Brüggen (2008) discovered via sub-grid method small-scale turbulence profoundly affects bubble morphology.

[6] The FLASH-code is outlined in chapter 3.

Possible heating mechanisms associated with a bubble include dissipation of induced turbulent motion (Churazov et al. (2004), Cattaneo and Teyssier (2007)). Effervescent heating is based on the notion that as the bubble rises adiabatically, done work in the wake of the bubble is equal to lost. As the wake is turbulent, the released kinetic energy is transformed into heat, a process known as effervescent heating (Begelman (2001), Ruszkowski and Begelman (2002)). Ruszkowski, Brüggen and Begelman (2004*a*) found evidence of the bubble surface generating sound waves, but weaker than those directly associated with AGN-activity and therefore probably a minor effect.

Considering the correlation between jets and bubbles, Reynolds, Heinz and Begelman (2001) and Reynolds, Heinz and Begelman (2002) inject a pair of non-relativistic supersonic jets from the origin in an axisymmetric grid, with the purpose to simulate bubble formation by a jet in a β-density profile. The overpressured cocoon initially expands, reaches pressure equilibrium, and rises buoyantly through the ICM as a bubble. Basson and Alexander (2003) extended this setup to three dimensions and included radiative cooling to monitor the effect of rising bubbles on the ICM on an extended period. It was found bubbles generate large-scale buoyancy-driven convective flows on time-scales much larger than the period of activity.

Omma et al. (2004) injected a jet through a back-to-back nozzle in the centre of an adaptive grid, refined near the point of injection away from the edge of the computational domain. The jet was fairly slow and less powerful than its predecessors, and inflated its bubbles noticeably closer to the cool cluster core. Vernaleo and Reynolds (2006) observed powerful jets vacate a corridor through the ICM through which matter subsequently is channelled, depositing all energy well beyond the cooling core. O'Neill and Jones (2010) simulates a similar but magnetised jet that displays the same issue. Heinz et al. (2006) found a dynamic anisotropic background solves this issue and properly distributes the energy. In a simulation associating the presence of cocoons and bubbles with FR II jets Vernaleo and Reynolds (2007) found no clear correlation with heating effectiveness. Two-dimensional simulations by Sternberg, Pizzolato and Soker (2007) indicate spherical bubbles are formed only if the opening angle of the jet is large (50°) and the jet speed is sufficiently high.

5.7.2 Ripples

Ripples in X-ray emission are associated with shock or sound wave activity, and may hint at a more important heating mechanism as some simulations indicate disappointing heat content of bubbles (e.g. Gardini (2007), Binney, Alouani Bibi and Omma (2007)). Shock discontinuities cause an entropy discontinuity in the ICM, which causes gas flowing across to release heat. Sound waves are intrinsically adiabatic, and the energy can be accessed only if the sound wave is dampened by viscous forces (Landau and Lifshitz, 1987).

Combining shocks and bubbles, Heinz and Churazov (2005) considered a shock front impacting on a bubble. This causes Richtmyer-Meshkov instability and is inferred to effectively release a substantial fraction of the energy. Brüggen et al. (2007) analyse efficiency of shock heating and find that the fraction of energy thermalised in the shocks accounts for but a few per cent of the heating, but successive shocks may constitute a significant heating mechanism. Fujita, Suzuki and Wada (2005) analysed the possibility of an amplifying sound wave in a spherically accreting spherically symmetric cluster, but such a wave has yet to be observed.

5.7.3 Mass sink

Feedback models offer an answer to piling up mass by modelling the black hole, and returning a fraction of the accreted energy. This includes the circulation flows (Mathews et al., 2003). Brighenti and Mathews (2006) implemented a mass sink and concluded the cooling flow is strongly suppressed. Cattaneo and Teyssier (2007) similarly coupled accretion to the jet parameters, and found an equilibrium is established in reasonable comparison with observations. Binney, Alouani Bibi and Omma (2007) implemented a jet through a back-to-back nozzle in an adaptive grid, and concluded correlating mass deposition rates with output is not realistic as the black hole disc constitutes a reservoir of accreted mass and consequently feedback may be delayed. More recent self-regulated feedback models on longer time-scales include Gaspari et al. (2011) and Dubois et al. (2010) (which included star formation), which have some minor inconsistencies with observations.

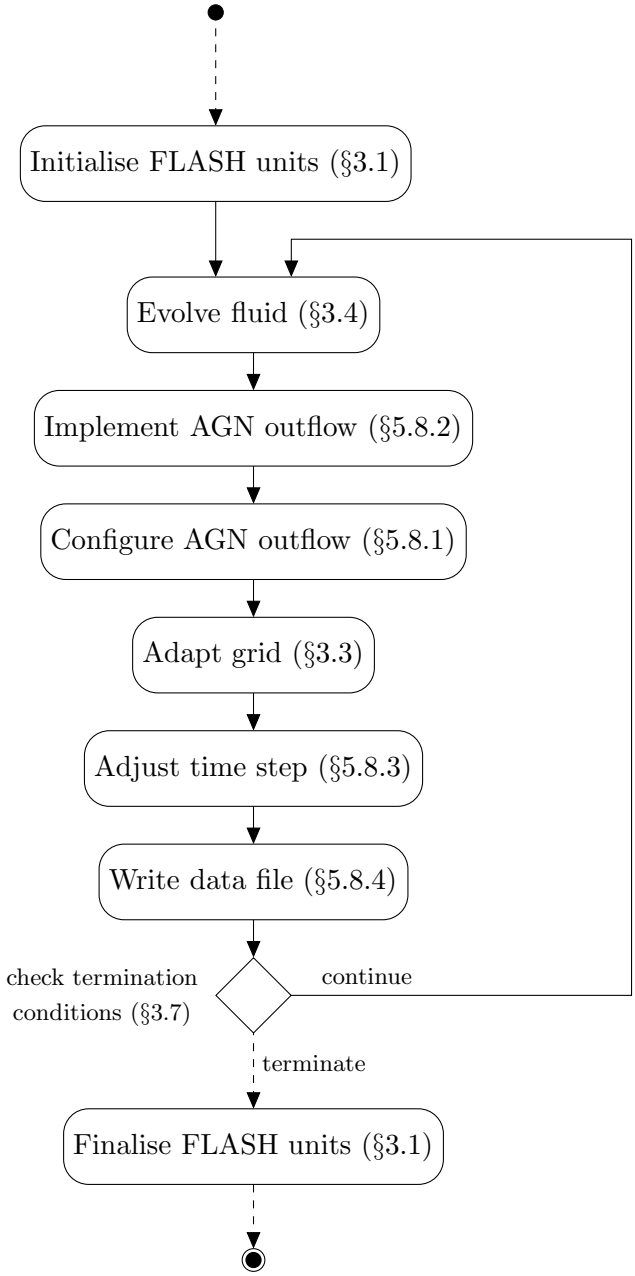

Figure 5.11: Activity diagram of the FLASH code in AGN Outflow set up. Dashed lines indicated unmentioned activities, which are less relevant for this chapter (cf. figure 3.1).

5.8 FLASH model of an AGN jet

Similar to the set-up first implemented by Omma et al. (2004), injecting jets through a pair of back-to-back nozzles located inside the grid. Compared to spherical polar coordinate grid-simulations injecting from the centre, this set-up has the distinct advantage that numerical perturbations that emanate from the external boundary influence the jet to a far lesser extent. Through these nozzles a pair of jets is injected in opposite direction, setting up a mass, momentum, and energy flux across the nozzle aperture. The implementation of the jet involves a number of additional subroutines in the FLASH-code. Figure 5.11 outlines the modified activity diagram for the FLASH-code using this set-up.

5.8.1 Configure jet

The jet source is modelled to have two modes: active or quiescent. The times at which the source switches to the active or quiescent mode is determined by the user in the FLASH parameter file.

The algorithm injects the flow through cell faces, therefore the source is translated toward the nearest cell face. The coordinates of the source and the orientation (xy-plane, yz-plane or xz-plane) and radius (in number of cells) of the apertures are provided as well the FLASH parameter file by the user. Refinement subroutines in the Grid unit have been modified as to keep the grid maximally refined about the source. This process is repeated if the grid refines changing cell ids during activity.

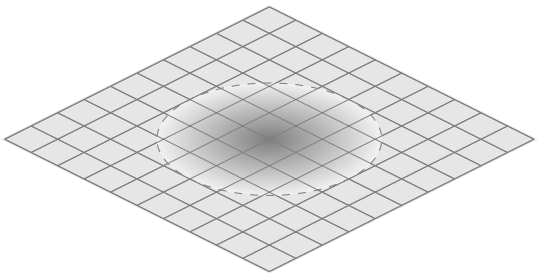

Figure 5.12: During the configuration phase, cell faces are marked for jet injection. The method attempts to generate a circular aperture with centre coordinates and radius supplied by the user.

If the jet mode switches from quiescent to active, all cell faces with their central position within required distance of the source in the plane specified by the user are marked as being part of the aperture (figure 5.12). The facing face in adjacent cell is marked as being part of the nozzle aperture of the counterjet.

The last step determining the jet's discharge (mass output), thrust (momentum output), and power (energy output) across the nozzle aperture from three parameters defined by the user in the FLASH parameter file. In set-ups designed for simulations in this thesis, the jet flow has conical morphology, the flow between projected source and nozzle demarcating a right circular cone with opening half-angle θ. The jet power P and speed v are two of the three user-defined parameters. Depending on the set-up, the last user-defined parameter is either the jet pressure p or the thermal power as a fraction of the total power P_{thermal}/P, where the thermal power is defined

$$P_{\text{thermal}} \equiv \int_{\text{S}} \rho h \vec{v} \cdot d\vec{A} = \frac{1}{1 + \frac{\gamma-1}{2}\mathcal{M}^2} P. \tag{5.4}$$

In this relation S denotes the nozzle aperture and $\mathcal{M}$ is the Mach number of the jet flow, which has been derived using the ideal gas equation of state $c_{\text{s}}^2/(\gamma - 1)$.

Selecting pressure as a variable amounts to flow through a diverging channel described in Landau and Lifshitz (1987), while selecting the thermal power fraction sets the Mach number across the jet. As the jet speed is also constant, speed of sound, temperature, specific internal energy and enthalpy are also constants. Considering the energy flux across the nozzle aperture and the defined jet power, the density can be determined. The speed of sound and density then define pressure.

5.8.2 Implement jet

After having evolved the grid as usual, the set-up transfers mass, momentum, and energy across marked nozzle aperture cell faces. For each cell face, a complete set of primitive variables is derived, i.e. the velocity components using the constant jet speed and the angle between the flow direction and the unit vector perpendicular to the nozzle aperture. Similar to the piecewise parabolic method's solution step described in section 3.4.3, the conserved variable fluxes across the nozzle aperture are derived, after which mass, momentum and energy are injected in associated cells.

5.8.3 Time-step adjustment

As outflow material poised for injection is not taken under consideration for when fixing the time-step, injected material is likely to lead to unstable solutions and unphysical fluid states.[7] This problem is solved by defining a Simulation time-step that limits the time-step to the side length of the smallest cell divided by the jet speed, which is in accordance with the CFL-condition for numerical stability.

5.8.4 Input/Output

Checkpoint files are dumped the moment the mode of the source changes (either from quiescent to active or vice versa), so that any simulation can be restarted from that point and all information on the fluid at these crucial times is available.

5.8.5 Ambient medium

A jet by definition has to been injected into a medium. In the case of AGN jets, the cooling core gas distribution as detailed by Ghizzardi et al. (2004) for the Virgo cluster core.[8] Implementing an astrophysical jet in this scenario is problematic, as observed jets are observed to be much narrower than computational resources can resolve within a cooling core of $\sim 100\,\mathrm{kpc}$. The jet and Virgo cluster core are therefore not to scale in any of the simulations.

Radiative cooling in the Virgo cluster core is an important process on simulation time scales of 80 Ma within $\sim 30\,\mathrm{kpc}$ of the cluster centre (beyond which the cooling time is more than 10 times the simulation time). Such a model can be implemented by using tabled cooling luminosities for a tenuous astrophysical plasma by Sutherland and Dopita (1993). Simulations discussed in this thesis are concerned with comparing heat mechanisms between jets with different intrinsic characteristics in a stratified medium. As radiative cooling might influence conclusions, while the research questions do not directly concern cooling, radiative cooling has not been implemented in simulations.

[7] The connection between numerical stability and time-step is described in paragraph 3.4.3.

[8] Chapter 4 details the model used for the Virgo cluster core.

5.9 FLASH module test

The efflux of material through the created apertures is tested for both sets of user-defined parameters using the Virgo cluster core module. Considering the purpose of supplying energy to the cluster core, tests will concern establishing whether an efflux is observed from both apertures, and whether the total energy in the grid rises with the injected amount.

5.9.1 Data acquisition

FLASH simulations with Virgo initial conditions supplies the necessary data. A $400\,\mathrm{kpc} \times 200\,\mathrm{kpc} \times 200\,\mathrm{kpc}$ cuboidal computational domain is used, with a cartesian grid comprising 2 cubic top blocks of identical shape lined up in x-direction. The refinement level is varied between 3 and 6, implying a resolution of 390 pc. The grid is kept maximally refined within a distance of 1 kpc of the centre of the computational domain. The domain boundary conditions are reflecting, meaning mechanical equilibrium is established across the domain perimeter.

The Virgo cluster is modelled using empirical density and temperature profiles as outlined by equations 4.1 and 4.2, using best-fit parameter values. The gravitational field is not active during simulations as the field would do work and complicate determination of the energy balance. The centre of the cluster coincides with the centre of the computational domain (corresponding to coordinates (200 kpc, 100 kpc, 100 kpc)). The double nozzle apertures are centred on the domain centre, and embedded in the yz-plane. The aperture has a diameter equal to 6 cells, which corresponds to 2.3 kpc.

opening half-angle	10°	10°
density contrast	0.22	0.13
pressure contrast	1.0	9.6
Mach number (internal)	5.1	1.7
Mach number (external)	15	15

Table 5.1: Dimensionless jet parameters used in test simulations.

A pair of simulations is run, each using a different set of user-defined parameters. In both simulations, the jet power is $P_\mathrm{j} = 10^{38}\,\mathrm{W}$, and the jet speed is $v_\mathrm{j} = 10^7\,\mathrm{m\,s^{-1}}$. The conical jet flow has an opening half-angle at the aperture of 10. Additionally, the pressure contrast[9] between jet and ambient medium is set to 1 in one simulation, while the thermal power fraction in the other simulation is $P_\mathrm{thermal,j}/P_\mathrm{j} = 0.5$. Derived dimensionless parameters are provided in table 5.1. Compared to other simulations, both jets are heavy (a density contrast of 0.01 is fairly standard). The two Mach numbers relate to the frame of reference and differing speed of sound. The external Mach number corresponds to the rest frame of the jet, in which the jet faces a headwind that is the ICM, while the internal Mach number represents the Mach number of the jet an ICM in rest faces.

The physical time covered by the simulation equals 10 Ma, covered with time steps ranging from a minimum of 1 a to a maximum of 100 ka. The jet is active between 3 Ma and 7 Ma.

5.9.2 Test specification

The module test is built up out of two tests.

1. Energy conservation test – the injected energy is compared to the increment of energy in the grid.
2. Efflux test – evaluation on whether an efflux of fluid is observed.

In the first test the total energy in the grid, which is isolated due to reflecting boundary conditions and the absence of any external forces, is monitored over the simulated physical time. The presumed rise between $t = 3\,\mathrm{Ma}$ and 7 Ma should correspond to the jet power

$$P_\mathrm{j} = 10^{38}\,\mathrm{W} = 3.2 \times 10^{51}\,\mathrm{J\,Ma^{-1}}. \tag{5.5}$$

The second test involves plotting the velocity field about the nozzle apertures.

[9] The pressure/density contrast is defined as the jet to ambient medium pressure/density ratio.

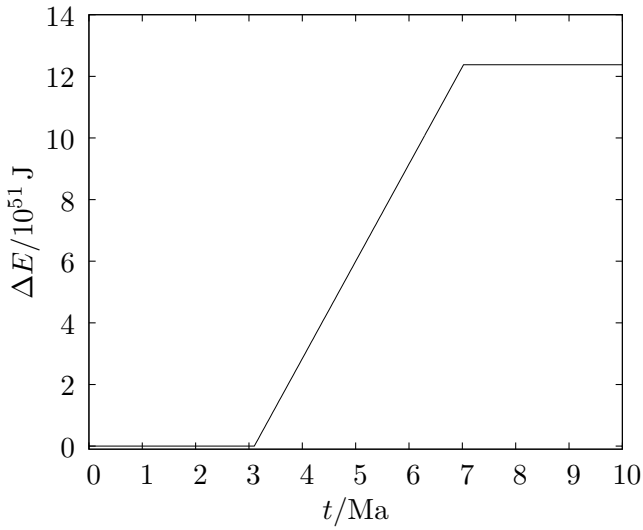

Figure 5.13: Evolution of the amount of energy in the grid during the AGN Outflow test simulation for testrun 1. There is an AGN outflow active between 3.0 Ma to 7.0 Ma, during which time energy increments steadily at a rate of 10^{38} W.

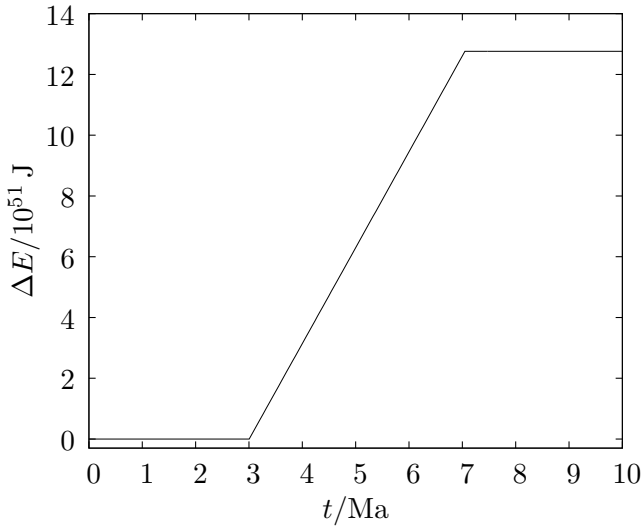

Figure 5.14: Evolution of the amount of energy in the grid during the AGN Outflow test simulation for test-run 2. There is an AGN outflow active between 3.1 Ma to 7.0 Ma, during which time energy increments steadily at a rate of 1.01×10^{38} W.

5.9.3 Findings

The time evolution of the total energy in the grid of both simulations is provided in figures 5.13 and 5.14. The slope of the lines is 10^{38} W and 1.01×10^{38} W respectively.

The velocity profile of test simulation 1 (figure 5.15) in a slice in the xy-plane through the centre of the grid provides evidence of a symmetrical outflow, while surface plots in the yz-plane of the velocity x-component (figures 5.16 and 5.17) show the nozzle apertures are indeed circular discs. Corresponding density (figure 5.18) and pressure profiles (figure 5.19) provide evidence of a bow shock.

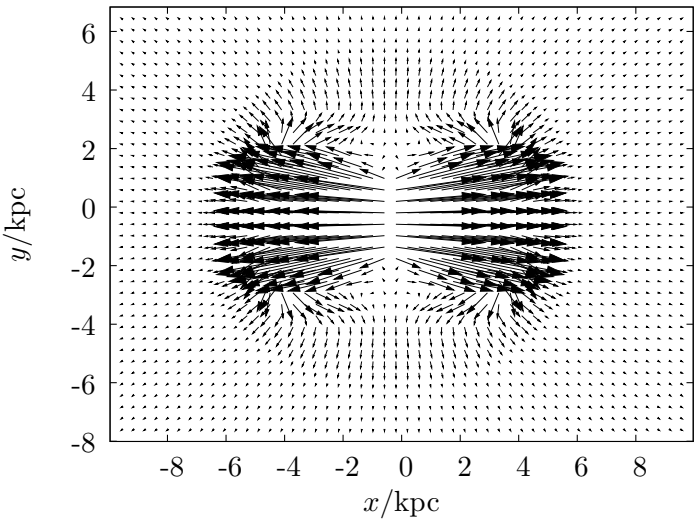

Figure 5.15: The velocity vectors $\vec{v}$ as projected onto the the xy-plane at $t = 5\,\mathrm{Ma}$; the nozzle is located in the centre of the image and configured to direct the jets symmetric about the x-axis at a 10° opening half-angle.

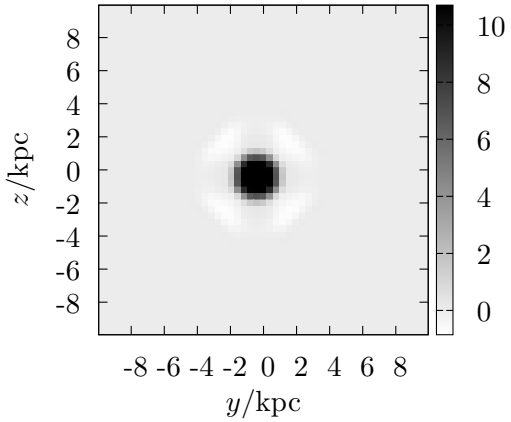

Figure 5.16: The x-component of the velocity vector field v_x (in $10^3\,\mathrm{km\,s^{-1}}$) in the yz-plane through the AGN at $t = 5\,\mathrm{Ma}$. The circular region of high-velocity is the jet.

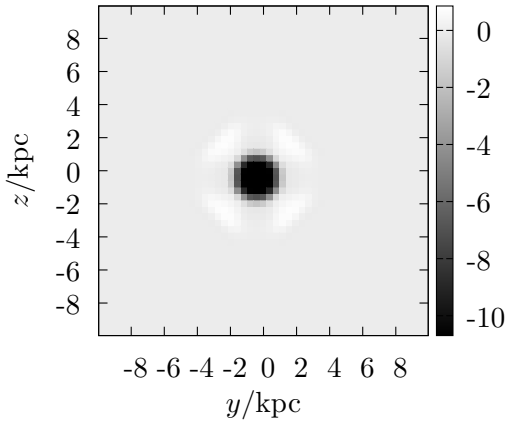

Figure 5.17: The x-component of the velocity vector field v_x (in $10^3\,\mathrm{km\,s^{-1}}$) in the yz-plane a resolution distance in the $-x$ direction of the AGN at $t = 5\,\mathrm{Ma}$. The circular region of high-velocity is the counterjet.

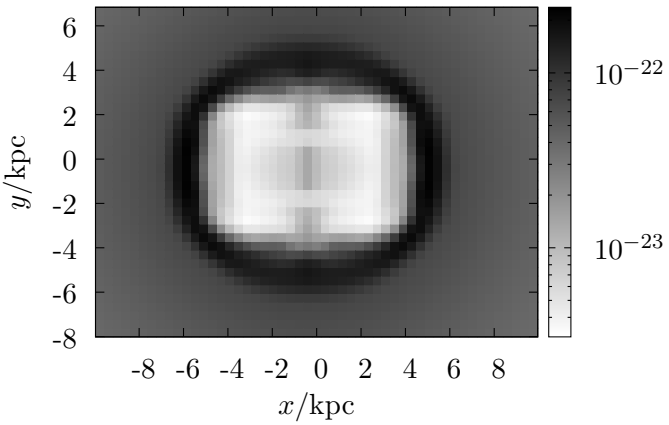

Figure 5.18: The density field ρ (in $\mathrm{kg\,m^{-3}}$) in the xy-plane at $t = 5\,\mathrm{Ma}$; the nozzle is located in the centre of the image.

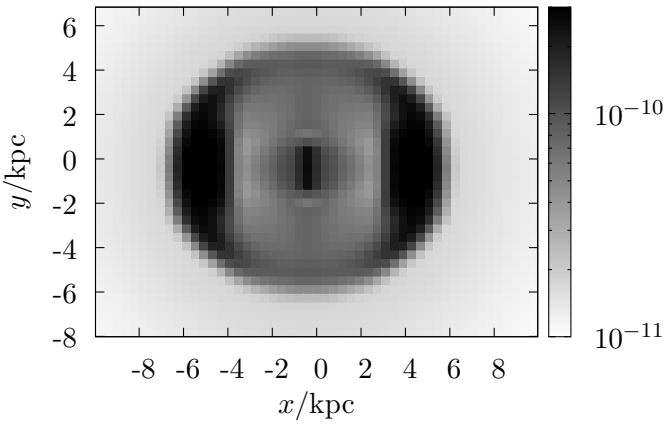

Figure 5.19: The pressure field p (in Pa) in the xy-plane at $t = 5\,\mathrm{Ma}$.

Chapter 6

From jets to winds

Considering the cooling flow problem on one side and heating by AGN outflows there is a rather obvious morphological problem. Catastrophic cooling cores are assumed to be spherical, while AGN outflows are directionally-biased being oriented along an axis. This leads to the possible scenario that the AGN outflow does indeed inject the required amount of energy, but it ends up overheating parts of the intracluster gas while leaving the cluster core outside the jet path untouched.

Considering the conical morphology of the flow upon injection, it seems reasonable to assume that a larger opening angle results in a jet with more intracluster gas in its path. In laminar jets, it is possible to observe the projected width of the narrow beam as a function of projected distance to the AGN. One can use half-intensity width as a measurement. The figure is likely to depend on the variable employed to derive the jet width, which may include density, pressure, velocity, or radio-intensity. Differences between these half-intensity widths can be appreciable in turbulent jets (e.g. Bicknell (1986*b*)).

Using inferred half-widths and projected distances, the opening angle can be determined. For supersonic flow maximum opening angles are achieved if the jet freely expands into a vacuum in Prandtl-Meyer expansion flow, allowing the jet to expand at an angle $\Delta\theta = \nu_\infty - \nu_\mathcal{M}$, where ν is the Prandtl-Meyer function.[1] In this chapter it is investigated whether an increased opening angle leads to a better distribution of energy throughout the cluster core.

[1] Prandtl-Meyer flow is detailed in paragraph 2.9.5.

6.1 Astrophysical background

Discussing opening angle in conjunction with observational evidence is slightly tricky, as the jet opening angle is inherently an artificial construct. If AGN outflows indeed start as conical outflows, that would be on sub-parsec scales in the vicinity of the black hole – below the resolution of the simulation and indeed below the resolution of any observationally obtained data. As these simulations target kpc-scale AGN outflows it makes sense to compare the artificial opening angle in the AGN Outflow unit to the opening angle of the jet at similar distance of the AGN.

The opening half-angle of AGN outflows is measured in but a few nearby cases, e.g. M87 (Virgo A, Junor, Biretta and Livio (1999)) and 3C 405 (Cygnus A, Carilli et al. (1996)). The FR I M87 jet is found to have different opening half-angle at different distances to the AGN. Junor, Biretta and Livio (1999) (figure 6.1) found for well-known M87 that the opening half-angle varies considerably at different characteristic length scales, decreasing from nearly 30° to about 3° at kiloparsec scales. The opening angle in the FR II jet of 3C 405 is significantly smaller around 1.6° (Carilli et al., 1996), i.e. the corresponding half-angle is less than a degree,

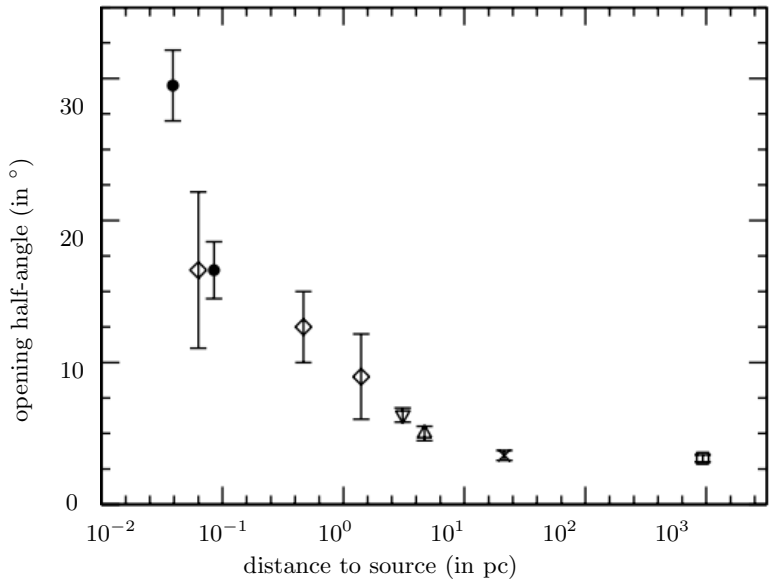

Figure 6.1: Jet opening half-angle as function of distance to the nucleus of M87. (Credit: Junor, Biretta and Livio (1999))

6.2 Technical set-up

A set of four FLASH simulations with Virgo initial conditions were done to acquire data. The cuboidal computational domain measures 400 kpc × 200 kpc × 200 kpc, with a Cartesian grid comprising 2 cubic top blocks of identical shape lined up in x-direction. The refinement level is varied between 3 and 6, corresponding to a resolution of 390 pc. The grid is kept maximally refined within a distance of 1 kpc of the centre of the computational domain. The domain boundary conditions allow for outflow of material.

opening half-angle	1°	5°	8°	10°
density contrast	0.1	0.1	0.1	0.1
pressure contrast	2.0	2.0	2.0	2.0
Mach number (internal)	2.7	2.7	2.7	2.7
Mach number (external)	15	15	15	15

Table 6.1: Dimensionless jet parameters used in simulations.

The Virgo cluster is modelled using empirical density and temperature profiles as outlined by equations 4.1 and 4.2, using best-fit parameter values. The gravitational field derived from the density and temperature profiles assuming hydrostatic equilibrium is applied. The centre of the cluster coincides with the centre of the computational domain and nozzle apertures (corresponding to coordinates (200 kpc, 100 kpc, 100 kpc)). The double nozzle apertures are centred on the domain centre, and embedded in the yz-plane. The aperture has a diameter equal to 6 cells, which corresponds to 2.3 kpc.

Each jet is defined by a combination of four parameters. The jet power $P_\mathrm{j} = 8.5 \times 10^{37}$ W, the jet speed is $v_\mathrm{j} = 10^7\,\mathrm{m\,s^{-1}}$, and the pressure contrast is 2.0. The remaining parameter is the opening half-angle of the jet, which is different for each simulation. Table 6.1 lists related dimensionless parameters.

The physical time covered by the simulation equals 80 Ma, covered with time steps ranging from a minimum of 1 a to a maximum of 100 ka. The jet is active between 0 and 10 Ma.

6.3 Results

The evolution of the total amount of energy in the grid is provided in figure 6.2. The figure appears to have one graph, but there are actually four graphs superposed. Each of the simulations therefore results in a net injection of the same amount of energy, and no observed difference can be attributed to unintended variations of energy fluxes between the jets.

Note that the increment compared to the inferred injected energy is likely to produce a discrepancy, as the computational domain is not isolated as in the module tests. The continuing increasing trend of the graphs after the jets become quiescent is due to work done by gravitational forces and the external boundaries allowing entrance and exit of gas.

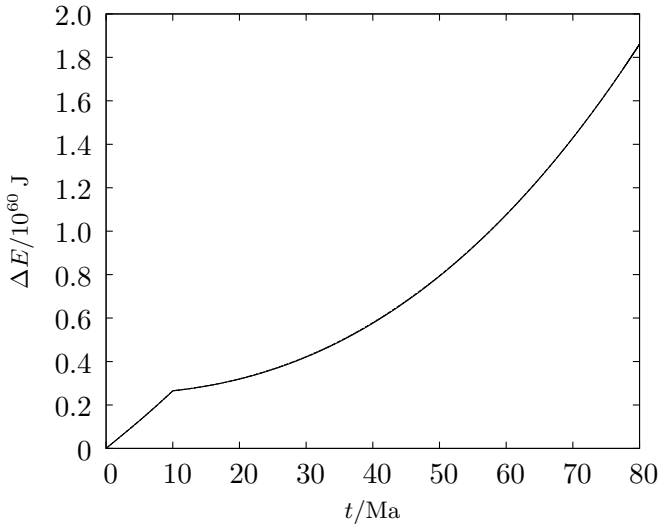

Figure 6.2: The total energy in the computational domain as a function of time for the four runs. The four graphs coincide which is why the figure only shows one line. The amount of energy in the computational domain continues to rise after the AGN quiesces, as the computational domain constitutes an open system.

A characteristic length scale is associated with the bow shock by moving from the domain edge at $(0, 100\,\text{kpc}, 100\,\text{kpc})$ in increments of 0.5 kpc in positive x-direction toward the AGN. The moment the Mach number jumps from lower than 0.1 to higher than 0.1 the bow shock is encountered, and the distance from that location to the AGN is the characteristic length scale.[2]

Figure 6.3 reflects the characteristic length scale of the bow shock for all four runs as a function of time. The key provides the opening angle corresponding to the indicated line.

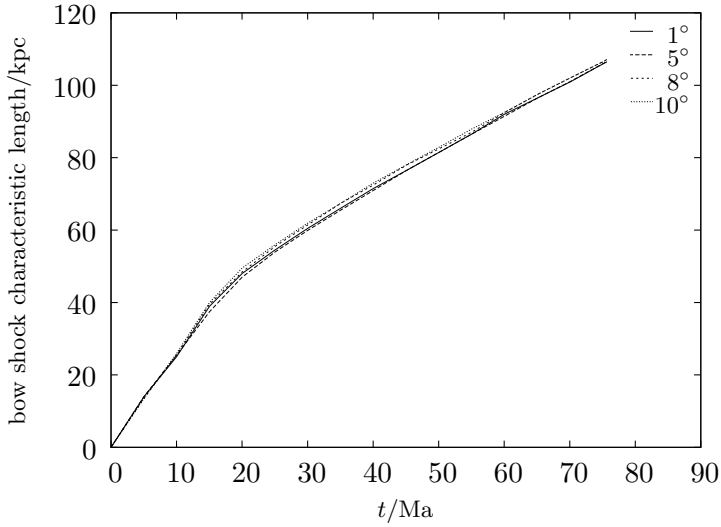

Figure 6.3: The characteristic length scale of the bow shock for all four runs as a function of time. The key indicates the opening half-angle associated with each graph.

[2]In later times motion in the cluster core periphery can give rise to Mach numbers exceeding 0.1, but the Mach number steadily drop as the fluid gets further from the domain edge.

Given the kpc error margin the difference between the lines is marginal to insignificant. As a varying opening angle affects the pre-injection outflow velocity field directly, and the energy output for all runs is the same, we would expect jets with a wide opening angle to lose energy sideways and have less available to burrow their way forward.

Figure 6.3 suggests jet evolution takes place in two phases. In the first phase the jet rapidly expands; this lasts from the onset at $t = 0$ until about $t = 20\,\mathrm{Ma}$. The second phase involves slower expansion, which continues at a steady pace up until the end of the runs. The explanation of this two-phase evolution is explained by the sound speed profile at $t = 20\,\mathrm{Ma}$ in figure 6.4. The sound speed in the region connecting the nozzle and the jet tip is on average $2 \times 10^6\,\mathrm{m\,s^{-1}}$; when the jet shut down at $t = 10\,\mathrm{Ma}$ it therefore took the information 20 Ma to bridge the 40 kpc. In other words the evolutionary pattern of the jet changes when news of the quiesced AGN reaches the jet tip.

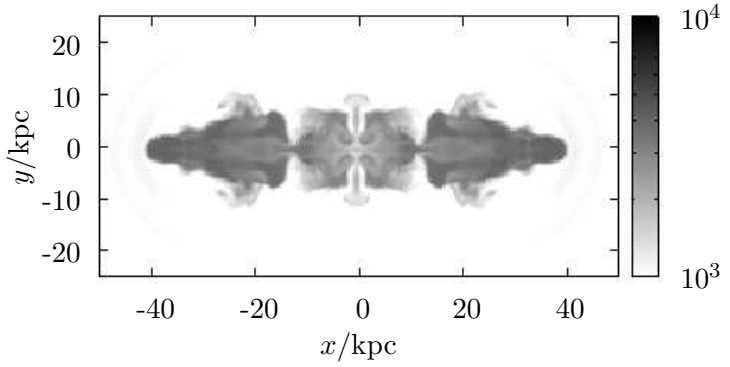

Figure 6.4: Sound speed profile about the jet with an opening half-angle of 1° (in $\mathrm{km\,s^{-1}}$) at $t = 20\,\mathrm{Ma}$.

Figures 6.5, 6.6, 6.7 and 6.8 show a snapshot of the cluster density profile at $t = 25\,\mathrm{Ma}$, early in the slow expansion phase. All four jets are quite turbulent and have very similar morphology.

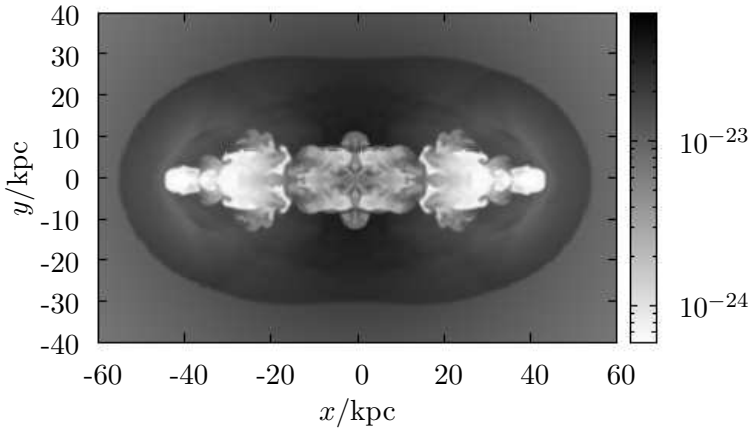

Figure 6.5: Density profile (in $\mathrm{kg\,m^{-3}}$) of the jet with an opening half-angle of 1° at $t = 25\,\mathrm{Ma}$.

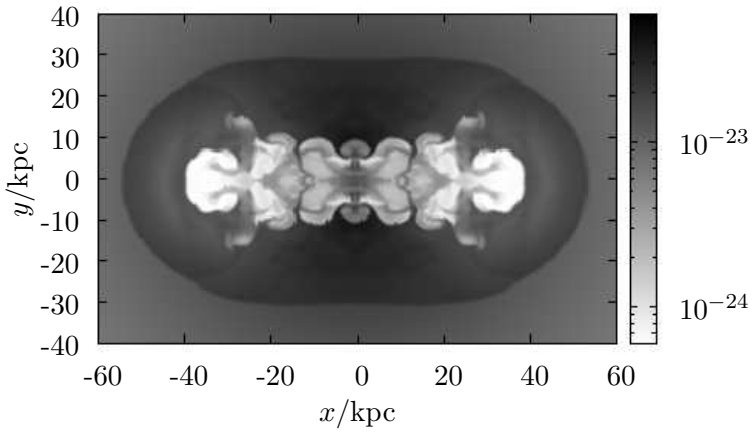

Figure 6.6: Density profile (in $\mathrm{kg\,m^{-3}}$) of the jet with an opening half-angle of 5° at $t = 25\,\mathrm{Ma}$.

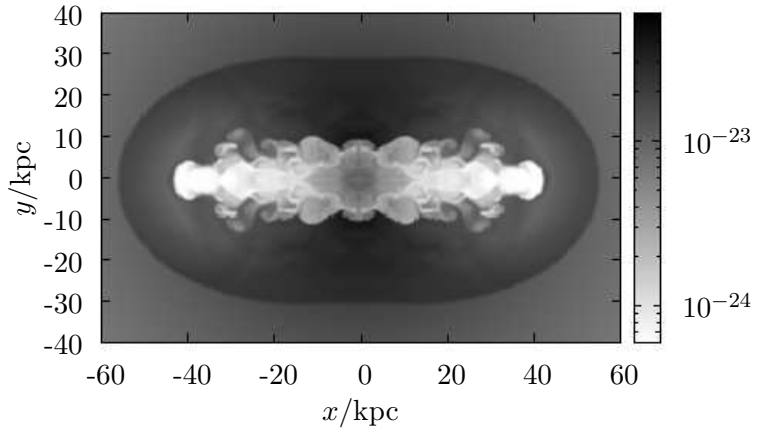

Figure 6.7: Density profile (in $\mathrm{kg\,m^{-3}}$) of the jet with an opening angle of 8° at $t = 25\,\mathrm{Ma}$.

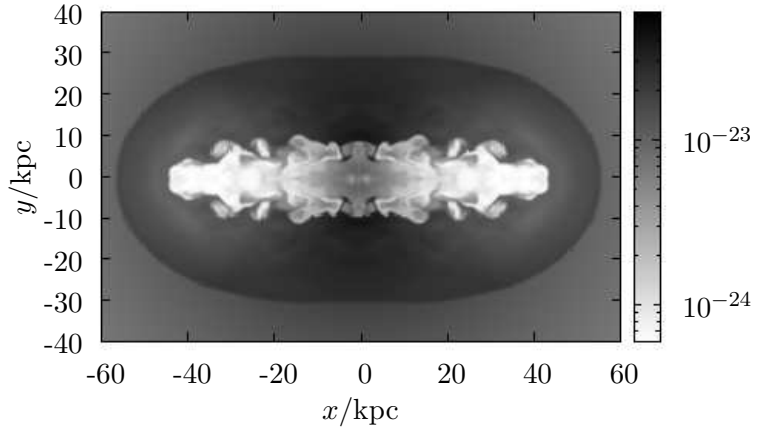

Figure 6.8: Density profile (in $\mathrm{kg\,m^{-3}}$) of the jet with an opening angle of 10° at $t = 25\,\mathrm{Ma}$.

The distribution of energy of the four jets throughout the grid is investigated by outlining a cone centred on the AGN with a top half-angle of 20°, oriented parallel to the x-axis. An outline of the evolution of the energy contained in the region in the jet line-of-fire demarcated by the cone and a sphere with radius 120 kpc is provided in figure 6.9. The graphs suggest there is no significant difference between the jets when the distribution of heat is concerned.

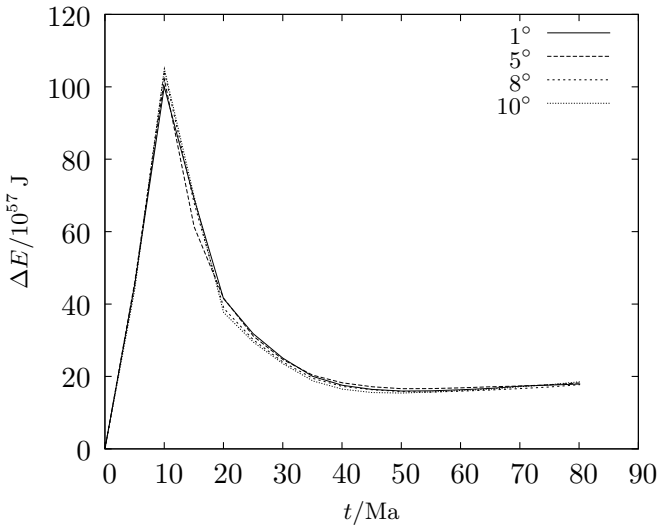

Figure 6.9: The change of energy in the computational domain within an area demarcated by a double cone, defined by the AGN as the apex and oriented parallel to the x-axis with an opening half-angle of 20°, and a sphere with radius 120 kpc. The key refers to the opening half-angle associated with the run.

The jets show signs of progressed Kelvin-Helmholtz and Rayleigh-Taylor instability, where especially the 5° half-opening angle jet shows a fully developed mushroom-shaped cloud at the jet tip. In all cases the cocoon has been shredded. Density profiles of the jets at $t = 80$ Ma are provided in figures 6.10, 6.11, 6.12 and 6.13. In all four cases a low-density region qualifyable as a bubble can be seen, with similar signs of instability.

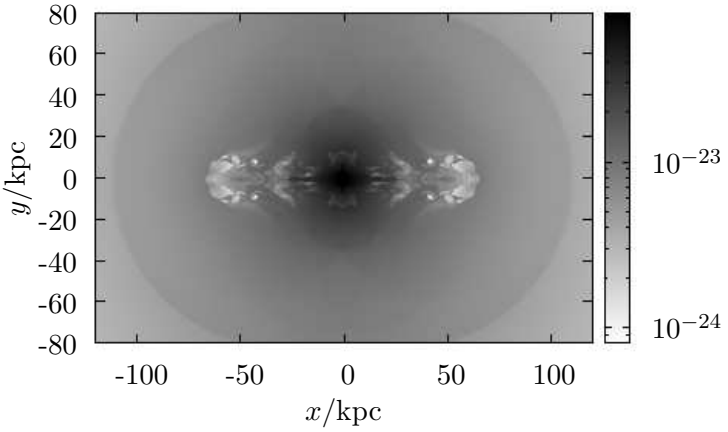

Figure 6.10: Density profile (in $\mathrm{kg\,m^{-3}}$) of the jet with an opening half-angle of 1° at $t = 80\,\mathrm{Ma}$.

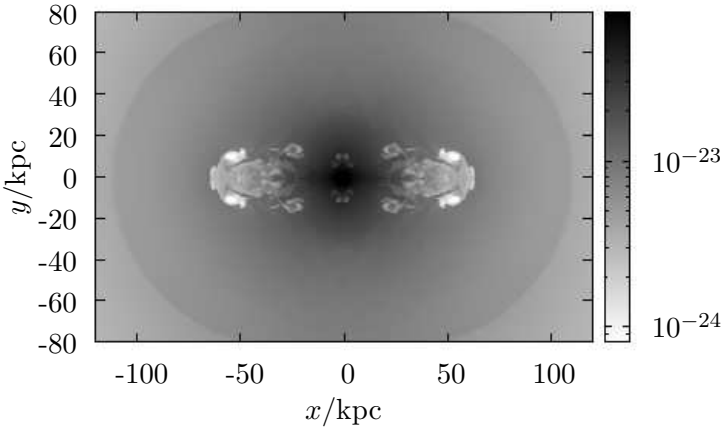

Figure 6.11: Density profile (in $\mathrm{kg\,m^{-3}}$) of the jet with an opening half-angle of 5° at $t = 80\,\mathrm{Ma}$.

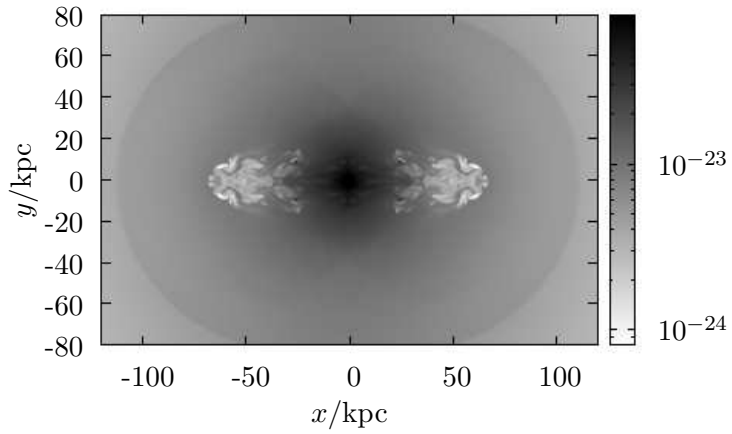

Figure 6.12: Density profile (in $\mathrm{kg\,m^{-3}}$) of the jet with an opening half-angle of 8° at $t = 80\,\mathrm{Ma}$.

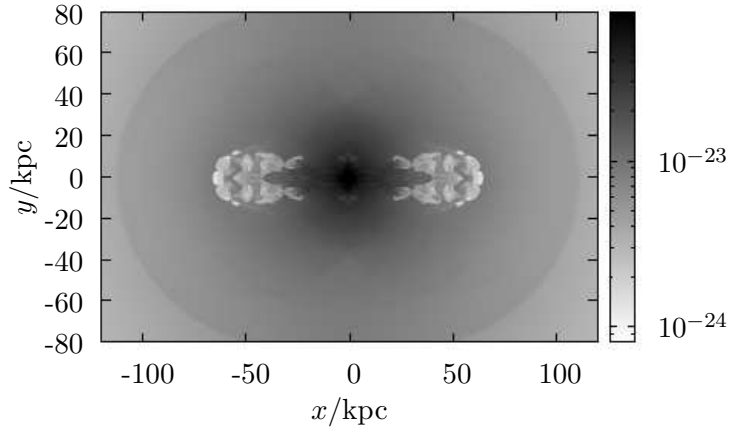

Figure 6.13: Density profile (in $\mathrm{kg\,m^{-3}}$) of the jet with an opening half-angle of 10° at $t = 80\,\mathrm{Ma}$.

6.4 Discussion

Comparing the density profiles with the Fanaroff-Riley classification scheme, all four jets bear the signature of an FR I jet. The modelled jets are all heavy compared to other simulations (given a density contrast of 0.01 is usual), and heavy jets are known to give rise to less stable cocoons (e.g. Norman et al. (1982)).

If the jet upon emerging from the nozzle has sufficient thrust to be effectively unrestrained by the ambient medium, it will expand in Prandtl-Meyer flow which will bend the jet with 37°. Even a sizable fraction of this will dwarf the opening angle difference at the nozzle aperture. After initial expansion, the jet will be reconfined by the ambient medium.

The collimation of a jet is primarily determined by the cocoon surrounding the jet, and Kelvin-Helmholtz instability developing on the interface between jet and cocoon. This instability is enhanced in the potential well where the density contrast between jet and ICM is the greatest. The resulting vortices cause entrainment of ambient gas into the jet, which reduces the jet speed (Bicknell, 1995).

It is likely that the mixing of cocoon material and the jet changes the jet thrust to the extent that the original opening angle at the nozzle aperture is not significant anymore. Despite the severely disrupted cocoons, all four jets are seen to be able to inflate bubbles on larger time-scales.

The more forceful FR II jets remain laminar until they terminate at a jet shock, do not entrain as much and in that case the opening angle at the aperture may make an observable difference at kiloparsec scales. However, FR II jets are rarely observed in cores of rich clusters. The selection of opening half-angles was limited to 10° or lower, and much larger angles may still make some observable difference. As there is no observational evidence that there are jets at kiloparsec scale that have large opening angles, the conclusion is that opening angle as a parameter has but a local effect as entrained matter changes the composition of the gas.

Chapter 7

Wave emission by jets

Dissipating waves broadcast by bubbles of cocoon has been proposed as heat transfer mechanisms between jet and ICM. A wave is defined as oscillatory motion of matter under influence of a restoring force. Such motion leads to wave formation, which is capable of transporting energy over large distances.

7.1 Theoretical background

There are different species of waves, identifiable by the nature of the restoring force. *Sound waves* compress the fluid. The resulting pressure gradient then forces the gas to rarefy, causing oscillatory motion.[1]

Gravity waves concern parcels of gas being displaced in a medium in hydrostatic equilibrium. The gravitational force acts as restoring force to bring the parcel back to equilibrium, resulting in oscillatory motion. If these waves oscillate within a stratified fluid, these are called *internal gravity waves*. If these waves take place on the interface with a different fluid, the waves are *surface gravity waves*.[2]

Considering a generic equation of state $\rho(p, s)$, density perturbations are due to a pressure perturbation in case of a sound wave, and due to an entropy perturbation for any other wave. The main purpose of this project is to establish the presence or absence of either wave species and infer the nature of ripples observed in observations.

[1] Sound waves were initially described in paragraph 2.8.

[2] Surface gravity waves are discussed in paragraph 2.12.2.

7.1.1 Acoustic-gravity waves

Consider oscillating linear perturbations in a static homogeneous medium, then conservation of mass and momentum imply[3]

$$\frac{\partial(\delta\rho)}{\partial t} + \rho\vec{\nabla}\cdot(\delta\vec{v}) = 0, \tag{7.1}$$

$$\rho\frac{\partial(\delta\vec{v})}{\partial t} = -\vec{\nabla}(\delta p). \tag{7.2}$$

Solving for $\delta\rho$ and $\delta\vec{v}$ using an equation of state $\delta p(\delta\rho)$ yields a wave equation, travelling at the speed of sound

$$c_{\mathrm{s}} = \sqrt{\left(\frac{\partial p}{\partial\rho}\right)_s}. \tag{7.3}$$

The Boussinesq approximation models a fluid as incompressible except in terms involving the gravitational field $\vec{g}$, which effectively eliminates sound waves from the solution. The fluid then obeys

$$\vec{\nabla}\cdot(\delta\vec{v}) = 0, \tag{7.4}$$

$$\rho\frac{\partial(\delta\vec{v})}{\partial t} = (\delta\rho)\vec{g} - \vec{\nabla}(\delta p). \tag{7.5}$$

where hydrostatic equilibrium implies $\vec{\nabla}p = \rho\vec{g}$. The equations of state imply $\delta\rho(\delta s)$ these equations yield a monochromatic wave solutions oscillating with an angular frequency $\omega = \pm\omega_{\mathrm{BV}}\sin\theta$, where

$$\omega_{\mathrm{BV}} = \sqrt{\frac{1}{\rho}\left(\frac{\partial s}{\partial\rho}\right)_p \vec{g}\cdot\vec{\nabla}s} \tag{7.6}$$

is the Brunt-Väisälä frequency and θ the angle between $\vec{g}$ and $\vec{k}$ (Landau and Lifshitz, 1987).

The general case of compressible waves in a stratified medium has been solved for an atmosphere by Lamb (1908). This yields a dispersion relation which allows for low-frequency gravity waves, and high-frequency sound waves, which cannot travel in the direction of stratification with an angular frequency below the atmosphere-dependent acoustic cut-off frequency (Lamb, 1945).

[3]More general sound wave solutions in a flowing fluid have been derived in paragraph 2.8.

7.1.2 Wave dissipation

Waves can dissipate if they are damped by viscous forces or thermal conduction. In case of sound waves the intensity decreases by a factor $\mathrm{e}^{-\gamma x}$, where x is the distance travelled and γ is the damping coefficient. Given the angular frequency ω, Landau and Lifshitz (1987) derives for associated damping coefficient

$$\gamma = \frac{\omega^2}{2\rho c_\mathrm{s}^3}\left[(\frac{4}{3}\eta + \zeta) + \kappa\left(\frac{1}{c_\mathrm{V}} - \frac{1}{c_\mathrm{p}}\right)\right], \tag{7.7}$$

where c_V and c_p are the specific heats at constant volume or pressure respectively divided by mass, η is the dynamic viscosity, ζ the second viscosity, and κ the thermal conductivity.

If second viscosity ζ and thermal conductivity κ are insignificant, the characteristic length scale for dissipation L at which the wave energy is reduced by a factor e^{-1} is

$$\frac{L}{\lambda} = \frac{1}{2\gamma\lambda} = \frac{3c_\mathrm{s}\lambda}{8\pi^2\nu}, \tag{7.8}$$

where $\nu = \eta/\rho$ is the kinematic viscosity. Given the wavelength of the sound wave, the kinematic viscosity, and the sound speed, it is possible to demarcate a spherical region within which a sizable fraction of the wave energy is deposited.

Internal gravity wave with angular frequency ω decrease with a factor $\mathrm{e}^{-\gamma t}$, where the damping coefficient is

$$\gamma = \frac{2\nu\omega^4}{g^2}, \tag{7.9}$$

and g is the gravitational acceleration (Landau and Lifshitz, 1987).

In an ideal fluid the coefficients of viscosity η and ζ, and the coefficient of thermal conductivity κ are zero. This implies that waves do not dissipate and wave heating is not a viable process. In the ICM these coefficients depend strongly on the configuration of the magnetic field. As there is much uncertainty in this respect, the role of wave heating is unavoidably arguable.

7.2 Astrophysical background

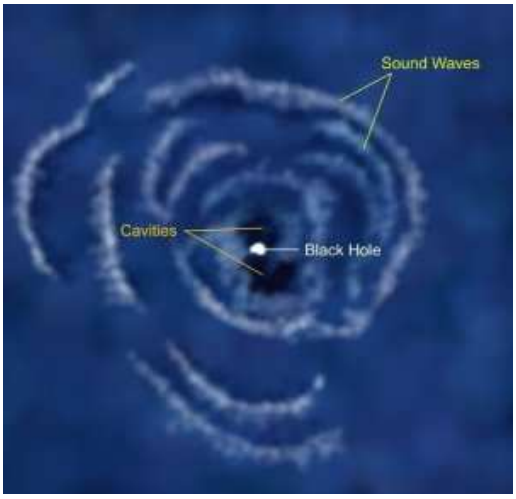

Figure 7.1: Observed ripples in the X-ray emission in the Perseus cluster are associated with sound waves (Credit: NASA/CXC/IoA/A.Fabian et al. Illustration: NASA/CXC/M.Weiss)

Figure 7.1 is a contrasted idealised image of data acquired of NGC 1275 in the Perseus cluster core. By smoothing an image and comparing it with the original, a pattern of quasi-spherical ripples emerges in the ICM (figure 7.1, see Fabian et al. (2003*a*)). This pattern can be interpreted considering X-ray emission in the ICM is predominantly caused by thermal bremsstrahlung. As the emissivity of thermal bremsstrahlung is strongly dependent on the density of the emitting gas[4], and therefore the ripples represent density perturbations.No correlated temperature or abundance profile is observed,

The wave pattern therefore suggests a compressible perturbation, comprising the linear oscillatory sound waves and non-linear steepened shocks.footnoteSee paragraph 2.9 for a description on non-linear steepening of sound waves. Though both phenomena are related, shock heating is implied by the entropy discontinuity, which is proportional to the cube of the pressure jump for weak shocks.[5] Sound waves require viscosity or thermal conductivity to dissipate their energy.

[4]See paragraph 1.3.6 for more information on the emissivity of thermal bremsstrahlung.
[5]See paragraph 2.9.4 on weak shocks.

Other observations of ripples in different systems include similar rings about M87 in the Virgo cluster (Forman et al., 2005), and rings in proximity of NGC 5128 (Centaurus A, Sanders and Fabian (2008)).

As the Perseus cluster is a cooling core cluster, Fabian et al. (2003*a*) proposed that sound waves emitted in proximity of bubbles as they grow might account for significant heating in the ICM. In convenient units equation 7.8 can be rewritten

$$\frac{L}{\lambda} \approx 7 \left(\frac{\lambda}{10\,\mathrm{kpc}} \right) \left(\frac{\lambda}{3 \times 10^4\,\mathrm{m}^{-3}} \right) \left(\frac{k_\mathrm{B} T}{5\,\mathrm{keV}} \right)^{-2}, \tag{7.10}$$

If the inferred wavelength of $\lambda = 10\,\mathrm{kpc}$ holds true, most of the wave energy is dissipated in or very near the cooling core. (Sanders and Fabian, 2007) inferred from observations that the waves carry sufficient energy to quench cooling.

7.2.1 Numerical simulations

In a three-dimensional simulation Ruszkowski, Brüggen and Begelman (2004*b*) attempted to estimate the effect of viscous dissipation of sound waves. Spitzer viscosity was assumed in order to obtain wave dissipation in the modelled fluid. Employing smoothing of images, similar wave patterns were found throughout the ICM, and found that energy dissipated by sound waves and weak shocks is comparable to the losses due to radiative cooling.

Sternberg and Soker (2009) show in a simulation that a pair of bubbles can account for the observed sound waves and shocks, due to turbulent motion within and about the bubbles. An alternative source of wave heating was proposed by Shabala and Alexander (2009), who remarked that the expanding cocoon upon reaching a state of mechanical equilibrium might overshoot and oscillate about its equilibrium position. Such oscillating motion would then give rises to emission of sound waves.

7.3 Technical set-up

The data is acquired by running a single FLASH simulation using Virgo initial conditions. The cuboidal computational domain measures 400 kpc × 200 kpc × 200 kpc, with a Cartesian grid comprising 2 cubic top blocks of identical shape lined up in x-direction. The refinement level is varied between 3 and 6, corresponding to a resolution of 390 pc. The grid is kept maximally refined within a distance of 1 kpc of the centre of the computational domain. The boundary conditions along the perimeter of the computational domain is set to outflow, resulting in an open domain.

opening half-angle	10°
density contrast	0.09
pressure contrast	4.6
Mach number (internal)	1.73
Mach number (external)	12.5

Table 7.1: Dimensionless jet parameters used in simulation.

The Virgo cluster is modelled using empirical density and temperature profiles as outlined by equations 4.1 and 4.2, using best-fit parameter values. The gravitational field derived from the density and temperature profiles assuming hydrostatic equilibrium is applied. The centre of the cluster coincides with the centre of the computational domain and nozzle apertures (corresponding to coordinates (200 kpc, 100 kpc, 100 kpc)). The double nozzle apertures are centred on the domain centre, and embedded in the yz-plane. The aperture has a diameter equal to 6 cells, which corresponds to 2.3 kpc.

Each jet is defined by a combination of four parameters. The jet power $P_\mathrm{j} = 10^{38}$ W, the jet speed is $v_\mathrm{j} = 10^7\,\mathrm{m\,s^{-1}}$, and the ratio of thermal power to total power is 0.5. The opening half-angle of the jet is set to 10°. Table 7.1 lists related dimensionless parameters.

The physical time covered by the simulation equals 80 Ma, covered with time steps ranging from a minimum of 1 a to a maximum of 100 ka. The jet is active between 0 and 10 Ma.

7.4 Results

When discussing wave heating in the ICM, the first thing that needs to be considered is where the heat is needed, and where the heat sources are. Commencing with the latter, an overall impression of the expansion of the bow shock is provided in figure 7.2, which shows the characteristic length scale associated with the bow shock as a function of time. Similar to earlier discussed simulations, there is evidence of two stages in jet evolution, which a change of expansion rate at 20 Ma.

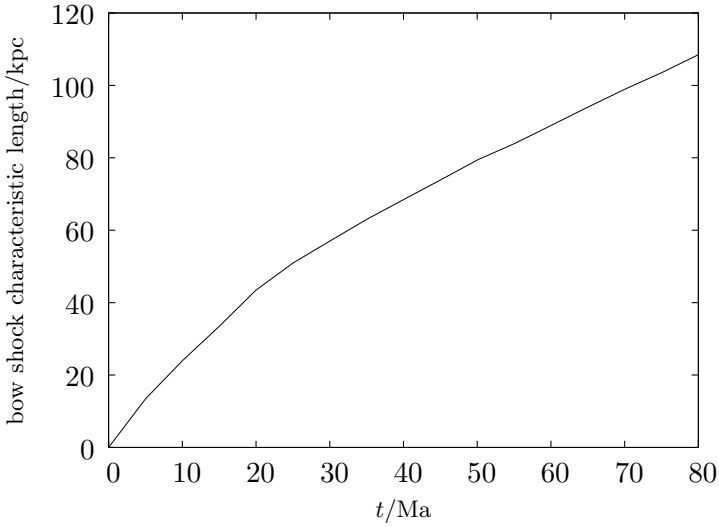

Figure 7.2: The characteristic length scale of the bow shock as a function of time.

In this chapter a different approach to wave detection is used, different from conventional methods (discussed by Graham, Fabian and Sanders (2008)). Consider two observations of the system taken a time-interval large for present sound waves, but small for any large-scale dynamical process. It is then possible to subtract the two data sets and effectively eliminate the quasi-equilibrium density profile. The remnant of the signal will then be perturbations, and if oscillatory waves. Compared to conventional method, this method has as an advantage that it does not require a masking method of arguable quality, while the difficulty is selecting an appropriate value for the time difference between the observations.

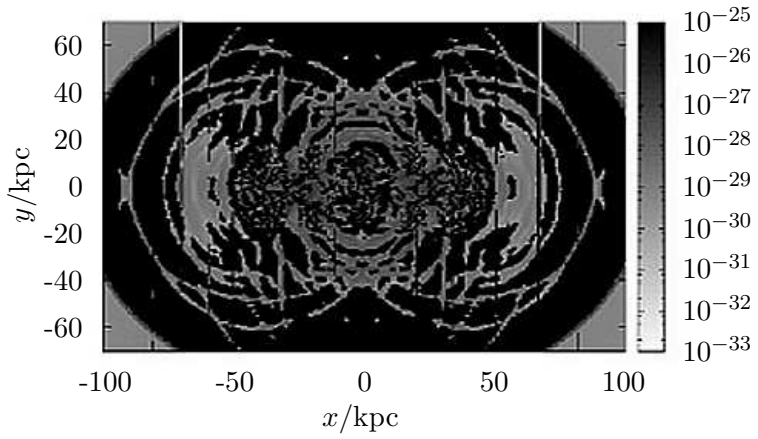

Figure 7.3: Density difference profile $\Delta\rho$ (in $\mathrm{kg\,m^{-3}}$) between $t = 79\,\mathrm{Ma}$ and $t = 80\,\mathrm{Ma}$ in the xy-plane; the AGN is in the image centre.

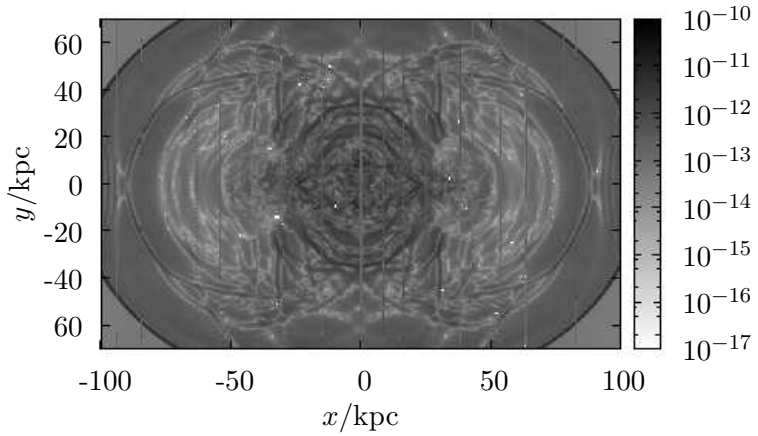

Figure 7.4: Pressure difference profile Δp (in Pa) between $t = 79\,\mathrm{Ma}$ and $t = 80\,\mathrm{Ma}$ in the xy-plane; the AGN is in the image centre.

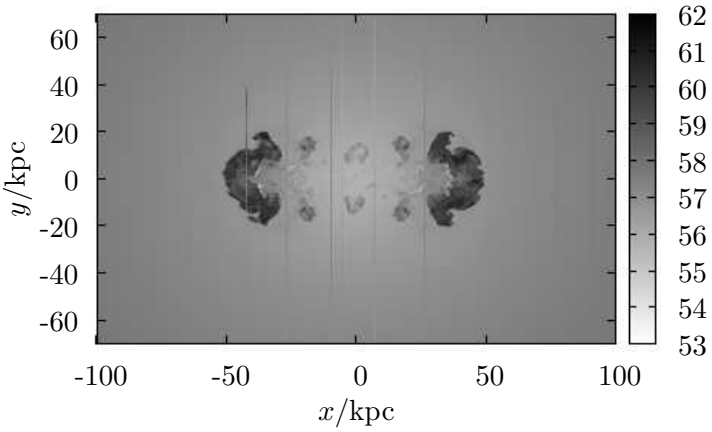

Figure 7.5: Entropy difference profile represented by $\Delta \ln(T\rho^{\gamma-1})$ between $t = 79\,\mathrm{Ma}$ and $t = 80\,\mathrm{Ma}$ in the xy-plane; the AGN is in the image centre.

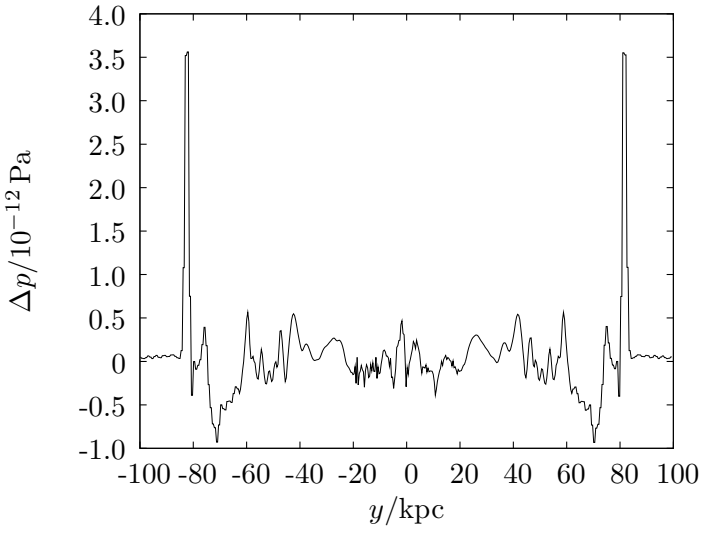

Figure 7.6: Pressure difference profile Δp (in $10^{-12}\,\mathrm{Pa}$) across a line parallel to the y-axis and traversing (-40 kpc,0,0).

Simulations of Ruszkowski, Brüggen and Begelman (2004*b*) indicate waves are best observed at later time-scales of up to 200 Ma. Fabian et al. (2003*a*) inferred a wavelength of ∼10 kpc, which considering sound speeds $\sim 10^2\,\mathrm{km\,s^{-1}}$ in the cluster indicates over a time of 1 Ma the observed amplitude is smaller by the phase shift 0.06 rad – which is still observable. The density difference profile between 79 Ma and 80 Ma is presented in figure 7.3 and has distinct circular ripples. From corresponding pressure and entropy profiles (figures 7.4 and 7.5) it is inferred ripples in the density profile coincide with pressure ripples. The entropy profile is quite featureless with exemption of the cocoon remnant itself. In accordance with Fabian et al. (2003*a*) the ripples are identified as sound waves.

Two interfering sources are visible in proximity of regions of high entropy difference and likely coincide with rising bubbles. Incoming waves facing the jet are artifacts produced due to the irregularities in grid refinement and resulting change in acoustic impedance, while vertical features are sampling artifacts. A plot of the pressure difference in y-direction through one of the sources located approximately 40 kpc in $-x$ direction of the AGN is given in figure 7.6. The spikes in the flanks of the graph represent the out-moving bow shock. Fourier analysis on a 128 point data set was attempted but inconclusive (figure 7.7).

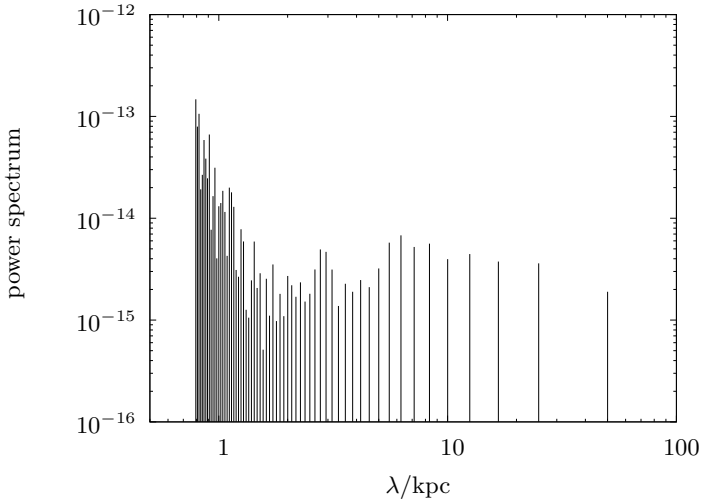

Figure 7.7: Fourier transform of the pressure difference profile in figure 7.6 using a set of 128 data points with y ranging from −80 kpc and −20 kpc.

7.5 Discussion

Ripples are seen to emanate from sources in apparent proximity to pockets of high entropy, coinciding with cocoon remnants which may or may not have the shape of bubbles. Given the pressure difference profile provides clear evidence of ripples at locations coinciding with the density ripples, no such ripples are observed in entropy difference profiles. Observed features are therefore identified as compressible perturbations. These features can include either shock discontinuities or sound waves. The expanding bow shock is clearly observable in the one-dimensional profile as a par of spikes, resulting in a sharp increase of pressure in the ICM as it moves into it.

No features associated with ripples are observed in the entropy difference profiles. No gravity wave activity is therefore observed in the jet region, which indicates that wave heating is confined to sound waves. A caveat is that waves with a period appreciably shorter than the sampling interval of 1 Ma are rendered unobservable by the profile comparison technique.

Attempts to quantify wave heating require measuring the wavelength of observed sound waves. To that extent the pressure difference profile was Fourier transformed across a line perpendicular to the jet axis from the inferred location of a source. Though the line plot revealed a series of oscillations, no clear pattern emerged from Fourier analysis. The result is hindered by the limited number of data points available for sampling in the region, and a higher resolution may yield more substantial results.

In absence of a dominant frequency further analysis would be based on estimates with large margin for errors. Given this the conclusion of the project is that the proposed method for observing yields results comparable to observations and other simulations, but that insufficient resolution and possibly more structural problems due to irregular sound wave emission or perturbations due to grid irregularities render quantitative analysis using Fourier techniques unfeasible.

Chapter 8

Jet thrust and thermal power

At the nozzle aperture, an AGN jet is defined by its discharge, thrust, and power. This project is concerned with comparing jets of the same power, but with a different discharge and thrust. This variation can be achieved by increasing or decreasing the thermal power to power ratio of the jet, or alternatively the internal Mach number with which a correlation exists. Jets need thrust to punch their way through the cluster core, but if the total power is fixed, this reduces the heating capability. The project therefore amounts to comparing the roles of jet thrust and thermal power.

Given that FR I jets are more common in cool cluster cores than FR II jets, the parameter space explored in this project include heavier jets (with a density contrast ~ 0.1 as compared to ~ 0.01 for most other simulations), at most a few times overpressured and with lower Mach numbers. This is expected to make the jet more prone to instability and turbulence (e.g. Norman et al. (1982)). As such, the pressure contrast is a lot less forceful than jets of Basson and Alexander (2003), and more comparable to jets modelled by Omma et al. (2004), which were observed to deposit their energy closer to the cluster core.

The balance between thermal power and thrust is thought to have important ramifications for the main heating mechanisms of the AGN, which depend on shock and bubble formation.

8.1 Theoretical background

Comparing the role of heating mechanisms requires rendering bubbles and shocks observable in simulation data. This paragraph outlines the techniques used to analyse shocks and bubbles.

Shocks are not easy to identify numerically because the distinction between continuous and discontinuous solutions vanished with the implementation of the finite volume method. A shock filter is designed based on the FLASH shock-finder (Fryxell et al., 2000), which employs an algorithm identifying shocks by considering the pressure gradient

$$\frac{|\langle p\rangle_{j+1} - \langle p\rangle_{j-1}|}{\min(\langle p\rangle_{j-1}, \langle p\rangle_{j+1})} \geq \frac{1}{3} \tag{8.1}$$

and the divergence of the velocity field (which indicates compression)

$$\langle v\rangle_{j+1} - \langle v\rangle_{j-1} < 0. \tag{8.2}$$

If both criteria are satisfied for a data point, a traversing shock is reported. Nulsen et al. (2007) suggests the significance of shock heating can be determined by reconstructing the entropy jump across the shock discontinuity. The heat released by gas flowing across the shock front is then

$$đq = T\delta s = \frac{h}{c_p} c_p \Delta \ln\left(\frac{p^{1/\gamma}}{\rho}\right) \Rightarrow \frac{q}{h} = \Delta \ln\left(\frac{p^{1/\gamma}}{\rho}\right). \tag{8.3}$$

The fraction of available enthalpy released as heat is thus expressed in terms of local observables.

X-ray cavities can be made observable in simulation data by constructing synthetic X-ray maps, which can be created by integrating the emissivity for thermal bremsstrahlung for a photon range from 2 to 10 keV, which yields the X-ray luminosity density

$$l_{2-10\,\mathrm{keV}} \propto \rho^2 T^{1/2} \left[\exp\left(-\frac{2.32\times10^7}{T/\mathrm{K}}\right) - \exp\left(-\frac{1.16\times10^8}{T/\mathrm{K}}\right)\right]. \tag{8.4}$$

This luminosity is subsequently integrated over all cells along the line of sight, which yields a synthetic X-ray luminosity L_X. If a region in those maps is observed to emit markedly less X-radiation than the surrounding medium, it is identified as a bubble.

8.2 Technical set-up

Five FLASH simulations with Virgo initial conditions were done to acquire data. The cuboidal computational domain measures 400 kpc × 200 kpc × 200 kpc, with a Cartesian grid comprising 2 cubic top blocks of identical shape lined up in x-direction. The refinement level is varied between 3 and 6, corresponding to a resolution of 390 pc, and the grid is maximally refined within 1 kpc of domain centre. The domain boundary conditions allow for outflow of material.

opening half-angle	10°	10°	10°	10°	10°
density contrast	0.09	0.12	0.14	0.16	0.2
pressure contrast	4.6	3.1	1.8	1.2	1.0
Mach number (internal)	1.73	2.5	3.5	4.2	4.9
Mach number (external)	12.5	12.5	12.5	12.5	12.5

Table 8.1: Dimensionless jet parameters used in simulations.

The simulation uses a synthetic Virgo cluster based on empirical density and temperature profiles as outlined by equations 4.1 and 4.2. Best-fit parameter values are implemented for each profile. The gravitational field derived from the density and temperature profiles assuming hydrostatic equilibrium is active during the simulation. The centre of the cluster coincides with the centre of the computational domain and nozzle apertures (corresponding to coordinates (200 kpc, 100 kpc, 100 kpc)). The double nozzle apertures are centred on the domain centre, and embedded in the yz-plane. The aperture has a diameter equal to 6 cells, which corresponds to 2.3 kpc.

Each jet is defined by a combination of four parameters. The jet power $P_\mathrm{j} = 10^{38}$ W, the jet speed is $v_\mathrm{j} = 10^7\,\mathrm{m\,s^{-1}}$, and the opening half-angle $\theta = 10°$. The remaining parameter is the thermal power to total power ratio $P_\mathrm{therm}/P_\mathrm{j}$, that is 50%, 33%, 20%, 14%, and 11% for each of the simulations listed above respectively. Table 8.1 lists related dimensionless parameters.

The physical time covered by the simulation equals 80 Ma, covered with time steps ranging from a minimum of 1 a to a maximum of 100 ka. The jet is active between 0 and 10 Ma.

8.3 Results

In comparing heating of jets with different characteristics, it is paramount that all jets result in a comparable increment of total energy in the computational domain. Figure 8.1 reflects the evolution of the total amount of energy in the grid. Discrepancies between the graphs are minimal during the active phase. Given the jet power of 10^{38} W and the duration of the active phase 10 Ma, the energy that was scheduled to be injected approximates 3×10^{52} J, which is in accordance with the graphs in figure 8.1.

Beyond the physical time of 10 Ma there is some deviation between the graphs, concerning the jets with the highest internal Mach numbers. The open nature of the computational domain provides a natural explanation of this behaviour: matter is free to leave and enter the domain and work done by gravitational forces depends on the matter configuration, which differs slightly per simulation.

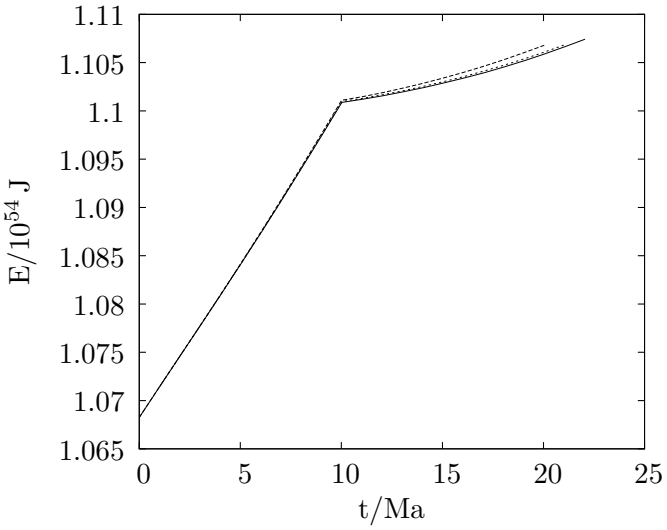

Figure 8.1: The total energy in the computational domain as a function of time for runs I to V of the simulation set-up. The five graphs coincide which is why the figure only shows one line. The amount of energy in the computational domain continues to rise after the AGN quiesces because of work done by the gravitational force on the intracluster gas. The visibly deviating graphs beyond 10 Ma concern the $\mathcal{M}_{\rm int} = 4.9$ (– –) and $\mathcal{M}_{\rm int} = 4.2$ (- -) jets.

The characteristic length of the bow shock is provided in figure 8.2 for all four runs as a function of time. The key provides the internal Mach number associated with to the indicated run. The graphs suggest there are two species of jets, with jets with internal Mach numbers of 4.2 and 4.9 belonging to one category, and those with 1.73, 2.5, 3.5.

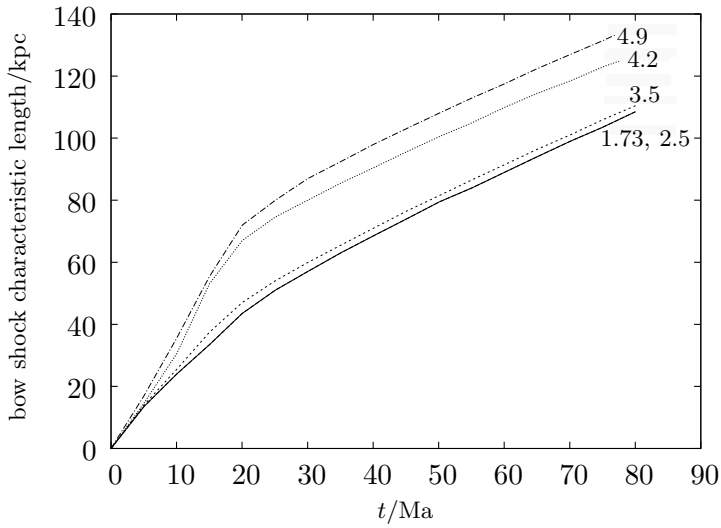

Figure 8.2: The characteristic length for the bow shock for all four runs as a function of time. The key indicates internal Mach number associated with each run.

8.3.1 The active jet

Profiles for density and pressure are displayed on the following five pages (figure 8.3 to 8.7) just prior to the quiescent phase at 10 Ma. Many basic components traditionally observed in jets are visible, such as a jet shock, cocoon, and bow shock. A difference is observed between the two jet categories defined from the characteristic bow shock length scale, which is the backflow flow pattern.

The jets with internal Mach numbers 4.2 and 4.9 seem to have the classical FR II jet structure, with a jet shock and hotspot near the bow shock, while the remaining jets are shocked and diverted prior to reaching the bow shock. Mach number profiles are provided in figure 8.8.

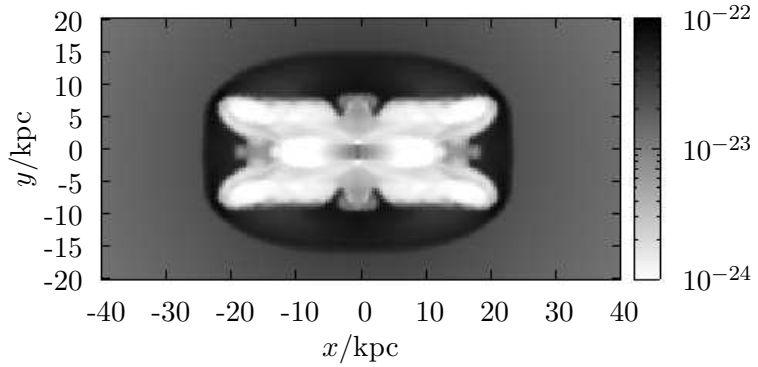

(a) Density.

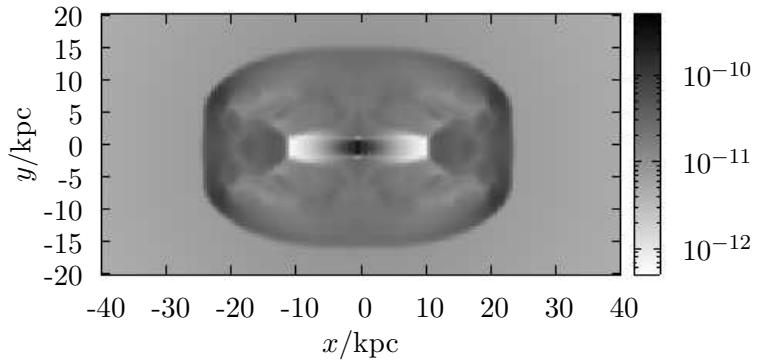

(b) Pressure.

Figure 8.3: Density (in $\mathrm{kg\,m^{-3}}$) and pressure (in Pa) profiles at $t = 10\,\mathrm{Ma}$ for the jet with an internal Mach number of 1.73.

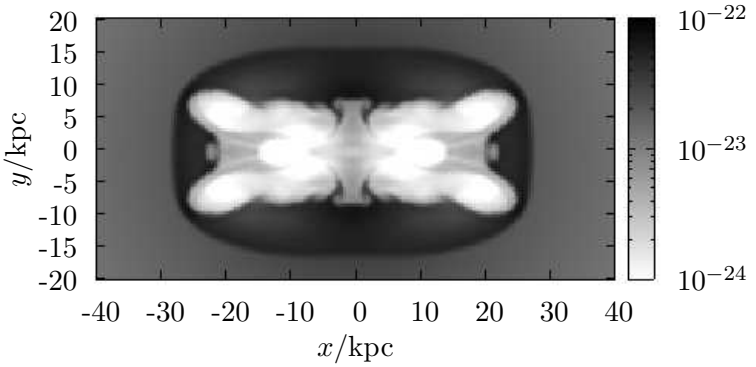

(a) Density.

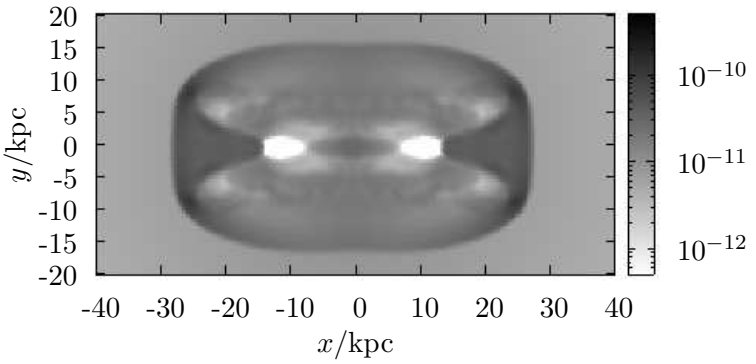

(b) Pressure.

Figure 8.4: Density (in $\mathrm{kg\,m^{-3}}$) and pressure (in Pa) profiles at $t = 10\,\mathrm{Ma}$ for the jet with an internal Mach number of 2.5.

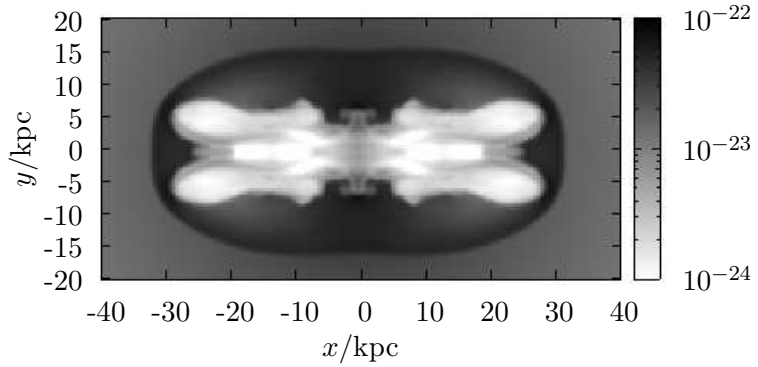

(a) Density.

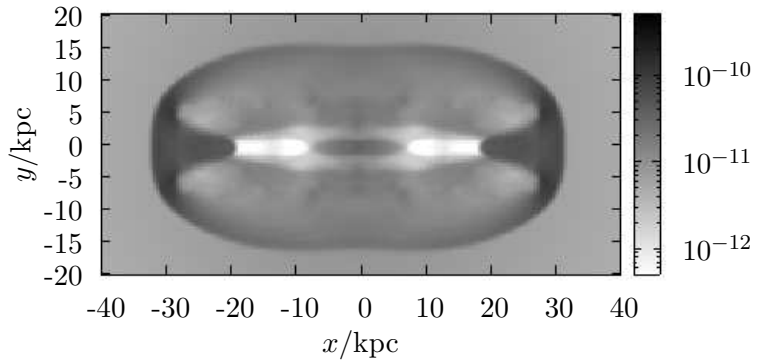

(b) Pressure.

Figure 8.5: Density (in $\mathrm{kg\,m^{-3}}$) and pressure (in Pa) profiles at $t = 10\,\mathrm{Ma}$ for the jet with an internal Mach number of 3.5.

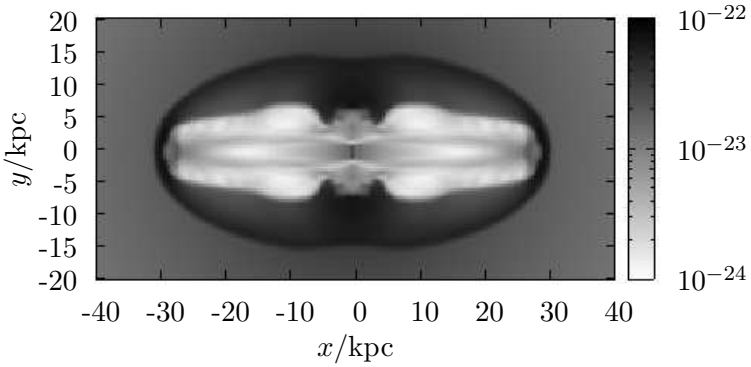

(a) Density.

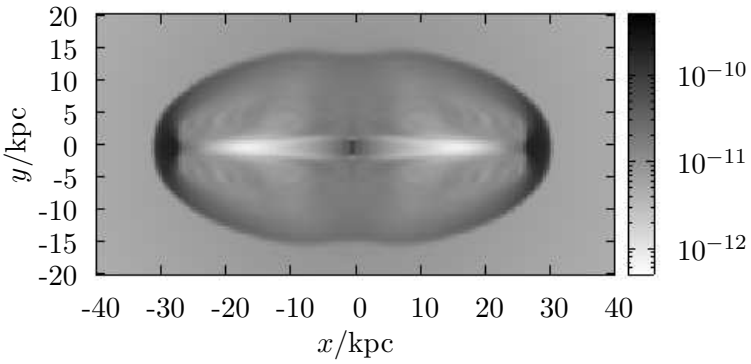

(b) Pressure.

Figure 8.6: Density (in $\mathrm{kg\,m^{-3}}$) and pressure (in Pa) profiles at $t = 10\,\mathrm{Ma}$ for the jet with an internal Mach number of 4.2.

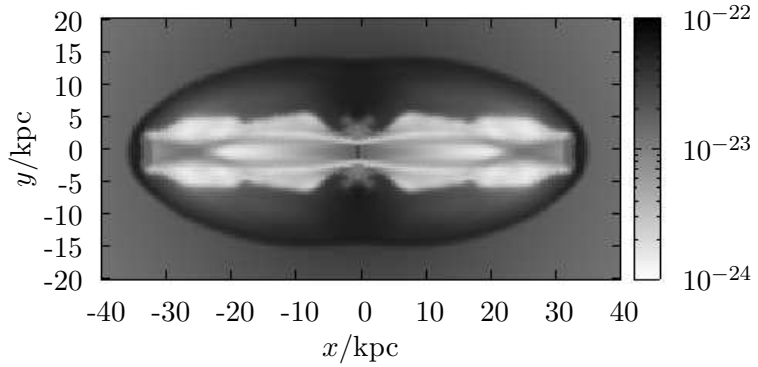

(a) Density.

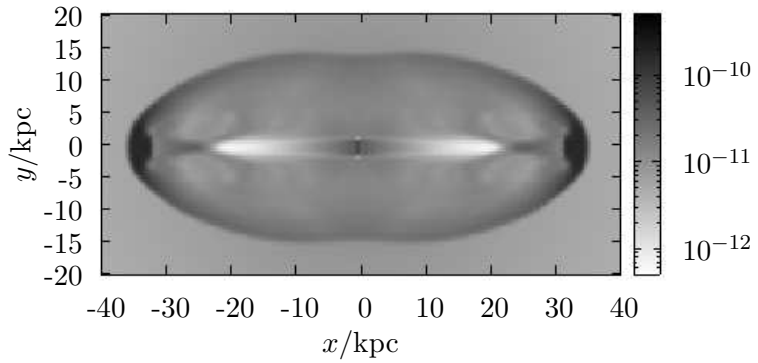

(b) Pressure.

Figure 8.7: Density (in $\mathrm{kg\,m^{-3}}$) and pressure (in Pa) profiles at $t = 10\,\mathrm{Ma}$ for the jet with an internal Mach number of 4.9.

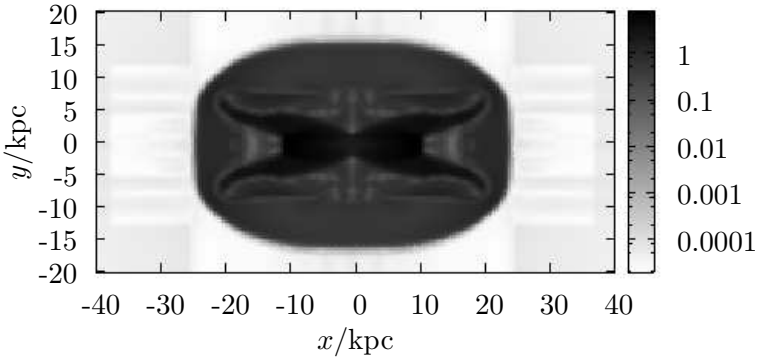

(a) $\mathcal{M}_{\rm int} = 1.73$.

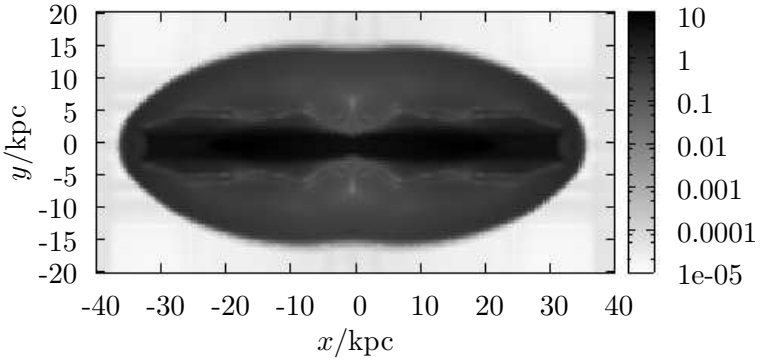

(b) $\mathcal{M}_{\rm int} = 4.9$.

Figure 8.8: Mach number profiles at $t = 10\,\mathrm{Ma}$ for the jets with an internal Mach number of 1.73 and 4.9.

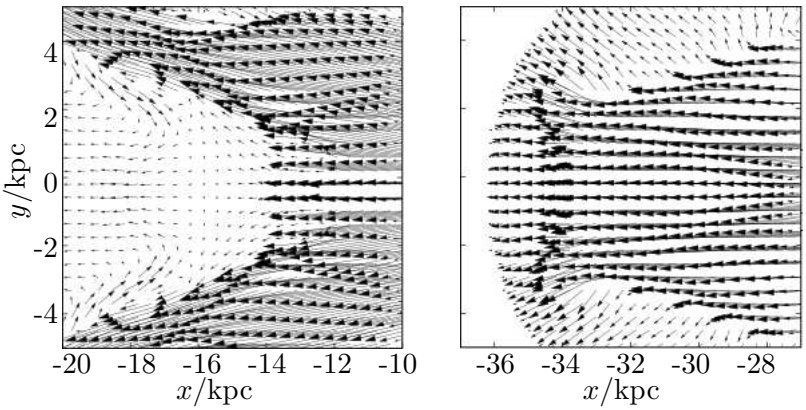

(a) $\mathcal{M}_{\text{int}} = 1.73$. (b) $\mathcal{M}_{\text{int}} = 4.9$.

Figure 8.9: Velocity profiles near the jet tip at $t = 10\,\text{Ma}$ for the jets with an internal Mach number of 1.73 and 4.9.

The flow pattern near the jet head is depicted in figure 8.9. There is a clear distinction between the backflow patterns. A straight and narrow backflow flowing tight along the jet is observed in the Mach 4.9 jet, though it is hard to identify it close to the jet head. In the second case the backflow bends in a wide curve near the jet shock that is placed further inward. A similar phenomenon was noticed by Mizuta, Kino and Nagakura (2010), who attributed a curved backflow to a slow jet head speed compared to the speed of sound at the hotspot. Figure 8.10 indicates for the Mach 1.73 jet a jet head speed of approximately $2\,\text{kpc}\,\text{Ma}^{-1}$, while the Mach 4.9 jet head moves faster at $4\,\text{kpc}\,\text{Ma}^{-1}$. Considering the sound speed ahead of the jet head an external Mach number of 0.7 and 1.8 respectively is inferred.

Shock discontinuity profiles using the shock detection algorithm of the two representative jets are provided in figure 8.11, indicating jets with a straight backflow become underpressured and collapse prior to reaching the jet shock. Between the jet and bow shock a pocket of underdense and overpressured, and therefore hot gas relatively to the ICM is caught, which presumably is the hotspot observed in FR II jets. Jets with a curved backflow do not collapse prior to reaching the jet shock, and have extensive reflected shock protrusions extending from the jet shock under an angle toward the bow shock. The bow shock is observed to have a more flattened shape due to the extended lateral structures.

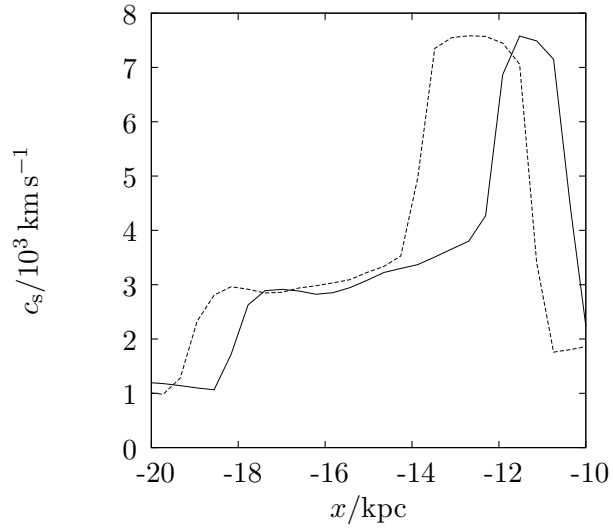

(a) $\mathcal{M}_{\mathrm{int}} = 1.73$.

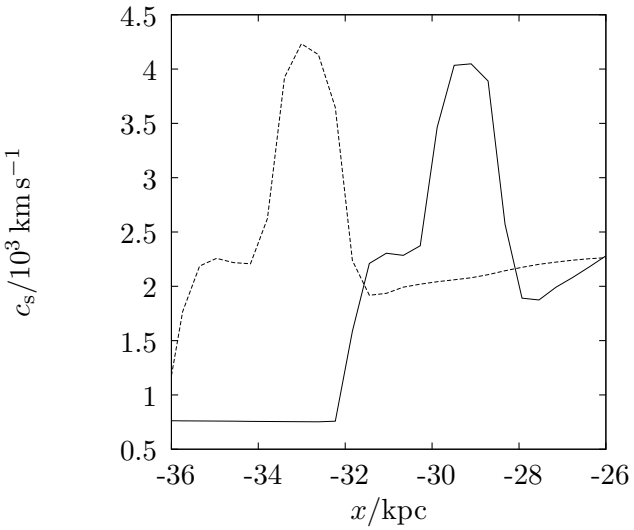

(b) $\mathcal{M}_{\mathrm{int}} = 4.9$.

Figure 8.10: Speed of sound profiles near the jet tip at $t = 9\,\mathrm{Ma}$ (solid line) and $10\,\mathrm{Ma}$ (dashed line) respectively for the jets with an internal Mach number of 1.73 and 4.9.

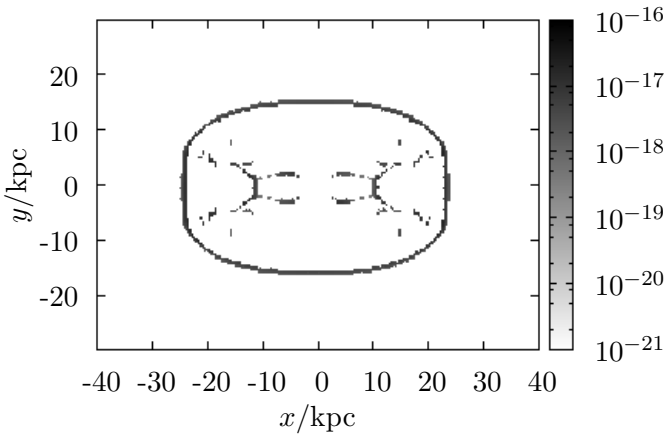

(a) $\mathcal{M}_{\rm int} = 1.73$.

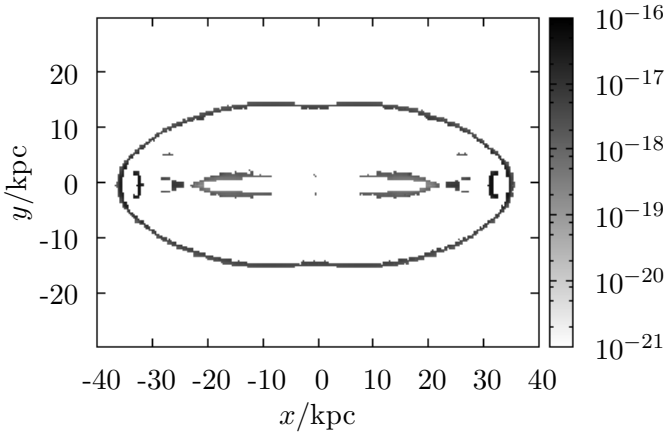

(b) $\mathcal{M}_{\rm int} = 4.9$.

Figure 8.11: Shock discontinuity profiles at $t = 10\,\mathrm{Ma}$ for the jets with an internal Mach number of 1.73 and 4.9.

8.3.2 Jet relics

At later time scales it has been observed that AGN jets tend to inflate regions of tenuous gas that emit very little X-ray radiation. These are observed as cavities in X-ray maps and are popularly called bubbles. They are assumed to be inflated during the last phase of jet evolution, and represent remnants of a cocoon. It is now investigated whether the different dynamics of the two established jet species influences bubble inflation.

Density and temperature profiles of the jet remnants 60 Ma after the jet was launched are provided in figures 8.12 and 8.13. The images provide evidence of extensive instability and shredding effects along the cocoon remnants of the Mach 4.9 jet, while the Mach 1.73 jet has managed to produced a much stabler construct.

The produced construct can be identified with an X-ray cavity by constructing synthetic X-ray maps, which has been done for both jets. These X-ray maps are shown in contour plots in figure 8.14, from which it is clear that whereas the cocoon remnant from the Mach 1.73 creates an observable cavity in the X-ray luminosity, the shredded cocoon of the Mach 4.9 jet is rather difficult to observe.

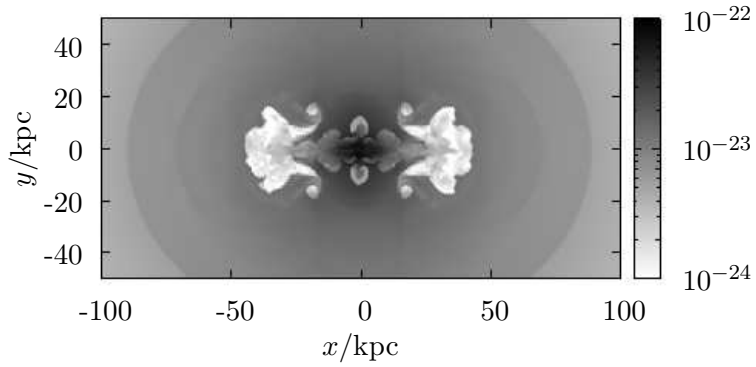

(a) Density profile.

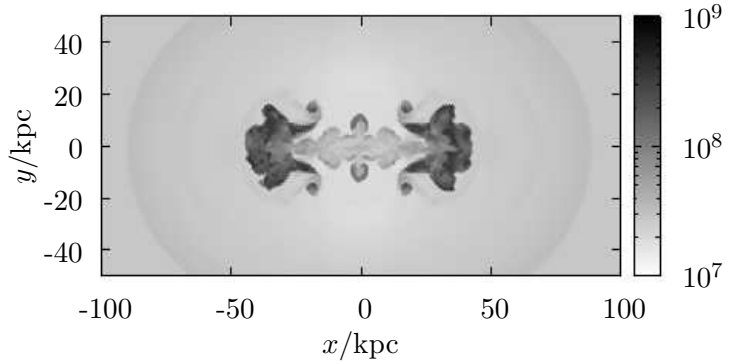

(b) Temperature profile.

Figure 8.12: Density and temperature profiles at $t = 60\,\mathrm{Ma}$ for the jets with an internal Mach number of 1.73.

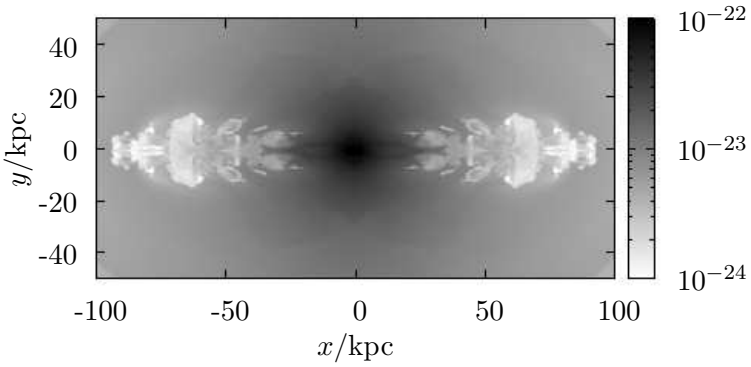

(a) Density profile.

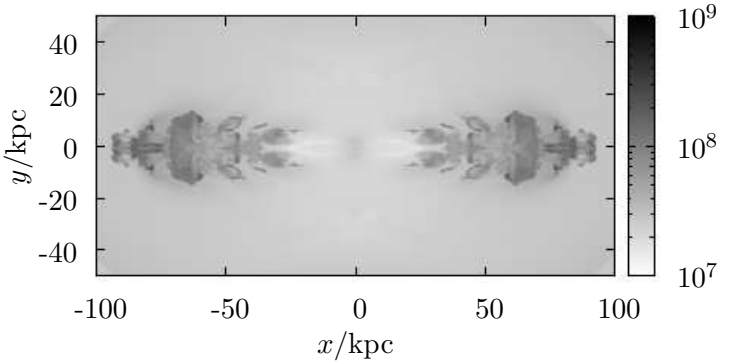

(b) Temperature profile.

Figure 8.13: Density and temperature profiles at $t = 60\,\mathrm{Ma}$ for the jets with an internal Mach number of 4.9.

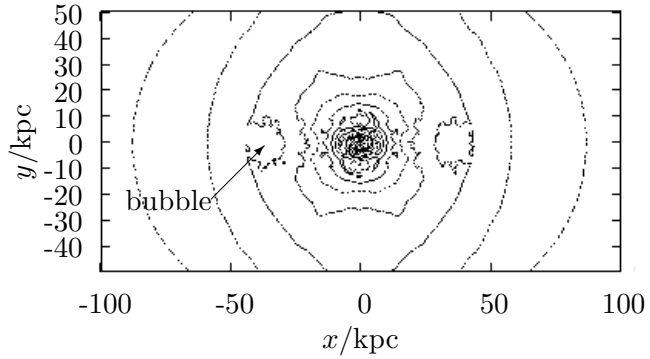

(a) $\mathcal{M}_{\rm int} = 1.73$.

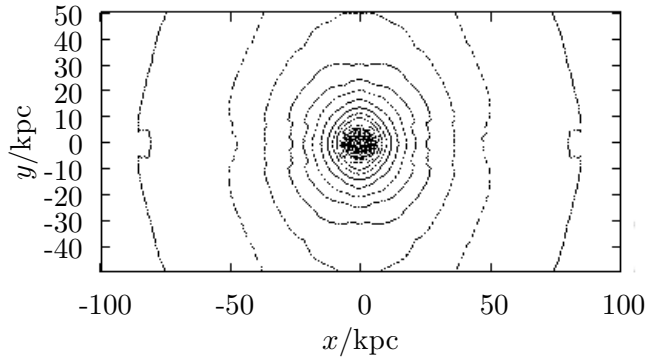

(b) $\mathcal{M}_{\rm int} = 4.9$.

Figure 8.14: X-ray maps at $t = 60\,$Ma in the 2-10 keV band. The image has been obtained by integrating over rows of zones in the line of sight (perpendicular to the jet axis).

8.3.3 Energy distribution

Figure 8.15 compares the evolution of the energy of all cells within 120 kpc of the AGN and at a half-opening angle of 45° with respect to the positive or negative x-axis. Or in other words, all cells which would be hit by a jet that emerged as a 90° opening angle jet along the x axis. Figure 8.15 gives the total amount of energy in this part of the grid at different times for three of the five runs. During a large part of the simulation jets with more thrust clearly deposit most of their energy in proximity of the x-axis, although as time progresses the difference is less relevant.

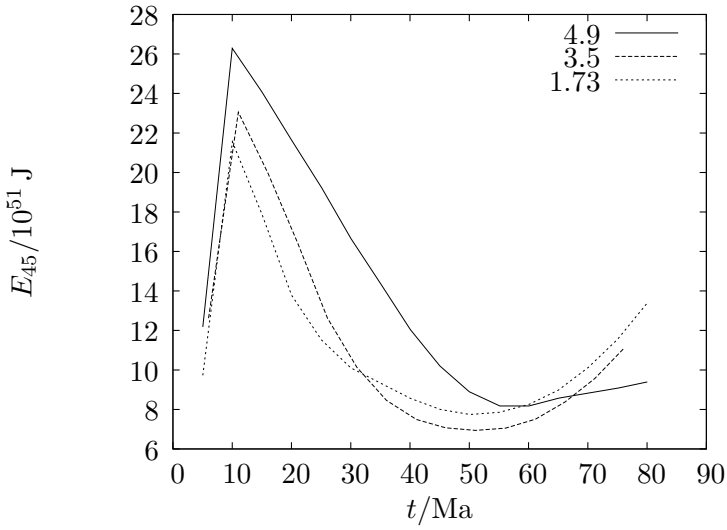

Figure 8.15: Energy in a section of the grid demarcated by a sphere with radius 120 kpc and a double cone directed in $\pm x$ directions with the AGN as apex and an opening angle of 90°. The key identifies associated run through the internal Mach number.

Using discussed shock finder routine the enthalpy in upstream cells is summed and plotted in figure 8.16. This is the total energy the shocks have available for heating. Across all shock fronts pre- and post-shock entropy values have also be constructed. The inferred enthalpy fraction released as heat is also provided.

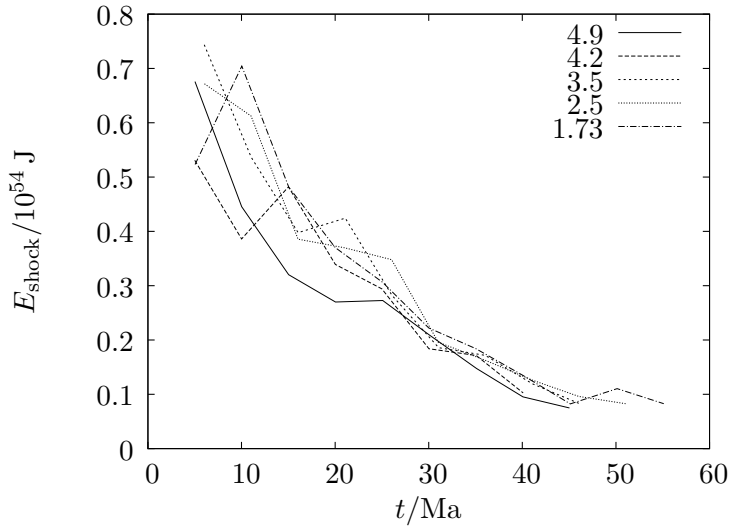

(a) Enthalpy of upstream gas.

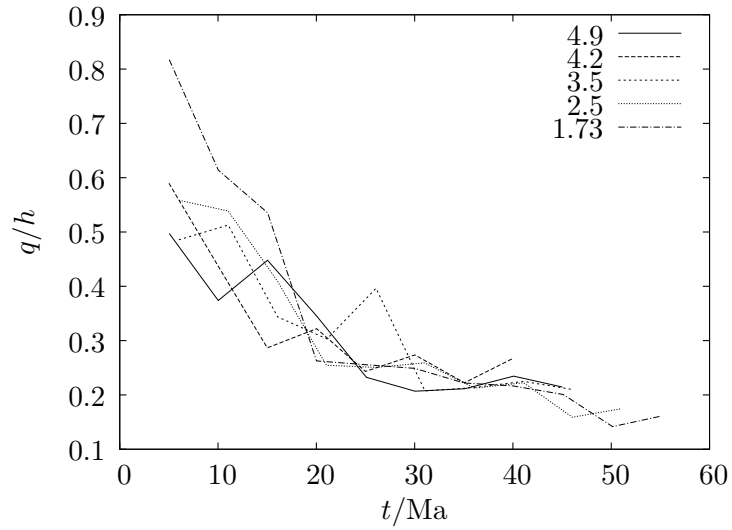

(b) Fraction of enthalpy released as heat.

Figure 8.16: Shock heating in the ICM is determined by the available enthalpy of the upstream gas and the efficiency of heat release. The key identifies associated run through the internal Mach number.

8.4 Discussion

Jets with similar power but a varying emphasis on thrust or thermal power yield a varied set of jet profiles. There appears to be a dichotomy, which is apparent based on the morphology of the backflow. For jets with an emphasis on thermal power, the jet head moves slow in comparison to the hotspot ahead of the jet shock. As a result a bow shock does not form ahead of the jet head. Instead, the backflow flanks the hotspots and moves ahead a significant distance until being diverted by shocked intracluster gas near the bow shock. This difference in morphological structure is observable only if the cocoon or bow shock is observable. During the late phase of jet evolution there are observable differences, as jets with a curved backflow form observable bubbles while the cocoon remnants of straight backflows are shredded prior to forming such structures.

Considering the energy output of the AGN, shock heating has been discussed as a potential heating mechanism. From spectral evidence, the cooling luminosity is inferred to be 10^{35} W for the region about M87 (Bîrzan et al., 2004).[1] Assuming the duty cycle of the jet is 0.1, the jet is required to compensate for 100 Ma of radiative cooling. For steady cooling this amounts to an energy loss of 10^{50} J. Comparing this number to figure 8.16 a conclusion that shock heating may be a viable mechanism is plausible. No significant difference in shock heating is observed between the jets. As only one category of jets inflates bubbles, and this heating mechanism has been discussed extensively, estimates of the bubble heat content are not made here.

It is concluded that a trade-off of jet heating power and thrust regulates the speed of the jet head. A dichotomy is the result of the jet head moving subsonically with respectively to the jet head when the jet head moves too slow. It is observed that jets with a curved backflow are more effective in inflating bubbles than jets with straight backflows, which has direct observable ramifications. There is no significant difference when the heating power of the bow shock is concerned between the jets. All bow shocks are inferred to be able to quench the cooling flow if heat is generated at the implied rate.

[1] See paragraph 5.6 for a discussion on the derivation of the cooling luminosity.

Chapter 9

Conclusion

In this project AGN outflows were modelled as outflows of gas obeying the laws of classical fluid mechanics. The observed system was designed to fit models based on observationally-obtained data to make the simulation as comparable to observations as possible.

The first part of the project comprised extending the FLASH code such that it would be able to inject a conical bipolar outflow through a back-to-back nozzle in the centre of the computational domain. This by itself required thorough understanding the underlying algorithms pertaining to the FLASH code, which is why the algorithms have been described in considerable detail.

Three projects were done with the AGN outflow unit, each discussing the effects of a single parameter on the heating capability of the AGN outflow. The least complicated of the three involved varying the opening angle of the conical outflows, which in theory would increase the coverage of the AGN outflow as the jet distributes its energy more sideways. It was observed that for more unstable jets such a parameter has little influence, as turbulent effects quickly negate any pre-set opening angle effects.

The second project discussed wave heating. It was based on the thought that if widening the outflow opening angle does not result in a more efficient distribution of heat, than heat might be transported by sound or internal gravity from the more energetic to the rapidly cooling regions. Waves were observed at later phases in accordance with other simulations.

Comparing density, pressure, and entropy profiles, these waves were identified as compressible waves. Attempts to Fourier analyse the waves and obtain frequencies were unsuccessful, as the wave patterns proved too irregular.

In the third project the jet's thermal power was regulated in compromise of jet thrust. It was found that jets with more thermal power have a slower moving jet head, which results in a curved backflow protruding ahead and sideways of the jet shock. As the bow shock envelops the entire system, the jet shock is found to be moved closer to the AGN compared and farther from the bow shock. Jets with a straight backflow have a classical FR II morphology with a compact hotspot. In longer time-scales it was found jets with a curved backflow are more likely to inflate observable X-ray cavities than their straight backflow counterparts, for which the cocoon remnants are completely shredded.

In the third project we tried to establish a link between the enthalpy and kinetic energy content of the jet on one side and the heating process of the intracluster medium on the other. Five runs were done, each with identical energy output but a differing enthalpy to total energy ratio. It was found that jets with proportionally more enthalpy have a strikingly different morphology then jets which have more kinetic energy. Bubbles were exclusively found in jets with more enthalpy, while the shock patterns of jets with more kinetic energy suggests they form hot spots. Though jets with more kinetic energy initially deposit their energy mostly in close proximity of the axis of injection, this effect becomes far less pronounced as time progresses and by the end of the period of quiescence (i.e. near the end of the runs) roles are reversed. Shock heating efficiency was also discussed, but the difference between the obtained figures was marginal. In other words there is no conclusive evidence that a varying jet enthalpy (under condition of a non-changing jet energy output) leads to more or less efficiently heating shock waves.

In the end it is expected that new measurement techniques and equipment and better computational facilities will lead to improved models and more accurate predictions. If progress continues, and specialists cooperate, then the future for computational research involving AGN outflows and the cluster cooling flow conundrum is definitely promising.

Appendix A

Notation conventions

The International System of Units (SI) and most associated notation conventions are employed throughout this thesis (Göbel, E. and Mills, I. M. and Wallard, A. J. 2006).

Vector quantities are identified by a right-pointing arrow (e.g. $\vec{x}$) above associated symbol. By definition the magnitude of a vector quantity $\vec{x}$ is denoted $x \equiv ||\vec{x}||$. Second or higher order tensors are marked by a double-pointing arrow (e.g. $\overleftrightarrow{x}$), while fluid state vectors are printed in bold face.

The dyadic product of a pair of vectors $\vec{u}$ and $\vec{v}$ in vector space $\mathbb{R}^3$ is defined

$$\vec{u}\,\vec{v} \equiv \vec{u} \otimes \vec{v}^{\mathsf{T}} = \begin{bmatrix} u_x\vec{v}^{\mathsf{T}} \\ u_y\vec{v}^{\mathsf{T}} \\ u_z\vec{v}^{\mathsf{T}} \end{bmatrix} = \begin{bmatrix} u_x v_x & u_x v_y & u_x v_z \\ u_y v_x & u_y v_y & u_y v_z \\ u_z v_x & u_z v_y & u_z v_z \end{bmatrix}, \tag{A.1}$$

where $\otimes$ denotes the Kronecker product.

A.1 Quantity symbols

Six of seven SI base units are used either explicitly or implicitly.

Base quantity	*Symbol*	*SI unit*	*Dimension*
Length	d, l, r	m	L
Mass	m	kg	M
Time	t	s	T
Electric current	I	A	I
Thermodynamic temperature	T	K	Θ

Continued on next page

Base quantity	*Symbol*	*SI unit*	*Dimension*
Amount of substance	n	mol	N

Derived quantity	*Symbol*	*SI unit*	*Dimension*
Adiabatic index	γ	1	1
Area	A	m^2	L^2
Canonical partition function	$\mathcal{Z}$	1	1
Cooling function	Λ	$\mathrm{W\,m^3}$	$\mathsf{L}^5\ \mathsf{M}\ \mathsf{T}^{-3}$
Current density	J	$\mathrm{A\,m^{-2}}$	$\mathsf{L}^{-2}\ \mathsf{I}^{-1}$
Dynamic viscosity	η	$\mathrm{Pa\,s}$	$\mathsf{L}^{-1}\ \mathsf{M}\ \mathsf{T}^{-1}$
Electrical conductivity	σ	$\mathrm{S\,m^{-1}}$	$\mathsf{L}^{-3}\ \mathsf{M}^{-1}\ \mathsf{T}^{3}\ \mathsf{I}^{2}$
Electric field	E	$\mathrm{V\,m^{-1}}$	$\mathsf{L}\ \mathsf{M}\ \mathsf{T}^{-3}\ \mathsf{I}^{-1}$
Emissivity	j	$\mathrm{W\,m^{-3}\,Hz^{-1}\,sr^{-1}}$	$\mathsf{L}^{-1}\ \mathsf{M}\ \mathsf{T}^{-2}$
Energy	E	J	$\mathsf{L}^2\ \mathsf{M}\ \mathsf{T}^{-2}$
Force divided by mass	f	$\mathrm{N\,kg^{-1}}$	$\mathsf{L}\ \mathsf{M}\ \mathsf{T}^{-2}$
Frequency	ν	Hz	T^{-1}
Gravitational acceleration	g	$\mathrm{m\,s^{-2}}$	$\mathsf{L}\ \mathsf{T}^{-2}$
Gravitational potential	Φ	$\mathrm{m^2\,s^{-2}}$	$\mathsf{L}^2\ \mathsf{T}^{-2}$
Heat divided by mass	q	$\mathrm{J\,kg^{-1}}$	$\mathsf{L}^2\ \mathsf{T}^{-2}$
Ion charge	Z	1	1
Kinematic viscosity	ν	$\mathrm{m^2\,s^{-1}}$	$\mathsf{L}^2\ \mathsf{T}^{-1}$
Lorentz factor	γ	1	1
Luminosity	L	W	$\mathsf{L}^2\ \mathsf{M}\ \mathsf{T}^{-3}$
Mach angle	μ	rad	1
Mach number	$\mathcal{M}$	1	1
Magnetic field	B	T	$\mathsf{M}\ \mathsf{T}^{-2}\ \mathsf{I}^{-1}$
(Mass) density	ρ	$\mathrm{kg\,m^{-3}}$	$\mathsf{L}^{-3}\ \mathsf{M}$
Mean free path	λ_{mfp}	m	L
Molar mass	μ	$\mathrm{kg\,mol^{-1}}$	$\mathsf{M}\ \mathsf{N}^{-1}$
Monochromatic flux	F_ν	$\mathrm{W\,m^{-2}\,Hz^{-1}}$	$\mathsf{M}\ \mathsf{T}^{-2}$
Number density	n	$\mathrm{m^{-3}}$	L^{-3}
Péclet number	Pe	1	1
Plane angle	θ, ψ, β	rad	1
Poynting vector	S	$\mathrm{W\,m^{-2}}$	$\mathsf{M}\ \mathsf{T}^{-3}$

Derived quantity	*Symbol*	*SI unit*	*Dimension*
Prandtl number	Pr	1	$\mathsf{1}$
Prandtl-Meyer function	ν	rad	$\mathsf{1}$
Pressure	p	Pa	$\mathsf{L}^{-1}\ \mathsf{M}\ \mathsf{T}^{-2}$
Reynolds number	Re	1	$\mathsf{1}$
Solid angle	Ω	sr	$\mathsf{1}$
Specific enthalpy	h	$\mathrm{J\,kg^{-1}}$	$\mathsf{L}^2\ \mathsf{T}^{-2}$
Specific entropy	s	$\mathrm{J\,K^{-1}\,kg^{-1}}$	$\mathsf{L}^2\ \mathsf{T}^{-2}\ \Theta^{-1}$
Specific energy	e	$\mathrm{J\,kg^{-1}}$	$\mathsf{L}^2\ \mathsf{T}^{-2}$
Specific heat capacity	c	$\mathrm{J\,kg^{-1}\,K^{-1}}$	$\mathsf{L}^2\ \mathsf{T}^{-2}\ \Theta^{-1}$
Specific Helmholtz free energy	a	$\mathrm{J\,kg^{-1}}$	$\mathsf{L}^2\ \mathsf{T}^{-2}$
Spectral radiant intensity	I_ν	$\mathrm{W\,Hz^{-1}\,sr^{-1}}$	$\mathsf{L}^2\ \mathsf{M}\ \mathsf{T}^{-2}$
Speed of sound	c_s	$\mathrm{m\,s^{-1}}$	$\mathsf{L}\ \mathsf{T}^{-1}$
Stress tensor	σ	Pa	$\mathsf{L}^{-1}\ \mathsf{M}\ \mathsf{T}^{-2}$
Surface brightness	S	$\mathrm{W\,m^{-2}}$	$\mathsf{M}\ \mathsf{T}^{-3}$
Thermal conductivity	κ	$\mathrm{W\,m^{-1}\,K^{-1}}$	$\mathsf{L}\ \mathsf{M}\ \mathsf{T}^{-3}\Theta^{-1}$
Velocity	v	$\mathrm{m\,s^{-1}}$	$\mathsf{L}\ \mathsf{T}^{-1}$
Velocity potential	ϕ	$\mathrm{m^2\,s^{-1}}$	$\mathsf{L}^2\ \mathsf{T}^{-1}$
Volume	V	$\mathrm{m^3}$	L^3
Wavelength	λ	m	L

A.2 Physical constants

Physical constant	*Symbol*	*Value*
Alpha particle mass	m_α	$6.644\,656\,20 \times 10^{-27}\,\mathrm{kg}$
Avogadro constant	N_A	$6.022\,141\,79 \times 10^{23}\,\mathrm{mol^{-1}}$
Boltzmann constant	k_B	$1.380\,650\,4 \times 10^{-23}\,\mathrm{J\,K^{-1}}$
Electric constant	ϵ_0	$8.854\,187\,817 \times 10^{-12}\,\mathrm{F\,m^{-1}}$
Electron mass	m_e	$9.109\,382\,15 \times 10^{-31}\,\mathrm{kg}$
Elementary charge	e	$1.602\,176\,5 \times 10^{-19}\,\mathrm{C}$
Fine structure constant	α	$7.297\,352\,537\,6 \times 10^{-3}$
Hubble constant	H_0	$73\,\mathrm{km\,s^{-1}\,Mpc^{-1}}$
Hubble time	t_H	$13\,\mathrm{Ga}$

Physical constant	*Symbol*	*Value*
Magnetic constant	μ_0	$1.256\,637\,061\,4 \times 10^{-6}\,\mathrm{N\,A^{-2}}$
Molar gas constant	R	$8.314\,472\,\mathrm{J\,mol^{-1}\,K^{-1}}$
Newtonian constant of gravitation	G	$6.674\,28 \times 10^{-11}\,\mathrm{m^3\,kg^{-1}\,s^{-2}}$
Planck constant	h	$6.626\,068\,96 \times 10^{-34}\,\mathrm{J\,s}$
Proton mass	m_p	$1.672\,621\,637 \times 10^{-27}\,\mathrm{kg}$
Speed of light in vacuum	c	$2.997\,924\,58 \times 10^{8}\,\mathrm{m\,s^{-1}}$

A.3 Units used outside the SI

Non-SI unit	*Symbol*	*Value in SI units*	*Dimension*
degree (angle)	°	$\pi/180$ rad	1
electronvolt	eV	$1.602\,176\,5 \times 10^{-19}\,\mathrm{J}$	$\mathsf{L}^2\ \mathsf{M}\ \mathsf{T}^{-2}$
minute (angle)	′	$\pi/10\,800$ rad	1
parsec	pc	$3.085\,678 \times 10^{16}\,\mathrm{m}$	L
solar luminosity	$\mathrm{L}_\odot$	$3.839 \times 10^{26}\,\mathrm{W}$	$\mathsf{L}^2\ \mathsf{M}\ \mathsf{T}^{-3}$
solar mass	$\mathrm{M}_\odot$	$1.9891 \times 10^{30}\,\mathrm{kg}$	M
year	a	$3.1536 \times 10^{7}\,\mathrm{s}$	T

Bibliography

Abell, G. O. (1958). 'The Distribution of Rich Clusters of Galaxies.' In: *Astrophysical Journal, Supplement* 3 (May 1958), pp. 211–+. DOI: 10.1086/190036.

Alexander, P. (2000). 'Evolutionary models for radio sources from compact sources to classical doubles'. In: *Monthly Notices of the RAS* 319 (Nov. 2000), pp. 8–16. DOI: 10.1046/j.1365-8711.2000.03711.x.

Allen, S. W. et al. (2006). 'The relation between accretion rate and jet power in X-ray luminous elliptical galaxies'. In: *Monthly Notices of the RAS* 372 (Oct. 2006), pp. 21–30. DOI: 10.1111/j.1365-2966.2006.10778.x. eprint: arXiv:astro-ph/0602549.

Ambartsumian, V. A. (1971). 'Introduction'. In: *Study Week on Nuclei of Galaxies*. Ed. by D. J. K. O'Connell, pp. 9–+.

Antonucci, R. (1993). 'Unified models for active galactic nuclei and quasars'. In: *Annual Review of Astronomy and Astrophysics* 31, pp. 473–521. DOI: 10.1146/annurev.aa.31.090193.002353.

Arfken, G. B. and H. J. Weber (1995). *Mathematical methods for physicists*. Ed. by Arfken, G. B. & Weber, H. J.

Ascasibar, Y. and M. Markevitch (2006). 'The Origin of Cold Fronts in the Cores of Relaxed Galaxy Clusters'. In: *Astrophysical Journal* 650 (Oct. 2006), pp. 102–127. DOI: 10.1086/506508. eprint: arXiv:astro-ph/0603246.

Baade, W. (1956). 'Polarization in the Jet of Messier 87.' In: *Astrophysical Journal* 123 (May 1956), pp. 550–551. DOI: 10.1086/146194.

Baade, W. and R. Minkowski (1954). 'Identification of the Radio Sources in Cassiopeia, Cygnus A, and Puppis A.' In: *Astrophysical Journal* 119 (Jan. 1954), pp. 206–+. DOI: 10.1086/145812.

Balbus, S. A. and C. S. Reynolds (2008). 'Regulation of Thermal Conductivity in Hot Galaxy Clusters by MHD Turbulence'. In: *Astrophysical Journal, Letters* 681 (July 2008), pp. L65–L68. DOI: 10.1086/590554. eprint: 0806.0940.

Basson, J. F. and P. Alexander (2003). 'The long-term effect of radio sources on the intracluster medium'. In: *Monthly Notices of the RAS* 339 (Feb. 2003), pp. 353–359. DOI: 10.1046/j.1365-8711.2003.06069.x. eprint: arXiv:astro-ph/0207668.

Bauer, F. E. et al. (2005). 'The prevalence of cooling cores in clusters of galaxies at z∼ 0.15-0.4'. In: *Monthly Notices of the RAS* 359 (June 2005), pp. 1481–1490. DOI: 10.1111/j.1365-2966.2005.08999.x. eprint: arXiv:astro-ph/0503232.

Beckwith, S. V. W. and A. I. Sargent (1993). 'The occurrence and properties of disks around young stars'. In: *Protostars and Planets III*. Ed. by E. H. Levy & J. I. Lunine, pp. 521–541.

Begelman, M. C. (2001). 'Impact of Active Galactic Nuclei on the Surrounding Medium'. In: *Gas and Galaxy Evolution*. Vol. 240. Astronomical Society of the Pacific Conference Series. eprint: arXiv:astro-ph/0207656.

Begelman, M. C. and D. F. Cioffi (1989). 'Overpressured cocoons in extragalactic radio sources'. In: *Astrophysical Journal, Letters* 345 (Oct. 1989), pp. L21–L24. DOI: 10.1086/185542.

Best, P. N. et al. (2007). 'On the prevalence of radio-loud active galactic nuclei in brightest cluster galaxies: implications for AGN heating of cooling flows'. In: *Monthly Notices of the RAS* 379 (Aug. 2007), pp. 894–908. DOI: 10.1111/j.1365-2966.2007.11937.x. eprint: arXiv:astro-ph/0611197.

Bicknell, G. V. (1984). 'A model for the surface brightness of a turbulent low Mach number jet. I - Theoretical development and application to 3C 31'. In: *Astrophysical Journal* 286 (Nov. 1984), pp. 68–87. DOI: 10.1086/162577.

— (1986*a*). 'A model for the surface brightness of a turbulent, low Mach number jet. II - The global energy budget and radiative losses'. In: *Astrophysical Journal* 300 (Jan. 1986), pp. 591–604. DOI: 10.1086/163836.

— (1986*b*). 'A model for the surface brightness of a turbulent low Mach number jet. III - Adiabatic jets of arbitrary density ratio: Application to NGC 315'. In: *Astrophysical Journal* 305 (June 1986), pp. 109–130. DOI: 10.1086/164232.

— (1994). 'On the relationship between BL Lacertae objects and Fanaroff-Riley I radio galaxies'. In: *Astrophysical Journal* 422 (Feb. 1994), pp. 542–561. DOI: 10.1086/173748. eprint: arXiv:astro-ph/9308033.

— (1995). 'Relativistic Jets and the Fanaroff-Riley Classification of Radio Galaxies'. In: *Astrophysical Journal, Supplement* 101 (Nov. 1995), pp. 29–+. DOI: 10.1086/192232. eprint: arXiv:astro-ph/9406064.

Binggeli, B. (1999). 'The Virgo Cluster - Home of M 87'. In: *The Radio Galaxy Messier 87*. Ed. by H.-J. Röser & K. Meisenheimer. Vol. 530. Lecture Notes in Physics, Berlin Springer Verlag, pp. 9–+. DOI: 10.1007/BFb0106414.

Binggeli, B., J. Huchra and P. Murdin (2000). 'Virgo Cluster'. In: *Encyclopedia of Astronomy and Astrophysics*. Ed. by Murdin, P. DOI: 10.1888/0333750888/1822.

Binggeli, B., A. Sandage and G. A. Tammann (1985). 'Studies of the Virgo Cluster. II - A catalog of 2096 galaxies in the Virgo Cluster area.' In: *Astronomical Journal* 90 (Sept. 1985), pp. 1681–1759. DOI: 10.1086/113874.

Binggeli, B., G. A. Tammann and A. Sandage (1987). 'Studies of the Virgo cluster. VI - Morphological and kinematical structure of the Virgo cluster'. In: *Astronomical Journal* 94 (Aug. 1987), pp. 251–277. DOI: 10.1086/114467.

Binney, J., F. Alouani Bibi and H. Omma (2007). 'Bubbles as tracers of heat input to cooling flows'. In: *Monthly Notices of the RAS* 377 (May 2007), pp. 142–146. DOI: 10.1111/j.1365-2966.2007.11575.x. eprint: arXiv:astro-ph/0701891.

Biretta, J. A., W. B. Sparks and F. Macchetto (1999). 'Hubble Space Telescope Observations of Superluminal Motion in the M87 Jet'. In: *Astrophysical Journal* 520 (Aug. 1999), pp. 621–626. DOI: 10.1086/307499.

Bîrzan, L. et al. (2004). 'A Systematic Study of Radio-induced X-Ray Cavities in Clusters, Groups, and Galaxies'. In: *Astrophysical Journal* 607 (June 2004), pp. 800–809. DOI: 10.1086/383519. eprint: arXiv:astro-ph/0402348.

Blandford, R. D. (1976). 'Accretion disc electrodynamics - A model for double radio sources'. In: *Monthly Notices of the RAS* 176 (Sept. 1976), pp. 465–481.

Blandford, R. D. and A. Königl (1979). 'Relativistic jets as compact radio sources'. In: *Astrophysical Journal* 232 (Aug. 1979), pp. 34–48. DOI: 10.1086/157262.

Blandford, R. D. and D. G. Payne (1982). 'Hydromagnetic flows from accretion discs and the production of radio jets'. In: *Monthly Notices of the RAS* 199 (June 1982), pp. 883–903.

Blandford, R. D. and M. J. Rees (1974). 'A 'twin-exhaust' model for double radio sources'. In: *Monthly Notices of the RAS* 169 (Dec. 1974), pp. 395–415.

Blandford, R. D. and R. L. Znajek (1977). 'Electromagnetic extraction of energy from Kerr black holes'. In: *Monthly Notices of the RAS* 179 (May 1977), pp. 433–456.

Blanton, E. L. et al. (2001). 'Chandra Observation of the Radio Source/X-Ray Gas Interaction in the Cooling Flow Cluster Abell 2052'. In: *Astrophysical Journal, Letters* 558 (Sept. 2001), pp. L15–L18. DOI: 10.1086/323269. eprint: arXiv:astro-ph/0107221.

Bodo, G. et al. (1994). 'Kelvin-Helmholtz instability of hydrodynamic supersonic jets'. In: *Astronomy and Astrophysics* 283 (Mar. 1994), pp. 655–676.

Bodo, G. et al. (1998). 'Three-dimensional simulations of jets'. In: *Astronomy and Astrophysics* 333 (May 1998), pp. 1117–1129.

Böhringer, H. et al. (1993). 'A ROSAT HRI study of the interaction of the X-ray-emitting gas and radio lobes of NGC 1275'. In: *Monthly Notices of the RAS* 264 (Oct. 1993), pp. L25–L28.

Böhringer, H. et al. (1994). 'The structure of the Virgo cluster of galaxies from Rosat X-ray images'. In: *Nature* 368 (Apr. 1994), pp. 828–831. DOI: 10.1038/368828a0.

Böhringer, H. et al. (2002). 'The new emerging model for the structure of cooling cores in clusters of galaxies'. In: *Astronomy and Astrophysics* 382 (Feb. 2002), pp. 804–820. DOI: 10.1051/0004-6361:20011708. eprint: arXiv:astro-ph/0111112.

Böhringer, H. et al. (2004). 'Implications of the central metal abundance peak in cooling core clusters of galaxies'. In: *Astronomy and Astrophysics* 416 (Mar. 2004), pp. L21–L25. DOI: 10.1051/0004-6361:20040047. eprint: arXiv:astro-ph/0402216.

Bolton, J. G. (1948). 'Discrete Sources of Galactic Radio Frequency Noise'. In: *Nature* 162 (July 1948), pp. 141–142. DOI: 10.1038/162141a0.

Braine, J. et al. (1995). 'CO(1-0) observations of the cooling flow galaxy NGC 1275 with the IRAM interferometer.' In: *Astronomy and Astrophysics* 293 (Jan. 1995), pp. 315–331.

Bridle, A. H. and R. A. Perley (1984). 'Extragalactic Radio Jets'. In: *Annual Review of Astronomy and Astrophysics* 22, pp. 319–358. DOI: 10.1146/annurev.aa.22.090184.001535.

Bridle, A. H. et al. (1994). 'Deep VLA imaging of twelve extended 3CR quasars'. In: *Astronomical Journal* 108 (Sept. 1994), pp. 766–820. DOI: 10.1086/117112.

Brighenti, F. and W. G. Mathews (2006). 'Stopping Cooling Flows with Jets'. In: *Astrophysical Journal* 643 (May 2006), pp. 120–127. DOI: 10.1086/502645. eprint: arXiv:astro-ph/0601555.

Brouillette, M. (2002). 'The richtmyer-meshkov instability'. In: *Annual Review of Fluid Mechanics* 34, pp. 445–468. DOI: 10.1146/annurev.fluid.34.090101.162238.

Brüggen, M. (2003). 'Simulations of Buoyant Bubbles in Galaxy Clusters'. In: *Astrophysical Journal* 592 (Aug. 2003), pp. 839–845. DOI: 10.1086/375731. eprint: arXiv:astro-ph/0301352.

Brüggen, M. and C. R. Kaiser (2001). 'Buoyant radio plasma in clusters of galaxies'. In: *Monthly Notices of the RAS* 325 (Aug. 2001), pp. 676–684. DOI: 10.1046/j.1365-8711.2001.04494.x. eprint: arXiv:astro-ph/0010023.

— (2002). 'Hot bubbles from active galactic nuclei as a heat source in cooling-flow clusters'. In: *Nature* 418 (July 2002), pp. 301–303. eprint: arXiv:astro-ph/0207354.

Brüggen, M., M. Ruszkowski and E. Hallman (2005). 'Active Galactic Nuclei Heating and Dissipative Processes in Galaxy Clusters'. In: *Astrophysical Journal* 630 (Sept. 2005), pp. 740–749. DOI: 10.1086/432112. eprint: arXiv:astro-ph/0501175.

Brüggen, M. et al. (2002). 'Simulation of radio plasma in clusters of galaxies'. In: *Monthly Notices of the RAS* 331 (Apr. 2002), pp. 545–555. DOI: 10.1046/j.1365-8711.2002.05233.x. eprint: arXiv:astro-ph/0108486.

Brüggen, M. et al. (2007). 'Shock heating by Fanaroff-Riley type I radio sources in galaxy clusters'. In: *Monthly Notices of the RAS* 380 (Sept. 2007), pp. L67–L70. DOI: 10.1111/j.1745-3933.2007.00351.x. eprint: 0706.1869.

Burbidge, G. R. (1956). 'On Synchrotron Radiation from Messier 87.' In: *Astrophysical Journal* 124 (Sept. 1956), pp. 416–+. DOI: 10.1086/146237.

— (1959). 'Estimates of the Total Energy in Particles and Magnetic Field in the Non-Thermal Radio Sources.' In: *Astrophysical Journal* 129 (May 1959), pp. 849–+. DOI: 10.1086/146680.

Burns, J. O. (1990). 'The radio properties of cD galaxies in Abell clusters. I - an X-ray selected sample'. In: *Astronomical Journal* 99 (Jan. 1990), pp. 14–30. DOI: 10.1086/115307.

Burns, J. O., E. D. Feigelson and E. J. Schreier (1983). 'The inner radio structure of Centaurus A - Clues to the origin of the jet X-ray emission'. In: *Astrophysical Journal* 273 (Oct. 1983), pp. 128–153. DOI: 10.1086/161353.

Byram, E. T., T. A. Chubb and H. Friedman (1966). 'Cosmic X-ray Sources, Galactic and Extragalactic'. In: *Science* 152 (Apr. 1966), pp. 66–71. DOI: 10.1126/science.152.3718.66.

Carilli, C. et al. (1996). 'The jets in Cygnus A: from pc- to kpc-scales'. In: *Cygnus A – Studay of a Radio Galaxy*. Ed. by Carilli, C. L. & Harris, D. E., pp. 76–+.

Carroll, B. W. and D. A. Ostlie (1996). *An Introduction to Modern Astrophysics*. Ed. by Carroll, B. W. & Ostlie, D. A.

Cattaneo, A. and R. Teyssier (2007). 'AGN self-regulation in cooling flow clusters'. In: *Monthly Notices of the RAS* 376 (Apr. 2007), pp. 1547–1556. DOI: 10.1111/j.1365-2966.2007.11512.x. eprint: arXiv:astro-ph/0611914.

Celotti, A. and A. C. Fabian (1993). 'The Kinetic Power and Luminosity of Parsecscale Radio Jets - an Argument for Heavy Jets'. In: *Monthly Notices of the RAS* 264 (Sept. 1993), pp. 228–+.

Churazov, E. et al. (2000). 'Asymmetric, arc minute scale structures around NGC 1275'. In: *Astronomy and Astrophysics* 356 (Apr. 2000), pp. 788–794. eprint: arXiv:astro-ph/0002375.

Churazov, E. et al. (2001). 'Evolution of Buoyant Bubbles in M87'. In: *Astrophysical Journal* 554 (June 2001), pp. 261–273. DOI: 10.1086/321357. eprint: arXiv:astro-ph/0008215.

Churazov, E. et al. (2003). 'XMM-Newton Observations of the Perseus Cluster. I. The Temperature and Surface Brightness Structure'. In: *Astrophysical Journal* 590 (June 2003), pp. 225–237. DOI: 10.1086/374923. eprint: arXiv:astro-ph/0301482.

Churazov, E. et al. (2004). 'XMM-Newton observations of the Perseus cluster - II. Evidence for gas motions in the core'. In: *Monthly Notices of the RAS* 347 (Jan. 2004), pp. 29–35. DOI: 10.1111/j.1365-2966.2004.07201.x. eprint: arXiv:astro-ph/0309427.

Clarke, D. A. and J. O. Burns (1991). 'Numerical simulations of a restarting jet'. In: *Astrophysical Journal* 369 (Mar. 1991), pp. 308–313. DOI: 10.1086/169762.

Clarke, D. A., M. L. Norman and J. O. Burns (1986). 'Numerical simulations of a magnetically confined jet'. In: *Astrophysical Journal, Letters* 311 (Dec. 1986), pp. L63–L67. DOI: 10.1086/184799.

Clarke, T. E. (2004). 'Faraday Rotation Observations of Magnetic Fields in Galaxy Clusters'. In: *Journal of Korean Astronomical Society* 37 (Dec. 2004), pp. 337–342. eprint: arXiv:astro-ph/0412268.

Clarke, T. E., P. P. Kronberg and H. Böhringer (2001). 'A New Radio-X-Ray Probe of Galaxy Cluster Magnetic Fields'. In: *Astrophysical Journal, Letters* 547 (Feb. 2001), pp. L111–L114. DOI: 10.1086/318896. eprint: arXiv:astro-ph/0011281.

Cohen, M. H. et al. (1971). 'The Small-Scale Structure of Radio Galaxies and Quasi-Stellar Sources at 3.8 Centimeters'. In: *Astrophysical Journal* 170 (Dec. 1971), pp. 207–+. DOI: 10.1086/151204.

Colella, P. and P. R. Woodward (1984). 'The Piecewise Parabolic Method (PPM) for Gas-Dynamical Simulations'. In: *Journal of Computational Physics* 54 (Sept. 1984), pp. 174–201. DOI: 10.1016/0021-9991(84)90143-8.

Cowie, L. L. and J. Binney (1977). 'Radiative regulation of gas flow within clusters of galaxies - A model for cluster X-ray sources'. In: *Astrophysical Journal* 215 (Aug. 1977), pp. 723–732. DOI: 10.1086/155406.

Cowie, L. L. et al. (1983). 'Two-dimensional spectrophotometry of the cores of X-ray luminous clusters'. In: *Astrophysical Journal* 272 (Sept. 1983), pp. 29–47. DOI: 10.1086/161259.

Cox, C. I., S. F. Gull and P. A. G. Scheuer (1991). 'Three-dimensional simulations of the jets of extragalactic radio sources'. In: *Monthly Notices of the RAS* 252 (Oct. 1991), pp. 558–585.

Croston, J. H., R. P. Kraft and M. J. Hardcastle (2007). 'Shock Heating in the Nearby Radio Galaxy NGC 3801'. In: *Astrophysical Journal* 660 (May 2007), pp. 191–199. DOI: 10.1086/513500. eprint: arXiv:astro-ph/0702094.

Curtis, H. D. (1918). 'The planetary nebulae.' In: *Publications of Lick Observatory* 13, pp. 55–74.

De Grandi, S. et al. (2004). 'On the iron content in rich nearby clusters of galaxies'. In: *Astronomy and Astrophysics* 419 (May 2004), pp. 7–18. DOI: 10.1051/0004-6361:20034228. eprint: arXiv:astro-ph/0310828.

De Lucia, G. and J. Blaizot (2007). 'The hierarchical formation of the brightest cluster galaxies'. In: *Monthly Notices of the RAS* 375 (Feb. 2007), pp. 2–14. DOI: 10.1111/j.1365-2966.2006.11287.x. eprint: arXiv:astro-ph/0606519.

De Young, D. S. (2003). 'Relic radio 'bubbles' and cluster cooling flows'. In: *Monthly Notices of the RAS* 343 (Aug. 2003), pp. 719–724. DOI: 10.1046/j.1365-8711.2003.06719.x. eprint: arXiv:astro-ph/0305167.

Domainko, W. et al. (2004). 'Feedback from intra-cluster supernovae on the ICM in cooling flow galaxy clusters'. In: *Astronomy and Astrophysics* 425 (Oct. 2004), pp. L21–L24. DOI: 10.1051/0004-6361:20040178. eprint: arXiv:astro-ph/0405493.

Dong, R., J. Rasmussen and J. S. Mulchaey (2010). 'A Systematic Search for X-ray Cavities in the Hot Gas of Galaxy Groups'. In: *Astrophysical Journal* 712 (Apr. 2010), pp. 883–900. DOI: 10.1088/0004-637X/712/2/883. eprint: 1002.2218.

Dubois, Y. et al. (2010). 'Jet-regulated cooling catastrophe'. In: *Monthly Notices of the RAS* 409 (Dec. 2010), pp. 985–1001. DOI: 10.1111/j.1365-2966.2010.17338.x. eprint: 1004.1851.

Dunn, R. J. H., A. C. Fabian and A. Celotti (2006). 'Using radio bubbles to constrain the matter content of AGN jets'. In: *Monthly Notices of the RAS* 372 (Nov. 2006), pp. 1741–1748. DOI: 10.1111/j.1365-2966.2006.10986.x. eprint: arXiv:astro-ph/0608466.

Dwarakanath, K. S., J. H. van Gorkom and F. N. Owen (1994). 'A VLA search for neutral hydrogen in cooling flow clusters'. In: *Astrophysical Journal* 432 (Sept. 1994), pp. 469–477. DOI: 10.1086/174586.

Edge, A. C. (1991). 'On the relation between the X-ray properties of clusters of galaxies and their brightest cluster member'. In: *Monthly Notices of the RAS* 250 (May 1991), pp. 103–110.

Edge, A. C. and G. C. Stewart (1991). 'EXOSAT observations of clusters of galaxies. I - The X-ray data. II - X-ray to optical correlations'. In: *Monthly Notices of the RAS* 252 (Oct. 1991), pp. 414–441.

Edge, A. C., G. C. Stewart and A. C. Fabian (1992). 'Properties of cooling flows in a flux-limited sample of clusters of galaxies'. In: *Monthly Notices of the RAS* 258 (Sept. 1992), pp. 177–188.

El-Zant, A. A., W.-T. Kim and M. Kamionkowski (2004). 'Dynamical-friction galaxy-gas coupling and cluster cooling flows'. In: *Monthly Notices of the RAS* 354 (Oct. 2004), pp. 169–175. DOI: 10.1111/j.1365-2966.2004.08175.x. eprint: arXiv:astro-ph/0403696.

Enßlin, T., C. Vogt and C. Pfrommer (2005). 'Magnetic Fields in Clusters of Galaxies'. In: *The Magnetized Plasma in Galaxy Evolution*. Ed. by K. T. Chyzy, K. Otmianowska-Mazur, M. Soida, & R.-J. Dettmar, pp. 231–238. eprint: arXiv:astro-ph/0501338.

Fabian, A. C. (2003). 'A gravitational contribution to the cooling flow problem'. In: *Monthly Notices of the RAS* 344 (Sept. 2003), pp. L27–L30. DOI: 10.1046/j.1365-8711.2003.07000.x.

Fabian, A. C. and P. E. J. Nulsen (1977). 'Subsonic accretion of cooling gas in clusters of galaxies'. In: *Monthly Notices of the RAS* 180 (Aug. 1977), pp. 479–484.

Fabian, A. C., P. E. J. Nulsen and C. R. Canizares (1982). 'Star formation in a cooling flow'. In: *Monthly Notices of the RAS* 201 (Dec. 1982), pp. 933–938.

— (1984). 'Cooling flows in clusters of galaxies'. In: *Nature* 310 (Aug. 1984), pp. 733–740. DOI: 10.1038/310733a0.

Fabian, A. C., L. M. Voigt and R. G. Morris (2002). 'On conduction, cooling flows and galaxy formation'. In: *Monthly Notices of the RAS* 335 (Sept. 2002), pp. L71–L74. DOI: 10.1046/j.1365-8711.2002.05884.x. eprint: arXiv:astro-ph/0206437.

Fabian, A. C. et al. (2002). 'The missing soft X-ray luminosity in cluster cooling flows'. In: *Monthly Notices of the RAS* 332 (May 2002), pp. L50–L54. DOI: 10.1046/j.1365-8711.2002.05510.x.

Fabian, A. C. et al. (2003*a*). 'A deep Chandra observation of the Perseus cluster: shocks and ripples'. In: *Monthly Notices of the RAS* 344 (Sept. 2003), pp. L43–L47. DOI: 10.1046/j.1365-8711.2003.06902.x. eprint: arXiv:astro-ph/0306036.

Fabian, A. C. et al. (2003*b*). 'The relationship between the optical Hα filaments and the X-ray emission in the core of the Perseus cluster'. In: *Monthly Notices of the RAS* 344 (Sept. 2003), pp. L48–L52. DOI: 10.1046/j.1365-8711.2003.06856.x. eprint: arXiv:astro-ph/0306039.

Fabian, A. C. et al. (2005). 'On viscosity, conduction and sound waves in the intracluster medium'. In: *Monthly Notices of the RAS* 363 (Nov. 2005), pp. 891–896. DOI: 10.1111/j.1365-2966.2005.09484.x. eprint: arXiv:astro-ph/0501222.

Fabian, A. C. et al. (2006). 'A very deep Chandra observation of the Perseus cluster: shocks, ripples and conduction'. In: *Monthly Notices of the RAS* 366 (Feb. 2006), pp. 417–428. DOI: 10.1111/j.1365-2966.2005.09896.x. eprint: arXiv:astro-ph/0510476.

Fanaroff, B. L. and J. M. Riley (1974). 'The morphology of extragalactic radio sources of high and low luminosity'. In: *Monthly Notices of the RAS* 167 (May 1974), 31P–36P.

Fath, E. A. (1909). 'The spectra of some spiral nebulae and globular star clusters'. In: *Lick Observatory Bulletin* 5, pp. 71–77.

Field, G. B. (1965). 'Thermal Instability.' In: *Astrophysical Journal* 142 (Aug. 1965), pp. 531–+. DOI: 10.1086/148317.

Finoguenov, A., L. P. David and T. J. Ponman (2000). 'An ASCA Study of the Heavy-Element Distribution in Clusters of Galaxies'. In: *Astrophysical Journal* 544 (Nov. 2000), pp. 188–203. DOI: 10.1086/317173. eprint: arXiv:astro-ph/9908150.

Finoguenov, A. and T. J. Ponman (1999). 'Constraining the role of Type IA and Type II supernovae in galaxy groups by spatially resolved analysis of ROSAT and ASCA

observations'. In: *Monthly Notices of the RAS* 305 (Apr. 1999), pp. 325–337. DOI: 10.1046/j.1365-8711.1999.02403.x. eprint: arXiv:astro-ph/9901100.

Fitch, W. S., A. G. Pacholczyk and R. J. Weymann (1967). 'Light Variations of the Seyfert Galaxy NGC 4151'. In: *Astrophysical Journal, Letters* 150 (Nov. 1967), pp. L67+. DOI: 10.1086/180095.

Forman, W. et al. (2005). 'Reflections of Active Galactic Nucleus Outbursts in the Gaseous Atmosphere of M87'. In: *Astrophysical Journal* 635 (Dec. 2005), pp. 894–906. DOI: 10.1086/429746. eprint: arXiv:astro-ph/0312576.

Friedman, H., S. W. Lichtman and E. T. Byram (1951). 'Photon Counter Measurements of Solar X-Rays and Extreme Ultraviolet Light'. In: *Physical Review* 83 (Sept. 1951), pp. 1025–1030. DOI: 10.1103/PhysRev.83.1025.

Fryxell, B. et al. (2000). 'FLASH: An Adaptive Mesh Hydrodynamics Code for Modeling Astrophysical Thermonuclear Flashes'. In: *Astrophysical Journal, Supplement* 131 (Nov. 2000), pp. 273–334. DOI: 10.1086/317361.

Fujita, Y., T. K. Suzuki and K. Wada (2005). 'Tsunamis in Galaxy Clusters: Heating of Cool Cores by Acoustic Waves'. In: *X-Ray and Radio Connections*. Ed. by L. O. Sjouwerman & K. K. Dyer.

Fujita, Y. et al. (2002). 'Chandra Observations of the Disruption of the Cool Core in A133'. In: *Astrophysical Journal* 575 (Aug. 2002), pp. 764–778. DOI: 10.1086/341352. eprint: arXiv:astro-ph/0204188.

Gardini, A. (2007). 'Buoyant bubbles in a cooling intracluster medium. I. Hydrodynamic bubbles'. In: *Astronomy and Astrophysics* 464 (Mar. 2007), pp. 143–154. DOI: 10.1051/0004-6361:20066427. eprint: arXiv:astro-ph/0611444.

Gaspari, M. et al. (2011). 'The dance of heating and cooling in galaxy clusters: three-dimensional simulations of self-regulated active galactic nuclei outflows'. In: *Monthly Notices of the RAS* 411 (Feb. 2011), pp. 349–372. DOI: 10.1111/j.1365-2966.2010.17688.x. eprint: 1007.0674.

Ghizzardi, S., M. Rossetti and S. Molendi (2010). 'Cold fronts in galaxy clusters'. In: *Astronomy and Astrophysics* 516 (June 2010), A32+. DOI: 10.1051/0004-6361/200912496. eprint: 1003.1051.

Ghizzardi, S. et al. (2004). 'Radiative Cooling and Heating and Thermal Conduction in M87'. In: *Astrophysical Journal* 609 (July 2004), pp. 638–651. DOI: 10.1086/421314. eprint: arXiv:astro-ph/0404060.

Giacconi, R. et al. (1962). 'Evidence for x Rays From Sources Outside the Solar System'. In: *Physical Review Letters* 9 (Dec. 1962), pp. 439–443. DOI: 10.1103/PhysRevLett.9.439.

Göbel, E. and Mills, I. M. and Wallard, A. J. (2006). *Le Système international d'unités / The International System of Units*.

Graham, J., A. C. Fabian and J. S. Sanders (2008). 'Detecting sound-wave-like surface brightness ripples in cluster cores'. In: *Monthly Notices of the RAS* 391 (Dec. 2008), pp. 1749–1757. DOI: 10.1111/j.1365-2966.2008.13861.x. eprint: 0808.2408.

Gropp, W., E. Lusk and R. Thakur (1999). *Using MPI-2: Advanced Features of the Message-Passing Interface*. MIT Press. ISBN: 0-262-57133-1.

Gull, S. F. and K. J. E. Northover (1973). 'Bubble Model of Extragalactic Radio Sources'. In: *Nature* 244 (July 1973), pp. 80–83. DOI: 10.1038/244080a0.

— (1975). 'Hot gas in clusters of galaxies'. In: *Monthly Notices of the RAS* 173 (Dec. 1975), pp. 585–603.

Gunn, J. E. and J. R. Gott III (1972). 'On the Infall of Matter Into Clusters of Galaxies and Some Effects on Their Evolution'. In: *Astrophysical Journal* 176 (Aug. 1972), pp. 1–+. DOI: 10.1086/151605.

Hanbury Brown, R., R. C. Jennison and M. K. D. Gupta (1952). 'Apparent Angular Sizes of Discrete Radio Sources: Observations at Jodrell Bank, Manchester'. In: *Nature* 170 (Dec. 1952), pp. 1061–1063. DOI: 10.1038/1701061a0.

Heinz, S. and E. Churazov (2005). 'Heating the Bubbly Gas of Galaxy Clusters with Weak Shocks and Sound Waves'. In: *Astrophysical Journal, Letters* 634 (Dec. 2005), pp. L141–L144. DOI: 10.1086/498301. eprint: arXiv:astro-ph/0507038.

Heinz, S. et al. (2006). 'The answer is blowing in the wind: simulating the interaction of jets with dynamic cluster atmospheres'. In: *Monthly Notices of the RAS* 373 (Nov. 2006), pp. L65–L69. DOI: 10.1111/j.1745-3933.2006.00243.x. eprint: arXiv:astro-ph/0606664.

Hey, J. S., S. J. Parsons and J. W. Phillips (1946). 'Fluctuations in Cosmic Radiation at Radio-Frequencies'. In: *Nature* 158 (Aug. 1946), pp. 234–+. DOI: 10.1038/158234a0.

Jansky, K. G. (1933). 'Radio Waves from Outside the Solar System'. In: *Nature* 132 (July 1933), pp. 66–+. DOI: 10.1038/132066a0.

Jennison, R. C. and M. K. Das Gupta (1953). 'Fine Structure of the Extra-terrestrial Radio Source Cygnus I'. In: *Nature* 172 (Nov. 1953), pp. 996–997. DOI: 10.1038/172996a0.

Johnstone, R. M., A. C. Fabian and P. E. J. Nulsen (1987). 'The optical spectra of central galaxies in southern clusters Evidence for star formation'. In: *Monthly Notices of the RAS* 224 (Jan. 1987), pp. 75–91.

Jones, C. and W. Forman (1984). 'The structure of clusters of galaxies observed with Einstein'. In: *Astrophysical Journal* 276 (Jan. 1984), pp. 38–55. DOI: 10.1086/161591.

Junor, W., J. A. Biretta and M. Livio (1999). 'Formation of the radio jet in M87 at 100 Schwarzschild radii from the central black hole'. In: *Nature* 401 (Oct. 1999), pp. 891–892. DOI: 10.1038/44780.

Kaastra, J. S. et al. (2001). 'XMM-Newton observations of the cluster of galaxies Sérsic 159-03'. In: *Astronomy and Astrophysics* 365 (Jan. 2001), pp. L99–L103. DOI: 10.1051/0004-6361:20000041. eprint: arXiv:astro-ph/0010423.

Kaiser, C. R. and P. Alexander (1997). 'A Self-Similar Model for Extragalactic Jets and the FRI/FRII Divide'. In: *IAU Colloq. 163: Accretion Phenomena and Related Outflows*. Ed. by D. T. Wickramasinghe, G. V. Bicknell, & L. Ferrario. Vol. 121. Astronomical Society of the Pacific Conference Series, pp. 732–+.

— (1999). 'Heating of the intergalactic medium by FR II radio sources'. In: *Monthly Notices of the RAS* 305 (May 1999), pp. 707–723. DOI: 10.1046/j.1365-8711.1999.02498.x. eprint: arXiv:astro-ph/9902018.

Kaiser, C. R. et al. (2005). 'The stability of buoyant bubbles in the atmospheres of galaxy clusters'. In: *Monthly Notices of the RAS* 359 (May 2005), pp. 493–503. DOI: 10.1111/j.1365-2966.2005.08902.x. eprint: arXiv:astro-ph/0502162.

Kellogg, E. et al. (1973). 'Clusters of Galaxies with a Wide Range of X-Ray Luminosities'. In: *Astrophysical Journal, Letters* 185 (Oct. 1973), pp. L13+. DOI: 10.1086/181311.

Khachikian, E. Y. and D. W. Weedman (1974). 'An atlas of Seyfert galaxies'. In: *Astrophysical Journal* 192 (Sept. 1974), pp. 581–589. DOI: 10.1086/153093.

Kim, K.-T., P. C. Tribble and P. P. Kronberg (1991). 'Detection of excess rotation measure due to intracluster magnetic fields in clusters of galaxies'. In: *Astrophysical Journal* 379 (Sept. 1991), pp. 80–88. DOI: 10.1086/170484.

Kim, W.-T., A. A. El-Zant and M. Kamionkowski (2005). 'Dynamical Friction and Cooling Flows in Galaxy Clusters'. In: *Astrophysical Journal* 632 (Oct. 2005), pp. 157–168. DOI: 10.1086/432976. eprint: arXiv:astro-ph/0506579.

Kraft, R. P. et al. (2003). 'X-Ray Emission from the Hot Interstellar Medium and Southwest Radio Lobe of the Nearby Radio Galaxy Centaurus A'. In: *Astrophysical Journal* 592 (July 2003), pp. 129–146. DOI: 10.1086/375533. eprint: arXiv:astro-ph/0304363.

Kravtsov, A. V. and G. Yepes (2000). 'On the supernova heating of the intergalactic medium'. In: *Monthly Notices of the RAS* 318 (Oct. 2000), pp. 227–238. DOI: 10.1046/j.1365-8711.2000.03771.x. eprint: arXiv:astro-ph/0004333.

Lamb, H. (1908). ': On the theory of waves propagated vertically in the atmosphere'. In: *Proceedings of the London Mathematical Society* 7, pp. 122–141.

— (1945). *Hydrodynamics*. Ed. by Lamb, H.

Landau, L. D. and E. M. Lifshitz (1980). *Statistical physics. Pt.1, Pt.2*. Ed. by Landau, L. D. & Lifshitz, E. M.

— (1987). *Fluid mechanics*. Second. Butterworth Heinemann. ISBN: 9780750627672.

LeVeque, R. J. (2002). *Finite volume methods for hyperbolic problems*. Cambridge University Press.

Lin, Y.-T. and J. J. Mohr (2004). 'K-band Properties of Galaxy Clusters and Groups: Brightest Cluster Galaxies and Intracluster Light'. In: *Astrophysical Journal* 617 (Dec. 2004), pp. 879–895. DOI: 10.1086/425412. eprint: arXiv:astro-ph/0408557.

Lind, K. R. et al. (1989). 'Numerical simulations of magnetized jets'. In: *Astrophysical Journal* 344 (Sept. 1989), pp. 89–103. DOI: 10.1086/167779.

Lohner, R. (1987). 'An adaptive finite element scheme for transient problems in CFD'. In: *Computer Methods in Applied Mechanics and Engineering* 61 (Apr. 1987), pp. 323–338. DOI: 10.1016/0045-7825(87)90098-3.

Lonsdale, C. J. and P. D. Barthel (1986). 'Double hotspots and flow redirection in the lobes of powerful extragalactic radio sources'. In: *Astronomical Journal* 92 (July 1986), pp. 12–22. DOI: 10.1086/114130.

Lovelace, R. V. E. (1976). 'Dynamo model of double radio sources'. In: *Nature* 262 (Aug. 1976), pp. 649–652. DOI: 10.1038/262649a0.

Lynden-Bell, D. (1969). 'Galactic Nuclei as Collapsed Old Quasars'. In: *Nature* 223 (Aug. 1969), pp. 690–694. DOI: 10.1038/223690a0.

Lyutikov, M. (2006). 'Magnetic draping of merging cores and radio bubbles in clusters of galaxies'. In: *Monthly Notices of the RAS* 373 (Nov. 2006), pp. 73–78. DOI: 10.1111/j.1365-2966.2006.10835.x. eprint: arXiv:astro-ph/0604178.

MacNeice, P. et al. (2000). 'PARAMESH: A parallel adaptive mesh refinement community toolkit'. In: *Computer Physics Communications* 126 (Apr. 2000), pp. 330–354. DOI: 10.1016/S0010-4655(99)00501-9.

Malagoli, A., R. Rosner and G. Bodo (1987). 'On the thermal instability of galactic and cluster halos'. In: *Astrophysical Journal* 319 (Aug. 1987), pp. 632–636. DOI: 10.1086/165483.

Markevitch, M. et al. (2000). 'Chandra Observation of Abell 2142: Survival of Dense Subcluster Cores in a Merger'. In: *Astrophysical Journal* 541 (Oct. 2000), pp. 542–549. DOI: 10.1086/309470. eprint: arXiv:astro-ph/0001269.

Markevitch, M. et al. (2002). 'A Textbook Example of a Bow Shock in the Merging Galaxy Cluster 1E 0657-56'. In: *Astrophysical Journal, Letters* 567 (Mar. 2002), pp. L27–L31. DOI: 10.1086/339619. eprint: arXiv:astro-ph/0110468.

Martel, A. R. et al. (1999). 'Hubble Space Telescope Snapshot Survey of 3CR Radio Source Counterparts. III. Radio Galaxies with z<0.1'. In: *Astrophysical Journal, Supplement* 122 (May 1999), pp. 81–108. DOI: 10.1086/313205.

Mathews, W. G. and J. N. Bregman (1978). 'Radiative accretion flow onto giant galaxies in clusters'. In: *Astrophysical Journal* 224 (Sept. 1978), pp. 308–319. DOI: 10.1086/156379.

Mathews, W. G. et al. (2003). 'Circulation Flows: Cooling Flows with Bubble Return'. In: *Astrophysical Journal* 596 (Oct. 2003), pp. 159–169. DOI: 10.1086/377596. eprint: arXiv:astro-ph/0306535.

Matsushita, K. et al. (2002). 'XMM-Newton observation of M 87. I. Single-phase temperature structure of intracluster medium'. In: *Astronomy and Astrophysics* 386 (Apr. 2002), pp. 77–96. DOI: 10.1051/0004-6361:20020087. eprint: arXiv:astro-ph/0201242.

Matthews, T. A. and A. R. Sandage (1963). 'Optical Identification of 3c 48, 3c 196, and 3c 286 with Stellar Objects.' In: *Astrophysical Journal* 138 (July 1963), pp. 30–+. DOI: 10.1086/147615.

McNamara, B. R. and R. W. O'Connell (1992). 'Color gradients in cooling flows in clusters of galaxies'. In: *Astrophysical Journal* 393 (July 1992), pp. 579–610. DOI: 10.1086/171529.

McNamara, B. R. et al. (2000). 'Chandra X-Ray Observations of the Hydra A Cluster: An Interaction between the Radio Source and the X-Ray-emitting Gas'. In: *Astrophysical Journal, Letters* 534 (May 2000), pp. L135–L138. DOI: 10.1086/312662. eprint: arXiv:astro-ph/0001402.

Mewe, R. (1999). 'Atomic Physics of Hot Plasmas'. In: *X-Ray Spectroscopy in Astrophysics*. Ed. by J. van Paradijs & J. A. M. Bleeker. Vol. 520. Lecture Notes in Physics, Berlin Springer Verlag, pp. 109–+.

Miley, G. (1980). 'The structure of extended extragalactic radio sources'. In: *Annual Review of Astronomy and Astrophysics* 18, pp. 165–218. DOI: 10.1146/annurev.aa.18.090180.001121.

Miller, L. (1986). 'Heating and cooling in clusters of galaxies'. In: *Monthly Notices of the RAS* 220 (June 1986), pp. 713–722.

Minkowski, R. (1960). 'A New Distant Cluster of Galaxies.' In: *Astrophysical Journal* 132 (Nov. 1960), pp. 908–910. DOI: 10.1086/146994.

Mirabel, I. F. and L. F. Rodríguez (1999). 'Sources of Relativistic Jets in the Galaxy'. In: *Annual Review of Astronomy and Astrophysics* 37, pp. 409–443. DOI: 10.1146/annurev.astro.37.1.409. eprint: arXiv:astro-ph/9902062.

Mitchell, R. J. et al. (1976). 'Ariel 5 observations of the X-ray spectrum of the Perseus Cluster'. In: *Monthly Notices of the RAS* 175 (May 1976), 29P–34P.

Mittal, R. et al. (2009). 'AGN heating and ICM cooling in the HIFLUGCS sample of galaxy clusters'. In: *Astronomy and Astrophysics* 501 (July 2009), pp. 835–850. DOI: 10.1051/0004-6361/200810836. eprint: 0810.0797.

Mizuta, A., M. Kino and H. Nagakura (2010). 'Hysteresis of Backflow Imprinted in Collimated Jets'. In: *Astrophysical Journal, Letters* 709 (Jan. 2010), pp. L83–L87. DOI: 10.1088/2041-8205/709/1/L83. eprint: 0912.3662.

Mushotzky, R. et al. (1996). 'Measurement of the Elemental Abundances in Four Rich Clusters of Galaxies. I. Observations'. In: *Astrophysical Journal* 466 (Aug. 1996), pp. 686–+. DOI: 10.1086/177541.

Mushotzky, R. F. (1984). 'X-ray emission from clusters of galaxies'. In: *Physica Scripta Volume T* 7, pp. 157–162. DOI: 10.1088/0031-8949/1984/T7/036.

Mushotzky, R. F. and A. E. Szymkowiak (1988). 'Einstein Observatory solid state detector observations of cooling flows in clusters of galaxies'. In: *NATO ASIC Proc. 229: Cooling Flows in Clusters and Galaxies*. Ed. by A. C. Fabian, pp. 53–62.

Mushotzky, R. F. et al. (1978). 'OSO 8 X-ray spectra of clusters of galaxies. I - Observations of twenty clusters: Physical correlations'. In: *Astrophysical Journal* 225 (Oct. 1978), pp. 21–39. DOI: 10.1086/156465.

Narayan, R. and M. V. Medvedev (2001). 'Thermal Conduction in Clusters of Galaxies'. In: *Astrophysical Journal, Letters* 562 (Dec. 2001), pp. L129–L132. DOI: 10.1086/338325. eprint: arXiv:astro-ph/0110567.

Netzer, H. (1990). 'AGN emission lines.' In: *Active Galactic Nuclei*. Ed. by R. D. Blandford, H. Netzer, L. Woltjer, T. J.-L. Courvoisier, & M. Mayor, pp. 57–160.

Neyman, J., T. Page and E. Scott (1961). 'CONFERENCE on the Instability of Systems of Galaxies (Santa Barbara, California, August 1O-12, 1961): Summary of the conference'. In: *Astronomical Journal* 66 (Dec. 1961), pp. 633–+. DOI: 10.1086/108476.

Norman, M. L. et al. (1982). 'Structure and dynamics of supersonic jets'. In: *Astronomy and Astrophysics* 113 (Sept. 1982), pp. 285–302.

Nulsen, P. E. J. (1986). 'Thermal instability in cooling flows'. In: *Monthly Notices of the RAS* 221 (July 1986), pp. 377–392.

Nulsen, P. E. J. et al. (2007). 'AGN Heating Through Cavities and Shocks'. In: *Heating versus Cooling in Galaxies and Clusters of Galaxies*. Ed. by H. Böhringer, G. W. Pratt, A. Finoguenov, & P. Schuecker, pp. 210–+. eprint: arXiv:astro-ph/0611136.

O'Dea, C. P., J. F. Gallimore and S. A. Baum (1995). 'A high spectral resolution VLA search for H I absorption towards A496, A1795, and A2584'. In: *Astronomical Journal* 109 (Jan. 1995), pp. 26–31. DOI: 10.1086/117253.

O'Dea, C. P., H. E. Payne and D. Kocevski (1998). 'An Arecibo Search for Broad 21 Centimeter Lines of Atomic Hydrogen in Clusters of Galaxies'. In: *Astronomical Journal* 116 (Aug. 1998), pp. 623–633. DOI: 10.1086/300457.

O'Dea, C. P. et al. (1994). 'Constraints on molecular gas in cooling flows and powerful radio galaxies'. In: *Astrophysical Journal* 422 (Feb. 1994), pp. 467–479. DOI: 10.1086/173742.

Oegerle, W. R. et al. (2001). 'FUSE Observations of Cooling-Flow Gas in the Galaxy Clusters A1795 and A2597'. In: *Astrophysical Journal* 560 (Oct. 2001), pp. 187–193. DOI: 10.1086/322246. eprint: arXiv:astro-ph/0106279.

Olsen, K. (2006). 'PARAMESH: A Parallel Adaptive Grid Tool'. In: *Parallel Computational Fluid Dynamics 2005: Theory and Applications*.

Olsen, K. and P. MacNeice (2005). 'An Overview of the PARAMESH AMR Software Package and Some of Its Applications'. In: *Adaptive Mesh Refinement - Theory and Applications: Proceedings of the Chicago Workshop on Adaptive Mesh Refinement Methods, Sept. 35, 2003* 41 (Dec. 2005), pp. 315–330.

Omma, H. et al. (2004). 'Heating cooling flows with jets'. In: *Monthly Notices of the RAS* 348 (Mar. 2004), pp. 1105–1119. DOI: 10.1111/j.1365-2966.2004.07382.x. eprint: arXiv:astro-ph/0307471.

O'Neill, S. M. and T. W. Jones (2010). 'Three-Dimensional Simulations of Bi-Directed Magnetohydrodynamic Jets Interacting with Cluster Environments'. In: *Astrophysical Journal* 710 (Feb. 2010), pp. 180–196. DOI: 10.1088/0004-637X/710/1/180. eprint: 1001.1747.

Osterbrock, D. E. (1977). 'Physical Conditions in Radio Galaxies and Quasars'. In: *Radio Astronomy and Cosmology*. Ed. by D. L. Jauncey. Vol. 74. IAU Symposium, pp. 183–+.

Osterbrock, D. E. and A. T. Koski (1976). 'NGC 4151 and Markarian 6 - two intermediate-type Seyfert galaxies'. In: *Monthly Notices of the RAS* 176 (Aug. 1976), 61P–66P.

Ostriker, J. P., P. Bode and A. Babul (2005). 'A Simple and Accurate Model for Intracluster Gas'. In: *Astrophysical Journal* 634 (Dec. 2005), pp. 964–976. DOI: 10.1086/497122. eprint: arXiv:astro-ph/0504334.

Peres, C. B. et al. (1998). 'A ROSAT study of the cores of clusters of galaxies - I. Cooling flows in an X-ray flux-limited sample'. In: *Monthly Notices of the RAS* 298 (Aug. 1998), pp. 416–432. DOI: 10.1046/j.1365-8711.1998.01624.x. eprint: arXiv:astro-ph/9805122.

Perley, R. A., J. W. Dreher and J. J. Cowan (1984). 'The jet and filaments in Cygnus A'. In: *Astrophysical Journal, Letters* 285 (Oct. 1984), pp. L35–L38. DOI: 10.1086/184360.

Peterson, J. R. et al. (2001). 'X-ray imaging-spectroscopy of Abell 1835'. In: *Astronomy and Astrophysics* 365 (Jan. 2001), pp. L104–L109. DOI: 10.1051/0004-6361:20000021. eprint: arXiv:astro-ph/0010658.

Peterson, J. R. et al. (2003). 'High-Resolution X-Ray Spectroscopic Constraints on Cooling-Flow Models for Clusters of Galaxies'. In: *Astrophysical Journal* 590 (June 2003), pp. 207–224. DOI: 10.1086/374830. eprint: arXiv:astro-ph/0210662.

Pipino, A. et al. (2002). 'SNe heating and the chemical evolution of the intra-cluster medium'. In: *New Astronomy* 7 (July 2002), pp. 227–247. DOI: 10.1016/S1384-1076(02)00136-7. eprint: arXiv:astro-ph/0204161.

Pizzolato, F. and N. Soker (2006). 'On the Rayleigh-Taylor instability of radio bubbles in galaxy clusters'. In: *Monthly Notices of the RAS* 371 (Oct. 2006), pp. 1835–1848. DOI: 10.1111/j.1365-2966.2006.10803.x. eprint: arXiv:astro-ph/0605534.

Rafferty, D. A. et al. (2006). 'The Feedback-regulated Growth of Black Holes and Bulges through Gas Accretion and Starbursts in Cluster Central Dominant Galaxies'. In:

Astrophysical Journal 652 (Nov. 2006), pp. 216–231. DOI: 10.1086/507672. eprint: arXiv:astro-ph/0605323.

Reber, G. (1944). 'Cosmic Static.' In: *Astrophysical Journal* 100 (Nov. 1944), pp. 279–+. DOI: 10.1086/144668.

Rees, M. J. (1966). 'Appearance of Relativistically Expanding Radio Sources'. In: *Nature* 211 (July 1966), pp. 468–470. DOI: 10.1038/211468a0.

— (1971). 'New Interpretation of Extragalactic Radio Sources'. In: *Nature* 229 (Jan. 1971), pp. 312–317. DOI: 10.1038/229312a0.

— (1978). 'The M87 jet - Internal shocks in a plasma beam'. In: *Monthly Notices of the RAS* 184 (Sept. 1978), 61P–65P.

Reipurth, B. and J. Bally (2001). 'Herbig-Haro Flows: Probes of Early Stellar Evolution'. In: *Annual Review of Astronomy and Astrophysics* 39, pp. 403–455. DOI: 10.1146/annurev.astro.39.1.403.

Renzini, A. et al. (1993). 'Production and Circulation of Iron in Elliptical Galaxies and Clusters of Galaxies'. In: *Astrophysical Journal* 419 (Dec. 1993), pp. 52–+. DOI: 10.1086/173458.

Reynolds, C. S., S. Heinz and M. C. Begelman (2001). 'Shocks and Sonic Booms in the Intracluster Medium: X-Ray Shells and Radio Galaxy Activity'. In: *Astrophysical Journal, Letters* 549 (Mar. 2001), pp. L179–L182. DOI: 10.1086/319159. eprint: arXiv:astro-ph/0011040.

— (2002). 'The hydrodynamics of dead radio galaxies'. In: *Monthly Notices of the RAS* 332 (May 2002), pp. 271–282. DOI: 10.1046/j.1365-8711.2002.04724.x. eprint: arXiv:astro-ph/0201271.

Reynolds, C. S. et al. (2005). 'Buoyant radio lobes in a viscous intracluster medium'. In: *Monthly Notices of the RAS* 357 (Feb. 2005), pp. 242–250. DOI: 10.1111/j.1365-2966.2005.08643.x. eprint: arXiv:astro-ph/0402632.

Robinson, K. et al. (2004). 'Morphology of Rising Hydrodynamic and Magnetohydrodynamic Bubbles from Numerical Simulations'. In: *Astrophysical Journal* 601 (Feb. 2004), pp. 621–643. DOI: 10.1086/380817. eprint: arXiv:astro-ph/0310517.

Roediger, E. and M. Brüggen (2007). 'Ram pressure stripping of disc galaxies orbiting in clusters - I. Mass and radius of the remaining gas disc'. In: *Monthly Notices of the RAS* 380 (Oct. 2007), pp. 1399–1408. DOI: 10.1111/j.1365-2966.2007.12241.x. eprint: 0707.2698.

Ruszkowski, M. and M. C. Begelman (2002). 'Heating, Conduction, and Minimum Temperatures in Cooling Flows'. In: *Astrophysical Journal* 581 (Dec. 2002), pp. 223–228. DOI: 10.1086/344170. eprint: arXiv:astro-ph/0207471.

Ruszkowski, M., M. Brüggen and M. C. Begelman (2004*a*). 'Cluster Heating by Viscous Dissipation of Sound Waves'. In: *Astrophysical Journal* 611 (Aug. 2004), pp. 158–163. DOI: 10.1086/422158. eprint: arXiv:astro-ph/0310760.

— (2004*b*). 'Three-Dimensional Simulations of Viscous Dissipation in the Intracluster Medium'. In: *Astrophysical Journal* 615 (Nov. 2004), pp. 675–680. DOI: 10.1086/424702. eprint: arXiv:astro-ph/0403690.

Ruszkowski, M. and S. P. Oh (2010). 'Shaken and Stirred: Conduction and Turbulence in Clusters of Galaxies'. In: *Astrophysical Journal* 713 (Apr. 2010), pp. 1332–1342. DOI: 10.1088/0004-637X/713/2/1332. eprint: 0911.5198.

Rybicki, G. B. and A. P. Lightman (1979). *Radiative processes in astrophysics*. Ed. by Rybicki, G. B. & Lightman, A. P.

Sakelliou, I. et al. (2002). 'High resolution soft X-ray spectroscopy of M 87 with the reflection grating spectrometers on XMM-Newton'. In: *Astronomy and Astrophysics* 391 (Sept. 2002), pp. 903–909. DOI: 10.1051/0004-6361:20020900. eprint: arXiv:astro-ph/0206249.

Salpeter, E. E. (1964). 'Accretion of Interstellar Matter by Massive Objects.' In: *Astrophysical Journal* 140 (Aug. 1964), pp. 796–800. DOI: 10.1086/147973.

Sandage, A. (1965). 'The Existence of a Major New Constituent of the Universe: the Quasistellar Galaxies.' In: *Astrophysical Journal* 141 (May 1965), pp. 1560–+. DOI: 10.1086/148245.

Sanders, J. S. and A. C. Fabian (2007). 'A deeper X-ray study of the core of the Perseus galaxy cluster: the power of sound waves and the distribution of metals and cosmic rays'. In: *Monthly Notices of the RAS* 381 (Nov. 2007), pp. 1381–1399. DOI: 10.1111/j.1365-2966.2007.12347.x. eprint: 0705.2712.

Sanders, J. S. and A. C. Fabian (2008). 'Sound waves in the intracluster medium of the Centaurus cluster'. In: *Monthly Notices of the RAS* 390 (Oct. 2008), pp. L93–L97. DOI: 10.1111/j.1745-3933.2008.00549.x. eprint: 0808.2384.

Sanders, J. S. et al. (2008). 'Cool X-ray emitting gas in the core of the Centaurus cluster of galaxies'. In: *Monthly Notices of the RAS* 385 (Apr. 2008), pp. 1186–1200. DOI: 10.1111/j.1365-2966.2008.12952.x. eprint: 0711.2456.

Sarazin, C. L. (1988). *X-ray emission from clusters of galaxies*. Ed. by Sarazin, C. L.

Scannapieco, E. and M. Brüggen (2008). 'Subgrid Modeling of AGN-driven Turbulence in Galaxy Clusters'. In: *Astrophysical Journal* 686 (Oct. 2008), pp. 927–947. DOI: 10.1086/591228. eprint: 0806.3268.

Scheuer, P. A. G. (1974). 'Models of extragalactic radio sources with a continuous energy supply from a central object'. In: *Monthly Notices of the RAS* 166 (Mar. 1974), pp. 513–528.

Scheuer, P. A. G. and A. C. S. Readhead (1979). 'Superluminally expanding radio sources and the radio-quiet QSOs'. In: *Nature* 277 (Jan. 1979), pp. 182–185. DOI: 10.1038/277182a0.

Schmidt, M. (1963). '3C 273 : A Star-Like Object with Large Red-Shift'. In: *Nature* 197 (Mar. 1963), pp. 1040–+. DOI: 10.1038/1971040a0.

— (1970). 'Space Distribution and Luminosity Functions of Quasars'. In: *Astrophysical Journal* 162 (Nov. 1970), pp. 371–+. DOI: 10.1086/150668.

Schuecker, P. et al. (2004). 'Probing turbulence in the Coma galaxy cluster'. In: *Astronomy and Astrophysics* 426 (Nov. 2004), pp. 387–397. DOI: 10.1051/0004-6361:20041039. eprint: arXiv:astro-ph/0404132.

Serlemitsos, P. J. et al. (1977). 'X-radiation from clusters of galaxies - Spectral evidence for a hot evolved gas'. In: *Astrophysical Journal, Letters* 211 (Jan. 1977), pp. L63–L66. DOI: 10.1086/182342.

Seyfert, C. K. (1943). 'Nuclear Emission in Spiral Nebulae.' In: *Astrophysical Journal* 97 (Jan. 1943), pp. 28–+. DOI: 10.1086/144488.

Shabala, S. S. and P. Alexander (2009). 'Sound waves in the intracluster medium'. In: *Monthly Notices of the RAS* 392 (Feb. 2009), pp. 1413–1420. DOI: 10.1111/j.1365-2966.2008.14125.x.

Silk, J. (1976). 'Accretion by galaxy clusters and the relationship between X-ray luminosity and velocity dispersion'. In: *Astrophysical Journal* 208 (Sept. 1976), pp. 646–649. DOI: 10.1086/154645.

Smith, S. (1936). 'The Mass of the Virgo Cluster'. In: *Astrophysical Journal* 83 (Jan. 1936), pp. 23–+. DOI: 10.1086/143697.

Soker, N., E. L. Blanton and C. L. Sarazin (2004). 'Cooling of X-ray emitting gas by heat conduction in the center of cooling flow clusters'. In: *Astronomy and Astrophysics* 422 (Aug. 2004), pp. 445–452. DOI: 10.1051/0004-6361:20034415. eprint: arXiv:astro-ph/0309633.

Soker, N. et al. (2001). 'A Moderate Cluster Cooling Flow Model'. In: *Astrophysical Journal* 549 (Mar. 2001), pp. 832–839. DOI: 10.1086/319433. eprint: arXiv:astro-ph/0009173.

Spitzer, L. (1962). *Physics of Fully Ionized Gases*. Ed. by Spitzer, L.

— (1978). *Physical processes in the interstellar medium*. Ed. by Spitzer, L.

Sternberg, A., F. Pizzolato and N. Soker (2007). 'Inflating Fat Bubbles in Clusters of Galaxies by Wide Jets'. In: *Astrophysical Journal, Letters* 656 (Feb. 2007), pp. L5–L8. DOI: 10.1086/512122. eprint: arXiv:astro-ph/0612760.

Sternberg, A. and N. Soker (2009). 'Sound waves excitation by jet-inflated bubbles in clusters of galaxies'. In: *Monthly Notices of the RAS* 395 (May 2009), pp. 228–233. DOI: 10.1111/j.1365-2966.2009.14566.x. eprint: 0808.2294.

Stewart, G. C. et al. (1984*a*). 'The mass profile and gas content of M87'. In: *Astrophysical Journal* 278 (Mar. 1984), pp. 536–543. DOI: 10.1086/161820.

Stewart, G. C. et al. (1984*b*). 'The prevalence of cooling flows in clusters of galaxies'. In: *Astrophysical Journal* 285 (Oct. 1984), pp. 1–6. DOI: 10.1086/162470.

Sutherland, R. S. (1998). 'Accurate free-free Gaunt factors for astrophysical plasmas'. In: *Monthly Notices of the RAS* 300 (Oct. 1998), pp. 321–330. DOI: 10.1046/j.1365-8711.1998.01687.x.

Sutherland, R. S. and M. A. Dopita (1993). 'Cooling functions for low-density astrophysical plasmas'. In: *Astrophysical Journal, Supplement* 88 (Sept. 1993), pp. 253–327. DOI: 10.1086/191823.

Tamura, T. et al. (2001). 'X-ray spectroscopy of the cluster of galaxies Abell 1795 with XMM-Newton'. In: *Astronomy and Astrophysics* 365 (Jan. 2001), pp. L87–L92. DOI: 10.1051/0004-6361:20000038. eprint: arXiv:astro-ph/0010362.

The HDF Group (2011). *http://www.hdfgroup.org/HDF5/*.

Thomas, P. A., A. C. Fabian and P. E. J. Nulsen (1987). 'Mass deposition in cooling flows - Analysis of the X-ray data'. In: *Monthly Notices of the RAS* 228 (Oct. 1987), pp. 973–991.

Urry, C. M. and P. Padovani (1995). 'Unified Schemes for Radio-Loud Active Galactic Nuclei'. In: *Publications of the ASP* 107 (Sept. 1995), pp. 803–+. DOI: 10.1086/133630. eprint: arXiv:astro-ph/9506063.

van Paradijs, J. and J. E. McClintock (1995). 'Optical and ultraviolet observations of X-ray binaries.' In: *X-ray Binaries*. Ed. by W. H. G. Lewin, J. van Paradijs, & E. P. J. van den Heuvel, pp. 58–125.

Vernaleo, J. C. and C. S. Reynolds (2006). 'AGN Feedback and Cooling Flows: Problems with Simple Hydrodynamic Models'. In: *Astrophysical Journal* 645 (July 2006), pp. 83–94. DOI: 10.1086/504029. eprint: arXiv:astro-ph/0511501.

— (2007). 'Energetic Impact of Jet-Inflated Cocoons in Relaxed Galaxy Clusters'. In: *Astrophysical Journal* 671 (Dec. 2007), pp. 171–180. DOI: 10.1086/523262. eprint: 0708.4015.

Vikhlinin, A., M. Markevitch and S. S. Murray (2001*a*). 'A Moving Cold Front in the Intergalactic Medium of A3667'. In: *Astrophysical Journal* 551 (Apr. 2001), pp. 160–171. DOI: 10.1086/320078. eprint: arXiv:astro-ph/0008496.

— (2001*b*). 'Chandra Estimate of the Magnetic Field Strength near the Cold Front in A3667'. In: *Astrophysical Journal, Letters* 549 (Mar. 2001), pp. L47–L50. DOI: 10.1086/319126. eprint: arXiv:astro-ph/0008499.

Vikhlinin, A. et al. (2006). 'Chandra Sample of Nearby Relaxed Galaxy Clusters: Mass, Gas Fraction, and Mass-Temperature Relation'. In: *Astrophysical Journal* 640 (Apr. 2006), pp. 691–709. DOI: 10.1086/500288. eprint: arXiv:astro-ph/0507092.

Voigt, L. M. and A. C. Fabian (2004). 'Thermal conduction and reduced cooling flows in galaxy clusters'. In: *Monthly Notices of the RAS* 347 (Feb. 2004), pp. 1130–1149. DOI: 10.1111/j.1365-2966.2004.07285.x. eprint: arXiv:astro-ph/0308352.

Voigt, L. M. et al. (2002). 'Conduction and cooling flows'. In: *Monthly Notices of the RAS* 335 (Sept. 2002), pp. L7–L11. DOI: 10.1046/j.1365-8711.2002.05741.x. eprint: arXiv:astro-ph/0203312.

von der Linden, A. et al. (2007). 'How special are brightest group and cluster galaxies?' In: *Monthly Notices of the RAS* 379 (Aug. 2007), pp. 867–893. DOI: 10.1111/j.1365-2966.2007.11940.x. eprint: arXiv:astro-ph/0611196.

Wardle, J. F. C. et al. (1998). 'Electron-positron jets associated with the quasar 3C279'. In: *Nature* 395 (Oct. 1998), pp. 457–461. DOI: 10.1038/26675.

Zel'Dovich, Y. B. (1964). 'The Fate of a Star and the Evolution of Gravitational Energy Upon Accretion'. In: *Soviet Physics Doklady* 9 (Sept. 1964), pp. 195–+.

Zirbel, E. L. (1996). 'Properties of Host Galaxies of Powerful Radio Sources'. In: *Astrophysical Journal* 473 (Dec. 1996), pp. 713–+. DOI: 10.1086/178184.

— (1997). 'The Megaparsec Environments of Radio Galaxies'. In: *Astrophysical Journal* 476 (Feb. 1997), pp. 489–+. DOI: 10.1086/303626.

Zwicky, F., E. Herzog and P. Wild (1961). *Catalogue of galaxies and of clusters of galaxies, Vol. I.* Ed. by Zwicky, F., Herzog, E., & Wild, P.

Index